Ascension et dégazage des magmas basaltiques : approche expérimentale

Nolwenn Le Gall

UNIVERSITÉ D'ORLÉANS

ÉCOLE DOCTORALE
ENERGIE, MATERIAUX, SCIENCES DE LA TERRE ET DE L'UNIVERS

Institut des Sciences de la Terre d'Orléans, ISTO

THÈSE présentée par :

Nolwenn LE GALL

soutenue le : **06 novembre 2015**

pour obtenir le grade de : **Docteur de l'université d'Orléans**
Discipline/ Spécialité : Science de la Terre et de l'Atmosphère

Ascension et dégazage des magmas basaltiques – Approche expérimentale

THÈSE dirigée par :

Michel PICHAVANT	Directeur de recherche, CNRS, ISTO, Orléans

RAPPORTEURS :

Don R. BAKER	Professeur, McGill University, Montréal
Didier LAPORTE	Directeur de recherche, CNRS, LMV, Clermont-Ferrand

---

JURY :

Bruno SCAILLET	Directeur de recherche, CNRS, ISTO, Orléans, Président du jury
Don R. BAKER	Professeur, McGill University, Montréal
Alain BURGISSER	Chargé de recherche, CNRS, ISTerre, Chambéry
Didier LAPORTE	Directeur de recherche, CNRS, LMV, Clermont-Ferrand
Michel PICHAVANT	Directeur de recherche, CNRS, ISTO, Orléans, Directeur de thèse
Massimo POMPILIO	Directeur de recherche, INGV, Pise

A Papa

Remerciements

La première personne que je tiens à remercier est bien évidemment Michel auprès de qui j'ai tout appris de la volcanologie expérimentale. Merci pour ta confiance accordée depuis mes années de Master, tes précieux conseils et ta disponibilité. Tu avais raison, le sujet de cette thèse m'a énormément plu !

Merci aux membres de mon jury, à Bruno Scaillet d'avoir présidé ma soutenance avec toujours autant d'humour, à Don Baker et Didier Laporte pour leurs rapports constructifs et leurs suggestions, ainsi qu'à Alain Burgisser et Massimo Pompilio pour leurs remarques. Un grand merci à vous !

J'en profite pour te remercier Massimo, pour ta passion partagée des volcans italiens, l'Etna puis le Stromboli, merci pour les missions de terrain et d'échantillonnage.

Merci à Didier Laporte et Jo Gottsmann pour la coordination de leurs deux projets de recherche, DEGAZMAG et VUELCO, dont les rencontres, les discussions et les évènements (notamment les exercices de simulation) ont été pour moi une formidable expérience.

Un grand merci à ceux de l'atelier avec en tête Rémi, Esteban, Philippe, Nicolas et Rémi (le petit !), ainsi qu'à Didier. Merci à vous pour votre grande disponibilité et votre patience (souvent mise à rude épreuve) !

Merci à Ida pour les analyses à la sonde et au MEB, et pour ses connaissances du Stromboli et de sa fameuse ponce PST-9 partagées depuis mes années de Master !

Merci à Alain d'avoir pris le temps de m'apprendre à me servir du microtomographe par rayons X, cette autonomie m'a été bien utile. Merci aussi à Philippe, Laurent et Olivier pour avoir géré le côté « technique » par la suite.

Merci aussi aux informaticiens, à Yohann, Laurent et Kévin.

Merci aux membres de l'ISTO (pour n'oublier personne) et plus particulièrement à l'équipe Magma. Je citerai Caroline pour nos discussions de bulles et ton sens de l'humour, Giada et Juan pour votre patience et votre aide avec les autoclaves, ainsi que Marina pour ton aide lors du lancement de mes premières manips de thèse et pour ta grande gentillesse. Un clin d'œil aussi à l'équipe Géodynamique, et notamment à Laurent, ainsi qu'à Patricia toujours prête à nous renseigner et nous dépanner en produits chimiques, lames minces, … !

Merci à Marie-Noëlle, Olivier, Marlène, Nathalie, Chantal et Fabienne, tant pour votre gentillesse et sympathie que pour les démarches administratives.

Merci à mon Valentin, pour la dose de bonne humeur quotidienne.

Merci aux filles, Leïla et Leslie, pour tous nos bavardages et votre amitié.

Merci aux autres thésards et post-docs, à ceux qui ont débuté leur thèse en même temps que moi, Colin (mon super co-bureau !), Dada, Malky et Memel, à ceux qui sont arrivés en cours, Alex (-andra et –andre !), Vincent, Yann, Rabi, Eloïse, Hugues et Jo, Papy et Sarah, Giulia et Cam', Anne-Aziliz, Hugo, Max, Adoum, Emmanuela,

Clément, Julie, Kévin, Mohammed, et à ceux qui sont partis entre temps, Anita, Mimick et Yves.

Merci aussi à Clairette et Momo, Ananas et P'tit Gui, Charlène, Virginie, Delphine et Nonette (vive nos soirées filles !).

Merci à ma famille, en particulier à Maman et Yann dont je suis très fière, à mes grands-parents adorés, à Danièle, Edith (j'ai une pensée émue pour toi…), Bruno et Pierre (merci pour votre accueil orléanais), à Emmanuel et Anita et à ma belle-famille.

"Voilà, c'est fini"…

Introduction 13

1. Dégazage et vésiculation des magmas 15
2. Objectifs et méthodes 16
3. Structure du manuscrit 17

Chapitre i : Cadre général 19

1. Le dégazage magmatique 21
1.1. Les volatils dans les magmas 21
1.1.1. *Solubilité des volatils dans les basaltes* 22
1.1.2. *Diffusivité des volatils dans les basaltes* 22
1.2. Comportement des volatils au cours de la décompression 24
1.2.1. *Le dégazage magmatique* 24
1.2.2. *Les mécanismes du dégazage magmatique* 25
1.2.3. *Implications pour la dynamique des éruptions* 26
2. Nucléation des bulles dans les magmas 27
2.1. Aspects théoriques 27
2.1.1. *Théorie classique de la nucléation* 27
2.1.2. *Nucléation homogène* 29
2.1.3. *Nucléation hétérogène* 29
2.1.4. *Effet de la tension de surface* 31
2.2. Aspects naturels 31
2.2.1. *Vésicularité* 31
2.2.2. *Densité numérique de bulles* 32
2.2.3. *Distribution de taille des bulles* 32
2.3. Aspects expérimentaux 35
2.3.1. *Travaux antérieurs* 35
2.3.2. *Pressions de sursaturation* 36
2.3.3. *Tensions de surface* 37
3. Modèles théoriques de dégazage des magmas basaltiques 38
3.1. Dégazage à l'équilibre 38
3.2. Inclusions vitreuses 38
3.3. Volcanisme basaltique explosif 39
4. Approche expérimentale 41
4.1. Stratégie expérimentale 41
4.2. Calage des expériences de décompression 43
4.2.1. *Choix du volcan de référence : Le Stromboli* 43
4.2.2. *Choix du matériel de départ : La ponce Strombolienne PST-9* 45
4.2.3. *Gaz volcaniques* 47

Chapitre ii : Méthodes expérimentales et techniques analytiques 49

1. Méthodes expérimentales 51
1.1. Préparation des verres de départ 51
1.1.1. *Préparation des capsules* 53
1.1.2. *Remplissage des capsules* 55
1.2. Dispositif expérimental 57

1.2.1. *Autoclave à chauffage interne* 57
1.2.2. *Mesure des conditions d'oxydoréduction* 59
1.3. Protocole expérimental 60
1.3.1. *Expériences de synthèse* 60
1.3.2. *Expériences de décompression* 61
2. Techniques analytiques 62
2.1. Préparation des échantillons 62
2.2. Microtomographie par rayons X 64
2.3. Microscopie électronique à balayage (MEB) 66
2.4. Microsonde électronique 68
2.5. Spectrométrie infrarouge à transformée de Fourier (FTIR) 70
2.6. Calculs thermodynamiques 71
2.6.1. *Vésicularités d'équilibre* 71
2.6.2. Equilibres liquide-vapeur 72
2.7. Calculs de bilan de masse 73

Chapitre iii : Nucléation homogène des bulles dans les systèmes basalte-H_2O et basalte H_2O-CO_2 75

Résumé 77

1. Introduction 80
2. Theoretical background 82
3. Experimental methods 84
3.1. Preparation of starting glasses 84
3.2. Equipment 85
3.3. Run procedure 86
4. Analytical methods 87
4.1. Sample preparation 87
4.2. Textural analyses 87
4.3. Scanning electron microscopy 89
4.4. Glass volatile contents 89
5. Experimental results 90
5.1. Volatile contents of pre-decompression glasses 90
5.2. Qualitative textural characteristics of post-decompression glasses 91
5.3. Quantitative study of internal textures 92
5.4. Volatile contents of post-decompression 94
6. Interpretation and discussion of experimental observations 96
6.1. Supersaturation pressures required for homogeneous bubble nucleation 96
6.2. Physical mechanisms of degassing and textures 98
6.2.1. *Vesicularities* 99
6.2.2. *Nucleation events* 99
6.2.3. *Bubble coalescence* 101
6.2.4. *Fragmentation* 102
6.3. Role of CO_2 on physical mechanisms of degassing and textures 103
6.4. Equilibrium vs. non-equilibrium degassing 103
7. Volcanological implications 105
7.1. Comparison between experimental and natural textural parameters 105
7.2. Use of BSD systematics 106

8. Conclusions **110**

Appendix **112**
References **113**
Figure captions **118**

Chapitre iv : Effet de la vitesse d'ascension sur la nucléation homogène des bulles dans les systèmes basalte-H_2O et basalte H_2O-CO_2 : Implications pour le volcan Stromboli **137**

Résumé **139**

1. Introduction **142**
2. Volcanological background **144**
3. Experimental methods **145**
3.1. Scaling of the decompression experiments 145
3.2. Starting material 146
3.3. Equipment 147
3.4. Run procedure 148
4. Analytical methods **149**
4.1. Sample preparation 149
4.2. Textural analyses 149
4.3. Glass volatile concentrations 150
5. Experimental results **152**
5.1. Redox conditions 152
5.2. H_2O and CO_2 concentrations in starting glasses 152
5.3. Textures of post-decompression glasses: qualitative observations 153
5.4. Textures of post-decompression glasses: quantitative observations 154
5.5. H_2O and CO_2 concentrations in post-decompression glasses 157
6. Interpretation and discussion of experimental observations **158**
6.1. Supersaturation pressures required for homogeneous bubble nucleation 158
6.2. Physical mechanisms of degassing and textures 160
6.2.1. *Vesicularities* 161
6.2.2. *Nucleation events* 161
6.2.3. *Bubble coalescence* 163
6.2.4. *Bubble size distributions* 165
6.2.5. *Fragmentation* 166
6.3. Equilibrium vs. non-equilibrium degassing 166
6.4. Effect of decompression rate on degassing mechanisms 167
7. Volcanological implications **169**
7.1. Comparison between experimental and Strombolian textural parameters 169
7.2. Implications for the dynamics of magma ascent at Stromboli volcano 171
8. Conclusions **172**

Appendix **174**
References **175**
Figure captions **180**

Chapitre v : Nucléation hétérogène des bulles dans les systèmes basalte-H_2O et basalte H_2O-CO_2 199

Résumé 201

1. Introduction 203
2. Experimental methods 205
2.1. Preparation of starting glasses 205
2.2. Equipment 206
2.3. Run procedure 207
2.4. Control of redox conditions 208
3. Analytical techniques 208
3.1. Sample preparation 208
3.2. Textural analyses 209
3.3. Volatile concentrations 210
4. Experimental results 211
4.1. Synthesis experiments 211
4.2. Decompression experiments 212
4.3. Quantitative textural observations 214
4.4. Volatile contents in post-decompression glasses 215
5. Interpretation and discussion of experimental observations 217
5.1. Heterogeneous vs. homogeneous bubble nucleation 217
5.2. Equilibrium vs. disequilibrium degassing 219
6. Volcanological implications 220
6.1. Heterogeneous bubble nucleation in basaltic magmas 220
6.2. Influence of Fe–Ti oxide crystals on degassing mechanisms 222
7. Conclusions 222

References 224
Figure captions 227

Chapitre vi : Partage du soufre entre liquide et gaz lors de l'ascension et du dégazage d'un magma basaltique contenant les volatils C-H-O-S 241

Résumé 243

1. Introduction 246
2. Experimental techniques 248
2.1. Starting material and capsule preparation 248
2.2. Apparatus and run procedure 249
3. Analytical techniques 251
3.1. Sample preparation 251
3.2. Textures 251
3.3. Major elements and sulfur 251
3.4. H_2O and CO_2 252
3.5. Fluid phase 253
3.6. Fluid-melt equilibrium computations 253
4. Experimental results 254
4.1. Charge-capsule interactions 254

4.2. Textural observations 254
4.3. Volatile contents of experimental glasses 255
4.4. Composition of experimental fluids 257
4.5. Sulfur partitioning 258
5. Discussion 258
5.1. Bubble textures 258
5.2. Comparison with glass inclusions 259
5.3. Comparison with volcanic gases 260
5.4. A degassing model for Stromboli volcano 262
6. Conclusions 265

References 267
Figure captions 271

Synthèse générale et perspectives 285

1. Rappel des principaux résultats 287
1.1. Basalte-H_2O 287
1.2. Basalte-H_2O-CO_2 288
1.3. Basalte-H_2O-CO_2-S 291
1.4. Influence de la vitesse d'ascension 292
1.5. Implications pour le volcan Stromboli 293
2. Spécificités des liquides basaltiques 294
2.1. Nucléation homogène des bulles 294
2.2. Nucléation hétérogène des bulles 295
2.3. Caractéristiques texturales 295
3. Améliorations et perspectives de recherche 296

Bibliographie 301

Liste des figures 313

Liste des tableaux 317

Introduction

1. Dégazage et vésiculation des magmas

Les éruptions volcaniques sont l'expression à la surface de la Terre, par l'émission de laves, de fragments magmatiques (cendres, lapillis, blocs et bombes) et de gaz, des processus qui interviennent en profondeur. Elles sont provoquées par le dégazage des magmas qui remontent dans le conduit volcanique, c.-à-d. par l'exsolution (ou perte) des volatils dissous dans le liquide silicaté. Ce processus se manifeste par la nucléation de bulles de gaz au sein du liquide (nucléation homogène des bulles), éventuellement sur la face de cristaux (nucléation hétérogène des bulles), et leur croissance diffusive.

Les éruptions volcaniques peuvent être effusives ou explosives, en lien avec le comportement de la phase gazeuse. Les éruptions effusives émettent des laves dégazées, sous forme de coulées pour les volcans basaltiques ; l'ascension du magma et des bulles de gaz est séparée (dégazage en système ouvert). Au contraire, les éruptions explosives sont souvent produites par des magmas contenant une importante fraction volumique de bulles de gaz (dégazage en système fermé). La capacité de la phase gazeuse à se séparer violemment ou non du magma dépend en grande partie des processus de nucléation (profondeur du dégazage), de croissance et de coalescence des bulles (développement de la perméabilité du magma favorisant la perte des volatils dissous), constituant le phénomène de la vésiculation.

Les impacts des éruptions volcaniques peuvent être conséquents pour l'homme et le climat (effet des émissions de gaz), d'où l'intérêt scientifique de mieux comprendre les processus de dégazage magmatique (processus syn-éruptifs). En particulier, celui de la nucléation des bulles de gaz qui constitue la première étape de la vésiculation des magmas, dont vont dépendre la croissance et la coalescence des bulles, ainsi que la fragmentation du magma.

Le processus de nucléation des bulles de gaz n'a été que peu étudié dans les systèmes basaltiques lesquels sont souvent considérés comme peu explosifs et donc peu dangereux. Or, les volcans basaltiques peuvent aussi développer des dynamismes très énergétiques conduisant à de violentes éruptions. Ces manifestations explosives, souvent appelées paroxysmes, sont connues sur plusieurs volcans basaltiques et notamment au Stromboli, le volcan référence dans notre étude. La dangerosité de ces éruptions réside dans le fait qu'elles apparaissent comme accidentelles dans l'histoire éruptive, et un des buts de la volcanologie moderne est donc d'identifier des signaux précurseurs permettant de mieux les prévoir. Au Stromboli, des avancées ont été faites dans ce sens, notamment par la mise en place de

systèmes de mesures géochimiques et géophysiques en continu (suite à la crise de 2002–2003) et, d'autre part, par l'étude texturale et pétrologique des produits éruptifs associés à ces paroxysmes. Cependant, dans le cas des mesures de gaz volcaniques, par exemple, leur interprétation se base sur un modèle de dégazage à l'équilibre des liquides basaltiques. Or, des expériences récentes (Pichavant et al., 2013) ont démontré la possibilité d'un comportement hors équilibre du CO_2 lors du dégazage des liquides basaltiques. L'interprétation des données de surveillance des volcans n'est donc pas évidente et requiert la connaissance fondamentale des mécanismes éruptifs mis en jeu. Pour ce faire, l'expérimentation est utile car elle permet d'approcher les conditions d'ascension des magmas et de la vésiculation des bulles de gaz (nucléation, croissance, coalescence) par des simulations en laboratoire en conditions contrôlées et réalistes ; l'objectif étant de comprendre les mécanismes qui contrôlent les caractéristiques texturales (nombre, taille, forme des bulles) et chimiques (teneur en volatils dissous, composition des gaz) des produits naturels et de les approcher.

2. Objectifs et méthodes

L'enjeu de cette thèse est de comprendre, à travers une étude expérimentale, quelles sont les conditions de nucléation (homogène/hétérogène) des bulles de gaz dans les liquides basaltiques. Les principaux objectifs étant d'apporter des contraintes sur l'influence des volatils majeurs (H_2O, CO_2, S) dissous dans ces liquides au cours des processus de dégazage (nucléation, croissance, coalescence, fragmentation), ainsi que sur les effets de la vitesse d'ascension, d'une part, et de la présence de cristaux, d'autre part, sur la cinétique de vésiculation.

Ce travail de thèse consiste en une étude expérimentale qui vise à simuler les conditions naturelles de la vésiculation lors de l'ascension d'un magma basaltique dans un conduit volcanique. Notre volcan cible est le Stromboli qui est un volcan de référence de par la connaissance importante dont on dispose de son activité et de ses produits. Les expériences menées ont été, d'une part, des synthèses pour produire des liquides basaltiques de départ contenant les volatils dissous en concentrations appropriées et, d'autre part, des décompressions pour simuler l'ascension et le dégazage de ces liquides silicatés riches en volatils. Une méthodologie de préparation des verres de départ et un protocole expérimental ont été établis, utilisés et éventuellement adaptés et modifiés au fur et à mesure des besoins de l'étude, notamment ceux liés à l'addition de soufre. L'analyse des échantillons, avant et après

décompression, a été à la fois chimique et texturale. La microsonde électronique et la spectrométrie infrarouge à transformée de Fourier ont été utilisées pour déterminer les concentrations en volatils de ces verres, ainsi que leur répartition spatiale. Tandis que la microtomographie par rayons X et la microscopie électronique à balayage ont été utilisées pour définir les principaux paramètres texturaux (taille et densité numérique de bulle, vésicularité) des verres décomprimés.

A noter que la problématique de cette thèse s'inscrit dans le cadre des projets français DEGAZMAG (DEGAZage MAGmatique, ANR Programme Blanc) et européens VUELCO (Volcanic Unrest in Europe and Latin America, FP7), tous deux ayant pour objectif l'apport d'informations quant aux mécanismes de dégazage des magmas basaltiques sources des signaux précurseurs (sismiques, géochimiques, géodésiques) des éruptions volcaniques.

3. Structure du manuscrit

La thèse comprend six chapitres, plus une introduction et une synthèse générale.

Le Chapitre i définit le cadre de l'étude en détaillant la problématique, ainsi que la stratégie expérimentale entreprise. Les notions générales du dégazage des magmas silicatés sont abordées, notamment par une présentation des approches théoriques, naturelles et expérimentales.

Le Chapitre ii est un chapitre technique, dans lequel les méthodes expérimentales et analytiques employées au cours de cette thèse sont présentées.

Les quatre chapitres suivants, iii, iv, v et vi, sont rédigés sous la forme d'articles scientifiques dans lesquels sont présentés les résultats de nos expériences sur la nucléation des bulles (Chapitre iii, iv, v) et le partage des volatils entre le liquide et le gaz (Chapitre vi). Ces expériences sont séparées en quatre principaux ensembles ; les trois premiers ont été menés en présence d'H_2O et de CO_2, tandis que dans le quatrième, le soufre a été introduit. A noter que les deux premiers ensembles traitent exclusivement de la nucléation homogène des bulles (Chapitre iii, iv), tandis que les deux derniers abordent la nucléation hétérogène des bulles, l'une sur les oxydes Fe–Ti (Chapitre v) et l'autre sur les sulfures de fer (Chapitre vi).

Vient ensuite une synthèse générale qui permet d'insister sur nos résultats importants et d'ouvrir sur de nouvelles perspectives de recherche.

Chapitre i

Cadre général

1. Le dégazage magmatique

1.1. Les volatils dans les magmas

Les volatils sont des éléments, ou composés chimiques, dissous en profondeur dans la phase liquide des magmas silicatés, et libérés sous forme gazeuse au cours de la remontée de ces derniers, lors d'une éruption volcanique par exemple (Sigurdsson, 2015**)**. Les volatils jouent un rôle important dans les systèmes volcaniques, puisqu'ils affectent les propriétés physico-chimiques des magmas (ex. viscosité, densité) et conditionnent la dynamique des éruptions (i.e. l'ascension et l'éruption des magmas). Ils sont donc fortement impliqués dans la génération des éruptions explosives, les plus spectaculaires et les plus dangereuses.

Les magmas silicatés, acides (plus de 63% SiO_2) ou basiques (de 45 à 52% SiO_2), contiennent différentes teneurs en volatils, de l'ordre de quelques % poids. Les espèces volatiles les plus abondantes (i.e. les volatils majeurs), aussi bien dans le liquide silicaté que dans les gaz volcaniques, sont l'eau, le dioxyde de carbone et le soufre (principalement SO_2 et H_2S dans les gaz) (ex. Symonds et al., 1994). Les informations quant aux teneurs en volatils des magmas sont fournies par l'analyse des inclusions vitreuses et des gaz volcaniques, ainsi que par les expériences d'équilibre de phases. Ces dernières consistent à reproduire en laboratoire l'assemblage minéralogique et les compositions des phénocristaux, ainsi que la teneur en volatils des verres naturels, en imposant des conditions de pression, température, teneur en volatils et d'oxydoréduction (reliées à la fugacité d'oxygène fO_2) représentatives des conditions pré-éruptives.

Les plus fortes teneurs en volatils se trouvent dans les magmas d'arc, en lien avec le contexte de subduction. A noter que c'est celui qui nous intéresse tout particulièrement puisque le Stromboli est un volcan d'arc. Sans entrer dans les détails, les zones de subduction participent pour beaucoup au recyclage des volatils issus de la dévolatilisation (et déshydratation dans 5–10 premiers km, ex. Moore et Vrolijk, 1992) de la plaque plongeante (croûte océanique altérée et sédiments, Wallace, 2005 ; Grove et al., 2012 ; Zellmer et al., 2015). Dans ces zones, les volatils jouent un rôle fondamental dans la genèse, l'évolution et l'ascension des magmas d'arc (Zellmer et al., 2015).

1.1.1. *Solubilité des volatils dans les basaltes*

Dans des conditions données (*P-T-f*O_2), la solubilité correspond à la quantité maximale d'une espèce volatile qui peut être dissoute dans un liquide silicaté ; on parle de conditions de saturation. Dans les basaltes, comme dans tous les magmas silicatés, la solubilité est propre à chaque volatil. Elle est déterminée par des études expérimentales (ex. Shishkina et al., 2010 ; Lesne et al., 2011a, b ; Fortin et al., 2015 ; Lesne et al., 2015) et donnée par les modèles qui en découlent (ex. Dixon, 1997 ; Newman et Lowenstern, 2002 ; Papale et al., 2006 ; Iacono-Marziano et al., 2012 ; Witham et al., 2012 ; Burgisser et al., 2015). La détermination expérimentale des lois de solubilité consiste à équilibrer un liquide silicaté (dont on mesure les concentrations en volatils dissoutes) avec une phase fluide en excès. Ces études ont montré que la solubilité des volatils est principalement dépendante de la pression (ou profondeur) ; elle l'est aussi de la température, de la composition du liquide silicaté (notamment des teneurs en alcalins pour le CO_2, Lesne, 2008, et en fer pour le soufre) et de la spéciation des éléments volatils (Mc Millan, 1994 ; Blank et Brooker, 1994 ; Zhang et al., 2007 ; Gonnermann et Manga, 2013). L'eau, présente sous forme moléculaire H_2O et de groupement hydroxyle OH^- (ex. Stolper, 1982), est l'espèce la plus soluble. Dans les basaltes d'arc (i.e. en contexte de subduction, Wallace, 2005), la solubilité de l'eau peut atteindre 6–8% pds. Le CO_2 est la seconde espèce la plus soluble ; ses solubilités sont un ou deux ordres de grandeur inférieurs à celles de l'eau (Baker et Alletti, 2012). Pour exemple, les basaltes d'arc peuvent contenir jusqu'à 2500 ppm de CO_2 (Wallace, 2005). Dans les liquides basaltiques, le carbonate CO_3^{2-} est l'espèce carbonée dominante, le CO_2 moléculaire est peu présent, voire absent, selon les concentrations en SiO_2 (ex. Wallace et al., 2015). Le soufre est la troisième espèce la plus soluble. Son comportement est complexe, fortement dépendant des conditions d'oxydoréduction (*f*O_2). En conditions réductrices, le soufre est présent sous forme de sulfure S^{2-} tandis qu'en conditions oxydantes, le soufre est dissous en tant que sulfate S^{6+} (Wallace et al., 2015). La solubilité du soufre semble davantage dépendante de la température que de la pression. Les basaltes d'arc contiennent, pour la plupart, entre 900 et 2500 ppm de soufre (Wallace, 2005).

1.1.2. *Diffusivité des volatils dans les basaltes*

Les constituants volatils majeurs (H_2O, CO_2, S) ont des diffusivités contrastées dans les liquides basaltiques, fortement dépendantes de leur spéciation. La diffusion de l'eau est

bien plus rapide que celles du CO_2 et du soufre (Baker et al., 2005 ; Zhang et Ni, 2010 ; Behrens et Stelling, 2011). Les équations citées ci-dessous sont celles que nous avons utilisées pour contraindre la diffusivité des volatils dans les liquides basaltiques.

La diffusivité de l'eau est la plus contrainte (ex. Zhang et Stolper, 1991 ; Okumura et Nakashima, 2006 ; Persikov et al., 2010) ; elle est, par exemple, donnée par Zhang et al. (2007 ; Zhang et Ni, 2010, Eq. i.1) :

$$D_{H2Ot} = C_{H2Ot}\exp(-8{,}56 - \frac{19110}{T}) \text{ (Eq. i.1)}$$

où D_{H2Ot} est le coefficient de diffusion (diffusivité en $m^2.s^{-1}$), T la température (en K) et C_{H2Ot} la teneur en H_2O totale ($H_2O_{moléculaire}$+OH^-) (en % pds). La diffusivité de l'eau semble dépendre de la teneur en H_2Ot et de la composition du liquide silicaté (teneur en SiO_2, alcalinité, Zhang et Ni, 2010). A noter que cette équation est donnée pour des teneurs en eau ≤ 1,1% pds (et pour 400–1500°C, ≤ 1 GPa), bien inférieures aux teneurs en eau de notre étude (jusqu'à ~5% pds).

La diffusivité du CO_2 est 7 à 10 fois inférieure à celle de H_2O (Zhang et Stolper, 1991 ; Pichavant et al., 2013). Elle est, par exemple, donnée par Zhang et al. (2007 ; Zhang et Ni, 2010, Eq. i.2) :

$$\ln D_{CO2t} = -13{,}99 - \frac{17367 + 1944{,}8P}{T} + \frac{(855{,}2 + 271{,}2P)}{T} C_{H2Ot} \text{ (Eq. i.2)}$$

où D_{CO2t} est le coefficient de diffusion (diffusivité en $m^2.s^{-1}$), T la température (en K), P la pression (en GPa) et C_{H2Ot} la teneur en H_2O totale (en % pds). Cette équation est commune à tous les liquides silicatés, basaltiques à rhyolitiques car, au contraire de la diffusivité de l'eau, celle du CO_2 ne semble dépendre ni de la teneur en CO_2, ni de la composition du liquide silicaté (Zhang et Ni, 2010). A noter que dans les liquides basaltiques, les diffusivités de H_2O et du CO_2 sont connues pour des conditions limitées de température et de composition chimique (Baker et al., 2005), l'effet de pression étant considéré comme négligeable. En revanche, la température et la teneur en eau dans le liquide ont pour effet d'augmenter la diffusivité de ces deux volatils majeurs (Zhang et Ni, 2010).

La diffusivité du soufre est comparativement moins bien connue (ex. Buchanan et Nolan, 1979 ; Watson et al., 1993 ; Freda et al., 2005). Dans les basaltes non hydratés, elle est 2 fois plus lente que la diffusion du CO_2 et de 2 ordres de grandeur plus lente que la diffusion

de H_2O (Freda et al., 2005). En présence d'eau (3,5% pds), comme c'est le cas dans notre étude bien que les conditions expérimentales ne soient pas les mêmes (1225–1450°C, 0,5–1 GPa), elle est, par exemple, donnée par Freda et al. (2005, Eq. i.3) :

$$D = 5{,}91.10^{-7}\exp\left(\frac{-130{,}8 \pm 82{,}6}{RT}\right) \text{ (Eq. i.3)}$$

où D est le coefficient de diffusion (diffusivité en $m^2.s^{-1}$), R la constante des gaz parfaits (8,3143 $J.K^{-1}.mol^{-1}$) et T la température (en K). La pression ne semble pas non plus avoir d'influence sur la diffusivité du soufre (Freda et al., 2005).

1.2. Comportement des volatils au cours de la décompression

1.2.1. *Le dégazage magmatique*

Lors de l'ascension et de la décompression d'un magma, les volatils s'exsolvent sous forme gazeuse : c'est le dégazage magmatique. L'exsolution (ou perte) des volatils dépend de leur solubilité, ainsi que de leur diffusivité au sein du liquide silicaté (ex. Gonnermann et Manga, 2007). La diminution de pression, engendrée par la remontée du magma, réduit la solubilité des volatils. Le magma est sursaturé dès lors que sa concentration en volatils dissous surpasse la solubilité. Le surplus en volatils induit la formation d'une phase gazeuse, i.e. la nucléation de bulles de gaz au sein du liquide. Il s'agit de la première étape du processus de dégazage des magmas. A noter que ce sont les bulles de gaz qui constituent la force motrice des éruptions volcaniques, notamment par leur capacité (ou plutôt incapacité) à se séparer du magma (Gonnermann et Manga, 2007).

L'exsolution des volatils, faisant suite à la sursaturation du liquide silicaté, peut être liée à une diminution de la pression lors de l'ascension magmatique (comme mentionné ci-dessus et dans le cadre de cette thèse), mais peut également être induite par une diminution de la température ou encore par la cristallisation.

Les différences de solubilité des espèces volatiles (voir la section 1.1.1) conduisent à une "séquence d'exsolution" (ex. Spilliaert, 2006). En théorie, le dioxyde de carbone serait la première espèce à s'exsolver à de grandes profondeurs (ou pressions), suivi de l'eau puis du soufre à de plus faibles profondeurs.

1.2.2. *Les mécanismes du dégazage magmatique*

Les mécanismes du dégazage incluent la nucléation, la croissance et l'éventuelle coalescence de bulles de gaz, ainsi que la fragmentation du magma. Les processus de nucléation, de croissance et de coalescence des bulles constituent le phénomène de la vésiculation (Fig. i.1).

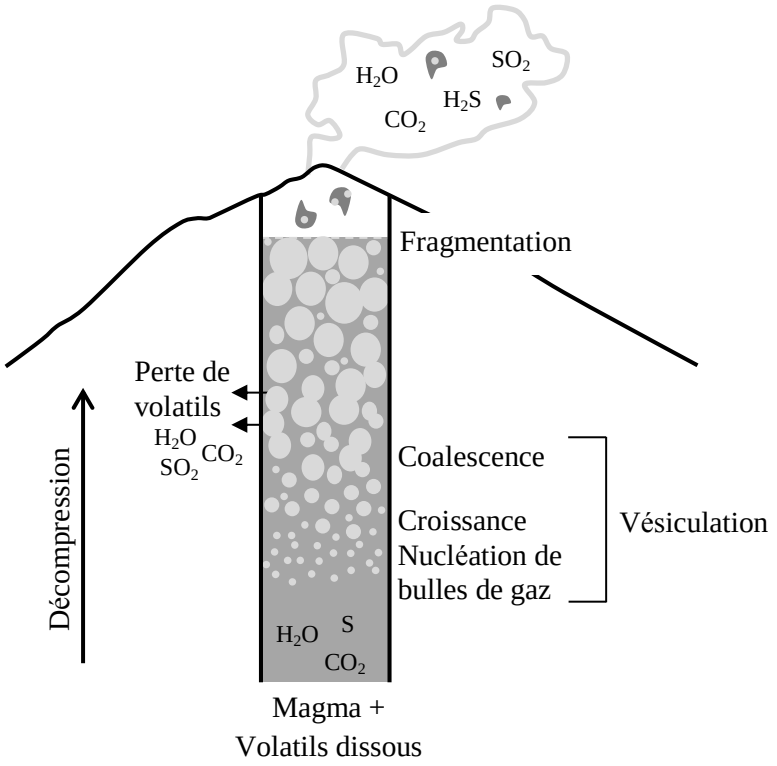

Fig. i.1. Représentation schématique des processus de dégazage des magmas intervenant dans le conduit volcanique.

Le processus de dégazage des magmas débute par la nucléation de bulles de gaz qui, une fois formées, grossissent par diffusion des volatils (transfert de la phase liquide à la phase gazeuse) et expansion volumique (en réponse à la décompression). Ces deux principaux mécanismes de croissance (ex. Sparks, 1978) tendent à réduire la distance entre les bulles, permettant leur interaction et leur coalescence. A noter que la croissance des bulles est aussi contrôlée par le taux de décompression, plus celui-ci est important et moins les bulles ont le temps de grossir. L'une des conséquences de la croissance et de la coalescence des bulles de gaz est la fragmentation du magma. Ce processus consiste en la transformation du magma, de manière explosive, en un mélange de gaz et de fragments de magma (Zhang, 1999). Selon certains auteurs (ex. Sparks, 1978 ; Sparks et al., 1994), ce phénomène serait associé à une

valeur seuil de la fraction volumique de bulles de gaz (i.e. de la vésicularité) de ~70–80%. Plusieurs mécanismes sont invoqués pour expliquer ce phénomène de déformation cassante : une surpression à l'intérieur des bulles de gaz conduisant à la rupture des fines parois entre les bulles une fois la résistance du magma dépassée (Alidibirov, 1994 ; Zhang, 1999 ; Spieler et al., 2004), la déformation du magma indépendante de la présence de bulles (Dingwell, 1996 ; Papale, 1999) et la propagation d'une onde de décompression (Mader et al., 1997).

1.2.3. *Implications pour la dynamique des éruptions*

La dynamique d'ascension des magmas est conditionnée par le comportement des volatils. Leur transfert du liquide silicaté vers les bulles, c.-à-d. de l'état dissous à l'état gazeux, puis l'évolution de la phase gazeuse (séparation magma/gaz) au cours de la remontée du magma sont déterminants pour le style et l'intensité des éruptions.

Lors de la remontée de magmas peu visqueux tels que les basaltes, les bulles de gaz peuvent se séparer du liquide par flottation, celles-ci étant moins denses (ex. Houghton et Gonnermann, 2008). C'est le cas en système ouvert, le magma perd des volatils au cours de sa lente ascension, arrivant presque dégazé en surface. L'éruption est alors effusive, associée à l'émission de produits peu vésiculés. La perte de volatils peut être favorisée par le développement de la perméabilité du magma, laquelle augmente avec la coalescence des bulles. Elle peut aussi être latérale dans les roches encaissantes (perte diffusive). Alternativement, les bulles peuvent coalescer et s'accumuler, formant de grandes poches de gaz (de l'ordre du mètre) qui se rompent à la surface. C'est le cas lors des explosions Stromboliennes (Gonnermann et Manga, 2013). En revanche, lorsque la vitesse d'ascension du magma est rapide, si bien que la différence de vitesse entre les bulles et le magma devient négligeable (Gonnermann et Manga, 2007), le magma arrive chargé de bulles de gaz en surface (système fermé). Cela se traduit par une éruption explosive, associée à la fragmentation du magma et l'émission de produits très vésiculés.

La vitesse d'ascension peut ainsi significativement influer sur le dégazage des magmas lors de leur remontée dans le conduit et, de ce fait, sur la dynamique des éruptions (Fig. i.2).

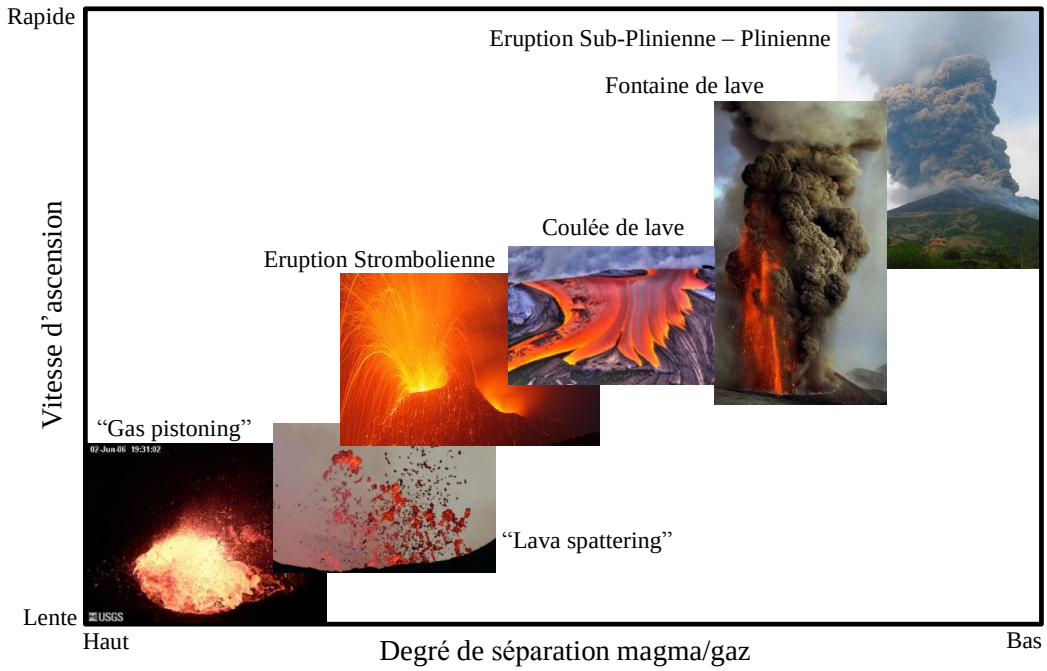

Fig. i.2. Régimes de séparation magma/gaz en fonction de la vitesse d'ascension dans les systèmes basaltiques, d'après Edmonds (2008). *(Sources : www.photovolcanica.com (R. Roscoe) ; www.swisseduc.ch (M. Fulle, A. Franssen); G. Brad Lewis ; USGS)*

2. Nucléation des bulles dans les magmas

2.1. Aspects théoriques

2.1.1. *Théorie classique de la nucléation*

Les bulles de gaz sont produites par un processus de nucléation, décrit par la théorie classique de la nucléation. Sa formulation repose sur les contributions de Gibbs, Laplace, Kelvin et beaucoup d'autres (Navon et Lyakhovsky, 1998). Cette théorie est rappelée et utilisée notamment dans les études récentes sur la nucléation des bulles dans les liquides rhyolitiques (Mourtada-Bonnefoi, 1998 ; Cluzel, 2007). Parmi les équations importantes, soulignons celle exprimant le taux de décompression nécessaire à la nucléation des bulles :

$$\Delta P = \sqrt{\frac{16\pi\sigma^3}{3kT\ln\left(\frac{J}{J_0}\right)}}$$ (Eq. i.4, Hirth et al., 1970 ; Hurwitz et Navon, 1994 ; Mourtada-Bonnefoi et Laporte, 2002)

où ΔP est la pression de sursaturation (en Pa), σ la tension de surface (ou énergie interfaciale, en $N.m^{-1}$), k la constante de Boltzmann ($1{,}3805.10^{-23}$ $J.K^{-1}$), T la température (en K), J le taux de nucléation (en $m^{-3}.s^{-1}$) et J_0 le taux de nucléation préexponentiel (en $m^{-3}.s^{-1}$).

La formation d'une interface bulle-liquide requiert une pression de sursaturation minimum pour surmonter la barrière énergétique fournie par la tension de surface du liquide silicaté (ex. Gonnermann et Manga, 2007). La phase gazeuse se forme pour maintenir un équilibre thermodynamique suite à la sursaturation en volatils dans le liquide (par décompression, Fig. i.3, refroidissement ou cristallisation). Ainsi, le magma ne nuclée pas de bulles dès le franchissement de son seuil de solubilité (P_{sat} pour pression de saturation, Fig. i.3), mais une fois un certain degré de sursaturation en volatils atteint. Si on note P_N la pression à laquelle on commence à observer la nucléation des bulles, on peut définir la pression de sursaturation ΔP_N comme la différence entre P_{sat} et P_N ($\Delta P_N = P_{sat} - P_N$, Fig. i.3).

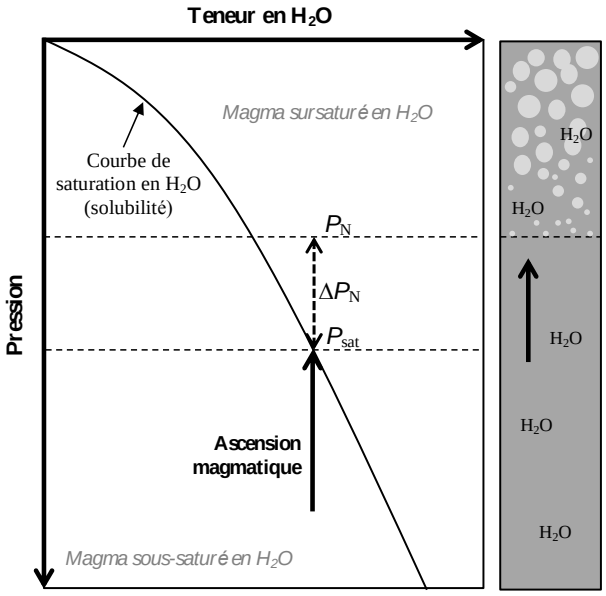

Fig. i.3. Illustration de la sursaturation en H_2O d'un magma lors de son ascension dans le conduit volcanique. Initialement, l'eau est dissoute dans le liquide silicaté.

La nucléation peut être homogène ou hétérogène, conduisant à deux modes distincts de formation des bulles de gaz.

2.1.2. *Nucléation homogène*

Lorsque le magma ne contient pas d'impuretés ou des discontinuités (phases cristallines, parois ou hétérogénéités), la nucléation des bulles de gaz se produit spontanément au sein du liquide (Fig. i.4a). L'initiation de cette nucléation uniforme, dite homogène, requiert de fortes sursaturations ; les bulles se forment bien au-dessus du niveau de saturation en volatils dans le conduit volcanique (ΔP_N élevé, Fig. i.4b). Les implications volcanologiques sont celles d'une nucléation tardive (superficielle) des bulles, d'un dégazage qui peut être alors hors équilibre (croissance limitée) et d'une vésiculation explosive pendant les éruptions volcaniques (Sparks et al., 1994, 1997 ; Mangan et Sisson, 2000).

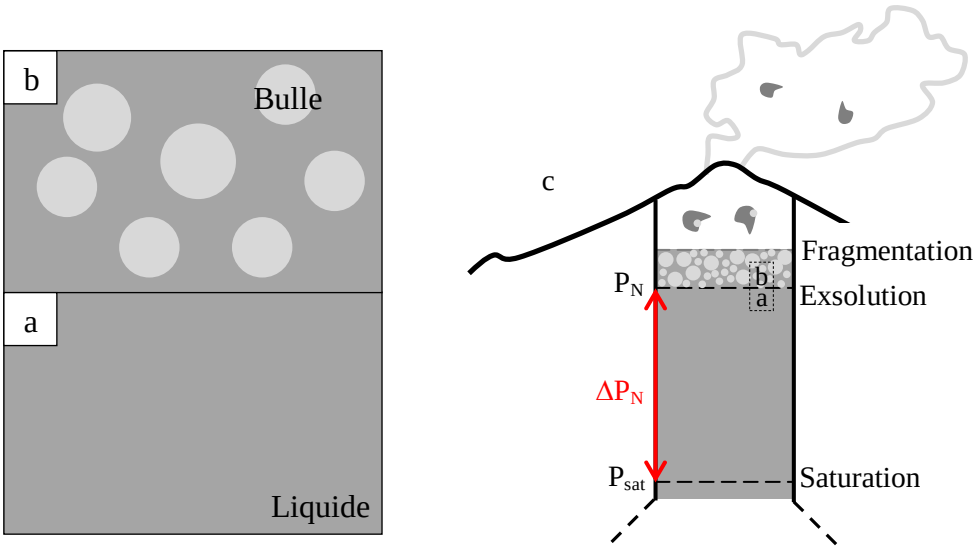

Fig. i.4. Schémas illustrant la nucléation homogène des bulles de gaz à l'échelle du liquide silicaté (b) et à l'échelle du conduit volcanique (c). (a) Etat initial du liquide silicaté : avant l'événement de nucléation homogène des bulles, les volatils sont sous forme dissoute.

2.1.3. *Nucléation hétérogène*

La nucléation est dite hétérogène lorsque les bulles se forment au contact d'impuretés ou de discontinuités telles que la surface des cristaux (Fig. i.5a). La présence de ces sites peut faciliter la nucléation des bulles de gaz, dès lors que l'énergie (ou tension) de surface σ entre la bulle et le cristal est inférieure à celle de l'interface bulle-liquide (Navon et Lyakhovsky, 1998). Dans ce cas, l'énergie d'activation ΔF requise à la nucléation d'une bulle de gaz sur la face d'un cristal est réduite d'un facteur ϕ (Hurwitz et Navon, 1994) ; la pression de sursaturation ΔP est elle aussi réduite.

$$\Delta F = \frac{16\pi\sigma^3\phi}{3\Delta P^2} \quad \text{(Eq. i.5)}$$

où ΔF est l'énergie libre de Helmholtz du système (en J) et ϕ un facteur géométrique compris entre 0 et 1, contrôlé par la relation de mouillage entre la bulle et le cristal et donné par la relation suivante :

$$\phi = \frac{(2 - \cos\theta)(1 + \cos\theta)^2}{4} \quad \text{(Eq. i.6)}$$

où θ est l'angle de mouillage défini par les valeurs relatives des tensions de surface entre le cristal, le liquide et la bulle, σ_{CL} (cristal/liquide), σ_{LB} (liquide/bulle) et σ_{CB} (cristal/bulle) (Fig. i.5b) :

$$\cos\theta = \frac{\sigma_{CB} - \sigma_{CL}}{\sigma_{LB}} \quad \text{(Eq. i.7)}$$

La nucléation des bulles peut être favorisée par leur capacité à mouiller le cristal. Si l'angle de mouillage est > à 90°, $\sigma_{CB} < \sigma_{CL}$, la bulle est mouillante. Au contraire, si $\theta < 90°$, $\sigma_{CB} > \sigma_{CL}$, la bulle est non mouillante. La morphologie des cristaux peut donc, elle aussi, avoir une influence sur la nucléation des bulles.

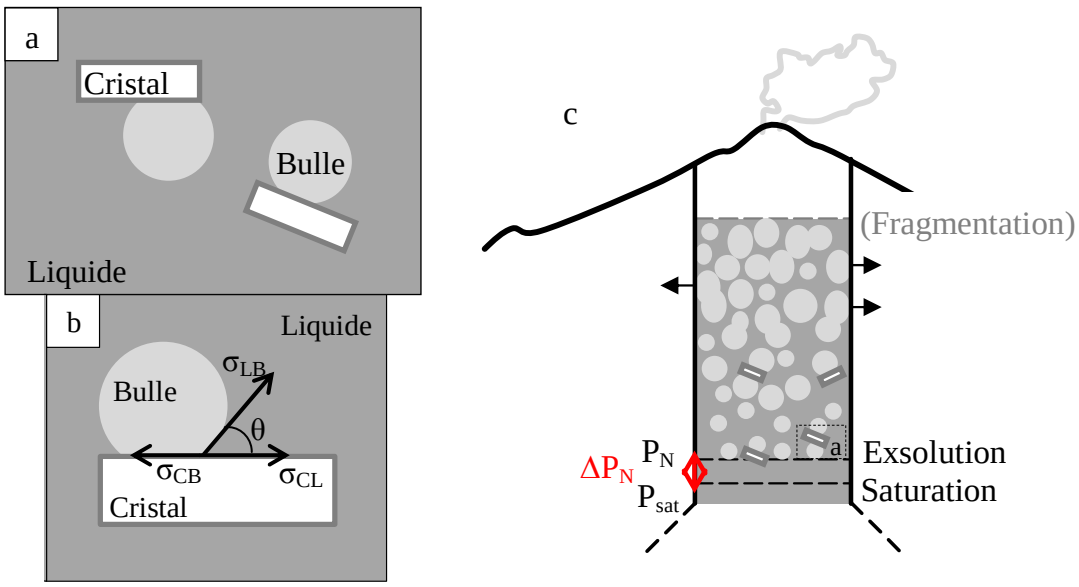

Fig. i.5. Schémas illustrant la nucléation hétérogène de bulles de gaz au sein du liquide silicaté (a) et dans le conduit volcanique (c). (b) Relation de mouillage entre cristal, liquide et bulle.

L'implication volcanologique est celle d'une nucléation précoce (en profondeur) des bulles, menant à un dégazage au voisinage de l'équilibre (ΔP_N petit, Fig. i.5c, ex. Hurwitz et Navon, 1994). Les bulles de gaz ont le temps de coalescer (augmentant la perméabilité du magma) et de se séparer du magma, conduisant à une éruption effusive ou peu explosive.

2.1.4. *Effet de la tension de surface*

La tension de surface est un paramètre clé de la théorie classique de la nucléation (Eq. i4). Elle a une grande influence sur le taux de nucléation ainsi que sur la pression de sursaturation nécessaire au déclenchement de la nucléation des bulles de gaz ; une légère variation de la tension de surface fait grandement (de plusieurs ordres de grandeur) varier le taux de nucléation (Mangan et Sisson, 2005). Cependant, la tension de surface est mal contrainte de par sa forte sensibilité à la composition du liquide, à la température et à la teneur en volatils (Navon et Lyakhovsky, 1998 ; Mangan et Sisson, 2000 ; Bagdassarov et al., 2000 ; Mangan et al., 2004). Sa mesure directe est difficile (Khitarov et al., 1979) et une des manières de l'obtenir est d'inverser les données expérimentales (voir la section 2.3.3).

2.2. Aspects naturels

La texture des ponces fournit de précieuses informations quant aux mécanismes de dégazage des magmas (ex. Shea et al., 2010). La forme, la taille et le nombre de bulles résultent des processus de nucléation, de croissance et de coalescence. Ces caractéristiques texturales, qui traduisent un état final des processus de vésiculation, sont utilisées pour approcher les conditions d'ascension et d'éruption des magmas.

2.2.1. *Vésicularité*

La vésicularité est la fraction volumique de bulles de gaz d'un magma. Elle augmente progressivement tout au long de la remontée de ce dernier. A noter que pour une pression donnée, la vésicularité tend à augmenter avec l'exsolution des volatils jusqu'à une valeur qui correspond à un état de saturation en volatil du liquide ; on parle dans ce cas de vésicularité à l'équilibre et d'équilibre textural. Dans les produits éruptifs basaltiques, la vésicularité varie

de quelques % à plus de 98 % vol (réticulite). Cette variété reflète la complexité des processus intervenant dans le conduit volcanique (Houghton et Gonnermann, 2008).

2.2.2. *Densité numérique de bulles*

La densité numérique de bulles (ou BND pour "bubble number density" en anglais) correspond au nombre de bulles par unité de volume de l'échantillon (c.-à-d. de liquide plus de bulles), ou de liquide. Lorsqu'il est défini par unité de volume de liquide, ce paramètre textural est un bon indicateur des processus de nucléation (augmentation de la BND), de croissance (maintien de la BND) et de coalescence des bulles (diminution de la BND), puisqu'il reste invariant à leur croissance (Proussevitch et al., 2007). Il peut également être utilisé pour estimer les vitesses d'ascension (Mourtada-Bonnefoi et Laporte, 2004 ; Toramaru, 2006), la densité numérique de bulles augmentant avec le taux de décompression (i.e. avec la vitesse d'ascension, Mourtada-Bonnefoi et Laporte, 2004 ; Cluzel et al., 2008). Les ponces basaltiques sont caractérisées par de grandes densités numériques de bulles (bien qu'inférieures aux ponces rhyolitiques), typiquement de 10^2 à 10^4 mm^{-3} (ex. Polacci et al., 2006, 2009 ; Sable et al., 2006, 2009 ; Costantini et al., 2010).

2.2.3. *Distribution de taille des bulles*

La distribution de taille des bulles résulte des processus de nucléation, de croissance et de coalescence. Il s'agit d'un paramètre important, dont l'évolution dans les produits expérimentaux, ainsi que dans les modèles numériques, peut aider à l'interprétation des textures de bulles naturelles (ex. Mangan et Cashman, 1996). Elle peut être représentée par le nombre ou par le volume, cumulés ou non, des bulles (cf. Shea et al., 2010, Fig. 1).

Trois principaux types de distribution de taille de bulles sont rencontrés dans les roches volcaniques : unimodale, en loi de puissance et exponentielle (Fig. i.6).

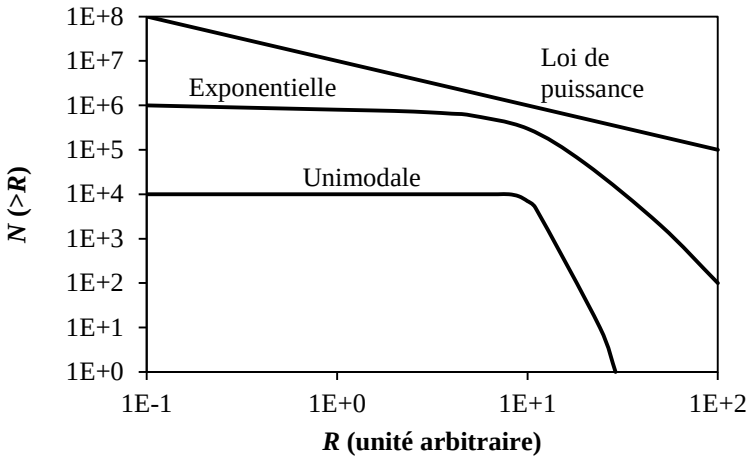

Fig. i.6. Distributions unimodale, en loi de puissance et exponentielle de la taille des bulles, d'après Blower et al. (2002).

Une distribution unimodale de la taille des bulles traduit un événement unique de nucléation, comme c'est souvent le cas dans les produits expérimentaux. Des distributions en loi de puissance et exponentielle ont toutes deux été mises en évidence dans des produits éruptifs basaltiques (laves, scories et ponces, ex. Gaonac'h et al., 1996 ; Simakin et al., 1999 ; Toramaru, 1990 ; Sable et al., 2006, 2009 ; Bai et al., 2008 ; Polacci et al., 2009 ; Costantini et al., 2010), ainsi que, plus rarement, dans des produits expérimentaux (ex. Navon et al., 1998 ; Simakin et al., 1999 ; Bai et al., 2008 ; Polacci et al., 2008 ; Masotta et al., 2014). Différentes interprétations sont données pour expliquer la formation de ces deux derniers types de distribution, en loi de puissance et exponentielle. Les résultats d'expériences analogiques menées par Blower et al. (2001) suggèrent qu'ils sont tous deux produits par un processus de nucléation continu au cours duquel des générations de bulles se forment successivement dans des "poches" de liquide encore sursaturées en volatils, localisées entre les bulles préexistantes (Fig. i.7). A noter que Blower et al. (2001) introduisent l'idée selon laquelle un processus de nucléation continu résulte d'un état de déséquilibre du système au cours de son dégazage ; les bulles évoluent successivement d'une distribution en loi de puissance à exponentielle au fur et à mesure de l'avancement des processus de nucléation et de croissance. L'obtention d'une distribution exponentielle traduit donc une approche vers un état d'équilibre textural (Baker et al., 2006 ; Bai et al., 2008).

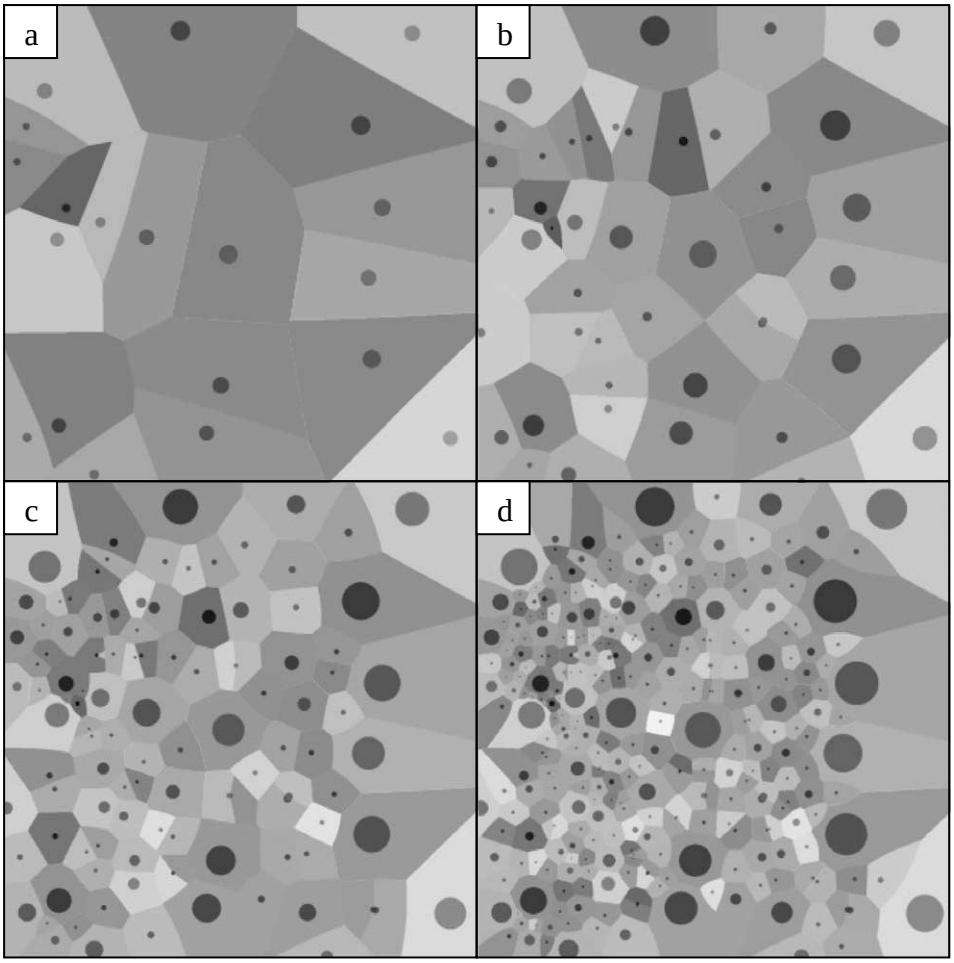

Fig. i.7. Modèle numérique de Blower et al. (2002). (a) Evénement de nucléation initial. Les parties grisées représentent les zones d'influence des différentes bulles dont les frontières sont à égale distance l'une de l'autre. (b) Nucléation d'une seconde génération de bulles entre les bulles préexistantes, au contact des zones d'influence de plusieurs bulles. (c) et (d) Deux nouvelles étapes dans l'évolution de la distribution des bulles.

Les auteurs (Blower et al., 2001, 2002) parlent d'"évènement de nucléation" pour introduire l'idée d'une nucléation par impulsions (évènements multiples de nucléation au cours d'un processus continu). Une distinction entre loi de puissance et distribution exponentielle est alors faite sur la base du nombre de ces événements ; au moins trois événements de nucléation produiraient une distribution exponentielle de la taille des bulles, tandis qu'au moins cinq de ces événements seraient à l'origine d'une distribution suivant une loi de puissance dans les produits naturels et expérimentaux. Selon ces auteurs, l'exposant de la loi de puissance augmente avec le nombre d'évènements de nucléation. Ainsi, les distributions en loi de puissance de la taille des bulles observées dans les échantillons naturels seraient produites par 7 à 10 évènements de nucléation. Cependant, ce modèle ne tient pas

compte de l'effet de la coalescence de bulles. Ce processus serait pourtant, selon Gaonac'h et al. (1996), à l'origine des lois de puissance.

Un autre modèle est avancé pour expliquer la formation des distributions exponentielles de la taille des bulles, basé sur la théorie de Marsh (1988) pour la distribution de taille des cristaux. Ce modèle assume un état stable du système, dans lequel les bulles nucléent et grossissent à taux constants, ce qui est discutable (cf. Blower et al., 2002).

2.3. Aspects expérimentaux

2.3.1. *Travaux antérieurs*

Ces dernières années, la nucléation des bulles de gaz a principalement été étudiée, par l'expérimentation, dans les systèmes rhyolitiques (ex. Hurwitz et Navon, 1994 ; Gardner et al., 1999 ; Mourtada-Bonnefoi et Laporte, 1999 ; Mangan et Sisson, 2000 ; Mourtada-Bonnefoi et Laporte, 2002, 2004 ; Gardner et Denis, 2004 ; Mangan et Sisson, 2005 ; Gardner, 2007 ; Cluzel et al., 2008 ; Gardner et Ketcham, 2011 ; Gondé et al., 2011) et dacitiques (ex. Mangan et al., 2004 ; Gardner et Ketcham, 2011). Ces études consistent en des expériences de décompression visant à simuler l'ascension et le dégazage des magmas silicatés dans des conditions voisines, ou non, des conditions naturelles. Quelques travaux expérimentaux sont consacrés aux systèmes phonolitiques (ex. Iacono-Marziano et al., 2007), les systèmes andésitiques (ex. Fiege et al., 2014a) et basaltiques (Lensky et al., 2006 ; Pichavant et al., 2013 ; Fiege et al., 2015) étant les moins étudiés. Cela s'explique par les difficultés expérimentales rencontrées pour ces liquides (notamment les hautes températures) et par le fait que les éruptions explosives les plus dangereuses et destructrices sont souvent produites par des magmas riches en silice.

Ces expériences de décompression se sont surtout concentrées sur le rôle de l'H_2O, ce volatil étant le plus abondant dans les magmas silicatés. Néanmoins, quelques études ont été menées en présence d'une phase volatile mixte, composée d'H_2O et de CO_2 (les deux volatils majeurs). C'est le cas des expériences de Mangan et Sisson (2000), Mourtada-Bonnefoi et Laporte (2002) et Cluzel (2007) dans les liquides rhyolitiques. Mourtada-Bonnefoi et Laporte (2002) ont d'ailleurs mis en évidence un effet découplé des teneurs en H_2O et en CO_2 sur la pression de sursaturation requise au déclenchement de la nucléation de bulles de gaz, ainsi que sur la densité numérique de bulles. Plus récemment, Fiege et al. (2014b, 2015) ont mené

des expériences de décompression dans des liquides andésitiques et basaltiques en présence d'H_2O, de S et de Cl. Cependant, ces études ne se sont pas focalisées spécifiquement sur la nucléation des bulles.

Certains des travaux antérieurs ont porté sur le processus de nucléation hétérogène (et non homogène) des bulles (Hurwitz et Navon, 1994 ; Gardner et al., 1999 ; Gardner et Denis, 2004 ; Mangan et al., 2004 ; Gardner, 2007 ; Cluzel et al., 2008). Il s'agit d'expériences de décompression menées en présence d'une phase cristalline dans les systèmes rhyolite-H_2O et dacite-H_2O. Les données montrent que la magnétite facilite la nucléation des bulles d'H_2O dans ces liquides (particulièrement dans les liquides rhyolitiques, Hurwitz et Navon, 1994 ; Gardner et Denis, 2004 ; Gardner, 2007) et, qu'au contraire, certains cristaux ne sont pas (plagioclase, quartz), ou peu (hématite, biotite, zircon, apatite), efficaces comme sites préférentiels de nucléation (Hurwitz et Navon, 1994 ; Gardner et Denis, 2004 ; Cluzel et al., 2008).

2.3.2. *Pressions de sursaturation*

La pression de sursaturation est la différence entre la pression de saturation et la pression de nucléation des bulles ($\Delta P_N = P_{sat} - P_N$, cf. page 28). Dans le cas de la nucléation homogène des bulles, de fortes pressions de sursaturation ont été trouvées dans les systèmes magmatiques hydratés, ~60–90 MPa dans les liquides dacitiques (H_2O ~5% pds, Mangan et Sisson, 2005; Gardner et Ketcham, 2011), ~100 MPa dans les liquides phonolitiques (H_2O ~5% pds, Iacono-Marziano et al., 2007) et ~95–150 MPa dans les liquides rhyolitiques (H_2O ~5–7% pds, Mangan et Sisson, 2000; Mourtada-Bonnefoi et Laporte, 2004; Gardner et Ketcham, 2011). Dans les systèmes hydratés et carbonatés (contenant du CO_2), des pressions de sursaturation encore plus fortes ont été trouvées, comprises entre 160 et 350 MPa dans les liquides rhyolitiques (4,6% pds H_2O et 800–1100 ppm CO_2, Mourtada-Bonnefoi et Laporte, 2002). Ces fortes pressions de sursaturation impliquent une nucléation plus tardive des bulles pouvant conduire à un dynamisme explosif.

Dans les liquides basaltiques, des résultats préliminaires dans le système basalte-H_2O-CO_2 (Pichavant et al., 2013), indiquent que de fortes sursaturations (< 150 MPa) sont requises pour la nucléation homogène des bulles. A noter qu'il s'agit de pressions de sursaturation maximales, les expériences de décompression de Pichavant et al. (2013) n'étant pas

spécifiquement destinées à étudier la nucléation des bulles. Lensky et al. (2006) ont quant à eux trouvé une pression de sursaturation de 200 ± 100 MPa pour initier la nucléation de bulles de CO_2 dans un liquide basaltique synthétique en conditions anhydres.

Dans le cas de la nucléation hétérogène des bulles, en présence de magnétite de très faibles pressions de sursaturation ont été trouvées, ≤ 1–5 MPa (Hurwitz et Navon, 1994) et < 20 MPa (Gardner et Denis, 2004) dans les liquides rhyolitiques hydratés, et 35 ± 5 MPa (Mangan et al., 2004) dans les liquides dacitiques hydratés. Ces résultats démontrent que les bulles d'H_2O mouillent les faces des magnétites (θ < 90°), et impliquent que la nucléation hétérogène des bulles est un processus important dans ces liquides. Cependant, comme mentionné précédemment, certains cristaux mouillent moins les bulles d'H_2O. C'est le cas de la biotite, de l'apatite et du zircon (ΔP < 30 MPa, Hurwitz et Navon, 1994), ainsi que de l'hématite, des pressions de sursaturation de 50–70 MPa (Gardner et Denis, 2004) et ~135 MPa (Cluzel et al., 2008) ayant été trouvées. Il ressort des expériences menées jusqu'à présent que seule la présence de magnétite permet d'abaisser significativement la sursaturation en volatils requise au déclenchement de la nucléation des bulles.

2.3.3. *Tensions de surface*

Les expériences de décompression peuvent être utiles à la détermination des tensions de surface, via la connaissance des pressions de sursaturation et l'utilisation de la théorie classique de la nucléation. Etant donné que les systèmes les plus étudiés sont riches en silice, la majorité des données de tension de surface publiées concernent ces compositions (haplogranite, rhyolite, dacite). Des valeurs de tension de surface comprises entre 0,032 $N.m^{-1}$ (Epel'baum et al., 1973 ; Epel'Baum, 1980) et 0,15 $N.m^{-1}$ (Bagdassarov et al., 1994) ont été déterminées dans les liquides rhyolitiques hydratés (Mangan et Sisson, 2000). Elles sont plus élevées que celles trouvées dans les liquides dacitiques hydratés (0,042–0,073 $N.m^{-1}$ pour 5,7–4,8% pds H_2O, Mangan et Sisson, 2005), ou encore dans les liquides andésitiques hydratés (0,028–0,063 $N.m^{-1}$, Fiege et al., 2014a). Dans les liquides basaltiques, des valeurs de 0,1 (liquides hydratés) à 0,4 $N.m^{-1}$ sont données par Khitarov et al. (1979), et de 0,18 $N.m^{-1}$ par Pichavant et al. (2013).

3. Modèles théoriques de dégazage des magmas basaltiques

3.1. Dégazage à l'équilibre

Il est communément admis que les magmas basaltiques, chauds, peu visqueux et dans lesquels les volatils diffusent rapidement, dégazent à l'équilibre chimique et textural au cours de la décompression (ex. Sparks et al., 1994), les volatils (sous forme de bulles) pouvant s'échapper facilement. Les modèles de dégazage des magmas basaltiques se basent sur les mesures de solubilité des volatils, lesquelles sont obtenues à l'équilibre chimique liquide-gaz. Ainsi, au cours de la décompression, le dégazage à l'équilibre des magmas basaltiques, régi par des différences de solubilité, se traduit par l'exsolution (à partir du liquide) du CO_2 en profondeur (i.e. à haute pression), suivi par celles d'H_2O puis du soufre à des niveaux plus superficiels (i.e. à basse pression). Dans le même temps, la composition chimique de la phase gazeuse évolue d'une phase dominée par le CO_2 à haute pression vers une phase dominée par l'H_2O à basse pression. A noter que ces modèles forment la base des interprétations des mesures de gaz volcaniques utiles à la surveillance des volcans.

3.2. Inclusions vitreuses

Plusieurs types d'observations contredisent cependant les modèles à l'équilibre de dégazage des magmas basaltiques. Parmi ces dernières, mentionnons tout d'abord les données d'inclusions vitreuses. Les inclusions vitreuses sont des gouttes micrométriques de liquide magmatique piégées dans les cristaux (olivine, clinopyroxène, plagioclase) lors de leur croissance. Leur analyse nous renseigne sur les conditions de stockage pré-éruptives du magma (pression ou profondeur de stockage, température, composition chimique, fO_2), ainsi que sur sa teneur en volatils. Certaines inclusions imparfaitement fermées (les "embayments") toutefois ne préservent pas les concentrations en volatils pré-éruptives ; elles sont susceptibles de se rééquilibrer au cours de la remontée du magma vers la surface, en perdant partiellement leur volatils. Leur analyse fournira alors des informations sur les conditions de remontée du magma vers la surface, notamment sur l'évolution des volatils dissous. Ces différents objets montrent que certains systèmes naturels (ex. Stromboli, Etna, Vésuve, Jorullo) contiennent des teneurs anormalement élevées en CO_2 (par rapport aux courbes de dégazage à l'équilibre, Fig. i.8). L'interprétation actuellement en faveur pour expliquer ces résultats fait intervenir des fluides riches en CO_2 en profondeur dans le système volcanique (modèle de CO_2 "fluxing", voir résumé dans Blundy et al., 2010). Cependant, ce modèle présente le

désavantage important de conduire à une déshydratation et de favoriser ainsi la cristallisation des magmas soumis au CO_2 "fluxing". Or, certains de ces magmas sont très peu riches en cristaux (ex. ponces Stromboliennes, voir la section 4.2.2).

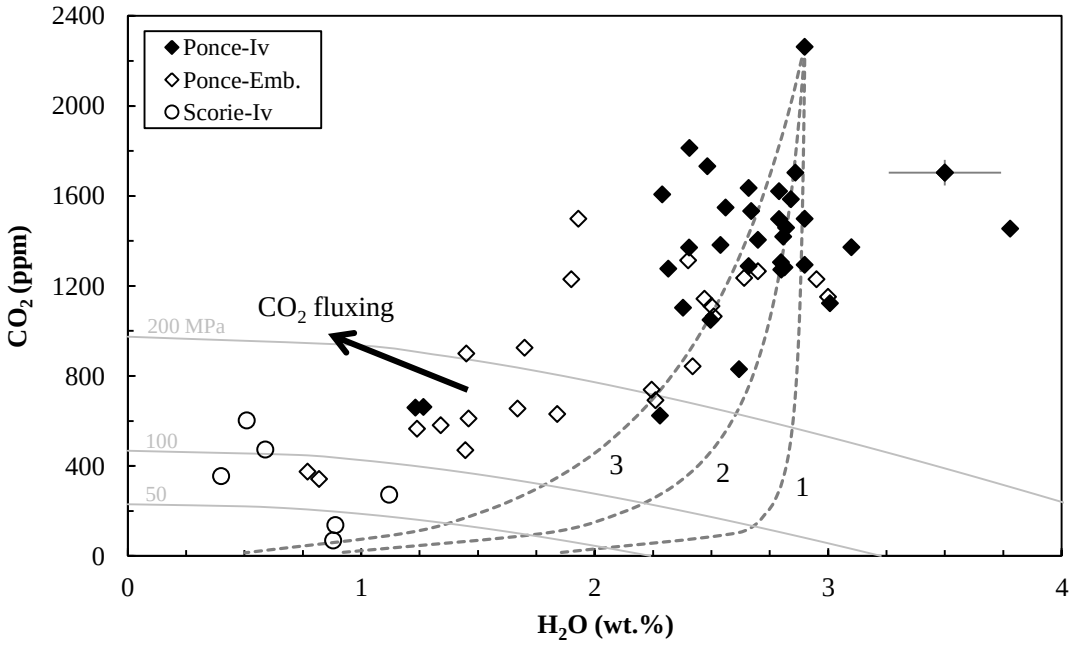

Fig. i.8. Teneurs en H_2O et en CO_2 dans les inclusions vitreuses (Iv) et les embayments (Emb.) des ponces et des scories Stromboliennes, d'après Métrich et al. (2010). Equilibres liquide-gaz (isobares 200, 100 et 50 MPa, chemins de dégazage en système fermé) calculés avec VolatileCalc (Newman et Lowenstern, 2002). Les chemins de dégazage ont été calculés pour une fraction de gaz initiale de 0% pds (courbe 1), 2,4% pds (courbe 2) et 10% pds (courbe 3) à 200 MPa.

3.3. Volcanisme basaltique explosif

Bien que les magmas basaltiques soient souvent associés à des éruptions effusives (Fig. i.9a) ou peu explosives (éruptions Hawaiiennes et Stromboliennes, Fig. i.9b), ils peuvent être à l'origine d'éruptions plus énergiques comme observé sur des volcans tels que le Stromboli (ex. Bertagnini et al., 2011 ; Fig. i9c) et l'Etna (Italie, Sable et al., 2006), le Masaya (Nicaragua, Costantini et al., 2010) et le Tarawera (Nouvelle-Zélande, Sable et al., 2009). Ces éruptions explosives, paroxysmales, sub-Pliniennes et Pliniennes, sont des phénomènes rares et dont l'initiation reste peu comprise (du moins donnant matière à débat), bien qu'elles constituent un risque majeur.

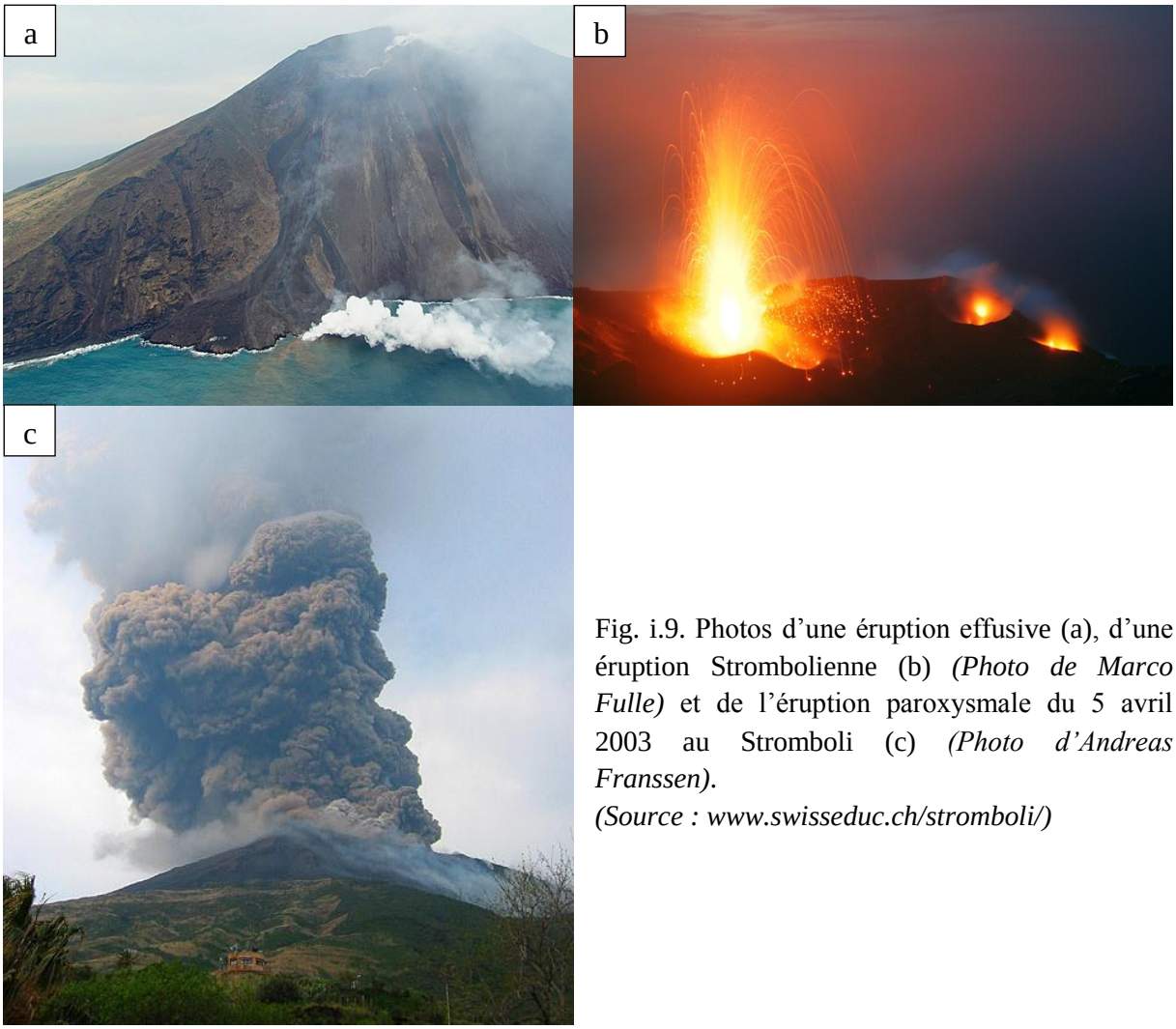

Fig. i.9. Photos d'une éruption effusive (a), d'une éruption Strombolienne (b) *(Photo de Marco Fulle)* et de l'éruption paroxysmale du 5 avril 2003 au Stromboli (c) *(Photo d'Andreas Franssen)*.
(Source : www.swisseduc.ch/stromboli/)

Ces éruptions basaltiques paroxysmales se traduisent par la projection de grandes quantités de gaz et de fragments (blocs et bombes, > 64 mm, lapillis, 2–64 mm, cendres, < 2 mm, Wilson et al., 2014) de magma à très haute altitude, suggérant la possibilité d'un dégazage hors équilibre des magmas basaltiques (libération soudaine et violente de volatils).

La prévision de ces éruptions passe par une meilleure compréhension des mécanismes éruptifs mis en jeu. Le dynamisme, effusif vs. explosif, est déterminé par le dégazage magmatique (nucléation des bulles de gaz, croissance, coalescence, fragmentation, Gonnermann et Manga, 2005). La transition de style dépend du régime de transfert de la phase gazeuse, ainsi que des changements du taux d'alimentation magmatique et de la vitesse d'ascension (ex. Pioli et al., 2008; Métrich et Wallace, 2008; Edmonds, 2008).

4. Approche expérimentale

Comme mentionné précédemment, plusieurs approches permettent d'appréhender les processus de dégazage des magmas : une approche naturelle par l'étude des textures des produits émis, notamment des ponces (ex. Mangan et Cashman, 1996 ; Polacci et al., 2006, 2009), une approche géochimique par la mesure des gaz volcaniques en sortie de conduit (composition chimique et flux) couplée à l'étude des inclusions vitreuses (ex. Aiuppa et al., 2010a ; Métrich et al., 2010), une approche théorique par l'utilisation de modèles numériques ou théoriques (ex. Toramaru, 1989, 1995 ; Blower et al., 2001, 2002 ; Yamada et al., 2005 ; Toramaru, 2006, 2014) et une approche expérimentale par la simulation en laboratoire des processus de vésiculation au moyen d'expériences de décompression à haute pression et haute température (ex. Hurwitz et Navon, 1994 ; Mourtada-Bonnefoi et Laporte, 1999, 2002, 2004 ; Gardner et al., 1999 ; Mangan et Sisson, 2000, 2005 ; Gardner et Denis, 2004 ; Iacono-Marziano et al., 2007 ; Cluzel et al., 2008 ; Gardner et Ketcham, 2011). C'est cette dernière approche que nous suivrons dans le cadre de cette thèse dont le programme fait partie des objectifs de l'ANR DEGAZMAG.

4.1. Stratégie expérimentale

Pour une meilleure compréhension de la dynamique d'ascension et d'éruption des magmas basaltiques, nous avons réalisé des expériences de décompression spécifiquement orientées pour documenter la nucléation des bulles de gaz ; ce processus, qui constitue la première étape du dégazage magmatique, conditionne l'évolution de la phase gazeuse (force motrice des éruptions explosives) dans le conduit volcanique. Les conditions naturelles (P, T, fO_2, composition basaltique, teneur en volatils, vitesse d'ascension) de la vésiculation ont été approchées. Nous avons mené des expériences systématiques dans le but de simuler les textures et la chimie des produits émis lors des éruptions basaltiques explosives. Les principaux objectifs de cette étude expérimentale ont été les suivants :

- Préciser les conditions de la nucléation des bulles de gaz en définissant la pression de sursaturation (et la tension de surface associée) requise au déclenchement de la nucléation homogène/hétérogène. Les liquides expérimentaux ont été trempés à différentes pressions finales (P_f = 200, 150, 100, 50 et 25 MPa, Fig. i.10) pour déterminer les pressions de nucléation, et permettre la caractérisation texturale et chimique des verres obtenus.

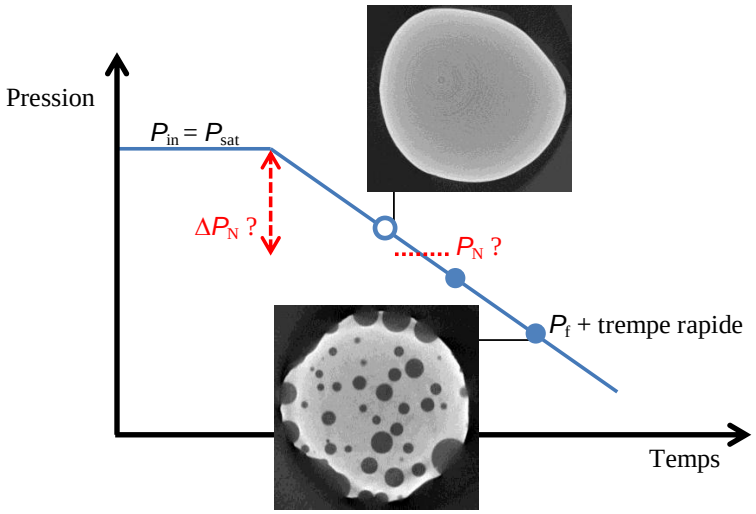

Fig. i.10. Détermination de la pression de nucléation des bulles (P_N), ou pression de sursaturation en volatils (ΔP_N), lors de l'étape de décompression. P_{in} : pression initiale ; P_{sat} : pression de saturation en volatils ; P_f : pression finale.

- Contraindre le comportement des volatils majeurs (H_2O, CO_2, S) lors de la remontée des magmas basaltiques (partage liquide/gaz), en particulier déterminer leur effet sur la nucléation des bulles. Pour ce faire, quatre compositions en volatils ont été examinées.
- Quantifier l'effet de la vitesse d'ascension sur la cinétique de nucléation des bulles de gaz. Pour ce faire, deux différents taux de décompression ont été appliqués, 39 et 78 kPa/s, correspondant à des vitesses d'ascension de 1,5 et 3 m/s, respectivement (Chapitre iv). Il s'agit de vitesses d'ascension réalistes pour les magmas basaltiques (ex. Vetere et al., 2007), et qui, dans le cas du Stromboli, correspondent potentiellement aux temps d'incubation des paroxysmes (voir ci-dessous).
- Tester l'importance de la nucléation hétérogène dans les liquides basaltiques et notamment l'efficacité des oxydes Fe–Ti comme sites de nucléation des bulles de gaz.

Nous avons pris pour cible le Stromboli, en Italie, car de nombreuses et diverses données (géochimiques, géophysiques et géodésiques) sont disponibles sur ce "volcan laboratoire", nous permettant de contraindre nos conditions expérimentales puis de confronter nos résultats aux données naturelles (texture et chimie des verres). De plus, ce volcan basaltique est caractérisé par une variété de styles éruptifs, effusif à explosif, reflétant sa richesse en volatils, avec notamment des événements très énergétiques de type paroxysmal.

4.2. Calage des expériences de décompression

Comme mentionné ci-dessus, les conditions expérimentales (conditions de stockage et de remontée : *P*, *T*, fO_2, composition basaltique, teneur en volatils, vitesse d'ascension) ont été contraintes par rapport au système volcanique du Stromboli.

4.2.1. *Choix du volcan de référence : Le Stromboli*

Le Stromboli est une île de l'archipel des Eoliennes, Italie, formée par un volcan basaltique actif (Fig. i.11). Il s'agit d'un volcan d'arc, s'élevant à ~924 m d'altitude. Son édifice s'étend à une profondeur de 1500–2600 m au-dessous du niveau de la mer (Di Roberto et al., 2008). Le Stromboli est un volcan basaltique de référence de par son intense activité, établie il y a 1300–1700 ans (Rosi et al., 2000). Il a d'ailleurs donné son nom à un type d'éruptions qui le caractérise : Strombolien. Ce dynamisme éruptif consiste en des explosions de basse énergie, manifestées par des jets de scories incandescentes et de cendres jusqu'à une hauteur de 150 mètres au-dessus des bouches éruptives sommitales. Celles-ci interviennent toutes les 10 à 20 minutes et sont associées à des émissions de gaz (H_2O, CO_2, SO_2, Aiuppa et al., 2010a) en continu. Selon Burton et al. (2007), les explosions Stromboliennes résultent de la remontée périodique (depuis < 3 km) puis de l'éclatement de poches de gaz ("gas slugs") en surface. Cette activité quasi-permanente, dite normale, peut être interrompue par des coulées de laves, voire par des événements plus énergiques et inhabituels : des explosions majeures (1–3 par an, Barberi et al., 1993) à paroxysmales (1 tous les 5–15 ans, Bertagnini et al., 2011 ; Rosi et al., 2013), définies comme des paroxysmes Stromboliens (Mercalli, 1907; Rosi et al., 2013). Lors de ces violentes éruptions, des bombes et des blocs de taille métrique, des cendres, ainsi que des gaz sont produits et éjectés jusqu'à plusieurs kilomètres de hauteur.

Les dangers associés à son activité (émissions de gaz, dépôts de cendres et de bombes volcaniques, éruptions de plus grande ampleur et tsunamis associés à la déstabilisation de ses flancs) en font un des volcans les plus surveillés ; il l'est continuellement. De ce fait, son système d'alimentation et son activité (notamment l'activité normale) sont assez bien connus.

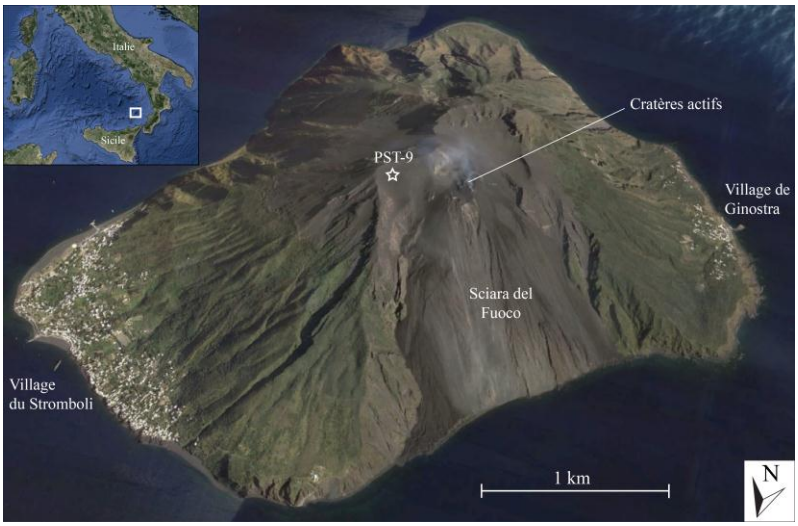

Fig. i.11. Géolocalisation du volcan Stromboli (vue satellite *Google Earth*).

Au Stromboli, il y a deux niveaux de stockage magmatique (Fig. i.12), occupés par deux magmas distincts : un premier réservoir profond (~8 km, Di Carlo et al., 2006 ; Pichavant et al., 2009 ; Métrich et al., 2010) occupé par les magmas parents non-dégazés, donc riches en volatils, (ponces jaunes), et un second réservoir plus superficiel (2–4 km, ex. Métrich et al., 2010) occupé par des magmas pauvres en volatils (scories noires). Ces derniers alimentent l'activité normale et les coulées de lave. Ils résultent de la cristallisation, à plus basse pression, des magmas parents qui rechargent régulièrement le réservoir superficiel (Pichavant et al., 2009, 2011 ; Métrich et al., 2010).

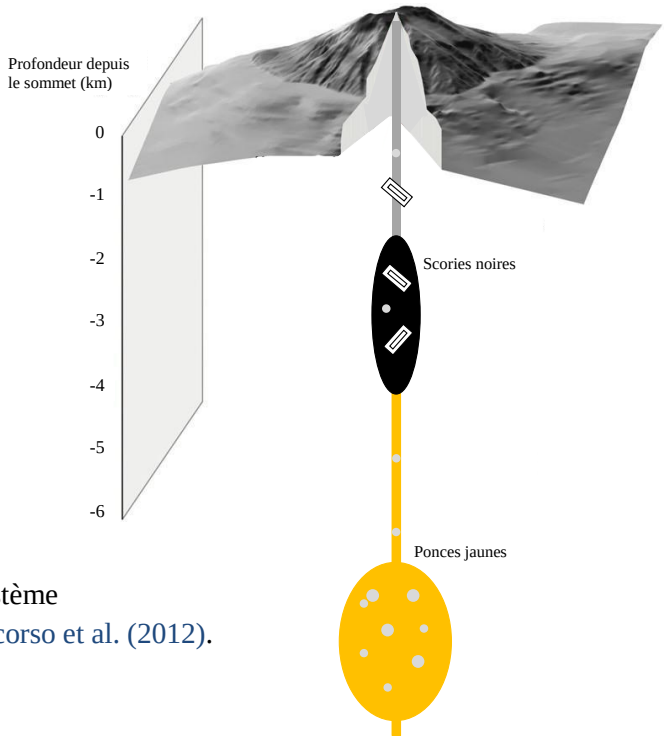

Fig. i.12. Représentation schématique du système d'alimentation du Stromboli, d'après Bonaccorso et al. (2012).

4.2.2. *Choix du matériel de départ : La ponce Strombolienne PST-9*

Le matériel de départ que nous avons choisi d'utiliser pour nos expériences est une ponce. Comme mentionné précédemment (voir la partie 2.2), l'étude texturale de ces produits éruptifs nous renseigne sur les étapes de la vésiculation du magma ; ce matériel est donc bien approprié à cette étude. Au Stromboli, ce produit est émis lors des éruptions paroxysmales. Il s'agit d'une ponce jaune (de couleur dorée) contenant peu de cristaux (~10% vol, clinopyroxène, olivine et plagioclase, Pichavant et al., 2011) et beaucoup de vésicules (~60% vol) (Fig. i.13). Elle a la particularité d'être souvent mélangée à la scorie noire, qui elle est riche en cristaux (~50% vol, plagioclase, clinopyroxène et olivine, Landi et al., 2004 ; Pichavant et al., 2011) ; certains de ces cristaux (les plagioclases) se retrouvent d'ailleurs souvent incorporés dans les ponces lors des éruptions. Celle que nous avons utilisée pour nos expériences (ponce PST-9, Di Carlo et al., 2006 ; Pichavant et al., 2009 ; 2011) a été émise entre 800 et 1600 ans après J.C. (Di Carlo et al., 2006), ce qui est récent dans l'histoire éruptive de ce volcan.

Fig. i.13. Photo de la ponce PST-9.

Pour préparer les expériences de décompression, il est important de connaître les conditions de stockage et d'ascension des magmas au Stromboli lesquelles vont nous fournir respectivement les conditions expérimentales initiales (correspondant à la synthèse des liquides) et finales (correspondant à leur décompression). La ponce PST-9 a été le matériel de départ des travaux expérimentaux visant à améliorer la compréhension du système d'alimentation du Stromboli (Di Carlo, 2004 ; Di Carlo et al., 2006 ; Lesne, 2008 ; Pichavant et al., 2009 ; 2011 ; Lesne et al., 2011a, b, 2015). Les conditions de stockage pré-éruptives sont donc relativement bien connues. Ainsi, pour nos expériences, nous avons fait le choix

d'une pression initiale de 200 MPa, correspondant à la position du réservoir profond (lieu de stockage des ponces jaunes) ; les pressions finales, comprises entre 150 et 25 MPa, correspondent à différents niveaux dans le conduit volcanique. Une température de 1200°C a été choisie pour placer nos liquides basaltiques au-dessus du liquidus des ponces jaunes (Di Carlo et al., 2006 ; Pichavant et al., 2009), de manière à s'affranchir de la cristallisation de silicates (condition importante de l'étude de la nucléation homogène des bulles). La composition de la ponce PST-9, entre basalte riche en potassium et shoshonite (Tabl. i.1), est représentative de la composition du magma en profondeur, à l'origine des éruptions explosives. Les teneurs en volatils pré-éruptives des ponces ont été déterminées par l'analyse des inclusions vitreuses (Métrich et al., 2001 ; Bertagnini et al., 2003 ; Métrich et al., 2005, 2010). Elles sont de 1,8–3,4% pds H_2O, 894–1689 ppm CO_2, et de 1520–2450 ppm S. Nous avons utilisé ces données pour ajuster les concentrations en volatils de nos verres expérimentaux avant décompression. Concernant les vitesses d'ascension des basaltes au Stromboli, des contraintes pétrologiques et texturales s'accordent sur une ascension rapide des ponces jaunes depuis une zone de stockage située à 7–8 km de profondeur. D'une part, la ponce PST-9 ne contient pas, ou très peu (Métrich et al., 2010), de microlites, ce qui implique des durées d'ascension < 10 h (Di Carlo et al., 2006 ; Pichavant et al., 2011). D'autre part, les modèles de vésiculation présentés par Polacci et al. (2009), indiquent que le temps d'incubation des paroxysmes pourrait être de l'ordre de la minute à quelques heures. Sur la base de vitesses d'ascension déterminées pour les magmas shoshonitiques de Vulcanello (0,27–3,2 m/s, Vetere et al., 2007), un système volcanique proche du Stromboli, nous avons choisi des vitesses de 3 et 1,5 m/s (de plus faibles vitesses ayant fait l'objet de l'étude de Pichavant et al., 2013). En ce qui concerne les conditions redox, Di Carlo et al. (2006) et Pichavant et al. (2009) ont déterminés des fO_2 proches de NNO+0,5 (NNO est le tampon d'oxygène Nickel-Oxyde de Nickel), qui seront imposées dans nos expériences.

Tableau i.1
Composition chimique de la ponce PST-9

Oxyde	SiO_2	TiO_2	Al_2O_3	Fe_2O_3	FeO	MnO	MgO	CaO	Na_2O	K_2O	P_2O_5	Cr_2O_3	NiO	Total
PST-9	49.4	0.79	15.75	1.3	6.5	0.15	7.96	12.73	2.27	1.85	0.43	–	–	99.1

Analyse en roche totale de la ponce PST-9 (Di Carlo et al., 2006).
Analyse effectuée au CRPG, Nancy, France, par ICP-AES pour les éléments majeurs (% pds) et par ICP-MS pour les éléments en trace (% pds).

Les textures des ponces Stromboliennes ont été étudiées de façon détaillée, notamment par Polacci et al. (2006, 2009). Ces données seront utilisées par la suite et nous n'avons pas considéré comme nécessaire de caractériser la texture de la ponce PST-9.

4.2.3. *Gaz volcaniques*

Le Stromboli est également un volcan basaltique de référence de par la quantité de gaz émis ; H_2O, CO_2 et SO_2 sont les espèces volatiles dominantes (Aiuppa et al., 2010a). L'étude des gaz en sortie de conduit (composition chimique et flux) a permis de mettre en évidence des variations de composition en lien avec des changements d'activité du volcan (ex. Aiuppa et Federico, 2004 ; Burton et al., 2007 ; Aiuppa et al., 2009, 2010a, b, 2011 ; Allard et al., 2008 ; Allard, 2010 ; La Spina et al., 2013 ; Fig. i.14). Les phases explosives, associées aux éruptions Stromboliennes et majeures, sont des phases enrichies en CO_2 (Fig. i.14b) et appauvries en H_2O. Ainsi, lors de ces phases, les rapports molaires CO_2/SO_2 (Fig. i.14) et SO_2/HCl sont élevés, contrairement au rapport molaire H_2O/CO_2 (Fig. i.14b). En raison de la faible solubilité du CO_2, son origine dans la phase gazeuse est considérée profonde, à l'inverse du soufre qui est dégazé superficiellement. Dans la suite, ces données de composition des gaz seront utilisées pour comparaison avec la composition des phases fluides expérimentales.

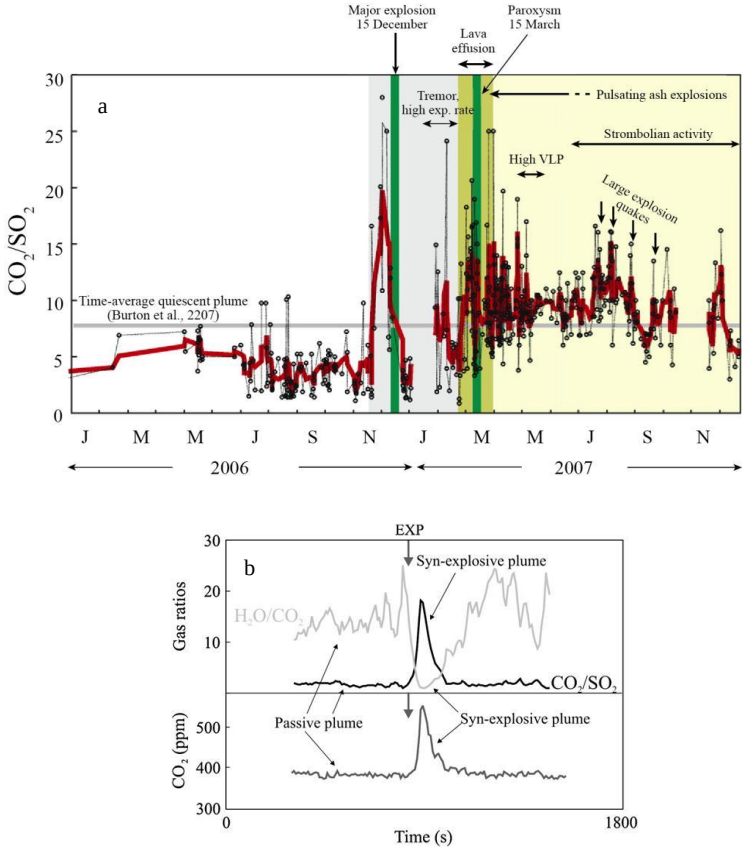

Fig. i.14. Illustration de la corrélation entre la composition des gaz (rapports molaires CO_2/SO_2 et H_2O/CO_2) et l'activité volcanique du Stromboli ((a) Aiuppa et al., 2009 ; (b) Aiuppa et al., 2010a). (a) Rapport molaire CO_2/SO_2 analysé en sortie de conduit sur la période 2006–2007. (b) : Gaz analysés en sortie de conduit, lors de périodes de dégazage passif et syn-explosives (éruptions Stromboliennes : EXP).

Chapitre ii

Méthodes expérimentales et techniques analytiques

Ce deuxième chapitre est consacré à la description des méthodes expérimentales et techniques analytiques employées au cours de cette thèse.

1. Méthodes expérimentales

Dans cette première partie sont détaillés la préparation des verres de départ, ainsi que le dispositif et le protocole expérimentaux.

Quatre principaux ensembles d'expériences ont été menés, faisant l'objet des chapitres iii, iv, v et vi. Le protocole expérimental mis en place pour les trois premiers ensembles d'expériences (basalte-H_2O-CO_2) est resté le même dans ses grandes lignes (voir ci-dessous). Pour le quatrième (basalte-H_2O-CO_2-S), ce protocole a été substantiellement modifié en raison de l'introduction de soufre (voir ci-dessous). Pour chaque ensemble d'expériences, deux types d'essais ont été menés : (1) *synthèse* et (2) *décompression*. La synthèse a pour but l'incorporation des volatils (H_2O, CO_2, S) dans les verres de départ, par dissolution à haute pression et haute température dans le liquide silicaté. La décompression simule l'ascension et le dégazage des liquides silicatés contenant les volatils dissous synthétisés lors de l'étape de synthèse. En général, les étapes de synthèse et de décompression ont été menées l'une après l'autre dans deux expériences distinctes, permettant la caractérisation systématique (chimique et éventuellement texturale) des échantillons avant qu'ils ne soient décomprimés lors de l'étape de décompression. Cependant, dans le quatrième ensemble d'expériences, les étapes de synthèse et de décompression ont été menées l'une après l'autre dans la même expérience, dans le but de réduire la durée totale des essais et ainsi de limiter les interactions entre la charge et les containers métalliques (voir ci-dessous).

1.1. Préparation des verres de départ

Comme mentionné précédemment, la ponce PST-9 a été utilisée comme matériel de départ dans toutes nos expériences (voir la section 4.2.2).

Afin d'obtenir des liquides basaltiques initialement (avant décompression) dépourvus de cristaux et de bulles (conditions indispensables à la réalisation de cette étude), la ponce PST-9 a été broyée en une fine poudre puis placée dans un creuset en platine et fondue à 1400°C, dans un four 1 atm Piézocéram, pendant 3 heures. Pour les trois ensembles

d'expériences des Chapitres iii, iv et v, le verre obtenu a été utilisé tel quel. Pour l'ensemble d'expériences mené avec du soufre (Chapitre vi), le verre obtenu a été re-broyé puis 1% d'oxyde de fer (Fe_2O_3) ajouté afin d'obtenir un mélange enrichi en fer servant à compenser la perte en fer vers la capsule de platine (voir ci-dessous). Le mélange verre-Fe_2O_3 a ensuite été fondu dans les conditions mentionnées ci-dessus. L'homogénéité des deux différents types de verres obtenus, enrichi et non enrichi en fer, a été contrôlée à la microsonde électronique ; leur composition est donnée dans le Tableau ii.1. Ces verres de départ ont ensuite été soit carottés (la majorité, Chapitres iii, iv et v) soit broyés (Chapitre vi), avant d'être utilisés dans les expériences de synthèse. Des cylindres de verre d'un diamètre de 2,5 mm et d'une longueur de quelques mm à plus d'1 cm ont été carottés directement dans le creuset. Des cylindres de 5 mm de diamètre et de ~6 mm de long ont également été carottés pour tester l'influence de la taille du matériel de départ sur la nucléation des bulles et la distribution des volatils lors de la décompression. L'utilisation de cylindres présente l'avantage de conserver une géométrie constante à tous les échantillons, ce qui facilite leur analyse texturale au microtomographe. Ce protocole présente également l'avantage de limiter la formation de bulles d'air ou d'argon lors de la synthèse, qui pourrait être favorisée par l'utilisation de poudres. L'inconvénient principal est que les durées de l'étape de synthèse doivent être importantes, suffisantes pour parvenir à une distribution homogène des volatils dissous par diffusion dans le cylindre de liquide basaltique. C'est la raison pour laquelle, dans certaines de nos expériences, notamment celles contenant su soufre (Chapitre vi), des poudres de verre ont été utilisées comme matériel de départ. On peut ainsi grandement limiter la durée de l'étape de synthèse ce qui minimise les interactions entre charge et container (voir ci-dessous), et augmente la durée de vie des capsules.

Tableau ii.1
Compositions chimiques des deux verres de départ enrichi et non enrichi en fer

Oxyde	Verre PST-9[a] (*n* = 54)	Verre PST-9 + 1% Fe[b] (*n* = 28)
SiO_2	50.9 (3)[c]	50.3 (3)
TiO_2	0.81 (8)	0.78 (9)
Al_2O_3	15.99 (28)	15.86 (21)
Fe_2O_3	nd	nd
FeO	7.7 (6)	8.5 (3)
MnO	0.16 (8)	0.11 (9)
MgO	7.21 (41)	7.53 (8)
CaO	12.34 (24)	12.11 (17)
Na_2O	2.39 (9)	2.29 (8)
K_2O	1.90 (12)	1.89 (8)
P_2O_5	0.55 (17)	0.52 (14)
Cr_2O_3	0.03 (4)	0.03 (3)
NiO	0.05 (6)	0.03 (5)
Total	97.4 (10)	98.8 (5)

[a] Composition chimique du verre obtenu par fusion de la ponce PST-9.
[b] Composition chimique du verre PST-9[a] enrichi en fer (ajout de 1% de Fe_2O_3) puis fondu.
[c] Ecart-type donné sur la dernière unité.
Les compositions données (en éléments majeurs et traces, % pds) sont moyennées sur la base de *n* analyses effectuées par microsonde électronique. Les % poids d'oxyde sont normalisés à 100%, excepté le total.
Tout le fer analysé est sous la forme FeO.
nd : non déterminé.

1.1.1. *Préparation des capsules*

La composition métallique des capsules a été choisie de façon à limiter leur interaction avec les charges expérimentales. Par exemple, l'utilisation de capsules en platine s'accompagne de pertes en fer pouvant être importantes (Brugier et al., 2015). Ainsi, des capsules constituées d'alliage or–palladium ($Au_{80}Pd_{20}$) ont principalement été utilisées (Chapitres iii, iv, v) ; la haute température de nos expériences (1200°C) ne nous a pas permis de travailler avec des capsules en or qui sont moins sensibles à la perte en fer mais dont le point de fusion est de 1064°C à 1 atm. Des capsules en Pt ont été utilisées, mais uniquement dans le quatrième ensemble d'expériences (Chapitre vi), le soufre réagissant sensiblement avec le Pd (ex. Lesne, 2008 ; Webster et Botcharnikov, 2011). Comme mentionné précédemment, la perte en fer associée à l'utilisation de Pt peut s'avérer importante ; des

alliages Fe–Pt ayant tendance à se former (Brugier et al., 2015). Nous avons donc compensé cette perte par l'ajout de fer (1% Fe_2O_3) dans le verre de départ (voir ci-dessus).

Il est important de noter que, tout comme les capsules en AuPd, les capsules en Pt se sont avérées sensibles à l'ajout de soufre (Chapitre vi). Après 1 heure d'expérience de synthèse (en utilisant des poudres de verre), des sulfures de platine ($Pt_{84–85}S_{15–16}$% pds élémentaire) se forment à l'interface verre-capsule ainsi que dans la paroi de la capsule de Pt (Fig. ii.1). Lors d'expériences préliminaires de synthèse utilisant des cylindres et non des poudres de verre, et donc de durée importante (72 h), une corrosion importante des capsules a été observée ; la durée de vie de la capsule est alors largement inférieure à la durée de l'expérience.

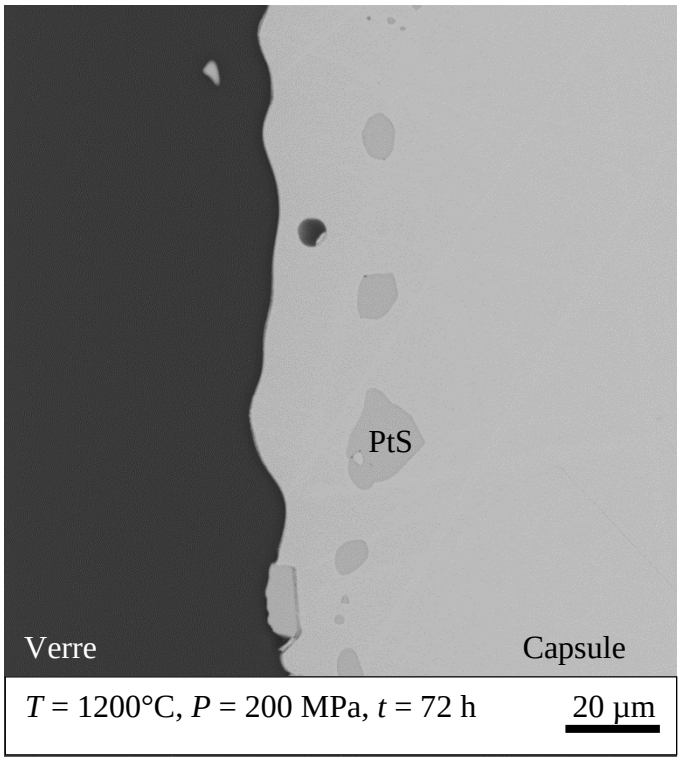

Fig. ii.1. Image MEB de sulfures de platine formés par interaction entre la charge et la capsule en Pt.

Les capsules ont été préparées à partir de tubes de 2,5 (surtout) et de 5 (moins souvent) mm de diamètre interne et de 0,2 mm d'épaisseur. Pour les expériences de synthèse, des tubes de 1,5 à 3,5 cm de longueur ont été découpés, de façon à laisser suffisamment d'espace aux éléments à charger (volatils + poudre ou carotte de verre), ainsi qu'à la phase fluide libre. Pour les expériences de décompression, la longueur des capsules a été ajustée de façon à accommoder l'expansion volumique du gaz, notamment celle de l'eau qui est importante à

basse pression. La longueur des capsules (de 1 à 5 cm) a donc été ajustée en fonction de la pression à laquelle les charges doivent être décomprimées. Les angles vifs des carottes de verre peuvent conduire à déchirer la paroi interne des tubes lors de la pressurisation de l'autoclave. Avant d'être soudés à une extrémité puis chargés, les tubes sont nettoyés à l'acide (mélange d'acide chlorhydrique et d'eau distillée) puis rincés à l'eau distillée, tous deux étant portés à ébullition. Ensuite, ils sont recuits au chalumeau pour les rendre plus malléables. Deux différents types de soudures ont été faites, l'une en pinçant l'extrémité du tube (tubes de Ø 2,5 mm) et l'autre en utilisant un "chapeau" plat (tubes de Ø 5 mm). Il s'agit d'une pièce métallique (de la composition de la capsule) moulée sur des tiges de différents diamètres et positionnée de façon à fermer le tube à plat (en "boîte de conserve") ce qui a l'avantage de conserver une géométrie cylindrique à la capsule.

1.1.2. *Remplissage des capsules*

Pour les expériences de synthèse, les volatils (H_2O, CO_2, S) ont été ajoutés au verre de départ (cylindre ou poudres) sous différentes formes : eau distillée pour H_2O, soufre élémentaire pour S, oxalate d'argent ($Ag_2C_2O_4$) ou acide oxalique di-hydraté ($C_2H_2O_4.2H_2O$) pour le CO_2 (Fig. ii.2). Le soufre ayant tendance à réagir avec l'argent pour former un précipité de sulfure ou de sulfate d'argent (Ag_2S ; Lesne, 2008 ; Webster et Botcharnikov, 2011), l'oxalate d'argent a été substitué par l'acide oxalique comme source de CO_2 dans le quatrième ensemble d'expériences (Chapitre vi).

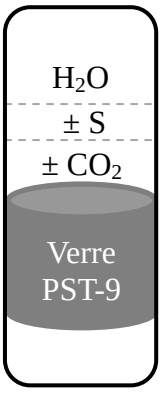

Fig. ii.2. Schéma du remplissage des capsules.

Nous avons fait varier la quantité de chaque espèce volatile introduite dans les capsules en fonction des deux rapports suivants :

$$XH_2O_{in} = \frac{mH_2O}{mH_2O + mCO_2} \text{ (Eq. ii.1) et } XCS_{in} = \frac{mCO_2}{mCO_2 + mS} \text{ (Eq. ii.2)}$$

avec XH_2O_{in} : fraction molaire d'eau initiale (correspondant à la quantité d'eau initialement introduite), XCS_{in} : fraction molaire de CO_2 initial (correspondant à la quantité de CO_2 initialement introduite) et m : masse de l'espèce volatile en mg.

En faisant varier ces deux paramètres, nous avons pu contrôler les quantités d'H_2O, de CO_2 et de S des liquides silicatés expérimentaux.

Dans les trois premiers ensembles d'expériences (Chapitres iii, iv, v), trois différentes proportions de H_2O et CO_2 ont été introduites dans les capsules, correspondant à XH_2O_{in} = 1, ~0.5 et 0. Lorsque XH_2O_{in} = 1, la charge est saturée en eau. Au contraire, lorsque XH_2O_{in} = 0 la charge est en principe anhydre. Cependant, de l'eau a systématiquement été produite au cours des expériences de synthèse réalisées dans ces conditions. L'analyse des verres après synthèse montre systématiquement des concentrations en H_2O significatives (0,71–1,12 % pds, Fig. ii.3). La production d'eau dans cette série de verres s'explique principalement par la réduction du Fe^{3+} du verre de départ (préparé en conditions oxydantes) par l'H_2 utilisé pour la pressurisation de l'autoclave et dans une moindre mesure par l'utilisation d'oxalate d'argent imparfaitement déshydraté comme source de CO_2.

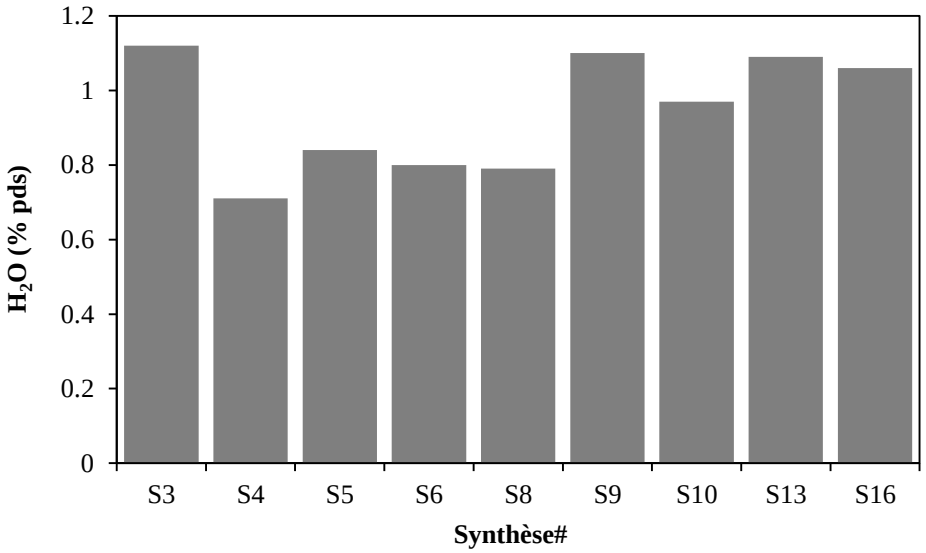

Fig. ii.3. Quantité d'H_2O (% pds) produite au cours des expériences de synthèse.

Lorsque $XH_2O_{in} \approx 0.5$, H_2O et CO_2 sont tous deux dissous dans le liquide silicaté. Pour les cylindres de 5 mm de diamètre, seul $XH_2O_{in} = 1$ a été considéré car l'homogénéisation par diffusion du CO_2 dans un tel matériel requiert une trop longue durée de synthèse (estimée à 5–6 jours).

Dans le quatrième ensemble d'expériences (Chapitre vi), les proportions de H_2O, CO_2 et S introduites ont été progressivement ajustées de façon à reproduire les teneurs en volatils des inclusions vitreuses des ponces du Stromboli (1.8–3.4 % pds H_2O, 894–1689 ppm CO_2, 1520–2450 ppm S, Métrich et al., 2001 ; Bertagnini et al., 2003 ; Métrich et al., 2010). Ceci nous a conduit à des valeurs de $XH_2O_{in} = 0.51–0.64$ et de $XCS_{in} = 0.45–0.59$.

Pour les expériences de décompression, une partie de chaque verre synthétisé (cylindre ou bloc, longueur ~4 mm, diamètre 2.5 ou 5 mm) a été chargée dans des nouvelles capsules sans aucun autre volatil ajouté, générant ainsi de faibles proportions de phase fluide libre dans les charges.

Une fois chargées, la deuxième extrémité des capsules est soudée afin d'assurer leur herméticité. Le poids des capsules est ensuite contrôlé, au début (après un passage à l'étuve de quelques heures à quelques jours à 120°C) et à la fin de chaque expérience, pour s'assurer que les volatils ne se soient pas échappés.

1.2. Dispositif expérimental

1.2.1. *Autoclave à chauffage interne*

Les expériences ont toutes été menées dans un autoclave à chauffage interne (Fig. ii.4), permettant de placer nos échantillons dans des conditions de *P*-*T*-fO_2 analogues à celles rencontrées dans la nature, et plus précisément dans celles régnant au Stromboli.

L'autoclave est équipé d'un système de trempe rapide qui permet de figer la texture et la chimie des échantillons en fin d'expérience (Di Carlo et al., 2006). Il est utilisé en position verticale pour minimiser la convection thermique. L'autoclave est pressurisé par des mélanges gazeux Ar-H_2, dont la composition permet de contrôler la fugacité d'hydrogène (fH_2) dans le milieu expérimental et indirectement celle d'oxygène (fO_2) dans chacune des capsules présentes lors de l'essai. La plupart des synthèses et des décompressions ont été menées avec une pression initiale d'1 bar H_2. Cependant, certaines de nos expériences ont été menées sans

H_2, générant des conditions plus oxydantes favorisant la cristallisation d'oxydes de Fe–Ti (Chapitre v). La pression totale est obtenue par une mise en pression initiale à froid (à hauteur d'un peu plus de 50% de la pression ciblée), puis par la montée en température du volume gazeux confiné dans l'autoclave. Ainsi, pour chacune de nos expériences, l'Ar a été pompé jusqu'à ~1200 bar à froid afin d'atteindre ~2000 bar à 1200°C. La pression totale est lue en continu sur un capteur calibré sur un manomètre Heise avec une précision de ± 20 bar.

Fig. ii.4. Photo d'un des deux autoclaves à chauffage interne utilisés.

Lors de l'expérience, les capsules sont placées dans un porte-échantillon en alumine suspendu par un fil de Pt dans la zone chaude d'un four molybdène. La température de cette zone, de 2–3 cm de long, est mesurée à l'aide de deux thermocouples de type S et contrôlée par un régulateur Eurotherm. Des conditions quasi-isothermes (gradient < 2–3°C/cm) sont maintenues dans le porte-échantillon. L'incertitude sur la mesure de la température est estimée meilleure que ± 5°C. A la fin de l'expérience, un courant électrique est envoyé à travers le fil de suspension, faisant tomber le porte-échantillon dans la zone froide (< 100°C) du four. Aucun cristal de trempe n'a été observé dans les verres expérimentaux, suggérant que leur refroidissement a été suffisamment rapide (~100°C/s, Di Carlo et al., 2006).

1.2.2. *Mesure des conditions d'oxydoréduction*

La fH_2 des expériences et indirectement la fO_2 des capsules, a été contrôlée par la technique du sensor solide (Taylor et al., 1992 ; Pownceby et O'Neill, 1994). Il s'agit d'une capsule en Pt de 2 cm de longueur (Ø 2,5 mm) contenant 15 ml d'eau, de la poudre de zirconium destinée à faire écran entre les réactifs et le métal de la capsule, et deux mélanges métal (alliage NiPd) oxyde (NiO) de rapport Ni/Pd différent ($X\text{Ni}_{in}$ = 0,15 et 0,85). De telles capsules (Fig. ii.5), perméables à l'H_2, ont été introduites dans certaines expériences de synthèse ; les expériences de décompression étant trop courtes pour équilibrer les alliages NiPd. Les conditions redox imposées lors de la synthèse sont supposées inchangées au cours de la décompression.

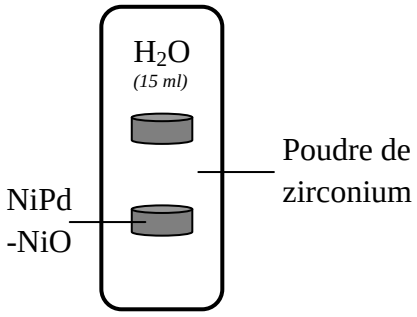

Fig. ii.5. Schéma du remplissage des capsules sensors.

Après l'expérience de synthèse, la composition (fraction molaire de Ni, XNi) des deux alliages NiPd est déterminée à la microsonde électronique, ce qui permet de calculer la fO_2 de la capsule sensor (Taylor et al., 1992 ; Pownceby et O'Neill, 1994). La fH_2 de l'expérience (la fH_2 étant la même pour toutes les charges, Eq. ii.3) est ensuite calculée à partir de la réaction de dissociation de l'eau (Eq. ii.4) en utilisant la fO_2 de la capsule sensor, la constante de dissociation de l'eau (K_e, Eq. ii.5, Robie et al., 1979) et la fugacité de l'eau pure à 200 MPa et 1200°C ($fH_2O°$, Burnham et al., 1969 ; Holloway, 1987). La fO_2 varie avec la teneur en eau des charges, exprimée par leur activité en eau aH_2O (ou fH_2O, Eq. ii.6), et donc au sein d'une même expérience. Pour déterminer la fO_2 de chacune des charges, la fH_2O est calculée à partir des teneurs en eau mesurées dans les verres synthétisés (par spectroscopie IR) en utilisant le modèle thermodynamique de Burnham (1979) pour l'eau dans les liquides silicatés.

L'expression de la fugacité d'hydrogène : $\log fH_2 = \log K_e + \log fH_2O - ½ \log fO_2$ (Eq. ii.3) est obtenue d'après la réaction de dissociation de l'eau : $H_2 + ½ O_2 \rightarrow H_2O$ (Eq. ii.4) qui a pour constante d'équilibre :

$$K_e = \frac{fH_2O}{fH_2 \, fO_2^{1/2}} \text{ (Eq. ii.5).}$$

La fugacité de l'eau est quant à elle reliée à l'activité de l'eau par la relation suivante :

$$fH_2O = aH_2O \cdot fH_2O° \text{ (Eq. ii.6).}$$

1.3. Protocole expérimental

1.3.1. *Expériences de synthèse*

Le but est d'obtenir des liquides basaltiques avec des concentrations et des distributions homogènes en volatils (H_2O, CO_2, S) dissous. Toutes les expériences de synthèse (Chapitre iii, iv, v et vi) ont été menées à 1200°C et 200 MPa (± 3.8 MPa), pour une fugacité d'oxygène comprise entre NNO–1,4 (XH_2O_{in} = 0) et NNO+4,3 (XH_2O_{in} = 1), NNO étant l'expression de la fO_2 rapportée au tampon Nickel–Oxyde de Nickel. Il s'agit de conditions au-dessus du liquidus de la ponce PST-9, sur la base d'expériences d'équilibre de phases antérieures (Di Carlo et al., 2006 ; Pichavant et al., 2009), ce qui permet de s'affranchir de la cristallisation de silicates. Jusqu'à quatre capsules (une pour chaque XH_2O_{in} examinée plus une capsule sensor) ont été placées dans l'autoclave pour des durées de 40 à 48 heures pour les expériences partant de cylindres (Chapitres iii, iv, v), et seulement de 1 heure pour les expériences partant de poudres (Chapitres iii, vi). De telles durées sont en accord avec les données de diffusivité pour H_2O, CO_2 et S (Freda et al., 2005 ; Zhang et Ni, 2010) dans les liquides basaltiques et en principe suffisantes pour que la distribution des volatils soit homogène dans les cylindres (Ø 2,5 mm) et les poudres de verre, respectivement. Pour les cylindres de 5 mm de diamètre, 24 heures se sont avérées suffisantes pour homogénéiser la distribution de l'eau et atteindre l'équilibre.

Les verres synthétisés sont dépourvus de cristaux et de bulles (Fig. ii.6). Ils sont ensuite utilisés comme verres de départ dans les expériences de décompression.

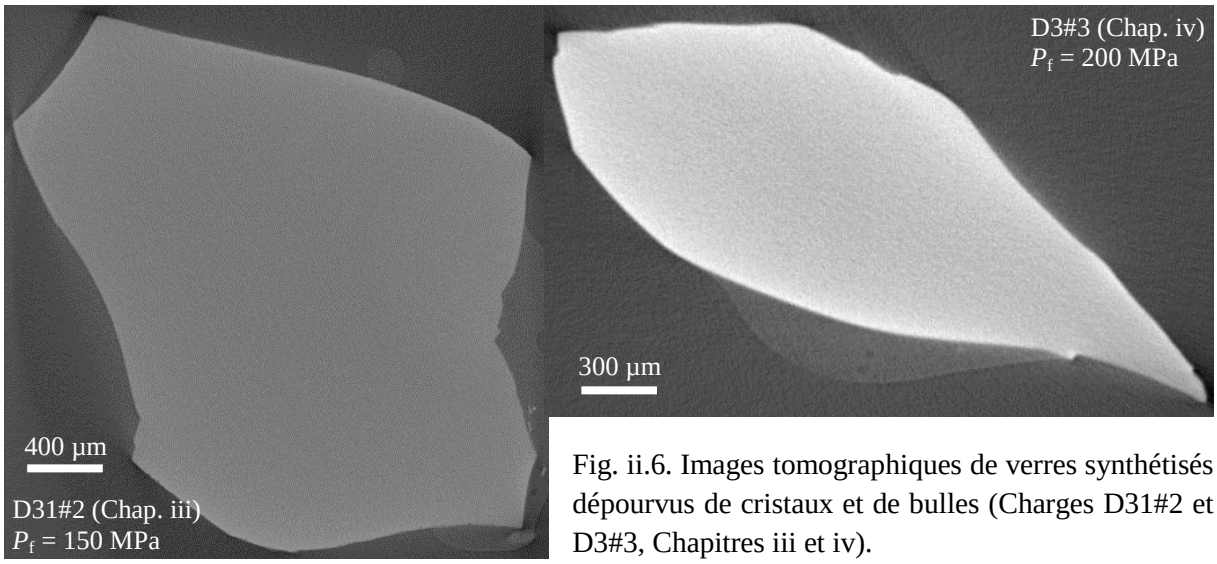

Fig. ii.6. Images tomographiques de verres synthétisés dépourvus de cristaux et de bulles (Charges D31#2 et D3#3, Chapitres iii et iv).

1.3.2. *Expériences de décompression*

Les expériences de décompression ont été conduites afin de simuler l'ascension et le dégazage des liquides basaltiques contenant les volatils (H_2O, CO_2, S). Une expérience de décompression comporte trois étapes : (1) la ré-homogénéisation des verres synthétisés, (2) la décompression, et (3) la trempe rapide (Fig. ii.7).

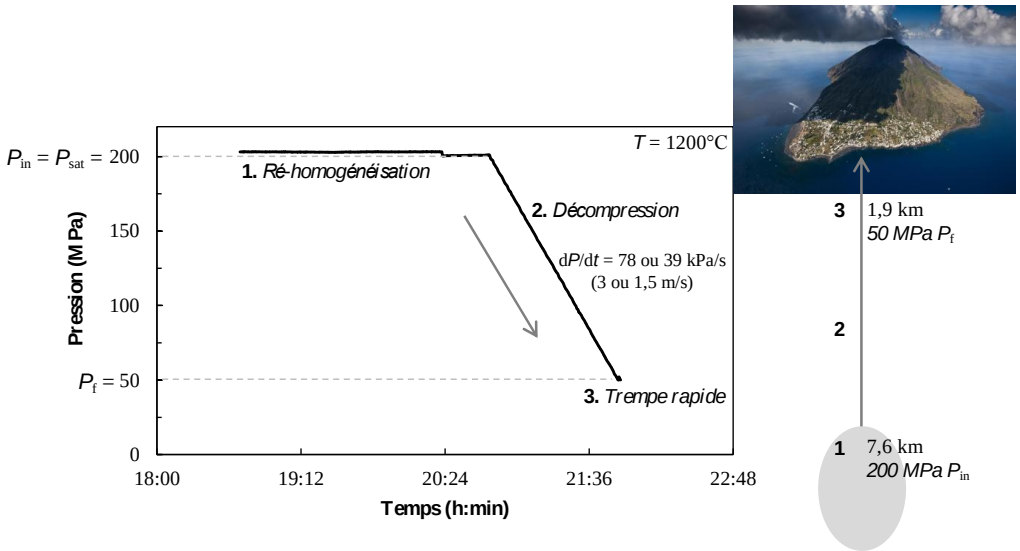

Fig. ii.7. Déroulement d'une expérience de décompression *(Photo du volcan Stromboli : Yann Arthus-Bertrand)*. P_{in} : pression initiale ; P_{sat} : pression de saturation ; P_f : pression finale (50 MPa pour exemple) ; dP/dt : taux de décompression ; 1, 2, 3 : étapes de l'expérience de décompression.

Chaque expérience de décompression inclut un maximum de trois capsules (une pour chaque XH_2O_{in} examinée). Pour commencer, (1) les verres synthétisés sont portés à 1200°C et 200 MPa pendant une heure, afin de les ré-homogénéiser suite à la montée en pression et en température. (2) La pression est ensuite réduite manuellement de 200 (P_{in} : pression initiale) à 150–25 MPa (P_f : pression finale) à un taux contrôlé de 39 ou 78 kPa/s (correspondant à des vitesses d'ascension de 1,5 et 3 m/s, respectivement). Cela se traduit par des durées de décompression totales de 10 à 75 min. Pendant la décompression, la pression est enregistrée en continu. Enfin, (3) les charges sont trempées en quelques secondes en conditions quasi isobares. A noter que certaines expériences ont été trempées à 200 MPa, c'est-à-dire directement après l'étape de ré-homogénéisation, sans avoir été décomprimées ($P_{in} = P_f$), afin de vérifier la procédure expérimentale en deux temps (synthèse puis décompression dans deux expériences distinctes) quant à la nucléation précoce de bulles ou encore la perte en volatils (notamment en eau) sur les bords des charges pendant la seconde montée en température et en pression.

Le poids des capsules est contrôlé à la fin de chaque expérience de synthèse et de décompression, et celles percées sont mises de côté (à l'exception d'une capsule, voir le chapitre iv). Elles sont ensuite ouvertes délicatement, afin de récupérer les verres puis de les analyser.

2. Techniques analytiques

La texture et la chimie des verres expérimentaux, avant et après décompression, ont été caractérisées à l'aide de différentes techniques analytiques : la microtomographie par rayons X, la microscopie électronique à balayage (MEB), la microsonde électronique et la spectrométrie infrarouge à transformée de Fourier (FTIR).

2.1. Préparation des échantillons

Après l'expérience de synthèse, chaque cylindre de verre a été divisé en plusieurs parties. L'une de ces parties a servi pour l'analyse des teneurs et distributions en volatils (par FTIR) et les autres ont été utilisées comme produits de départ dans les expériences de décompression (Fig. ii.8).

Après l'expérience de décompression, une analyse par microtomographie aux rayons X a tout d'abord été faite sur chaque cylindre de verre, lequel a été analysé en entier (totalité de la carotte). A noter que cette technique ne requiert aucune préparation particulière des échantillons. Les blocs de poudre obtenus après synthèse et décompression dans l'ensemble d'expériences avec du soufre ajouté (Chapitre vi) n'ont pas été analysés au microtomographe, leur texture a uniquement été observée au MEB par faute de temps. Une fois l'analyse par microtomographie aux rayons X effectuée, les échantillons ont subi des préparations spécifiques, pour l'analyse FTIR, d'une part, ou les analyses à la microsonde électronique et au MEB, d'autre part. Dans les deux cas, les cylindres de verre ont été sectionnés en plusieurs tronçons perpendiculairement à leur grand axe, comme illustré dans la figure ii.8.

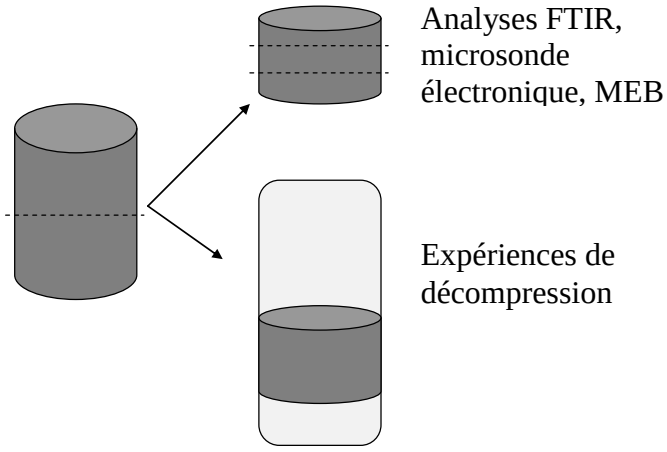

Fig. ii.8. Découpe des cylindres de verre.

Pour l'analyse FTIR, les sections de verre ont été polies sur les deux faces jusqu'à atteindre une épaisseur de l'ordre de quelques dizaines de microns. Pour ce faire, les échantillons ont été enrobés dans une résine pour orthodontie. Une fois double-polis, les verres ont été nettoyés à l'acétone. L'optimisation des mesures d'absorbances de l'eau totale et du CO_2 (CO_3^{2-}) ne requérant pas la même épaisseur (~50 µm pour l'H_2O et ~150 µm pour le CO_2), plusieurs fragments de verre d'un même échantillon ont parfois été préparés puis analysés.

Pour les analyses à la microsonde électronique et au MEB, les sections ont été incorporées dans une résine époxy. Les pastilles ainsi formées ont ensuite été polies puis métallisées au carbone. A noter que certains fragments de verre non polis, ainsi que des double-polis préalablement analysés à l'IR, ont été métallisés puis observés au MEB.

2.2. Microtomographie par rayons X

La microtomographie par rayons X a été utilisée pour imager l'intérieur des verres expérimentaux (le plus souvent les verres post-décompression) en trois dimensions, afin d'en déduire les principaux paramètres texturaux (taille et densité numérique de bulle, vésicularité). Chaque cylindre de verre, monté sur une tige en fibres de carbone avec de la colle thermoplastique, a subi une rotation de 360° pendant laquelle des projections radiographiques ont été collectées selon différents angles lors de son exposition aux rayons X. Les scans ont été acquis avec le microtomographe Phoenix Nanotom 180 de l'ISTO, Orléans, exploité entre 90 et 110 kV pour des courants de filaments variant entre 40 et 170 µA. Un filament de tungstène et une cible de molybdène, ou plus rarement de tungstène, ont été utilisés. Ces conditions conduisent à des voxels de 2,42 à 6,77 µm de côté. Cependant, cette résolution spatiale s'est parfois avérée insuffisante pour détecter les plus petites bulles, d'où le besoin d'utiliser une seconde technique d'imagerie (MEB, voir ci-dessous).

La reconstruction des projections tomographiques à l'aide du logiciel Phoenix datos|x produit une pile d'images en deux dimensions de l'échantillon. Trois types de corrections ont été appliqués pour améliorer la qualité des images reconstruites, en lien avec : (1) la présence de pixels défectueux produisant des artéfacts circulaires ("ring artefacts") sur les images, (2) le mouvement de l'échantillon et (3) le durcissement du faisceau ("beam hardening"). Une fois les images tomographiques, en niveau de gris, corrigées du bruit généré par le détecteur, l'échantillon et le faisceau lors de leur acquisition, le volume de l'échantillon en trois dimensions est obtenu grâce au logiciel de traitement d'images ImageJ (Abràmoff et al., 2004 ; Fig. ii.9a).

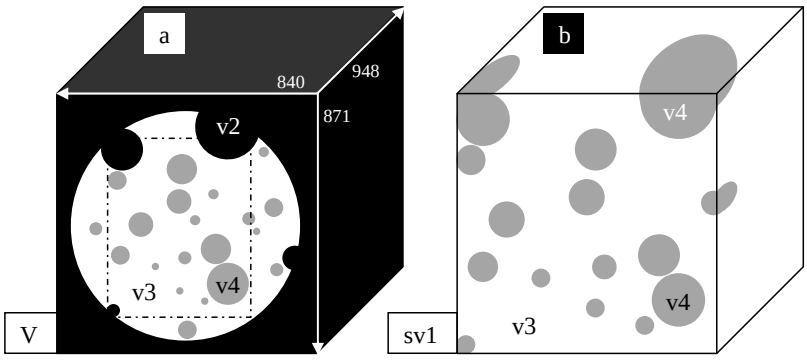

Fig. ii.9. Schémas représentatifs du volume total (a) et d'un sous-volume de l'échantillon (b).

Ce rendu volumique, correspondant au volume total étudié (V, Fig. ii.9a), a la dimension de l'ensemble de la pile d'images en trois dimensions. Il est composé de plusieurs sous-volumes : le volume de l'espace vide entourant l'échantillon (v2), le volume de verre (v3) et le volume de bulles (v4). La détermination du volume de l'espace vide, associée à celle du volume des bulles, en utilisant ImageJ, permet de déterminer le volume de verre (en soustrayant la somme des volumes de l'espace vide (v2) et des bulles (v4) au volume total étudié (V), v3 = V – (v2+v4)) et ainsi par suite les paramètres texturaux. Pour ce faire, la pile d'images de l'échantillon est manuellement segmentée. La valeur de seuil, correspondant à une valeur de niveaux de gris, est déterminée puis appliquée aux images afin de les partitionner. Ce procédé produit une pile d'images binaires dans lesquelles les objets d'intérêt (les bulles et l'espace vide, en noir) sont séparés du verre (en blanc, Fig. ii.10a). Suite à la segmentation des images, le volume de chaque objet est calculé à l'aide du plugin "3D Object Counter" (Bolte et Cordelières, 2006). Ce dernier identifie les particules présentes (espace vide + chaque bulle), les numérote puis détermine leur volume. La numérotation de ces objets permet de rejeter les artéfacts (fissures, bruit) ; cela a été fait pour chaque échantillon.

A partir de ces données, les principaux paramètres texturaux ont pu être déterminés. La taille (diamètre, *D*) des bulles est calculée à partir des volumes de bulles mesurés, en les considérant comme parfaitement sphériques. La densité numérique de bulles (*BND*) est le nombre de bulles soit par unité de volume de l'échantillon (verre + bulles), soit par unité de volume de verre (sans les bulles). A noter que les valeurs de *BND* définies par volume de verre restent invariantes à la croissance des bulles et peuvent donc être utilisées comme indicateurs des processus de nucléation (Proussevitch et al., 2007). C'est la raison pour laquelle nous avons préféré utiliser les *BND*s définies par volume de verre. La vésicularité correspond à la somme des volumes de bulles divisée par la somme des volumes de verre plus de bulles. Deux méthodes de détermination de la vésicularité ont été appliquées car l'une d'entre elles a l'inconvénient de dépendre du volume de l'espace vide (via la détermination du volume de verre, v3 = V – (v2+v4), Fig. ii.9a). Or, ce dernier comprend les bulles ouvertes situées à la bordure du cylindre de verre qui ne sont donc pas prises en compte dans le calcul de la vésicularité. Par cette méthode, la vésicularité des échantillons peut donc être sous-estimée, d'où l'introduction d'une seconde méthode de détermination de la vésicularité. Celle-ci considère des sous-volumes représentatifs de l'échantillon et non plus son volume total (V), ce qui permet d'exclure l'espace vide (v2) (Fig. ii. 9b). La vésicularité de chaque

échantillon est alors la moyenne de calculs effectués, à l'aide du plugin Voxel Counter, sur quatre sous-volumes ((sv1+sv2+sv3+sv4)/4 ou la notation sv représente un sous-volume).

La proportion d'oxydes (titanomagnétites) présents dans certaines charges a été déterminée sur un ou plusieurs sous-volumes représentatifs. Cette proportion est exprimée en densité numérique de cristaux (*CND*), définie par unité de volume de verre. Les objets d'intérêt n'étant plus les bulles mais les oxydes, la segmentation des images de chaque sous-volume s'est faite à partir d'une valeur de seuil différente ; les oxydes sont alors séparés du verre plus des bulles (Fig. ii. 10b). Suite à la segmentation, le volume de chaque oxyde a été déterminé avec le plugin "3D Object Counter" (Bolte et Cordelières, 2006). Le volume de verre devant être connu pour déterminer les *CND*, l'opération a été répétée (segmentation du sous-volume puis utilisation du plugin "3D Object Counter") afin d'obtenir le volume des bulles présentes dans chaque sous-volume analysé ; les bulles étant séparées du verre plus des oxydes.

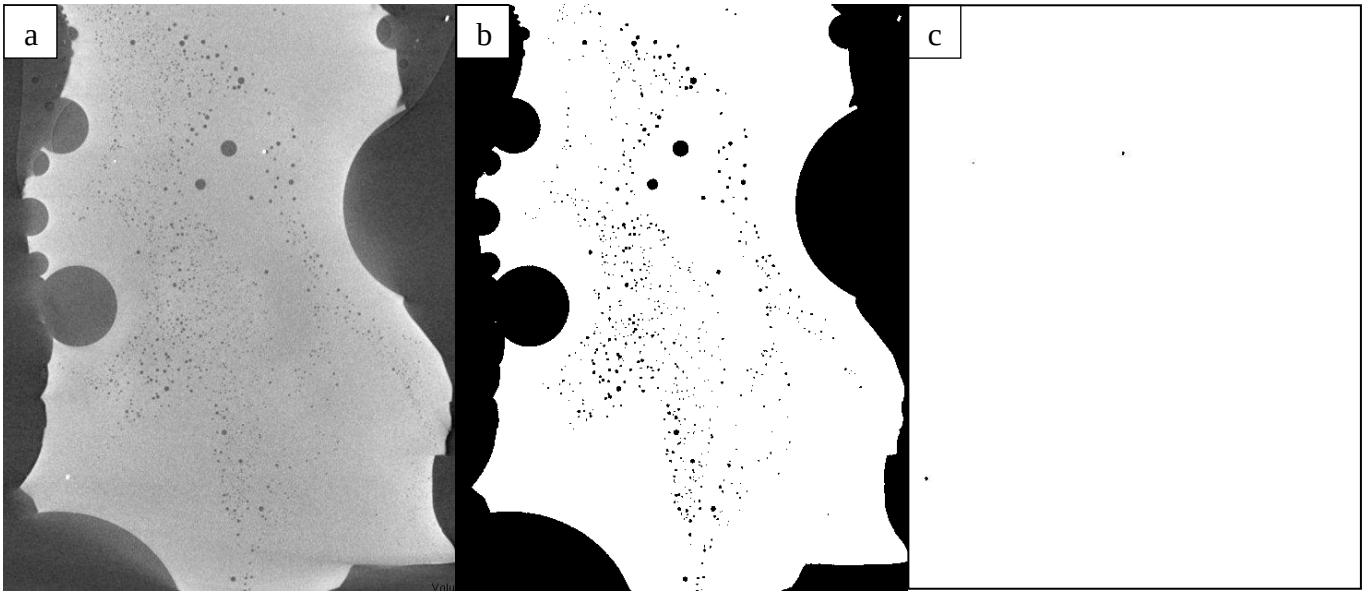

Fig. ii.10. Exemples de segmentation manuelle de l'image tomographique d'un verre décomprimé à 25 MPa ((a), Charge D13#3, Chapitre v). (b) Extraction des bulles et (c) des oxydes.

2.3. Microscopie électronique à balayage (MEB)

Cette méthode a été utilisée, de façon quasi systématique, pour observer la texture des verres expérimentaux après décompression. Nous avons cherché à savoir si de petites bulles n'ayant pas été détectées au microtomographe à cause de leur taille (< résolution spatiale) étaient présentes. De plus, le MEB nous a permis de détailler la relation entre les bulles et les

oxydes ou les sulfures de fer présents dans certaines charges. La composition des sulfures a d'ailleurs été estimée grâce au MEB. Pour cette thèse, nous avons fait usage du microscope TESCAN MIRA3 XMU de l'ISTO, Orléans. Une tension d'accélération de 15, 20 ou 25 kV a été appliquée.

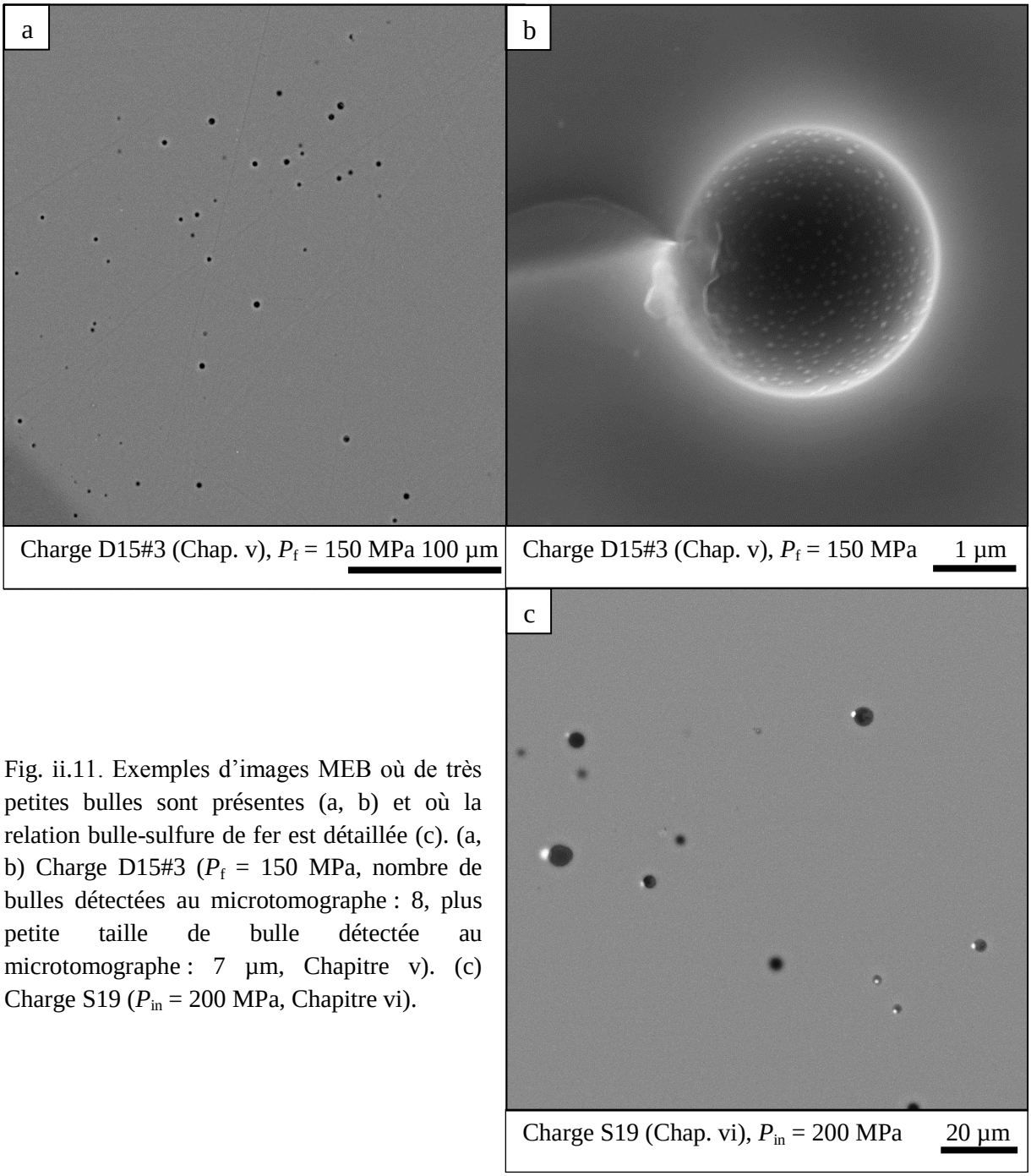

Fig. ii.11. Exemples d'images MEB où de très petites bulles sont présentes (a, b) et où la relation bulle-sulfure de fer est détaillée (c). (a, b) Charge D15#3 (P_f = 150 MPa, nombre de bulles détectées au microtomographe : 8, plus petite taille de bulle détectée au microtomographe : 7 µm, Chapitre v). (c) Charge S19 (P_{in} = 200 MPa, Chapitre vi).

Cette technique d'imagerie est la seule à avoir été utilisée pour l'analyse texturale des verres expérimentaux contenant du soufre (Chapitre vi). Une image MEB de chaque échantillon (où l'ensemble de la surface est observée) a été analysée à l'aide du logiciel

ImageJ afin d'en déterminer la vésicularité. Là encore, des sous-volumes ont été délimités afin d'exclure l'espace vide entourant l'échantillon. Les vésicularités sont la moyenne de quatre mesures effectuées avec le plugin Voxel Counter sur quatre sous-volumes représentatifs ; celles-ci étant le rapport du nombre de voxels segmentés (correspondant aux bulles) sur tous les voxels présents dans le sous-volume.

2.4. Microsonde électronique

Les compositions chimiques des phases expérimentales (verres et sensors) ont été analysées à la microsonde électronique Cameca SX FIVE du service commun de microanalyse BRGM-CNRS-Université d'Orléans. Des analyses chimiques ponctuelles ont été réalisées afin de déterminer, et de contrôler tout au long de la thèse, la composition des verres de départ en éléments majeurs (Si, Ti, Al, Fe, Mn, Mg, Ca, Na, K, P, Cr et Ni, Tableau ii.1). Des traversées ont également été réalisées pour s'assurer de l'homogénéité des verres après fusion, synthèse et décompression, notamment pour le fer et le soufre. Pour la calibration de ce dernier, de la barytine ($BaSO_4$) a été utilisée. Les conditions d'analyse suivantes ont été appliquées : tension d'accélération de 15 kV, courant échantillon (faisceau défocalisé, 5 µm) de 6 nA et temps de comptage de 10 s. La dé-focalisation du faisceau, pour l'analyse des verres, permet de limiter la migration des éléments alcalins (Na, K). Des analyses chimiques ponctuelles ont été réalisées dans les phases métalliques des sensors, requérant un courant échantillon de 20 nA. L'analyse ponctuelle des sulfures et du soufre dans les capsules en Pt requiert également d'autres conditions analytiques : courant échantillon (faisceau focalisé, 1 µm) de 20 nA et tension d'accélération de 20 ou 15 kV. Des standards de pyrite (pour Fe et S) et de Pt métallique (pour Pt) ont été utilisés pour la calibration.

Des cartographies des éléments S, Fe et Pt ont été faites pour représenter leur distribution dans la capsule en Pt (Fig. ii.12), suite aux interactions charge-capsule. Celles-ci ont été utiles aux calculs de bilan de masse. En plus d'être partagé entre le liquide basaltique et le fluide, une fraction importante de soufre est mobilisée dans les sulfures de platine et le fer du liquide silicaté forme un alliage Fe-Pt sur une partie de la capsule (sur une distance < 15 µm, Fig. ii.12). A noter que le fer est absent des sulfures de platine.

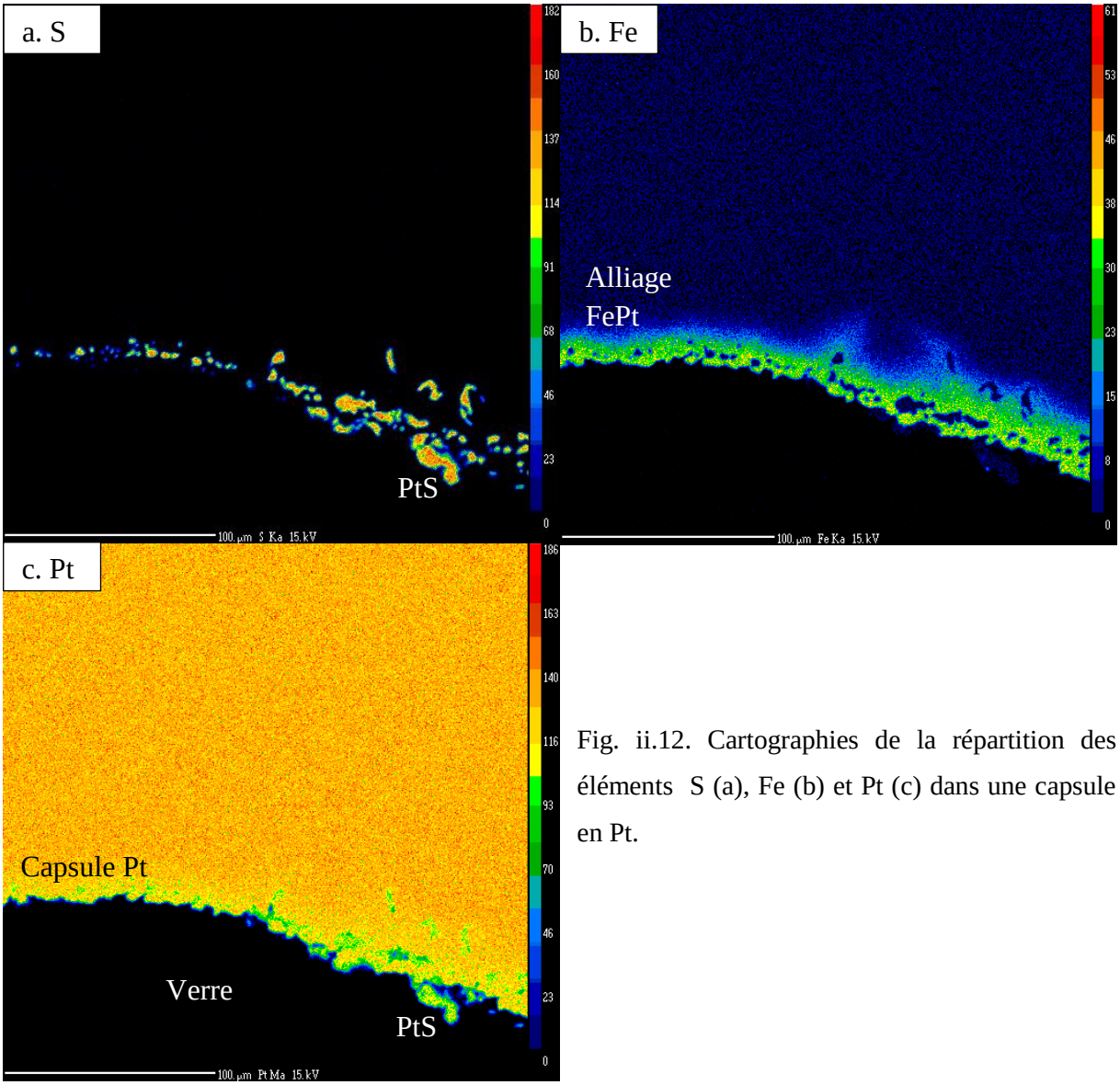

Fig. ii.12. Cartographies de la répartition des éléments S (a), Fe (b) et Pt (c) dans une capsule en Pt.

Les teneurs en soufre (S total) de deux verres standards, synthétisés pendant 72 heures, ont été déterminées par analyse élémentaire CS au CRPG, Nancy, afin de valider la méthode d'estimation du soufre à la microsonde électronique. Des teneurs comparables ont été obtenues par les deux méthodes (0,34% pds S par analyse élémentaire CS et 0,36 ± 0,03% pds S par microsonde électronique). Les multiples analyses (n = 243) à la microsonde électronique d'un des deux verres standards (S = 3583 ppm) ont fourni une dispersion analytique de 300 ppm, qui a été prise comme l'erreur analytique sur le soufre à la microsonde électronique.

2.5. Spectrométrie infrarouge à transformée de Fourier (FTIR)

La microspectrométrie infrarouge à transformée de Fourier a été utilisée pour analyser les verres expérimentaux pour l'H_2O et le CO_2 dissous, avant et après décompression. Nous avons effectué nos mesures à l'aide du spectromètre Nicolet 6700 couplé au microscope IR Continuµm de l'ISTO, Orléans. Celui-ci est équipé d'une lumière IR, d'une séparatrice KBr et d'un détecteur MCT-A (Mercure, Cadmium, Tellurium). Des profils avec un pas de 50 à 350 µm, ainsi que des analyses ponctuelles ont été réalisés pour vérifier la distribution des teneurs en H_2O et en CO_2. A noter que certaines charges ont été analysées plusieurs fois. Un spot de 50 µm de diamètre (parfois 100 µm) a été utilisé. Chaque spectre IR est la moyenne de 128 mesures effectuées à une résolution de 4 cm^{-1}.

Les concentrations en volatils sont obtenues à partir de la loi de Beer-Lambert :

$$C = \frac{100 A M}{\varepsilon \rho e} \quad \text{(Eq. ii.7)}$$

où C est la concentration de l'espèce volatile dissoute dans le verre silicaté (en % poids), A l'absorbance de l'espèce volatile, M la masse molaire de l'espèce volatile (en $g.mol^{-1}$), ε le coefficient d'absorptivité molaire (en $L.mol^{-1}.cm^{-1}$), ρ la densité du verre (en $g.cm^{-3}$) et e l'épaisseur de l'échantillon (en cm).

Pour l'H_2O, nous avons utilisé la bande d'absorption de l'H_2O totale ($H_2O_{moléculaire}$+OH^-) située à 3535 cm^{-1} (Fig. ii.13). L'absorbance de cette bande a été mesurée à l'aide d'une ligne de base rectiligne placée entre ~3850 et ~2500 cm^{-1}. Le coefficient d'absorptivité utilisé pour l'H_2O est de 64 $L.mol^{-1}.cm^{-1}$ (Dixon et al., 1995). Pour le CO_2, nous avons utilisé la bande d'absorption des carbonates (CO_3^{2-}) située à 1515 cm^{-1} (Fig. ii.13). L'absorbance de cette bande a été déterminée par soustraction de spectres ; le spectre utilisé pour la soustraction a été obtenu sur un verre de départ sec (dépourvu d'eau et de CO_2 dissous). Le coefficient d'absorptivité utilisé pour le CO_2 a été calculé d'après l'équation de Dixon et Pan (ε^{1525} = 451 – 342 [Na / (Ca + Na)] ; 1995), donnant une valeur de 363 $L.mol^{-1}.cm^{-1}$.

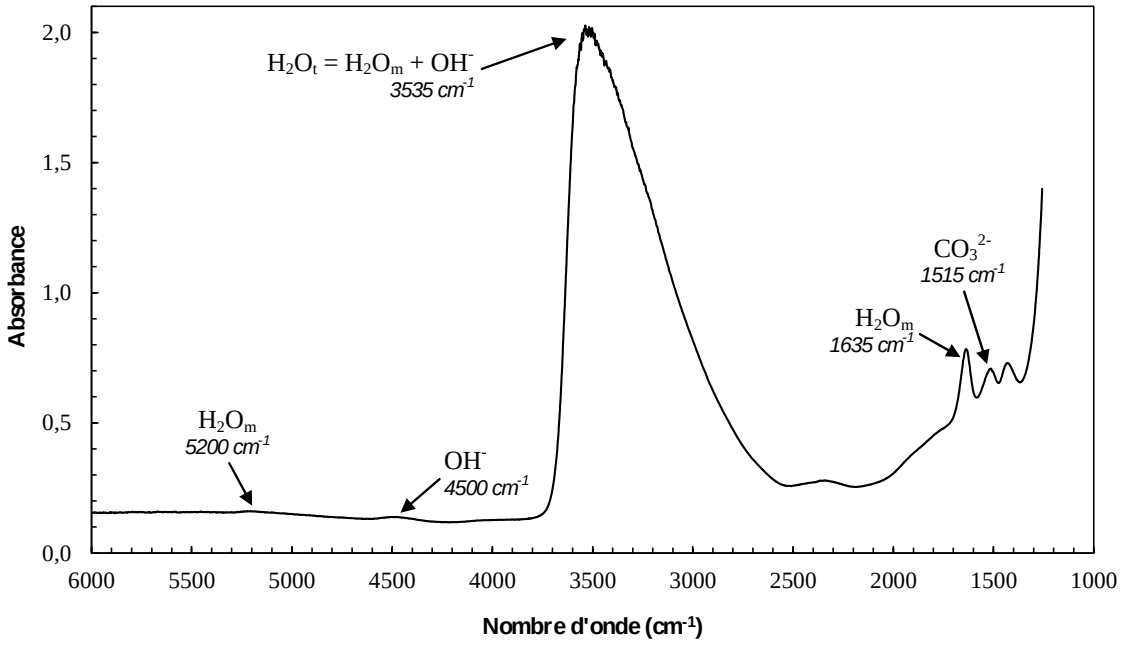

Fig. ii.13. Exemple de spectre IR typique pour l'analyse de l'eau et du CO_2 (CO_3^{2-}).

Les teneurs en volatils étant très sensibles à l'épaisseur des échantillons, il est important de les connaître avec précision. Pour ce faire, nous avons fait usage d'un microscope optique précis à ± 1–2 µm. La densité des verres expérimentaux a été déterminée à partir de la densité du verre de départ sec, et en utilisant les travaux de Richet et al. (2000). Un volume molaire partiel d'H_2O de 12 cm^3/mol a été pris en compte. Par cette méthode, seule l'influence de l'eau sur la densité du verre est considérée, les effets du CO_2 et du S sont supposés négligeables (Lange, 1994 ; Bourgue et Richet, 2001 ; Lesne et al., 2011a). La densité du verre sec (ρ = 2,747 ± 0,001) a, quant-à-elle, été mesurée à l'aide d'un dispositif de détermination de la masse volumique. Cet appareil repose sur le principe de la poussée d'Archimède en appliquant la méthode de la double pesée, une fois dans l'air, une fois dans l'éthanol.

2.6. Calculs thermodynamiques

2.6.1. *Vésicularités d'équilibre*

Les vésicularités d'équilibre de la ponce PST-9 pour l'eau et le CO_2 purs ont été déterminées de 200 à 1 MPa, dans le but de les comparer aux vésicularités mesurées dans nos

verres expérimentaux. La vésicularité d'équilibre est donnée par la relation suivante (Jaupart et Tait, 1990 ; Martel, 1996 ; Cluzel, 2007) :

$$V = \frac{x_0 - x}{x_0 - x + \frac{\rho \mathrm{fl}}{\rho \mathrm{liq}}(1 - x_0)} \quad \text{(Eq. ii.8)}$$

où x_0 est la solubilité de l'espèce volatile à la pression initiale (P_{in} = 200 MPa), x la solubilité de l'espèce volatile à une pression donnée, ρ_{fl} la masse volumique du fluide supercritique et ρ_{lid} la masse volumique du liquide silicaté saturé en volatils.

Plutôt que de calculer les vésicularités d'équilibre pour des mélanges de fluides H_2O-CO_2, nous avons préféré faire les calculs pour les deux cas extrêmes correspondants à des fluides H_2O et CO_2 purs. Pour les calculs, nous avons utilisé les modèles de solubilité de Lesne et al. pour l'eau (2011b) et le CO_2 (2011a) pour la composition PST-9 à 1200°C et aux différentes pressions. Les masses volumiques de l'eau supercritique ont été déterminées de 200 à 1 MPa, en utilisant une équation d'état de type Redlich-Kwong (d'après Holloway, 1981; Ferry et Baumgartner, 1987). Pour le CO_2 supercritique, les masses volumiques ont été obtenues à partir d'une droite de régression des données de fCO_2 de Dixon et al (1995) à 1200°C. La masse volumique du liquide basaltique a été supposée constante et égale à 2,64 g/cm^3 (avec l'eau) ou 2,75 g/cm^3 (avec le CO_2).

2.6.2. *Equilibres liquide-vapeur*

Pour les trois premiers ensembles d'expériences (Chapitre iii, iv, v), menées dans le système basalte-H_2O-CO_2, les équilibres liquide-vapeur (solubilités de l'eau et du CO_2 en fonction de la pression et de la température, chemins de dégazage à l'équilibre en système fermé et isobares) ont été déterminés avec le modèle VolatileCalc de Newman et Lowenstern (2002), pour un basalte contenant 49% pds de SiO_2. Les teneurs en volatils (H_2O, CO_2) mesurées dans les verres synthétisés ont également été comparées avec les solubilités expérimentales obtenues par Lesne et al. (2011a, b) et Shishkina et al. (2010), à 200 MPa et 1200–1250°C. A noter que les solubilités de Lesne et al. (2011a, b) ont été déterminées pour la composition PST-9. Dans le système incluant le soufre (basalte-H_2O-CO_2-S, Chapitre vi), le récent modèle D-Compress de Burgisser et al. (2015) a été utilisé pour simuler le dégazage lors d'une décompression connaissant P_{in}, T, fO_2, la fraction de gaz initiale et les concentrations en volatils (H_2O, CO_2, S) initiales.

2.7. Calculs de bilan de masse

La composition de la phase fluide contenue dans les capsules de synthèse et de décompression a été déterminée par bilan de masse. Les calculs ont uniquement concerné le quatrième ensemble d'expériences (basalte-H_2O-CO_2-S, Chapitre vi). Ils nécessitent de connaître les quantités de verre basaltique et de volatils (H_2O, CO_2, S) initialement introduites dans les capsules, ainsi que les concentrations en volatils des verres expérimentaux. Ces calculs ont été corrigés de la quantité d'H_2O produite par la réduction du Fe^{3+}. Cependant, dans cet ensemble d'expériences, la teneur en H_2O produite n'est pas connue. Nous l'avons donc contrainte (0,75% pds) d'une part à partir de nos données obtenues dans les trois autres ensembles d'expériences (voir section 1.1.2) et, d'autre part, à partir des données de Lesne et al. (2011c).

Dans nos expériences, le soufre n'est pas uniquement distribué entre le liquide basaltique et la phase fluide. Comme indiqué précédemment, du soufre est systématiquement présent dans la capsule de Pt, par la formation de sulfures de platine ($Pt_{84–85}S_{15–16}$% pds élémentaire). A noter que la quantité de sulfures de platine formés varie d'une capsule à l'autre, nous l'avons estimée par bilan de masse. De 23 à 51% du soufre initialement introduit est retenu dans ces sulfures. Cette proportion est prise en compte dans les calculs. Le soufre peut également être présent dans certaines charges en tant que sulfures de fer. Leur quantité étant infime, on ne les a pas considérés dans les calculs.

Chapitre iii

Nucléation homogène des bulles dans les systèmes basalte-H_2O et basalte-H_2O-CO_2

Résumé

Ce chapitre se présente sous la forme d'un article, dans lequel est détaillé un ensemble d'expériences de décompression menées dans les systèmes basalte-H_2O et basalte-H_2O-CO_2. Ces expériences ont pour but d'étudier le processus de nucléation homogène de bulles riches en H_2O, d'une part, et en CO_2, d'autre part, dans les liquides basaltiques, permettant ainsi de contraindre le comportement de ces deux volatils majeurs au cours du dégazage magmatique. Trois compositions en volatils ont été examinées : série #1 : 4,91% pds H_2O ; série #2 : 2,41% pds H_2O, 973 ± 63 ppm CO_2 ; série #3 : 0,98% pds H_2O, 872 ± 45 ppm CO_2. Des liquides basaltiques issus du Stromboli (composition PST-9) ont été synthétisés à 1200°C, 200 MPa (P_{in}), avant d'être décomprimés jusqu'à une pression finale (P_f) allant de 150 à 25 MPa et rapidement trempés. Les verres obtenus ont été caractérisés texturalement (vésicularités, nombre et taille des bulles) et chimiquement (teneur en volatils dissous). La particularité de l'ensemble d'expériences qui fait l'objet de ce chapitre est le taux de décompression qui est relativement élevé. Il est de 78 kPa/s, ce qui correspond à une vitesse d'ascension de 3 m/s environ. De cette façon, la durée des décompressions est relativement courte et la perte en eau des liquides basaltiques par diffusion au cours de la décompression est relativement limitée.

Nos résultats expérimentaux démontrent que de faibles sursaturations sont requises pour initier la nucléation homogène de bulles riches en H_2O (<< 50 MPa, série #1) d'une part, et en CO_2 (< 100 MPa, séries #2) d'autre part, dans les liquides basaltiques. Ces données sont en accord avec celles de Pichavant et al. (< 150 MPa, 2013) dans le système basalte-H_2O-CO_2, mais contrastent avec les données préexistantes pour des liquides magmatiques plus évolués. Nos résultats indiquent une légère influence du CO_2 sur la pression de nucléation homogène des bulles, un léger retard à la nucléation étant observé. Ainsi, la pression de sursaturation varie avec la concentration en CO_2, de << 50 MPa (pas de CO_2, série #1), ≤ 50 MPa (872 ± 45 ppm CO_2, série #3) à < 100 MPa (973 ± 63 ppm CO_2, série #2). Les textures de nos trois séries de verres expérimentaux résultent des processus de nucléation, croissance et coalescence des bulles, ainsi que de leur fragmentation. Les différences texturales observées entre la série #1, d'une part, et les séries #2 et #3, d'autre part, témoignent des effets contrastés de H_2O et du CO_2 sur le dégazage des liquides basaltiques. Tout d'abord, dans la série #1 (H_2O) la nucléation homogène des bulles intervient en deux évènements distincts, l'un (le plus important) à haute pression ($200 < P_f < 150$ MPa) et l'autre à basse pression ($50 < P_f < 25$ MPa), juste avant le niveau de fragmentation. En comparaison, dans les séries #2 et #3 (H_2O-CO_2) la nucléation homogène des bulles est un processus continu,

plusieurs événements de nucléation se succédant au cours de la décompression. La coalescence des bulles est observée dans les trois séries de verres entre 100 et 50 MPa. Cependant, seules les bulles de la série #1 coalescent dès 150 MPa. De plus, l'équilibre chimique pour les volatils est uniquement atteint dans les verres de la série #1. Les séries #2 et #3 ont des verres dont les teneurs en volatils sont systématiquement hors d'équilibre. A noter que des concentrations élevées en CO_2 persistent dans ces verres malgré de fortes vésicularités (jusqu'à 23% vol à 25 MPa). Un processus de fragmentation est identifié dans une expérience de la série #1 décomprimée à 25 MPa. Les verres expérimentaux présentent des distributions variables de la taille des bulles, unimodales, exponentielles et en loi de puissance, et qui sont en lien direct avec la composition en volatils (séries #1, #2, #3), les caractéristiques texturales et le mode de dégazage. Les textures des produits expérimentaux reproduisent, pour certaines caractéristiques (formes et petites tailles des bulles, densités numériques de bulles des ponces Stromboliennes), ou approchent, pour d'autres (vésicularités, densités numériques de bulles des produits émis lors des éruptions Pliniennes), celles des produits basaltiques associés aux éruptions explosives.

Homogeneous bubble nucleation in H_2O- and H_2O-CO_2-bearing basaltic melts: results of high temperature decompression experiments

Nolwenn Le Gall[1, 2, 3] · **Michel Pichavant**[1, 2, 3]

[1] Université d'Orléans, ISTO, UMR 7327, 45071, Orléans, France
[2] CNRS/INSU, ISTO, UMR 7327, 45071, Orléans, France
[3] BRGM, ISTO, UMR 7327, BP 36009, 45060, Orléans, France

Abstract High pressure and temperature decompression experiments were conducted to provide experimental information on the conditions of homogeneous bubble nucleation in basaltic melts. Experiments were performed on H_2O- and H_2O-CO_2-bearing natural melts from Stromboli. Three starting volatile compositions were investigated: series #1 (4.91 wt.% H_2O, no CO_2), series #2 (2.41 ± 0.04 wt.% H_2O, 973 ± 63 ppm CO_2) and series #3 (0.98 ± 0.16 wt.% H_2O, 872 ± 45 ppm CO_2). The volatile-bearing glasses were synthesized at 1200°C and 200 MPa, prior to be continuously decompressed in the pressure range 150–25 MPa and rapidly quenched. A fast decompression rate of 78 kPa/s (or 3 m/s) was applied to limit diffusive water loss from the melt cylinders. Post-decompression glasses were characterized texturally by X-ray CT. Experimental results demonstrate that homogenous bubble nucleation in basaltic melts requires supersaturation pressures (difference between saturation pressure and pressure at which homogeneous bubble nucleation is observed, ΔP_{HoN}) ≤ 50–100 MPa. ΔP_{HoN} varies with the dissolved CO_2 concentration, from << 50 MPa (no CO_2, series #1) to ≤ 50 MPa (872 ± 45 ppm CO_2, series #3) to < 100 MPa (973 ± 63 ppm CO_2, series #2). Melt vesiculation results from different sub-processes that include bubble nucleation, growth and coalescence, to fragmentation. A major difference in the mechanism of bubble nucleation exists between series #1, on the one hand, and series #2 and #3, on the other hand. In series #1, homogeneous nucleation occurs as two distinct events, the first and most important at high P_f ($200 < P_f < 150$ MPa) and the second, restricted to low P_f ($50 < P_f < 25$ MPa), just below the fragmentation level. In contrast, homogenous nucleation in series #2 and #3 melts is a continuous process. Bubble coalescence occurs in the three glass series and is the more strongly marked in the same pressure range (100–50 MPa). Chemical equilibrium is reached or approached during decompression in the series #1 melts. In contrast, non-equilibrium

degassing occurs systematically in the series #2 and #3 melts which retain high CO_2 concentrations even for high vesicularities (up to 23% at 25 MPa). Fragmentation was observed in one series #1 charge decompressed to 25 MPa P_f. Our experimental observations underline a significant effect of CO_2 on physical mechanisms of basaltic melts. Unimodal, exponential to power law BSDs were encountered and correlated with the different melt series, textural characteristics and types of degassing. Our experimental decompression textures either reproduce or approach the characteristics of explosive basaltic eruptions, in terms of vesicularity, *BND*s, bubble textures and sizes.

Keywords Basalt . Degassing . Decompression . Volatiles . Bubble nucleation . Bubble size distribution

1. Introduction

CO_2-oversaturated basaltic melts have been generated during experimental simulations of magma ascent and degassing (Pichavant et al., 2013), questioning the commonly accepted vision that, due to their relatively high temperatures and low viscosities, basaltic magmas degas near equilibrium (Sparks et al., 1994). The classical degassing model implies that volatiles (mainly H_2O and CO_2) exsolve following solubility laws (e.g. Dixon and Stolper, 1995 ; Dixon et al., 1995), i.e. with CO_2 being extensively lost to the gas phase at high pressure (therefore earlier upon ascent) and H_2O negligibly lost until the latest stages of degassing (Blundy et al., 2010).

Further observations that imply deviation from theoretical equilibrium degassing either under simple open- (the gas phase escapes from the magma) or closed-system (the gas phase stays with the magma) include in particular (1) the occurrence of CO_2-rich melt inclusions and (2) basaltic explosive volcanism.

(1) Melt inclusions having CO_2 contents higher than predicted from H_2O-CO_2 equilibrium degassing paths have been commonly found at basaltic volcanoes. For example, they occur at Etna, Stromboli and Vesuvius volcanoes in Italy, and at Jorullo volcano in Mexico (e.g. Marianelli et al., 2005; Spillaert et al., 2006; Johnson et al., 2008; Métrich and Wallace, 2008; Métrich et al., 2010). These data have been interpreted mainly to result from

the percolation of CO_2-rich magmatic fluids of deep provenance (Blundy et al., 2010). However, such a re-equilibration of the magma with a relatively CO_2-rich fluxing vapor phase (Blundy et al., 2010) would among other things cause magma dehydration which would promote crystallization. Alternatively, mixing of ascending and descending magmas (Witham, 2011; Beckett et al., 2014) has been suggested as a possibility to generate melt inclusions with CO_2 contents displaced compared to calculated degassing trends. Lastly, Pichavant et al. (2013) proposed that the generation of CO_2-rich melts is possible during basaltic magma ascent and degassing, as a result of a disequilibrium degassing behavior of CO_2. So far, disequilibrium degassing is an idea accepted for silicic compositions, like phonolitic or rhyolitic melts (e.g. Gonnermann and Manga, 2005; Iacono-Marziano et al., 2007), but not really considered for basalts.

(2) Basaltic volcanoes are commonly characterized by effusive to low-intensity Hawaiian and Strombolian explosive eruptions (Sable et al., 2006; Costantini et al., 2010). However, some of these volcanoes (e.g. Etna, Stromboli, Tarawera in New Zealand and Masaya in Nicaragua) may erupt occasionally in high-intensity paroxysmal, subplinian to Plinian explosive eruptions (e.g. Sable et al., 2006, 2009; Costantini et al., 2010). Magma degassing is thought to play a fundamental role in determining effusive versus explosive eruptive behavior (Gonnermann and Manga, 2005); the transition is thought to depend on the regime of gas bubble transfer and to be caused by changes in magma supply and ascent rates (e.g. Pioli et al., 2008; Métrich and Wallace, 2008; Edmonds, 2008).

Mechanisms of magma degassing include the nucleation, growth and coalescence of gas bubbles in magmas and are studied from different approaches including characterization of natural samples (e.g. Polacci et al., 2006, 2008, 2009; Shea et al., 2010), theoretical modeling (e.g. Toramaru 1989, 1995; Yamada et al., 2005; Toramaru, 2006, 2014) and experimental simulations (e.g. Mourtada-Bonnefoi and Laporte, 1999; Mangan and Sisson, 2000; Mourtada-Bonnefoi and Laporte, 2002, 2004; Mangan and Sisson, 2005; Iacono-Marziano et al., 2007; Gardner and Ketcham, 2011). Such experimental simulations are available for silicic melts, but are still lacking for basaltic melts. This type of work, which consists in determining when and how volatiles separate from magma, is nevertheless essential for the understanding of basaltic explosive volcanism (e.g. Bottinga and Javoy, 1990; Herd and Pinkerton, 1997; Edmonds, 2008; Polacci et al., 2008; Gardner, 2012).

Although the experiments of Pichavant et al. (2013) were not specifically designed to study bubble nucleation, two characteristic distances controlling the degassing process of basaltic melts were identified: (1) the gas interface distance (distance either between bubbles or to gas-melt interfaces) and (2) the volatile diffusion distance. In this way, on the basis of differing H_2O and CO_2 melt diffusivities, CO_2/H_2O concentration ratios may record nonequilibrium degassing (e.g. Gonnermann and Manga, 2005). Other studies have proposed that the rate of nucleation controls the final melt volatile concentrations through two fundamental parameters (Sparks 1978; Toramaru 1995; Cluzel et al., 2008): the pressure at which bubbles begin to nucleate and the number density of bubbles.

In line with these critical observations, continuous decompressions of H_2O- and H_2O-CO_2-bearing basaltic melts have been performed to systematically simulate bubble nucleation and improve the modeling of volatile evolution during magma ascent and degassing.

2. Theoretical background

During magma ascent and decompression, volatile supersaturation builds up in the melt. Bubble nucleation is initiated upon lowering pressure below the volatile saturation pressure P_{sat}. For $P < P_{sat}$, a critical level of volatile supersaturation is attained, and bubbles tend to nucleate to maintain chemical equilibrium. Gas bubbles can nucleate heterogeneously at interfaces or discontinuities within the melt (for example at the surface of mineral phases, e.g. Hurwitz and Navon, 1994; Gardner et al., 1999; Gardner and Denis, 2004; Mangan et al., 2004; Gardner, 2007; Cluzel et al., 2008). For homogeneous nucleation to take place, a minimum pressure drop below P_{sat} is necessary (e.g. Mangan and Sisson, 2000; Mourtada-Bonnefoi and Laporte, 2002). During homogeneous nucleation, bubbles are not associated with discontinuities, such as created by interfaces between phases, surfaces of specific crystalline phases or capsule walls as in our experiments. Theoretically, high degrees of volatile supersaturation are required to initiate homogeneous nucleation. This nucleation barrier is controlled by the melt-vapor surface tension. According to the classical nucleation theory, the surface tension (σ, in $N.m^{-1}$) and the nucleation rate (J, in $m^{-3}.s^{-1}$) determine the minimum supersaturation pressure (defined as the difference between the volatile saturation pressure and the pressure where bubbles start to nucleate homogeneously, ΔP_{HoN}) necessary for bubble nucleation according to the following expression (Hurwitz and Navon, 1994; Mourtada-Bonnefoi and Laporte, 2002):

$$\Delta P_{HoN} = \sqrt{\frac{16\pi\sigma^3}{3kT\ln\left(\frac{J}{J_0}\right)}} \quad \text{(Eq. 1)}$$

where k is the Boltzmann constant ($1.38.10^{-23}$ $J.K^{-1}$), T is the temperature (in K) and J_0 is the preexponential nucleation rate (in $m^{-3}.s^{-1}$, see Appendix for details).

Equation Eq. 1 indicates that homogeneous bubble nucleation in silicate melts can be viewed as a competition between volatile supersaturation (which tends to promote volatile exsolution) and the surface tension (which tends to resist the formation of a separate phase in the melt). The determination of the surface tension of silicate melts is difficult because it is highly sensitive to melt composition, temperature and dissolved volatile content (Bagdassarov et al., 2000; Mangan et al., 2004). This explains why σ was very rarely measured for basaltic melts. The only data available come from Khitarov et al. (1979), who determined σ from 0.1 to 0.4 $N.m^{-1}$ for basaltic melts (the lowest end of the range for hydrous compositions at 1200°C). More recently, Pichavant et al. (2013) obtained σ ranging between 0.177 and 0.188 $N.m^{-1}$. These values were calculated from the determination of ΔP_{HoN} and J, in decompression experiments on basaltic melts containing dissolved H_2O and CO_2. This is the approach followed in the present study to further constrain σ for basaltic melts, especially its dependence with the nature and concentration of dissolved volatiles.

Although the classical nucleation theory provide an adequate theoretical background for the experiments presented in this study, there are several specificities in our approach that are worth being outlined. First, natural basaltic magmas generally contain dissolved CO_2 and S species, in addition to H_2O. These different volatile components have very contrasted individual solubilities in basaltic melts. It follows that conditions of melt saturation are not simply dependent on pressure (and of melt composition to some extent) but become a strong function of the respective dissolved volatile concentrations. The volatile saturation surface is no longer a line in pressure-H_2O concentration (e.g. Mourtada-Bonnefoi and Laporte, 1999, 2002) but a complex multicomponent space. Another issue is that volatile saturation pressures for basaltic magmas may be very high given the possibly of percolation of CO_2-rich gases coming from depth (i.e. $P_{sat} >> P_{storage}$). Second, degassing mechanisms take place at high temperature (> 1100°C) in basaltic melts, in a range where the diffusive mobility of volatiles (particularly H_2O, Zhang and Ni, 2010) is effective and impact the bubble nucleation process (e.g. Mangan and Sisson, 2000; Pichavant et al., 2013).

3. Experimental methods

3.1. Preparation of starting glasses

Decompression experiments were conducted on volatile-bearing glasses made from a Strombolian high-K basalt. The PST-9 "golden" pumice (so designated because of its yellowish color) was used as starting material (Di Carlo et al., 2006; Pichavant et al., 2009, 2011). It was selected because it was previously used in phase equilibrium and crystallization experiments (Di Carlo et al., 2006; Pichavant et al., 2009, 2013), and because it is a sample well-characterized petrographically, mineralogically and geochemically (Pichavant et al., 2011). It is the most primitive "golden" pumice (Métrich et al., 2001; Bertagnini et al., 2003; Francalanci et al, 2004; Métrich et al., 2005; Di Carlo et al., 2006; Pichavant et al., 2009) and, as such, is representative of Stromboli pumices that are emitted during paroxysms and major explosions (Pichavant et al., 2011). Its bulk composition is given in Table 1. PST-9 is slightly porphyritic, containing about 10% of crystals of clinopyroxene, olivine and plagioclase, and lapilli are highly vesicular (~60 vol.% vesicles). To obtain a crystal- and bubble-free glass, the sample was hand crushed to a fine powder and then fused at 1 atm and 1400°C in a Pt crucible for 3 hours. This process gave a homogeneous glass whose composition is listed in Table 1. The glass was then either cored to cylinders (2.5 mm in diameter and about 10 mm long) or crushed to a fine powder (~10–50 µm).

For the synthesis experiments (Table 2), charges were made from glass cylinders (140.5–206.4 mg) or glass powder (about 30 mg). Using cylinders has the advantage of keeping a constant geometry in all samples, which facilitates the textural analysis. It also has the advantage to prevent the formation of bubbles in samples during the synthesis experiments. Nevertheless, glass powder was also used for practical reasons in a few experiments. Distilled water and carbon dioxide as silver oxalate ($Ag_2C_2O_4$) were added to generate volatile-bearing melts. $Au_{80}Pd_{20}$ capsules (2–3 cm height, 2.5 mm inner diameter, 0.2 mm wall thickness) were used as containers. Such a metal composition was adopted to minimize iron loss from the experimental charge to the capsule (Di Carlo et al., 2006; Pichavant et al., 2009). Three different proportions of H_2O and CO_2 were introduced in the capsules, corresponding to XH_2O_{in} (molar H_2O / (H_2O + CO_2)) = 1 (series #1: only H_2O dissolved in glass, no CO_2 present), ~0.58 (series #2: H_2O and CO_2 both dissolved in glass, high dissolved H_2O/CO_2) and 0 (series #3: H_2O and CO_2 both dissolved in glass, low dissolved H_2O/CO_2, see below for the origin of H_2O).

For the decompression experiments (Table 3), the synthesized volatile-bearing glass cores (2.5 mm in diameter and about 4 mm long) were fitted in $Au_{80}Pd_{20}$ capsules. No additional volatile was introduced, and this resulted in low proportions of free fluid in the decompression charges. Capsules of identical diameter (2.5 mm) but variable lengths (up to 5 cm for the capsules decompressed to the lowest pressures) yielded variable and large void spaces to accommodate gas expansion during decompression.

All capsules were welded shut and weighed, and then reweighed after being placed several hours in an oven to ensure that no leaks occurred.

3.2. Equipment

Experiments were performed in an internally heated pressure vessel (IHPV) working vertically and fitted with a drop-quench device. To control the redox conditions, the vessel was pressurized with gas mixtures made of Ar and H_2. All synthesis and decompression experiments were performed with an initially applied pressure of 1 bar H_2. Then, Ar was pumped into the vessel up to the pressure needed to attain the final target conditions (Pichavant et al., 2013).

Determinations of experimental fH_2 have not been performed specifically for this study, for example with redox sensors (Taylor et al., 1992; Di Carlo et al., 2006). Below, we use fH_2 measurements made from Ni-NiPd sensors in similar experiments performed in the same IHPV and under the same *P*-*T*-fH_2 conditions (Le Gall and Pichavant, 2015a). They indicate fO_2 conditions ranging from NNO–1.3 (series #3) to NNO+1.7 (series #1), NNO being the fO_2 of the Ni-NiO equilibrium at the *P*-*T* of interest.

The capsules were placed in a sample holder made of Al_2O_3. It was suspended by a thin Pt wire in a Mo furnace having a 2–3 cm long hotspot. Temperature was monitored with a Eurotherm controller and measured by two S-type thermocouples located along the capsules. Near-isothermal conditions (gradient < 2–3°C/cm) were maintained in the sample holder. Pressure and temperature were read continuously, with uncertainties of ± 20 bars and ± 5°C. At the end of the experiments, an electrical current was applied to the Pt suspension wire resulting in the sample holder falling to the cold part of the IHPV (< 100°C), leading to a quench rate of about 100°C/sec (Di Carlo et al., 2006).

3.3. Run procedure

Generally, synthesis and decompression experiments were performed independently from each other.

The synthesis experiments (Table 2) were performed at 200 MPa and 1200°C, which are conditions known to be above the PST-9 liquidus on the basis of previous phase equilibrium experiments (Di Carlo et al., 2006; Pichavant et al., 2009). Up to three capsules (one for each series#) were placed together in the vessel for durations of about 46–48 hours, in order to attain an equilibrium distribution of dissolved H_2O and CO_2 in the 2.5 mm diameter cores, according to the H_2O and CO_2 melt diffusion data (Zhang and Ni, 2010). The synthesized crystal- and bubble-free volatile-bearing glasses were used as starting materials in the degassing experiments (Table 3).

The decompression runs also included up to three capsules (Table 3). Experiments were conducted at a constant temperature of 1200°C, from an initial pressure (P_{in}) of 200 MPa to final pressures (P_f) varying between 150 and 25 MPa. All runs began with an approximately one-hour step at 200 MPa and 1200°C, to re-equilibrate the pre-synthesized glasses. Pressure was then decreased manually to P_f at a fast decompression rate of 78 kPa/s (or 3 m/s taking a rock density of 2.65 kg/m^3), which leads to decompression durations of 10–40 min depending on P_f. Decompression charges were isobarically quenched immediately (within ~1–2 s) after attainment of P_f, to freeze the glass textures and chemistries.

Less frequently, synthesis and decompression steps were conducted the one after the other in the same run. This is the case of three synthesis + decompression experiments which were performed using glass powder as starting material (Table 4). Consequently, in those three cases, glasses were not analyzed after being synthesized. Each synthesis + decompression experiments included only one capsule from the series #1. The synthesis-step lasted for about 40–60 min at 1200°C and 200 MPa. Then, the continuous decompression-step consisted in a manual reduction of pressure until P_f was attained (150, 100 and 25 MPa) at a fast rate of 78 kPa/s.

After quenching, capsules were weighed again to check that no volatile loss occurred during the experiments, and then opened.

4. Analytical methods

4.1. Sample preparation

After each synthesis experiment, a part of the glass core obtained was analyzed to check for its volatile concentration and distribution. To do so, sections were cut perpendicular to the long axis of the glass cylinders and double-polished. Volatile concentrations were determined by IR microspectroscopy (FTIR).

After the decompression and also the few synthesis + decompression experiments, the glass cylinders were carefully removed from their containers and their textures studied by X-ray microtomography, the analysis being performed on the entire glass core. Then, glass cylinders were subdivided into several sections cut perpendicular to the cylinder long axis. One section (or several sections when numerous analyses were needed) was doubly-polished for the determination of the glass volatile contents by FTIR. Another section (or small glass fragments) was mounted in epoxy resin and polished for scanning electron microscope (SEM) imaging.

4.2. Textural analyses

Textures of all decompressed charges were analyzed by X-ray computed tomography (X-ray CT). The Nanotom 180 instrument by GE Sensing, phoenix|x-ray, of ISTO was used. It was operated between 90 and 101 kV for variable filament currents (40–170 µA), using a tungsten target. Between 750 and 1100 two-dimensional projections were acquired from the rotation (through 360°) of samples during x-ray exposure; the glass cylinders were mounted on carbon fiber rods with thermoplastic adhesive. Although voxel edge lengths of 2.42–3.91 µm were produced, this spatial resolution was insufficient for detecting the smaller bubbles (≤ 3–4 µm). The reconstruction of the tomographic projections, using a phoenix program (datos|x reconstruction), creates an image stack of the sample. When processed with the ImageJ software package (Abràmoff et al., 2004), a complete three-dimensional reconstruction of the sample is produced. This volume rendering has the dimension of the whole image stack in three dimensions (e.g. for D28#2 charge volume is equal to $840\times871\times948\times2.42^3$ µm^3, Fig. 1a). This total volume investigated, V in Fig. 1a, is composed of the following sub-volumes: the volume of void space (v2), the volume of melt (v3) and the

volume of bubbles (v4). The void space volume corresponds to the volume left when excluding the volume of the sample (v3 + v4) to the total volume investigated (e.g. v2 = V – (v3 + v4)). Both v2 and v4 can be measured using ImageJ. This allows the determination of v3 (by subtracting the sum of the volumes of void space (v2) and bubbles (v4) to the total volume investigated (V), v3 = V – (v2 +v4), Fig. 1a), and thus of the textural parameters (bubble size, bubble number density and vesicularity).

To do so, the whole image stack (V, Fig. 1a) was segmented using manual thresholding; the objects of interest (bubbles and void space, in gray (for illustration) and black on Fig. 1a) were separated from the glass (in white on Fig. 1a). Following segmentation, the volume of these objects was measured using the 3D Object Counter plugin (Bolte and Cordelières, 2006); the void space and the volume of each bubble were separated, labeled and counted. The fact that thresholded objects are labeled allows rejecting particles which are artifacts, like cracks or noise. This was minutely done after each image analysis.

Bubble sizes (expressed as diameters) were determined from the measured bubble volumes, assuming that they have a spherical shape. *Bubble number density* (*BND*) was calculated in two different ways, either as the number of bubbles per unit volume of bulk sample (glass + bubbles, *BND*, Tables 3 and 4) or per unit volume of melt (BND_{melt}, Tables 3 and 4). Following Proussevitch et al. (2007), we have chosen to use the *BND* values defined per melt volume (BND_{melt}) because they remain invariant as bubbles grow and thus may be used as indicators of nucleation processes. However, both *BND* values were computed and are given in Tables 3 and 4 for comparison. *Vesicularity* was determined as the sum of the bubble volumes divided by the volumes of melt and bubbles. As mentioned above, the volume of melt v3 depends on the void space volume v2. But, this latter includes the broken bubbles located at the rim of the samples, which thereby are not included in our measurements of vesicularity (V^c, Tables 3 and 4, Fig. 1a). Thus, this method underestimates the vesicularity for samples having a large bubbly rim. This is the case especially for series #1 glasses decompressed to P_f = 50 and 25 MPa (D10#1 and S+D38#1, Tables 3 and 4) and for series #2 and #3 glasses decompressed to P_f = 25 MPa (D28#2 and D25#3, Table 3). Thus, these samples underlined the need for a modification of the vesicularity determination method. In the modified method, representative sub-volumes (V_{sub}, Fig. 1b) together with the Voxel Counter plugin were used instead of total volumes (V, Fig. 1a) and the 3D Object Counter plugin. The broken bubbles located at the rim of the sample are now counted as bubbles (and not as voids, v2) which leads to higher bubble volumes (v4). The vesicularity is the average of

calculations performed on 4 representative sub-volumes for each sample (V^d, Tables 3 and 4). Both V^c and V^d are given (Tables 3 and 4), yet only V^d values are used below in the text and figures.

For comparison with the vesicularities measured in our run products, equilibrium vesicularities were computed for the PST-9 melt composition. Two end-member cases were considered corresponding to the degassing of pure H_2O and pure CO_2, respectively. The equilibrium vesicularity is given by (e.g. Cluzel, 2007):

$$V = \frac{X_0 - X_s}{X_0 - X_s + \frac{\rho_{fluid}}{\rho_{liq}}(1 - X_0)} \quad \text{(Eq. 2)}$$

where X_0 is the weight fraction of initial water, X_s the solubility of the volatile species at a given pressure, ρ_{fluid} the density of the supercritical fluid and ρ_{melt} the density of the saturated silicate liquid.

For the calculations, we used the solubility models of Lesne et al. (2011a, b) to obtain the H_2O and CO_2 solubilities for PST-9 at 1200°C and the P of interest (25–200 MPa). The density of the liquid is assumed to be constant and equal to 2.64 g.cm^{-3} (with H_2O) and about 2.75 g.cm^{-3} (with CO_2). The density of the pure H_2O supercritical fluid was determined at the pressure of interest, using the Holloway-Flowers version of the Redlich-Kwong equation of state (from Holloway, 1981; Ferry and Baumgartner, 1987). For the pure CO_2 supercritical fluid, it was obtained from a regression of the fCO_2 data of Dixon et al. (1995) at 1200 °C.

4.3. Scanning electron microscopy

Scanning electron microscope (SEM) imaging was used for the observation of the smaller bubbles which cannot be detected by X-ray microtomography because of their size (≤ 3–4 µm in diameter). To do so, the MIRA3 TESCAN FEG instrument at Orléans was used. An accelerating voltage of 15, 20 or 25 kV was applied.

4.4. Glass volatile contents

H_2O and CO_2 (as CO_3^{2-}) concentrations in the experimental glasses were determined by the Fourier transform infrared spectroscopy (FTIR) technique. A Nicolet 6700 spectrometer and a Continuμm IR microscope equipped with an IR light, a KBr beamsplitter and a liquid nitrogen cooled MCT/A detector were used together. Profiles (step 50–350 μm) were performed to check for the homogeneity of H_2O and CO_2 concentrations. The diameter of the analyzed spot was 50 μm, 100 μm in a few cases. FTIR spectra were accumulated for 128 scans at a resolution of 4 cm^{-1} on doubly polished samples, with thicknesses ranging between 29 and 171 μm (Table 5). H_2O and CO_2 concentrations were calculated from the Beer-Lambert law. For H_2O, the absorbance of the 3530 cm^{-1} total H_2O band (H_2O_{mol} + OH^-) was measured with a straight base line between ~3850 and ~2500 cm^{-1}. An extinction coefficient (ε^{3530}) of 64 $L.mol^{-1}.cm^{-1}$ was used (Dixon et al., 1995). For CO_2, the absorbance of the 1515 cm^{-1} carbonate ions band was determined on subtracted spectra. The spectrum used for the subtraction was obtained on a starting glass without dissolved volatiles. We calculated an extinction coefficient (ε^{1515}) of 363 $L.mol^{-1}.cm^{-1}$ from the equation of Dixon and Pan (1995). Sample thicknesses were measured with an optical microscope to within 1–2 μm. Densities of experimental glasses were estimated from the density of the volatile-free starting glass measured using a Mettler balance equipped with a density accessory kit (ρ = 2.747 ± 0.001) and considering a partial molar volume of H_2O of 12 $cm^3.mol^{-1}$ (Richet et al., 2000). In this way, we consider only the influence of dissolved H_2O on the glass density and assume that the effect of CO_2 is negligible (Lange, 1994; Bourgue and Richet, 2001; Lesne et al., 2011a).

Equilibrium gas-melt computations (volatile solubilities as a function of *P-T*, isobaric solubility curves and closed-system degassing paths) were calculated with the silicate melt-H_2O-CO_2 model (VolatileCalc) of Newman and Lowenstern (2002), for a basalt with 49 wt.% SiO_2. H_2O and CO_2 concentrations in glasses from the synthesis experiments were also compared with the recent experimental solubilities of Lesne et al. (2011a, b) and Shishkina et al. (2010), determined for a pressure of 200 MPa and a temperature of 1200–1250°C.

5. Experimental results

5.1. Volatile contents of pre-decompression glasses

All glass cylinders obtained in the synthesis experiments (hereafter designated as pre-decompression glasses) were bubble- and crystal-free. Their H_2O and CO_2 concentrations are

given in Tables 2 and 5. Considering the standard deviations and given the analytical error for CO_2 measurements (~100 ppm), glasses have homogeneous volatile contents. Although the data are averaged in the tables, the FTIR profiles show that H_2O and CO_2 are homogeneously distributed in the glass cylinders. Near-rim volatile concentrations are identical within error to the other values. Glasses divide into three groups of compositions consistent with their synthesis conditions: series #1 (4.91 ± 0.01 wt.% H_2O, 0 ppm CO_2), series #2 (2.41 ± 0.04 wt.% H_2O, 973 ± 63 ppm CO_2) and series #3 (0.98 ± 0.16 wt.% H_2O, 872 ± 45 ppm CO_2). H_2O and CO_2 concentrations of pre-decompression glasses are within the range of experimental solubilities found both for PST-9 (Lesne et al., 2011a, b) and other basaltic melts (Shishkina et al., 2010) under similar *P-T* conditions. Although water was not introduced in the series #3 capsules, H_2O was found to be present as a component dissolved in all pre-decompression glasses of this series. H_2O (concentration range: 0.80–1.09 wt.%, Tables 2 and 5) is generated during synthesis through the reduction of the ferric iron of the starting glass by H_2 from the pressurizing medium. The reduction reaction can be written (e.g. Lesne et al., 2011a):

$$Fe_2O_{3(melt)} + H_{2(vap/melt)} = 2FeO_{(melt)} + H_2O_{(melt)} \quad \text{(Eq. 3)}$$

However, part of the water in the series #3 glasses most probably comes from the silver oxalate used as the CO_2 source because reaction (Eq. 3) is not sufficient to account for the measured glass H_2O contents.

Glasses from the few synthesis + decompression experiments (#1, Table 4) were not analyzed and are assumed to have the same water content as glass S9#1 (4.91 wt.%, Table 2) since the conditions of synthesis are identical (XH_2O_{in}, *P*, *T*). Water diffusivity data for basaltic melts (Zhang and Ni, 2010) suggest that, under the *P-T* conditions investigated here, a few minutes is sufficient to homogenize the H_2O concentration in our basaltic glasses, when starting from powder (Lesne et al., 2011b).

5.2. Qualitative textural characteristics of post-decompression glasses

The glass cylinders from the decompression experiments and from the few synthesis + decompression experiments (hereafter designated as post-decompression glasses) were generally recovered as single cylindrical blocks, except a series #1 charge (S+D38#1, Table 4) which yielded a partially powdered run product, suggesting partial fragmentation. A

detailed microscopic observation revealed the presence of numerous bubbles in the fragmented part of S+D38#1. All run products were crystal-free with the exception of the D25#3 charge (Table 3) which contains some plagioclases. These crystals (5–10 µm long) are found exclusively near bubbles and are absent from bubble-free glass areas. When present, no preferential association was noted between the bubbles and the crystals. In the other charges, the absence of crystals was checked by optical microscopy on the doubly polished sections prepared for FTIR and also by SEM. Almost all the charges contain some rare oxide crystals (Ti-bearing magnetite, Di Carlo et al., 2006). In some of them, evidence for bubble nucleation on those micron-sized Fe–Ti oxides (Le Gall and Pichavant, 2015b) was observed, but only for a negligible proportion of nucleated bubbles. The post-decompression glasses contained various amounts of bubbles (Tables 3 and 4), allowing us to distinguish two types of glasses depending on the internal texture of the samples (Fig. 2). The *first* type corresponds to bubble-free glasses (Fig. 2a). Only charge D31#2 (Table 3) is completely devoid of bubbles, but at the contact with the capsule (< 10 µm), a thin bubbly rim is present. In contrast, the *second* (and largely dominant) type of glasses is characterized by a densely nucleated core and a bubbly rim ranging from ~10 to 110 µm µm (Fig. 2b). A distinction was made between bubbles having nucleated inside the glass and those located at the glass-capsule interface. These latter are thought to result from heterogeneous nucleation along the glass-capsule interface (Mangan and Sisson, 2000) and are not considered further in this study. Given the uniform spatial distribution of bubbles and the absence of crystals (hence of possible nucleation sites), we interpret the textures of type 2 glasses to result from homogeneous bubble nucleation. Charge D31#3 is characterized by a somewhat heterogeneous distribution of relatively large bubbles (8–42 µm, Table 3). However, SEM imaging revealed the presence of a population of smaller (< 5 µm) homogeneously distributed bubbles.

The interior of post-decompression glasses is devoid of bubbles until P_f = 150 MPa for series #1 and #3, and until P_f = 100 MPa for series #2. In this study, no experimental check was performed at P_f = 200 MPa but similar work at a lower decompression rate confirmed that bubbles are absent in experiments decompressed to $P_f = P_{in} = P_{synthesis}$ (Le Gall and Pichavant, 2015a).

5.3. Quantitative study of internal textures

Textural data are given in Tables 3 and 4 and depicted in Figures 3–6.

Vesicularities range from 1.01 to 25.6 vol.% (series #1), 0 to 22.7 vol.% (series #2) and from 0 to 4.97 vol.% (series #3). They generally increase with decreasing P_f from 150 to 25 MPa (Tables 3 and 4, Fig. 3a). The increase of vesicularity with decreasing P_f is more important between P_f = 50 and 25 MPa. In addition to the dependence on P_f, vesicularities are also specific of the volatile series (Fig. 3a). The highest vesicularities are for the H_2O-rich glasses of the series #1. For example, when lowering the glass H_2O content at a constant P_f (P_f = 25 MPa, Fig. 3a), vesicularities decrease from 25.6% (series #1) to 22.7% (series #2), to 4.97% (series #3). Vesicularities for series #2 and #3 glasses are in qualitative agreement with the calculated equilibrium vesicularity curves (since they plot in-between the two end-members theoretical curves, Fig. 3a). This is not really the case for the series #1 glasses whose measured vesicularities are low compared to the theoretical values (Tables 3 and 4, Fig. 3a).

The average bubble diameter (D) ranges from 28 to 218 µm (series #1), 10 to 31 µm (series #2) and 10 to 12 µm (series #3) (Tables 3 and 4). In the fragmented part of the series #1 S+D38#1 charge, bubbles have sizes ranging from about 10 to 110 µm, much lower than in the non-fragmented part (76–414 µm; Fig. 3b). As for vesicularity, D generally increases with decreasing P_f although we note that the trend is not really strongly marked for series #3 glasses (Fig. 3b). D is also a function of the concentration of dissolved volatiles. The larger bubble sizes are for the H_2O-rich glasses of series #1 (on average 218 µm at P_f = 25 MPa), decreasing with lowering the glass H_2O concentration (31 µm for series #2 and 12 µm for series #3).

Bubble size distributions (BSDs) are analyzed from histograms constructed for each series# (Fig. 4a–c). They display two main distributions, unimodal and power law (Fig. 4). Each of the three series shows a specific evolution of BSD with decreasing pressure (Fig. 4). The CO_2-free glasses (series #1, Fig. 4a) show a unimodal BSD with a slight dissymmetry at left diminishing from 150 to 100 MPa, the main peak diameter increasing from 25 to 43 µm (Table 4). Then, at P_f = 50 MPa and 25 MPa, BSDs shift toward larger sizes and multiple peaks occur (Table 4 and Fig. 4b). This corresponds to a decrease of the number of small bubbles and to an increase of the number of large bubbles. For example, at P_f = 150 MPa bubble sizes range from 8 to 86 µm while at P_f = 25 MPa bubble sizes range between 76 and 414 µm (Table 4 and Fig. 4b). For series #2 samples, the BSD initially (at P_f = 100 MPa, i.e. at the pressure where bubbles start to nucleate) has a power law shape (Fig. 4b). Upon decreasing P_f to 25 MPa, the BSD evolves to an unimodal shape with a strong dissymmetry at

left implying that the number of small bubbles (< 10 µm) decreases (Fig. 4c). Lastly, series #3 glasses have power law distributions both at P_f = 150 and 25 MPa (Fig. 4c), with small bubbles (< 10 µm) predominating until the lowest P_f.

Bubble number densities (*BND*s) range from about 10^0 to 10^4 mm^{-3} for the three glass series (Tables 3 and 4, Fig. 3c). Generally, *BND*s of series #1 glasses decrease with decreasing P_f, from about 10^2 (150 MPa) to 10^1 mm^{-3} (25 MPa). Conversely, *BND*s of series #2 and #3 glasses generally increase when lowering P_f (from about 10^0 to 10^4 mm^{-3}), except between P_f = 100 and 50 MPa where *BND*s decrease.

5.4. Volatile contents of post-decompression glasses

H_2O and CO_2 concentrations in glasses from decompression experiments are reported in Table 5 and shown in Fig. 5. The H_2O concentrations of series #1 post-decompression glasses range from 4.16 wt.% (P_f = 150 MPa) to 1.71 wt.% (P_f = 25 MPa). Thus, a general decrease of the concentration of dissolved H_2O is observed when decreasing the final pressure (Fig. 5). Considering that analytical uncertainties (corresponding to the error bars in Fig. 5) are < 0.1% (Table 5), the H_2O contents of series #1 post-decompression glasses are in agreement with H_2O solubilities calculated from VolatileCalc (Newman and Lowenstern, 2002); the correspondence between the data points and the calculated 150–25 MPa isobars is very close (Fig. 5). However, the correspondence is slightly less good if comparison is made with measured solubilities (Lesne et al., 2011b) rather than with VolatileCalc: post-decompression glasses have H_2O concentrations slightly exceeding solubilities. Most series #1 charges have near-equilibrium H_2O concentrations. The exception is charge S+D38#1 (P_f = 25 MPa) which shows a supersaturation of 0.15–0.25 absolute wt.% H_2O. In addition, analytical dispersions of H_2O contents along FTIR profiles are higher than typical analytical errors, suggesting some degrees of heterogeneity in the H_2O distribution in post-decompression glasses (Fig. 6a). The spatial distribution of H_2O in all series #1 charges seems influenced by the proximity of the glass-capsule interface, as illustrated for example by D10#1 and S+D38#1 samples (Fig. 6a). The glass H_2O concentration is also affected by the proximity to gas bubbles, which shows that the H_2O concentration is close to the solubility value near the bubbles or the glass-capsule interface and slightly higher away from them (Fig. 6a, b), consistent with a mechanism of diffusive motion of H_2O inside the melt toward the gas phase.

Series #2 post-decompression glasses have H_2O concentrations ranging from 1.96 to 0.95 wt.% and CO_2 concentrations ranging between 786 and 206 ppm (Table 5). Taken globally, concentrations of dissolved H_2O and CO_2 in post-decompression glasses progressively decrease with decreasing P_f (Fig. 5). However, the drop in H_2O concentration is not linear with P_f contrary to CO_2. For example, the glass decompressed to P_f = 150 MPa has a lower H_2O content (1.28 wt.%, D31#2) than two glasses decompressed to 100 (1.55 wt.%, D34#2) and 50 MPa P_f (1.96 wt.%, D9#2). The glass decompressed to 25 MPa (0.95 wt.%, D28#2) has the lowest H_2O concentration. Post-decompression glass CO_2 concentrations progressively decrease from 786 (D31#2, P_f = 150 MPa), 613–678 (D34#2 and D23#2, P_f = 100 MPa), 556 (D9#2, P_f = 50 MPa) to 206 ppm (D28#2, P_f = 25 MPa). The trend of decreasing H_2O and CO_2 concentrations upon decreasing pressure differs from the closed-system equilibrium decompression trend in that the observed H_2O loss is more important than theoretically expected. At P_f = 150 MPa, the measured CO_2 concentration is in agreement with the gas-melt saturation isobar calculated with VolatileCalc (Newman and Lowenstern, 2002) despite that the H_2O content is much lower than the concentration expected along the theoretical degassing trend. In comparison, the data points at P_f = 100 and 50 MPa plot well above their respective gas-melt saturation isobars. Measured CO_2 contents in these post-decompression glasses (556–678 ppm) largely exceed the calculated values (< 250 ppm at 100 MPa and < 50 ppm at 50 MPa) for closed-system equilibrium degassing, the departure from equilibrium being the most marked for the 50 MPa P_f point. The P_f = 25 MPa point also plots above its respective gas-melt saturation isobar.

Post-decompression glasses from series #3 have H_2O concentrations between 1.06 and 0.49 wt.% and CO_2 concentrations ranging from 777 to 423 ppm (Table 5). With decreasing pressure, melt CO_2 contents decrease progressively at approximately constant H_2O concentrations, except for charge D25#3 which lost most of its water (from 1.09 wt.% H_2O at 200 MPa to 0.49 wt.% H_2O at 25 MPa, Table 5 and Fig. 5). However, the decompressed glasses keep CO_2 concentrations that plot generally above their respective gas-melt saturation isobars. For example, the glass decompressed to P_f = 50 MPa has a higher CO_2 content (619 ppm, D9#3) than the calculated value (< 200 ppm) for closed-system equilibrium degassing. FTIR profiles show that H_2O and CO_2 are homogeneously distributed in the post-decompression glasses.

6. Interpretation and discussion of experimental observations

6.1. Supersaturation pressures required for homogeneous bubble nucleation

Two main arguments support the homogeneous nature of bubble nucleation in our samples (Mourtada-Bonnefoi and Laporte, 2002). (1) The lack of crystals in our experimental charges implies that there are no or little discontinuities to serve as nucleation sites in the melts. (2) The homogeneity of textures, in particular the lack of spatial variations in bubble number densities and average bubble sizes in the post-decompression glasses, are consistent with a general rather than a local bubble nucleation mechanism.

The supersaturation pressure required for homogenous bubble formation, i.e. the difference between the starting pressure ($P_{in} = P_{sat}$) and the final pressure at which bubbles begin to nucleate homogeneously, can be determined from our decompression experiments. We observed homogeneously distributed bubbles in the core of series #1 glasses from P_f = 150 MPa (sample S+D36#1, Table 4). However, the bubbles appear to have been formed at a much higher pressure. Indeed, most of the bubbles have a subspherical shape attesting of slight deformation after being formed. Furthermore, small bubbles (< 10 µm) are almost absent (2%, Fig. 4a) and bubble growth seems already efficient (main peak diameter of 25 µm, Table 4 and Fig. 4a). Accordingly, the supersaturation pressure required to nucleate bubbles homogeneously in our H_2O-bearing, CO_2-free melts (series #1 with 4.91 wt.% H_2O initially) must be much less than 50 MPa (ΔP_{HoN} << 50 MPa). This value is lower than supersaturation pressures found in several studies for more evolved compositions. For example, the degree of supersaturation required to trigger homogeneous bubble nucleation is ~60–90 MPa in dacite melts (H_2O ~5 wt.%, Mangan and Sisson, 2005; Gardner and Ketcham, 2011), ~100 MPa in phonolite (H_2O ~5 wt.%, Iacono-Marziano et al., 2007) and ~95–150 MPa in rhyolite melts (for ~5–7 wt.% H_2O, Mangan and Sisson, 2000; Mourtada-Bonnefoi and Laporte, 2004; Gardner and Ketcham, 2011). Therefore, ΔP_{HoN} values << 50 MPa as found in this study appear specific of basaltic compositions and suggest that bubble nucleation is an easy process taking place at low supersaturations in hydrous basaltic melts. This conclusion is consistent with previous results: Polacci et al. (2008) observed that in hydrous basaltic melts bubbles nucleate in response to small amounts of volatile supersaturation, which is suggestive of low ΔP_{HoN} in their experiments.

In series #2 charges, the experiment decompressed to 150 MPa P_f (sample D31#2, Table 3) yielded a bubble-free glass by X-ray CT (Fig. 2a), which was confirmed by SEM

examination. In contrast, the two charges decompressed to P_f = 100 MPa (D23#2 and D34#2, Table 3 and Fig. 2b) contain small bubbles (main peak diameters of 6–7 µm) uniformly distributed in the glass, suggesting that homogeneous bubble nucleation takes place between 150 and 100 MPa P_f. Therefore, a critical supersaturation pressure of 100 MPa maximum and 50 MPa minimum is inferred for our series #2 H_2O- and CO_2-bearing basaltic melts (with 2.41 wt.% H_2O and 973 ppm CO_2 on average). For comparison, Pichavant et al. (2013) found a supersaturation pressure of 150 MPa maximum in their experiments performed on compositions similar to our series #2 melts. However, no data were given for P_f > 50 MPa, and so it cannot be excluded that, in their decompression experiments, homogeneous bubble nucleation would start at pressures > 50 MPa, leading to ΔP_{HoN} << 150 MPa. A critical supersaturation pressure of 200 ± 100 MPa was found by Lensky et al. (2006) for CO_2 bubbles in a synthetic mafic melt decompressed from 1.5 GPa, which is in the same range or larger than determined here for series #2 melts. However, it is worth specifying that Lensky et al. (2006) worked on nominally H_2O-free melts. For more evolved melts, ΔP_{HoN} values determined for H_2O- and CO_2-bearing rhyolitic melts (4.6 wt.% H_2O and 800–1100 ppm CO_2, Mourtada-Bonnefoi and Laporte, 2002) range from 160 to 350 MPa, significantly above our ΔP_{HoN} values for series #2 melts. Therefore, it appears that the influence of CO_2 in increasing supersaturation pressures and ΔP_{HoN} values is lower for basaltic than for rhyolitic melts.

In series #3 glasses, bubbles begin to form from P_f = 150 MPa (sample D31#3, Table 3). These bubbles are so small (< 5 µm) that they were mostly undetected by X-ray CT (smallest bubble size detected in D31#3: 8 µm). Thus, a critical ΔP_{HoN} of 50 MPa maximum is also inferred for the series #3 melts. The series #3 results confirm the relatively low supersaturation pressures and ΔP_{HoN} values for basaltic melts, even when H_2O-poor (0.8–1.09 wt.%) and CO_2-bearing (840–923 ppm).

Our experimental results for basaltic melts suggest that the H_2O concentration has a small and, in detail, a complex effect on the critical supersaturation pressure needed to overcome the nucleation barrier (expressed as the ΔP_{HoN} value). The H_2O-richer (4.91 wt.%, series #1) and the H_2O-poorer (0.98 ± 0.16 wt.%, series #3) melts require apparently the same range of ΔP_{HoN} values (either < or ~50 MPa). Nevertheless, ΔP_{HoN} differences between our three series can be masked by our relatively large P_f steps (50 MPa). In this sense, the available textural evidence for the series #1 melts suggests that ΔP_{HoN} is in fact much lower than 50 MPa. In contrast, for series #3 melts, textural evidence for bubble nucleation at P_f > 150 MPa is lacking, suggesting that ΔP_{HoN} is in fact very close to 50 MPa. Comparison

between results for series #1 and #3 implies a negative but small influence of the melt H_2O concentration on ΔP_{HoN}. However, the increase of ΔP_{HoN} observed between series #3 ($\Delta P_{HoN} \leq 50$ MPa, 0.98 ± 0.16 wt.% H_2O) and series #2 glasses ($\Delta P_{HoN} < 100$ MPa, 2.41 ± 0.04 wt.% H_2O) is not in agreement with a linear decrease of ΔP_{HoN} with increasing the dissolved H_2O content. Our experiments do not reveal a systematic influence of the H_2O concentration on bubble nucleation in basaltic melts, as suggested for example in the case of rhyolitic melts (e.g. Gondé et al., 2011).

The presence of dissolved CO_2 has been considered to influence the degree of supersaturation required for homogeneous nucleation. Although the individual influence of CO_2 is difficult to separate from H_2O (since the two volatile concentrations usually vary together in the experiments) there are indications for supersaturation pressures and ΔP_{HoN} being positively correlated with the melt CO_2 concentration (Mourtada-Bonnefoi and Laporte, 2002; Bai et al., 2008). In our experiments, ΔP_{HoN} appears to increase linearly (although moderately) with increasing the melt CO_2 content, from << 50 MPa (no CO_2, series #1) to ≤ 50 MPa (872 ± 45 ppm CO_2, series #3) to < 100 MPa (973 ± 63 ppm CO_2, series #2). Although other factors (redox state) would need to be considered, our experimental results for the three series are consistent with a moderately important inhibiting role of CO_2 on bubble nucleation in basaltic melts.

Surface tensions have been calculated (Appendix) by taking the different supersaturation pressures for each series and our measured experimental nucleation rates. Because our P_f steps are large (50 MPa) and so supersaturation pressures given are maxima, calculated surface tensions (σ) are upper limits. Results give σ values of 0.058–0.059 $N.m^{-1}$ for series #1 and #3 melts, respectively, and of 0.091 $N.m^{-1}$ for series #2 melts. For comparison, Khitarov et al. (1979) obtained surface tensions of 0.1 to 0.4 $N.m^{-1}$ for basaltic melts at 1200°C and 100–500 MPa, the lowest end of the range corresponding to hydrous compositions. Pichavant et al. (2013) fitted σ data from their decompression experiments performed on compositions similar to this study. They found a maximum σ of 0.18 $N.m^{-1}$ higher than in this study but consistent with their higher ΔP_{HoN} values.

6.2. Physical mechanisms of degassing and textures

Below we discuss the physical mechanisms of degassing that occur in our experiments, from nucleation, growth and coalescence of gas bubbles to magma fragmentation. Emphasis is placed on textural differences between the three series of post-decompression glasses.

6.2.1. *Vesicularities*

The data for the three glass series show a general increase in vesicularity upon decompression magma ascent and decreasing P_f. More in detail, specificities appear between the different series (vesicularities of series #3 glasses are always very low below 5%, Fig. 3a). It is also worth noting that for series #1 and #2 glasses, the increase in vesicularity is more important between P_f = 50 and 25 MPa. Our measured vesicularities never reach the range for Stromboli pumices which have values between 47 and 67% (Polacci et al., 2006). However, it is recalled that the series #1 25 MPa P_f sample is partially fragmented, suggesting that the measured vesicularity is a minimum. The progressive increase in vesicularity with decreasing P_f is consistent with a mechanism of progressive melt vesiculation which is associated with decompression. This melt vesiculation mechanism is the result of different sub-processes that include bubble nucleation, growth and coalescence, up to fragmentation. These different sub-processes are examined below.

6.2.2. *Nucleation events*

Textural evidence (bubble size distributions and bubble number densities) can be used to distinguish between single vs. multiple bubble nucleation events (or pulses) in our experiments. In series #1 glasses, the presence of numerous (1908) bubbles in the charge decompressed to P_f = 150 MPa (S+D36#1, Table 4), as well as its unimodal BSD (Fig. 4a), imply that a single event of nucleation occurred at P_f > 150 MPa. Then, *BND* remains relatively constant from P_f = 150 to 100 MPa, and even decrease slightly (from 275 to 210 mm^{-3}, Table 4 and Fig. 3c). This plateau marks the end of the nucleation event, attesting the beginning of bubble growth, deformation and coalescence (e.g. Martel and Iacono-Marziano, 2015). In short, this event of nucleation appears to begin before P_f = 150 MPa and to end between P_f = 150 and 100 MPa, i.e. it is restricted to a narrow P_f range. The presence of newly nucleated bubbles (< 5–110 µm) in the fragmented part of S+D38#1 sample (P_f = 25

MPa) is remarkable because it implies that a second bubble nucleation event occurs between P_f = 50 and 25 MPa. Thus, two distinct nucleation events take place in our H_2O-rich melts (series #1), both restricted to narrow P_f intervals.

In series #2 samples, a strong increase of *BND* is observed from P_f = 150 (BND_{melt} = 0 mm^{-3}) to 100 MPa (BND_{melt} = 269–10331 mm^{-3}) (Table 3, Fig. 3c) which corresponds to the beginning of the homogeneous bubble nucleation process. Below 100 MPa, two cases are possible, either a continuous increase of the *BND* (D23#2) or a decrease of the *BND* (D34#2). The first case suggests the continuation of the same process of bubble nucleation below 100 MPa, an interpretation supported by the continuous increase in the number of bubbles, from 1692 (P_f = 100 MPa, D23#2), 11609 (P_f = 50 MPa, D9#2) to 16187 (P_f = 25 MPa, D28#2). In addition, bubble diameters give evidence for the appearance of small (< 10 µm) newly formed bubbles, and thus indicate the occurrence of secondary nucleation events. The second case is interpreted to reflect the sur-imposition of bubble coalescence on a mechanism of continuous bubble nucleation. The distance between bubbles in charge D34#2 is 28 µm, significantly lower (96 µm) than in the other charge (D23#2) for the same P_f, consistent with the possibility that coalescence can take place, thus decreasing the *BND*. In both cases, the evolution below 50 MPa and down to 25 MPa P_f is marked by an increase of *BND*s which is interpreted as the continuation of the nucleation process.

In series #3 samples, as in series #2, the *BND* first increases from 150 to 100 MPa P_f (BND_{melt} = 4 to 836 mm^{-3}, Fig. 3c, Table 3). Then, it decreases up to 50 MPa (BND_{melt} = 17 mm^{-3}) because of bubble coalescence (the number of bubbles is reduced from 5768 to 160, Table 3), before increasing again to 25 MPa (BND_{melt} = 8799 mm^{-3}). This increase is interpreted as the continuation of the same bubble nucleation process. This is supported by the observation that, as degassing continues, small (< 10 µm) bubbles begin to form along the decompression path from 150 to 25 MPa P_f. In addition, this indicates the occurrence of multiple nucleation events.

In series #2 and #3 post-decompression glasses, no *BND* stabilization (which would mark by a horizontal line in Fig. 3c) is observed. According to the classical nucleation theory, *BND* stabilization would reflect the end of a nucleation event (e.g. Toramaru, 2006). Consequently, the *BND* results for series #2 and #3 are consistent with a continuous, rather than limited to narrow P_f ranges, bubble nucleation, as observed in series #1 glasses and in other studies as well (e.g. Mourtada-Bonnefoi and Laporte, 2002, Cluzel et al., 2008).

Continued multiple nucleation events have been proposed to yield power law distributions because small bubbles continue to form as volatile supersaturation is maintained (Blower et al., 2001, 2002; Yamada et al., 2005; Bai et al., 2008). This is precisely what is observed in our series #2 and #3 glasses which are both characterized by power law distributions (see below).

We conclude to a major difference in the mechanism of bubble nucleation between series #1, on the one hand, and series #2 and #3, on the other hand. In series #1 glasses, a discontinuous mechanism of nucleation takes place, leading to two bubble nucleation events in narrow P_f intervals. In contrast, in series #2 and #3 glasses, a single mechanism of continuous nucleation occurs, leading to multiple bubble nucleation events. In series #2 and #3, the length of the nucleation period is continuous over a substantial P_f interval along the decompression path.

6.2.3. *Bubble coalescence*

Bubble coalescence takes place in H_2O-bearing, CO_2-free, glasses (series #1) although, in detail, differences appear along the decompression path. From P_f = 150 to 100 MPa, bubble coalescence is evidenced by a slight decrease of the bubble number density, from 275 (S+D36#1) to 210 mm^{-3} (S+D39#1, Table 4, Fig. 3c). Common coalescence structures of dimpling (Castro et al., 2012) are present in charge S+D36#1. In addition, the number of bubbles decreases from 150 (1908) to 100 (776, Table 4) MPa while, at the same time, the average and the main bubble sizes increase (Table 4, Fig. 3b). Lastly, the evolution of the bubble size distribution from unimodal to exponential (see below) indicates the presence of larger bubbles interpreted to result from coalescence (Fig. 9a). Therefore, in series #1 glasses bubble coalescence begins very early along the decompression path.

Bubble coalescence is the most extensively marked between 100 (S+D39#1) and 50 (D10#1) MPa P_f. This is evidenced by a sharp decrease of *BND* (from 210 to 8 mm^{-3}, Tables 3 and 4, Fig. 3c), a strong decrease in the number of bubbles (from 776 to 38, Tables 3 and 4) and a sharp increase in the average bubble size (from 47 to 161 µm, Tables 3 and 4, Fig. 3b). Processes of bubble deformation and coalescence are preserved in 50 MPa P_f, as well as in 25 MPa P_f charges, suggesting that the mechanism of bubble coalescence continues below 50 MPa until 25 MPa P_f. In the latter charge, typical coalescence textures (Fig. 7) are

characterized by deformed bubble walls, interpenetrating bubbles, dome-into-dimple shapes and vestiges of dimple structures, suggesting bending, stretching and dimpling mechanisms (Castro et al., 2012; Martel and Iacono-Marziano, 2015). It is worth mentioning that bubble coalescence is also observed in the fragmented parts of S+D38#1 sample.

In contrast with series #1, typical coalescence textures generally cannot be observed in series #2 and #3 glasses and, therefore, evidence for coalescence between 100 and 50 MPa P_f only comes from a decrease of *BND*s and bubble numbers and an increase in bubble sizes. However, in series #2, coalescence is not systematic. *BND* values can either decrease or increase between 100 and 50 MPa P_f (Table 3, Fig. 3c). We interpret this difference to reflect variations in distances between bubbles in the two series #2 100 MPa P_f charges. The average distance between bubbles in charge D23#2 (96 µm) is larger than in charge D34#2 (28 µm), consistent with the absence of bubble coalescence when starting from a 100 MPa charge such as D23#2. Between 50 and 25 MPa P_f, the mechanism of bubble coalescence continues despite an increase of the *BND*. However, coalescence textures were observed in a series #2 glass at P_f = 25 MPa (D28#2, Table 3). The mechanism of bubble coalescence is partially hidden by the continuing bubble nucleation (Fig. 3c).

We conclude that bubble coalescence occurs and that it is the more strongly marked in the same pressure range (100–50 MPa) for the three glass series.

6.2.4. *Fragmentation*

Fragmentation was observed in one series #1 charge decompressed to P_f = 25 MPa. It was never observed at P_f = 50 MPa. The 25 MPa charge is only partially fragmented. Therefore, the available evidence suggests a fragmentation threshold near 25 MPa. Although the vesicularity of the charge is only 25.6% (Table 4), it is worth reminding that it has been measured in the non-fragmented part of the charge. The vesicularity of the bulk charge is necessarily much higher. Note that the equilibrium vesicularity calculated at 25 MPa is 72.5% (Table 3, Fig. 3a), in the range expected to induce fragmentation (Sparks et al., 1994). A detailed discussion of the fragmentation mechanisms is outside the scope of this paper. However, our data provide clear evidence that fragmentation is intimately related to the second bubble nucleation event that occurs between 50 and 25 MPa in series #1 melts. Indeed, this second nucleation event was observed only in the fragmented part of S+D38#1.

The existence of a second nucleation event enhancing magma fragmentation has been previously proposed by e.g. Massol and Koyaguchi (2005).

6.3. Role of CO_2 on physical mechanisms of degassing and textures

Our experimental observations underline a significant effect of CO_2 on physical mechanisms of basaltic melts, as previously proposed by e.g. Bai et al. (2008). First of all, the concentration of CO_2 appears to increase (although moderately) the degree of supersaturation required for homogeneous nucleation ΔP_{HoN}. In addition, vesicularities of CO_2-bearing melts are lower than those of H_2O-rich melts, but we note that our CO_2-bearing compositions have reduced melt H_2O concentrations compared to our H_2O-rich melts. The mechanism of bubble nucleation in CO_2-bearing melts is continuous (it extends along a large P_f interval), leading to successive generations of new bubbles. In contrast, bubbles nucleate in two narrow P_f intervals in H_2O-rich melts. Bubble coalescence is generally much less marked in CO_2-bearing than in H_2O-rich melts. In the P_f ranges where both coalescence and nucleation occur together, the effect of bubble nucleation dominates for CO_2-bearing melts and the opposite for H_2O-rich melts.

The effect of CO_2 on bubble growth is also significant (Fig. 4d–f; Mourtada-Bonnefoi and Laporte, 2004; Bai et al., 2008). Bubble growth in basaltic melts is mainly controlled by volatile diffusion (Bai et al., 2008). H_2O and CO_2 having different diffusivities (Zhang and Ni, 2010), H_2O-dominant bubbles (series #1) and CO_2-dominant bubbles (series #2 and #3) do not grow at the same rate. Thus, because of the high diffusivity of H_2O relative to CO_2, bubbles in series #1 glasses (Fig. 4d) grow larger than in series #2 and then #3 glasses (Fig. 4e, f). Large bubbles allow the reduction of the distance between them which facilitates their interaction and coalescence, as observed for series #1 melts and less so for series #2 and #3 melts. Bubble sizes are the lowest in the series #3 experiments which are performed with the least H_2O-rich melts.

6.4. Equilibrium vs. non-equilibrium degassing

Chemical equilibrium, as classically assumed for basaltic melts (Sparks et al., 1994), is reached or approached in our H_2O-bearing, CO_2-free, melts (series #1). Melts decompressed

to 150, 100 and 50 MPa P_f exhibit near-equilibrium H_2O concentrations (Fig. 5). However, deviation from equilibrium is encountered in the charge decompressed to 25 MPa P_f (S+D38#1) which shows glass H_2O contents in excess (supersaturation of 0.15–0.25 wt.% absolute H_2O, Fig. 6) to the equilibrium solubility (Lesne et al., 2011b). Although this charge is particular (partially fragmented), we interpret our measured H_2O concentrations to indicate the possibility of non-equilibrium degassing in series #1 melts at very low pressures, providing the driving force for the occurrence of the second bubble nucleation event. Despite chemical equilibrium being approached, textural equilibrium is not reached in the series #1 melts which have vesicularities lower than expected from equilibrium degassing (Fig. 3a). This indicates that, in order to achieve chemical equilibrium, H_2O can be lost diffusively from the melts during decompression. Although clear evidence for H_2O diffusion in our glass samples is lacking, several observations (Fig. 6) are consistent with a mechanism of diffusive motion of H_2O inside the melt toward the gas phase (gas bubbles and capsule-melt interface).

Non-equilibrium degassing occurs systematically in the CO_2-bearing melts (series #2 and #3). CO_2 is retained within these melts at elevated concentration levels. In parallel, H_2O is lost in significant amounts. The combination of high melt CO_2 concentrations and H_2O losses generates a degassing trend that is in marked contrast with theoretical equilibrium closed-system degassing trends (Fig. 5). The unusual degassing trends observed in our experiments for the series #2 and #3 melts were previously found in the decompression experiments of Pichavant et al. (2013). The authors stressed the importance of two characteristic distances (the distance between bubbles and the volatile diffusion distance) in the control of the degassing process. This model attributes an important role to differences in diffusivities between the volatile components in the melt. As an illustration, at P_f = 50 MPa (D9#2), the calculated distance for CO_2 diffusion is only 150 µm in the time interval of the decompression experiment (Zhang and Ni, 2010) while the H_2O diffusion is 1060 µm, i.e. 7 times faster. In that charge the average distance between bubbles is 62 µm which would appear to be small enough for equilibrium degassing to be reached. However, this is not what is observed since CO_2 is kept at concentrations much higher than expected along the 50 MPa isobar (Fig. 5). As an explanation, it is worth mentioning that the distance between bubbles is an average and also that there are large uncertainties on the timescales used for the diffusion distance calculations. Despite the general non-equilibrium behavior in all series #2 and #3 charges, the series #2 charge decompressed to P_f = 25 MPa (D28#2) approaches equilibrium CO_2 concentration. This charge is characterized by relatively large (31 µm) gas bubbles and a high

vesicularity (23%). The glass CO_2 concentration vs. vesicularity plot (Fig. 8) shows a negative trend (Pichavant et al., 2013). In comparison, e.g. Cluzel et al. (2008) emphasized the importance of the *BND* parameter, the extent of degassing being positively correlated with the *BND*. However, our data show high and variable *BND*s correlated with large supersaturations in CO_2. Equilibrium degassing requires both numerous and large bubbles, i.e. the expression of a high vesicularity. This demonstrates that the mode of degassing and the textural parameters are related.

7. Volcanological applications

7.1. Comparison between experimental and natural textural parameters

Despite the fact that our experimental products do not simulate the last stages of degassing near the surface and post-fragmentation processes, the comparison of bubble textures between experimental and eruptive products can provide insights on degassing processes occurring in the volcanic conduit. The comparison focuses on products from three well-documented basaltic Plinian eruptions (Tarawera in 1886, Masaya and Etna in 122 BC, Sable et al., 2006, 2009; Costantini et al., 2010) and on products of Strombolian paroxysms (Polacci et al., 2009). At P_f = 25 MPa (i.e. at the pressure corresponding to the shallower depth in our experiments), the H_2O-rich charge (S+D38#1, Fig. 4d) exhibit a population of relatively large (76–414 µm) interacting bubbles which could be assimilated to a premise of the interconnected bubble-chains and complex shapes observed in products of the basaltic Plinian eruptions (Sable et al., 2006, 2009; Costantini et al., 2010). From our results, these bubble-chains would be generated by interaction between coalesced bubbles, in agreement with previous interpretations (Sable et al., 2006, 2009; Costantini et al., 2010). In addition, at P_f = 25 MPa, the CO_2-bearing charges (D28#2 and D25#3, Fig. 4e, f) exhibit a population of small (< 10 µm) to large (up to 0.4 mm) bubbles. The products of basaltic Plinian eruptions and Strombolian paroxysms also show a wide range of bubble sizes. The former have bubble sizes which range from 2–10 µm to 3–5 mm (Tarawera and Etna samples; Sable et al., 2006, 2009) up to 1.2 cm (Masaya samples; Costantini et al., 2010). The latter have a narrower range of bubble sizes ranging from 21–23 µm to 1 mm (Polacci et al., 2009). In both cases, the natural products exhibit larger bubbles than our experimental products. In the Plinian eruptions, the bubbles have either spherical to subspherical shapes or complex shapes (as discussed above). In contrast, the pumices from the paroxysmal Stromboli explosions display

only the spherical to subspherical bubbles. From our results, the larger bubbles could have grown from high pressure, as a result of the combination of growth and coalescence processes. In contrast, the presence of small bubbles is always indicative of a mechanism of continuous nucleation occurring up to magma fragmentation, in agreement with the interpretation of Costantini et al. (2010). However, the absence of bubbles < 20 µm in the Strombolian pumices suggests that the mechanism of nucleation was ended before magma fragmentation. The lack of large (> 1 mm) bubbles with complex shapes implies that coalescence was not the dominant process, as observed in our CO_2-bearing charges.

Our experimental products have low vesicularities which extend up to 25.6% (series #1), 22.7% (series #2) and 4.97% (series #3). These values are much lower than the vesicularities measured in basaltic explosive products. For comparison, vesicularities of Strombolian pumices range from 47 to 67% (Polacci et al., 2006; Fig. 3a) and those of the Plinian products from the Masaya eruption are even higher, ranging between 70 and 78% (Costantini et al., 2010). It is reasonable to expect that the field of Stromboli pumices can be attained by extrapolating the data for the series #2 compositions to P_f << 25 MPa. For the H_2O-rich compositions, the 25 MPa P_f charge is partially fragmented and the measured vesicularity is a minimum.

The *BND*s found in Strombolian pumices (6–9.10^2 mm^{-3}, Polacci et al., 2009; Fig. 3c) are in the same range as the *BND*s measured in our CO_2-bearing run products (up to 10^4 mm^{-3} in series #2 and #3). In detail, at P_f = 25 MPa, the natural pumices have *BND*s lower by one order of magnitude than the series #2 and #3 charges. The H_2O-rich charges (series #1, Fig. 3c) are much less bubble-rich. The basaltic Plinian products from the Masaya eruption have *BND*s (3–8.10^4 mm^{-3}, Costantini et al., 2010) higher than all our experimental products.

We conclude that our decompression experiments either reproduce or approach the natural textures of explosive basaltic eruptions, in terms of vesicularity, *BND*s, bubble textures and sizes.

7.2. Use of BSD systematics

Below, we extend the comparison between our experimental products and the basaltic explosive products selected above to include BSDs. Vesicle size distribution is one of the most common textural parameter measured to understand processes of bubble nucleation and

growth in natural products (e.g. Blower et al., 2001; Shea et al., 2010). Volcanic rocks are typically characterized by power law and exponential distributions of vesicle sizes (e.g. Gaonac'h et al., 1996; Bai et al., 2008; Polacci et al., 2009), but these are rarely reproduced in degassing experiments using natural or synthetic silicate melts (Blower et al., 2001). Generally, in experiments, a single event of nucleation is recorded and interactions between bubbles are limited (e.g. Lyakhovsky et al., 1996; Mourtada-Bonnefoi and Laporte, 1999; Gardner et al., 1999; Mourtada-Bonnefoi and Laporte, 2002; Cluzel et al., 2008), producing a unimodal BSD (Blower et al., 2002). However, in a few experiments, products with BSDs more complex than unimodal have been encountered, such as in the study of Simakin et al. (1999), the analogue experiments of Blower et al. (2001, 2002) and in the degassing experiments of Bai et al. (2008), Polacci et al. (2008) and Masotta et al. (2014). Below, methods developed for the interpretation of natural BSDs are applied to our experimental results.

To do so, we have represented our experimental BSDs in cumulative number density plots, as commonly used (Fig. 9). These were obtained by regressing the number of bubbles per mm^3 against the bubble volume. In doing so, two main BSD types were encountered in our experimental samples: exponential and power law. Regressions were performed with the Excel software. Very good fits were generally obtained yielding $R^2 > 0.99$ for more than 50% charges. One charge (S+D36#1) yielded a relatively poor exponential fit ($R^2 = 0.86$), consistent with its unimodal BSD (Figs. 4a, 9a).

The three post-decompression glass series show a different evolution of the BSD (Figs. 4 and 9). Upon decreasing P_f, the BSD of series #1 glasses evolves from a unimodal (S+D36#1, P_f = 150 MPa, Figs. 4a and 9a), mixed power law–exponential (S+D39#1, P_f = 100 MPa) to an exponential distribution (D10#1 and S+D38#1, P_f = 50–25 MPa, Fig. 9a). The mixed distribution recognized in charge S+D39#1 corresponds to two classes of bubble sizes. The small to medium bubbles (volumes ~10^2–10^5 µm^3) can be fitted by an exponential function whereas the larger bubbles (volumes ~10^5–10^6 µm^3) are best described by a power law with an exponent of 1.45. Texturally, it is clear that these large bubbles result from coalescence.

In series #2 samples, both power law and exponential bubble size distributions were observed when decreasing P_f from 100 to 25 MPa (Fig. 9b). At P_f = 100 MPa (i.e. at the pressure where bubbles start to nucleate), the BSDs of the two D23#2 and D34#2 duplicate

charges are best described by power laws (Fig. 9b). In contrast, at P_f = 50 and 25 MPa, the BSDs in charges D9#2 and D28#2 can be described by mixed power law–exponential distributions: the small-to-medium sized bubbles can be fitted with an exponential relation (Fig. 9b) whereas the medium-to-large bubbles follow a power law relation. Series #2 power law exponents range from 0.78 to 2.24. The low and high values of the range are for the two duplicate charges decompressed to 100 MPa P_f. If the power law exponents of these two charges are averaged (α = 1.51), all series #2 power law exponents appear to be tightly grouped (1.38–1.62).

In series #3 post-decompression glasses (Fig. 9c), only power law distributions were observed when decreasing P_f from 150 to 25 MPa, with the exception of the medium-sized bubbles (volumes ~10^3–10^5µm^3) in the D9#3 charge (P_f = 50 MPa) which are best fitted with an exponential distribution (bubble coalescence effect). The series #3 glasses display power law exponents of 0.62 to 1.23, slightly lower than in series #2 glasses.

We conclude to a systematic change in the BSD evolution with decreasing P_f between the three glass series. The H_2O-rich, CO_2-free, post-decompression glasses (series #1) are the only ones with a unimodal distribution and also the only ones with exponential distributions for all classes of bubble sizes. In contrast, the CO_2-bearing post-decompression glasses (series #2 and #3) are characterized by power law distributions. Among the CO_2-bearing glasses, only the series #2 show a transition from a power law to a mixed power law–exponential distribution. Series #3 glasses are characterized by predominantly power law BSDs.

Two distinct mechanisms have been invoked to explain the occurrence of power law bubble size distributions in volcanic rocks. A mechanism of diffusive bubble growth, allowing "cascading" coalescence, was involved by Gaonac'h et al. (1996) whereas, according to Blower et al. (2001, 2002), such distributions would be more indicative of far-from-equilibrium degassing, leading to a mechanism of continuous bubble nucleation and multiple nucleation events (in the absence of bubble coalescence). Exponential distributions would result from steady-state bubble nucleation and growth and thus would imply near-equilibrium degassing (Baker et al., 2006; Bai et al., 2008).

In our experiments, a unimodal distribution was found in the H_2O-rich series (S+D36#1) at a high P_f, i.e. at the pressure the closest to the beginning of the nucleation mechanism. The latter takes place in a narrow P_f interval, leading to a single bubble nucleation event. The melt H_2O concentration in that charge is equal to the solubility.

Therefore, charge S+D36#1 provides evidence that a unimodal bubble distribution implies gas-melt equilibrium, despite the fact that its vesicularity is significantly less than the theoretical value. Exponential distributions are also specific of the H_2O-rich series whose post-decompression glasses have generally (except the partially fragmented charge S+D38#1) equilibrium melt H_2O concentrations. Again, our experimental data support the interpretation that exponential BSDs are generated by a system evolving under near-equilibrium conditions (Blower et al., 2001; Baker et al., 2006; Bai et al., 2008) despite vesicularities being lower than theoretical values. The evolution from a unimodal to an exponential distribution would thus result from post-nucleation mechanisms (growth and coalescence), leading to larger bubble sizes and lower bubble number densities. Power law distributions are specific of the CO_2-bearing charges which are characterized by a single mechanism of continuous nucleation, leading to multiple bubble nucleation events. Small bubbles continue to form because the level of volatile supersaturation in the melts in maintained. This is consistent with the preservation of high out-of-equilibrium CO_2 concentrations in the glasses. Therefore, our data confirm the model of Blower et al. (2001, 2002) in that power law distributions are associated with far-from-equilibrium degassing. Mixed power law–exponential distributions would thus correspond to an intermediate case where bubble nucleation is dominated by a coalescence process.

On this basis, we examine below natural textures of the selected basaltic explosive eruptions above. The microtextural data available for those different explosive products exhibit a range of BSDs. The bubble size distributions of Plinian eruptions products (Sable et al., 2006, 2009; Costantini et al., 2010) follow power law trends with power law exponents of the order of 1.5 (when exponents are expressed as volume, Baker et al., 2012). In comparison, pumice samples from Strombolian paroxysmal explosions are best fit by mixed power law–exponential distributions with a power law exponent of 1.4 (Polacci et al., 2009). From our results, the power law distributions found for the Plinian products imply disequilibrium degassing, leading to continuous bubble nucleation and growth, in agreement with previous interpretation (Costantini et al., 2010). The mixed power law–exponential found in Strombolian pumices would be indicative of a system where coalescence is superimposed on a continuous bubble nucleation process. This would correspond to a disequilibrium degassing situation and to an evolution toward equilibrium (compare with Polacci et al., 2009).

8. Conclusions

We have performed high pressure and temperature decompression experiments to study the systematics of homogeneous bubble nucleation in basaltic magmas. Compared to previous works (Lensky et al., 2006; Pichavant et al., 2013) this study is the first to provide systematic textural information along the decompression path for three series of volatile concentrations. The main conclusions are the following:

(1) Degrees of supersaturation required for homogeneous bubble nucleation (ΔP_{HoN}) are ≤ 50–100 MPa, weakly dependent on the melt H_2O concentration but possibly dependent on the melt CO_2 concentration. These ΔP_{HoN} are significantly lower than found for silicic melt compositions which stresses that bubble nucleation in basaltic magmas is comparatively easy.

(2) In the H_2O-rich melts, homogeneous nucleation occurs as two distinct events taking place in narrow P_f intervals. The first and most important nucleation of bubbles occurs at high P_f ($200 < P_f < 150$ MPa) and the second nucleation of bubbles is restricted to low P_f ($50 < P_f < 25$ MPa), in close association with fragmentation. In contrast, in the CO_2-bearing melts, a single continuous mechanism of nucleation occurs over a substantial P_f interval along the decompression path, leading to multiple bubble nucleation events.

(3) Post-nucleation mechanisms include bubble growth, coalescence and possibly collapse, and lead to larger bubble sizes and lower *BND*s. Specific bubble coalescence textures and progressive *BND* decreases were observed with decreasing P_f. In both H_2O-rich and CO_2-bearing melts, coalescence is the more strongly marked in the same pressure range of 100–50 MPa.

(4) Both near-equilibrium and disequilibrium degassing occur in our experiments. The former is associated with the H_2O-rich, CO_2-free, melts while the latter occurs systematically in the CO_2-bearing melts. Post-decompression glasses retain CO_2 concentrations much higher than equilibrium values. There is a systematic link between textures and mode of degassing (equilibrium vs. disequilibrium). Near-equilibrium degassing requires both numerous and large bubbles and so high vesicularities.

(5) Partial fragmentation occurred in one H_2O-rich charge decompressed to 25 MPa, intimately related to the second event of bubble nucleation.

(6) Our experiments underline a significant effect of CO_2 on mechanisms (ΔP_{HoN} values, vesicularities, bubble sizes and densities) of basaltic melt degassing. The main difference between CO_2-bearing and CO_2-free melts concerns the mechanism of nucleation, continuous vs. discontinuous in the case of CO_2-bearing vs. CO_2-free melts.

(7) Our experimental decompression textures approach the characteristics of basaltic products from explosive eruptions. Vesicularities, *BND*s, bubble textures and sizes bring constraints on degassing processes occurring in the conduit.

(8) Our experimental products exhibit different BSDs, unimodal, exponential and power law with the volatile series. A relation is established between mechanisms of melt degassing, textures, volatile concentrations and type of BSDs. This provides a test on existing BSD based models to interpret natural degassing mechanisms.

Appendix

Surface tensions (σ) have been calculated from our supersaturation pressures (ΔP_{HoN}) and nucleation rates (J) computed from our measured bubble number densities and decompression timescales, using Eq. 1. To do this, the parameter J_0 which is given by (e.g. Mourtada-Bonnefoi and Laporte, 2004):

$$J_0 = \frac{(2\Omega_L n_0^2 D)}{a_0 \left(\frac{\sigma}{kT}\right)^{1/2}} \text{ (Eq. 4)},$$

where Ω_L is the volume of water molecules in the liquid ($\Omega_L = 3.10^{-29}$ m^3), n_0 is the number of water molecules per unit volume of liquid, a_0 is the mean distance between water molecules ($a_0 \approx n_0^{-1/3}$) and D is the water diffusivity in the liquid, has been estimated. D is taken from the equation of Zhang and Ni (2010) which takes into consideration the effects of H_2O content and temperature. n_0 is defined as $6.02.10^{23} X_m \rho_{liq}/m$, where $6.02.10^{23}$ is the Avogadro number, X_m is the mass fraction of molecular water in the liquid, ρ_{liq} is the liquid density (2650 kg/m^3), and m is the molar mass of water (0.018 kg/mol). Ω_L and X_m parameters are poorly constrained in basalt melts and we have used the values given by Mourtada-Bonnefoi and Laporte (2004), determined for rhyolitic liquids. Checks were performed to evaluate their influence on the calculated results and found to be small (< 0.001 N.m^{-1}). In the same way, the choice of the D equation leads to very small (< 0.001 N.m^{-1}) differences in σ.

References

Abràmoff, M.D., Magalhães, P.J., Ram, S.J., 2004. Image processing with ImageJ. Biophotonics International 11, 36–43.

Bagdassarov, N., Dorfman, A., Dingwell, D.B., 2000. Effect of alkalis, phosphorus, and water on the surface tension of haplogranite melt. American Mineralogist 85, 33–40.

Bai, L., Baker, D.R., Rivers, M., 2008. Experimental study of bubble growth in Stromboli basalt melts at 1 atm. Earth and Planetary Science Letters 267, 533–547. doi:10.1016/j.epsl.2007.11.063

Baker, D.R., Lang, P., Robert, G., Bergevin, J.-F., Allard, E., Bai, L., 2006. Bubble growth in slightly supersaturated albite melt at constant pressure. Geochimica et Cosmochimica acta 70, 1821–1838.

Baker, D.R., Brun, F., O'Shaughnessy, C., Mancini, L., Fife, J.L., Rivers, M., 2012. A four-dimensional X-ray tomographic microscopy study of bubble growth in basaltic foam. Nature Communications 3:1135.

Beckett, F.M., Burton, M., Mader, H.M., Phillips, J.C., Polacci, M., Rust, A.C., Witham, F., 2014. Conduit convection driving persistent degassing at basaltic volcanoes. Journal of Volcanology and Geothermal Research 283, 19–35.

Bertagnini, A., Métrich, N., Landi, P., Rosi, M., 2003. Stromboli volcano (Aeolian Archipelago, Italy): An open window on the deep-feeding system of a steady state basaltic volcano. Journal of Geophysical Research: Solid Earth 108, 2336. doi:10.1029/2002JB002146

Blower, J.D., Keating, J.P., Mader, H.M., Phillips, J.C., 2001. Inferring volcanic degassing processes from vesicle size distributions. Geophysical Research Letters 28, 347–350.

Blower, J.D., Keating, J.P., Mader, H.M., Phillips, J.C., 2002. The evolution of bubble size distributions in volcanic eruptions. Journal of Volcanology and Geothermal Research 120, 1–23.

Blundy, J., Cashman, K.V., Rust, A., Witham, F., 2010. A case for CO_2-rich arc magmas. Earth and Planetary Science Letters 290, 289–301.

Bolte, S., Cordelières, F.P., 2006. A guided tour into subcellular colocalization analysis in light microscopy. Journal of Microscopy 224, 213–232.

Bottinga, Y., Javoy, M., 1990a. Mid-ocean ridge basalt degassing: Bubble nucleation. Journal of Geophysical Research 95, 5125-5131.

Bottinga, Y., Javoy, M., 1990b. MORB degassing: Bubble growth and ascent. Chemical Geology 81, 255–270.

Bourgue, E., Richet, P., 2001. The effects of dissolved CO_2 on the density and viscosity of silicate melts: a preliminary study. Earth and Planetary Science Letters 193, 57–68.

Castro, J.M., Burgisser, A., Schipper, C.I., Mancini, S., 2012. Mechanisms of bubble coalescence in silicic magmas. Bulletin of Volcanology 74, 2339–2352.

Cluzel, N., 2007. Simulation expérimentale de l'ascension et de la vésiculation des magmas rhyolitiques : application à la cinétique de nucléation des bulles et implications volcanologiques. Ph.D. Thesis, Univ. Clermont-Ferrand 2, France.

Cluzel, N., Laporte, D., Provost, A., Kannewischer, I., 2008. Kinetics of heterogeneous bubble nucleation in rhyolitic melts: implications for the number density of bubbles in volcanic conduits and for pumice textures. Contributions to Mineralogy and Petrology 156, 745–763. doi:10.1007/s00410-008-0313-1

Costantini, L., Houghton, B.F., Bonadonna, C., 2010. Constraints on eruption dynamics of basaltic explosive activity derived from chemical and microtextural study: the example of the Fontana Lapilli Plinian eruption, Nicaragua. Journal of Volcanology and Geothermal Research 189, 207–224.

Di Carlo, I., Pichavant, M., Rotolo, S.G., Scaillet, B., 2006. Experimental Crystallization of a High-K Arc Basalt: the Golden Pumice, Stromboli Volcano (Italy). Journal of Petrology 47, 1317–1343. doi:10.1093/petrology/egl011

Dixon, J.E., Pan, V., 1995. Determination of the molar absorptivity of dissolved carbonate in basanitic glass. American Mineralogist 80, 1339–1342.

Dixon, J.E., Stolper, E.M., 1995. An experimental study of water and carbon dioxide solubilities in mid-ocean ridge basaltic liquids. Part II: applications to degassing. Journal of Petrology 36, 1633–1646.

Dixon, J.E., Stolper, E.M., Holloway, J.R., 1995. An experimental study of water and carbon dioxide solubilities in mid-ocean ridge basaltic liquids. Part I: calibration and solubility models. Journal of Petrology 36, 1607–1631.

Edmonds, M., 2008. New geochemical insights into volcanic degassing. Philosophical Transactions of the Royal Society A: Mathematical, Physical and Engineering Sciences 366, 4559–4579. doi:10.1098/rsta.2008.0185

Ferry, J.M., Baumgartner, L., 1987. Thermodynamic models of molecular fluids at the elevated pressures and temperatures of crustal metamorphism. Reviews in Mineralogy and Geochemistry 17, 323–365.

Francalanci, L., Tommasini, S., Conticelli, S., 2004. The volcanic activity of Stromboli in the 1906–1998 AD period: mineralogical, geochemical and isotope data relevant to the understanding of the plumbing system. Journal of Volcanology and Geothermal Research 131, 179–211. doi:10.1016/S0377-0273(03)00362-7

Gaonac'h, H., Stix, J., Lovejoy, S., 1996. Scaling effects on vesicle shape, size and heterogeneity of lavas from Mount Etna. Journal of Volcanology and Geothermal Research 74, 131–153.

Gardner, J.E., 2007. Heterogeneous bubble nucleation in highly viscous silicate melts during instantaneous decompression from high pressure. Chemical Geology 236, 1–12. doi:10.1016/j.chemgeo.2006.08.006

Gardner, J.E., 2012. Surface tension and bubble nucleation in phonolite magmas. Geochimica et Cosmochimica Acta 76, 93–102. doi:10.1016/j.gca.2011.10.017

Gardner, J.E., Denis, M.-H., 2004. Heterogeneous bubble nucleation on Fe-Ti oxide crystals in high-silica rhyolitic melts. Geochimica et Cosmochimica Acta 68, 3587–3597. doi:10.1016/j.gca.2004.02.021

Gardner, J.E., Ketcham, R.A., 2011. Bubble nucleation in rhyolite and dacite melts: temperature dependence of surface tension. Contributions to Mineralogy and Petrology 162, 929–943. doi:10.1007/s00410-011-0632-5

Gardner, J.E., Hilton, M., Carroll, M.R., 1999. Experimental constraints on degassing of magma: isothermal bubble growth during continuous decompression from high pressure. Earth and Planetary Science Letters 168, 201–218.

Gondé, C., Martel, C., Pichavant, M., Bureau, H., 2011. In situ bubble vesiculation in silicic magmas. American Mineralogist 96, 111–124. doi:10.2138/am.2011.3546

Gonnermann, H., Manga, M., 2005. Nonequilibrium magma degassing: Results from modeling of the ca. 1340 A.D. eruption of Mono Craters, California. Earth and Planetary Science Letters 238, 1–16. doi:10.1016/j.epsl.2005.07.021

Herd, R.A., Pinkerton, H., 1997. Bubble coalescence in basaltic lava: its impact on the evolution of bubble populations. Journal of Volcanology and Geothermal Research 75, 137–157.

Holloway, J.R., 1981. Volatile Interactions in Magmas, in: Newton, R.C., Navrotsky, A., Wood, B.J. (Eds.), Thermodynamics of Minerals and Melts, Advances in Physical Geochemistry. Springer New York, pp. 273–293.

Hurwitz, S., Navon, O., 1994. Bubble nucleation in rhyolitic melts: Experiments at high pressure, temperature, and water content. Earth and Planetary Science Letters 122, 267–280.

Iacono-Marziano, G., Schmidt, B.C., Dolfi, D., 2007. Equilibrium and disequilibrium degassing of a phonolitic melt (Vesuvius AD 79 "white pumice") simulated by decompression experiments. Journal of Volcanology and Geothermal Research 161, 151–164. doi:10.1016/j.jvolgeores.2006.12.001

Johnson, E.R., Wallace, P.J., Cashman, K.V., Granados, H.D., Kent, A.J., 2008. Magmatic volatile contents and degassing-induced crystallization at Volcán Jorullo, Mexico: implications for melt evolution and the plumbing systems of monogenetic volcanoes. Earth and Planetary Science Letters 269, 478–487.

Khitarov, N.I., Lebedev, E.B., Dorfman, A.M., Bagdasarov, N.S., 1979. Effect of temperature, pressure and volatiles on the surface tension of molten basalt. Geochemistry International 16, 78–86.

Le Gall, N., Pichavant, M., 2015a (to be submitted). Effect of ascent rate on homogeneous bubble nucleation in the system basalt-H_2O-CO_2: Implications for Stromboli volcano.

Le Gall, N., Pichavant, M., 2015b (to be submitted). Heterogeneous bubble nucleation on Fe–Ti oxides in H_2O- and H_2O-CO_2-bearing basaltic melts.

Lange, R.A., 1994. The effect of H_2O, CO_2, and F on the density and viscosity of silicate melts. Reviews in Mineralogy and Geochemistry 30, 331–369.

Lensky, N.G., Niebo, R.W., Holloway, J.R., Lyakhovsky, V., Navon, O., 2006. Bubble nucleation as a trigger for xenolith entrapment in mantle melts. Earth and Planetary Science Letters 245, 278–288.

Lesne, P., Scaillet, B., Pichavant, M., Beny, J.-M., 2011a. The carbon dioxide solubility in alkali basalts: an experimental study. Contributions to Mineralogy and Petrology 162, 153–168.

Lesne, P., Scaillet, B., Pichavant, M., Iacono-Marziano, G., Beny, J.-M., 2011b. The H_2O solubility of alkali basaltic melts: an experimental study. Contributions to Mineralogy and Petrology 162, 133–151.

Lyakhovsky, V., Hurwitz, S., Navon, O., 1996. Bubble growth in rhyolitic melts: experimental and numerical investigation. Bulletin of Volcanology 58, 19–32.

Mangan, M., Sisson, T., 2000. Delayed, disequilibrium degassing in rhyolite magma: decompression experiments and implications for explosive volcanism. Earth and Planetary Science Letters 183, 441–455.

Mangan, M., Sisson, T., 2005. Evolution of melt-vapor surface tension in silicic volcanic systems: Experiments with hydrous melts. Journal of Geophysical Research: Solid Earth (1978–2012) 110, B01202. doi:10.1029/2004JB003215

Mangan, M.T., Sisson, T.W., Hankins, W.B., 2004. Decompression experiments identify kinetic controls on explosive silicic eruptions. Geophysical Research Letters 31, L08605. doi:10.1029/2004GL019509

Marianelli, P., Sbrana, A., Metrich, N., Cecchetti, A., 2005. The deep feeding system of Vesuvius involved in recent violent strombolian eruptions. Geophysical Research Letters 32, L02306. doi:10.1029/2004GL021667

Martel, C., Iacono-Marziano, G., 2015. Timescales of bubble coalescence, outgassing, and foam collapse in decompressed rhyolitic melts. Earth and Planetary Science Letters 412, 173–185.

Masotta, M., Ni, H., Keppler, H., 2014. In situ observations of bubble growth in basaltic, andesitic and rhyodacitic melts. Contributions to Mineralogy and Petrology 167, 1–14.

Massol, H., Koyaguchi, T., 2005. The effect of magma flow on nucleation of gas bubbles in a volcanic conduit. Journal of Volcanology and Geothermal Research 143, 69–88.

Métrich, N., Wallace, P.J., 2008. Volatile abundances in basaltic magmas and their degassing paths tracked by melt inclusions. Reviews in Mineralogy and Geochemistry 69, 363–402.

Métrich, N., Bertagnini, A., Di Muro, A., 2010. Conditions of magma storage, degassing and ascent at Stromboli: new insights into the volcano plumbing system with inferences on the eruptive dynamics. Journal of Petrology 51, 603–626.

Métrich, N., Bertagnini, A., Landi, P., Rosi, M., 2001. Crystallization driven by decompression and water loss at Stromboli volcano (Aeolian Islands, Italy). Journal of Petrology 42, 1471–1490.

Métrich, N., Bertagnini, A., Landi, P., Rosi, M., Belhadj, O., 2005. Triggering mechanism at the origin of paroxysms at Stromboli (Aeolian Archipelago, Italy): the 5 April 2003 eruption. Geophysical Research Letters 32, L103056. doi:10.1029

Mourtada-Bonnefoi, C.C., Laporte, D., 1999. Experimental study of homogeneous bubble nucleation in rhyolitic magmas. Geophysical Research Letters 26, 3505–3508.

Mourtada-Bonnefoi, C.C., Laporte, D., 2002. Homogeneous bubble nucleation in rhyolitic magmas: an experimental study of the effect of H_2O and CO_2. Journal of Geophysical Research 107 (B4). doi:10.1029/2001JB00290

Mourtada-Bonnefoi, C.C., Laporte, D., 2004. Kinetics of bubble nucleation in a rhyolitic melt: an experimental study of the effect of ascent rate. Earth and Planetary Science Letters 218, 521–537.

Newman, S., Lowenstern, J.B., 2002. VolatileCalc: a silicate melt–H_2O–CO_2 solution model written in Visual Basic for Excel. Computers & Geosciences 28, 597–604.

Pichavant, M., Pompilio, M., D'Oriano, C., Di Carlo, I., 2011. Petrography, mineralogy and geochemistry of a primitive pumice from Stromboli: implications for the deep feeding system. European Journal of Mineralogy 23, 499–517.

Pichavant, M., Di Carlo, I., Le Gac, Y., Rotolo, S.G., Scaillet, B., 2009. Experimental constraints on the deep magma feeding system at Stromboli volcano, Italy. Journal of Petrology 50, 601–624.

Pichavant, M., Di Carlo, I., Rotolo, S.G., Scaillet, B., Burgisser, A., Le Gall, N., Martel, C., 2013. Generation of CO_2-rich melts during basalt magma ascent and degassing. Contributions to Mineralogy and Petrology 166, 545–561.

Pioli, L., Erlund, E., Johnson, E., Cashman, K., Wallace, P., Rosi, M., Granados, H.D., 2008. Explosive dynamics of violent Strombolian eruptions: the eruption of Parícutin Volcano 1943–1952 (Mexico). Earth and Planetary Science Letters 271, 359–368.

Polacci, M., Baker, D.R., Bai, L., Mancini, L., 2008. Large vesicles record pathways of degassing at basaltic volcanoes. Bulletin of Volcanology 70, 1023–1029.

Polacci, M., Baker, D.R., Mancini, L., Tromba, G., Zanini, F., 2006. Three-dimensional investigation of volcanic textures by X-ray microtomography and implications for conduit processes. Geophysical Research Letters 33, L13312. doi:10.1029/2006GL026241

Polacci, M., Baker, D.R., Mancini, L., Favretto, S., Hill, R.J., 2009. Vesiculation in magmas from Stromboli and implications for normal Strombolian activity and paroxysmal explosions in basaltic systems. Journal of Geophysical Research 114, B01206. doi:10.1029/2008JB005672

Proussevitch, A.A., Sahagian, D.L., Tsentalovich, E.P., 2007. Statistical analysis of bubble and crystal size distributions: Formulations and procedures. Journal of Volcanology and Geothermal Research 164, 95–111.

Richet, P., Whittington, A., Holtz, F., Behrens, H., Ohlhorst, S., Wilke, M., 2000. Water and the density of silicate glasses. Contributions to Mineralogy and Petrology 138, 337–347.

Sable, J.E., Houghton, B.F., Del Carlo, P., Coltelli, M., 2006. Changing conditions of magma ascent and fragmentation during the Etna 122 BC basaltic Plinian eruption: evidence from clast microtextures. Journal of Volcanology and Geothermal Research 158, 333–354.

Sable, J.E., Houghton, B.F., Wilson, C.J.N., Carey, R.J., 2009. Eruption mechanisms during the climax of the Tarawera 1886 basaltic Plinian eruption inferred from microtextural characteristics of the deposits. Studies in volcanology. The legacy of George Walker. Geological Society, London 129–154.

Shea, T., Houghton, B.F., Gurioli, L., Cashman, K.V., Hammer, J.E., Hobden, B.J., 2010. Textural studies of vesicles in volcanic rocks: an integrated methodology. Journal of Volcanology and Geothermal Research 190, 271–289.

Shishkina, T.A., Botcharnikov, R.E., Holtz, F., Almeev, R.R., Portnyagin, M.V., 2010. Solubility of H_2O-and CO_2-bearing fluids in tholeiitic basalts at pressures up to 500MPa. Chemical Geology 277, 115–125.

Simakin, A.G., Armienti, P., Epel'baum, M.B., 1999. Coupled degassing and crystallization: experimental study at continuous pressure drop, with application to volcanic bombs. Bulletin of Volcanology 61, 275–287.

Sparks, R.S.J., 1978. The dynamics of bubble formation and growth in magmas: a review and analysis. Journal of Volcanology and Geothermal Research 3, 1–37.

Sparks, R.S.J., Barclay, J., Jaupart, C.P.M.A., Mader, H.M., Phillips, J.C., 1994. Physical aspects of magma degassing I. Experimental and theoretical constraints on vesiculation. American Society of Mineralogy Reviews 30, 413–445.

Spilliaert, N., Allard, P., Métrich, N., Sobolev, A.V., 2006. Melt inclusion record of the conditions of ascent, degassing, and extrusion of volatile-rich alkali basalt during the powerful 2002 flank eruption of Mount Etna (Italy). Journal of Geophysical Research: Solid Earth (1978–2012) 111, B04203. doi:10.1029/2005JB003934

Taylor, J.R., Wall, V.J., Pownceby, M.I., 1992. The calibration and application of accurate redox sensors. American Mineralogist 77, 284–295.

Toramaru, A., 1989. Vesiculation process and bubble size distributions in ascending magmas with constant velocities. Journal of Geophysical Research: Solid Earth (1978–2012) 94, 17523–17542.

Toramaru, A., 1995. Numerical study of nucleation and growth of bubbles in viscous magmas. Journal of Geophysical Research: Solid Earth (1978–2012) 100, 1913–1931.
Toramaru, A., 2006. BND (bubble number density) decompression rate meter for explosive volcanic eruptions. Journal of Volcanology and Geothermal Research 154, 303–316.
Toramaru, A., 2014. On the second nucleation of bubbles in magmas under sudden decompression. Earth and Planetary Science Letters 404, 190–199.
Witham, F., 2011. Conduit convection, magma mixing, and melt inclusion trends at persistently degassing volcanoes. Earth and Planetary Science Letters 301, 345–352.
Yamada, K., Tanaka, H., Nakazawa, K., Emori, H., 2005. A new theory of bubble formation in magma. Journal of Geophysical Research: Solid Earth (1978–2012) 110, B02203. doi:10.1029/2004JB003113
Zhang, Y., Ni, H., 2010. Diffusion of H, C, and O components in silicate melts. Reviews in Mineralogy and Geochemistry 72, 171–225.

Figure captions

Figure 1. Three dimensional representations of the samples and methods of determination of vesicularities used in this study. V: total volume investigated; v2: void space volume; v3: melt volume; v4: bubble volume. (a) Vesicularity (V^c, Tables 3 and 4) determined from the total sample volume V (V^c = 100*v4/(v3+v4)), see text for the determination of v3 and v4. (b) Vesicularity (V^d, Tables 3 and 4) determined from a delimited sub-volume V_{sub} (V^d = 100*v4/(v3+v4)), see text for the determination of v4. The broken bubbles located at the rim of the sample appear in black in both (a) and (b). In (a), these are considered as voids (v2) while, in (b), these are counted as bubbles (v4). In (a), the trace of the sub-volume is delimited by the dashed square

Figure 2. Representative types of textures of post-decompression samples. (a) Tomographic slice of a sample quenched at a pressure above the critical pressure of homogeneous bubble nucleation (sample D31#2, P_f = 150 MPa): the sample is bubble-free. (b) Tomographic slice of a sample quenched at a pressure just below the pressure of homogeneous bubble nucleation (sample D34#2, P_f = 100 MPa): the sample is densely vesiculated with small and homogeneously distributed bubbles. The black arrow indicates the bubbly rim. See Table 3 for details about the experimental conditions and textural results.

Figure 3. (a) Vesicularity *V*, (b) average bubble diameter *D* and (c) bubble number density per unit volume of melt BND_{melt} plotted as a function of final pressure P_f for the post-decompression glasses of this study. Experimental data in Tables 3 and 4. For the partially fragmented sample S+D38#1, data from the unfragmented part are from Table 4. See text for bubble diameters in the fragmented part. The three glass series are distinguished (see text). Series #1: black circles; series #2: gray circles; series #3: white circles. In (a), equilibrium vesicularities (thick black and gray lines) calculated respectively for pure H_2O and CO_2 degassing (see text) are shown for comparison with the experimental data. The *V*, *D* and BND_{melt} values for Strombolian pumices and Masaya clasts (for this one only BND_{melt} values are shown) are plotted (data come from Polacci et al., 2006, 2009 and Costantini et al., 2010, respectively) for comparison with the experimental data points.

Figure 4. Evolution of the bubble size distribution (BSD) during decompression within each glass series. (a) Series #1, (b) series #2, (c) series #3 post-decompression glasses. For each glass series, two post-decompression glass samples are detailed, one representative of the early and the other of the late stage of the nucleation process. For each post-decompression glass sample, histograms show frequencies (normalized to 100) of diameters of individual bubbles in the population using size classes of 10 µm each. In (a) and (c), the unimodal and the power law BSD curves represent a fit to the data for charges S+D36#1 and D31#3, respectively, in order to illustrate examples of an unimodal and of a power law distributions. The average bubble diameter of the population can be found in Tables 3 and 4. Details about experimental conditions and

other textural data in Tables 3 and 4. For illustration, bubble textures of series #1, #2 and #3 glasses decompressed to 25 MPa are shown respectively in (d), (e) and (f).

Figure 5. H_2O and CO_2 concentrations in glasses from the synthesis and decompression experiments. Black symbols: series #1 glasses; gray symbols: series #2 glasses; white symbols: series #3 glasses. Circles: pre-decompression glasses synthesized at 200 MPa P_{in} (initial pressure); rectangles: glasses decompressed to 150 MPa P_f (final pressure); triangles: glasses decompressed to 100 MPa P_f; squares: glasses decompressed to 50 MPa P_f; diamonds: glasses decompressed to 25 MPa P_f. Error bars (standard deviations, Table 5) are indicated on the data points. Thin continuous lines: fluid-melt equilibrium saturation isobars (25–250 MPa); dashed curves: equilibrium decompression paths calculated for a series #2 and a series #3 pre-decompression melt assuming closed-system behavior. Isobars and decompression paths both calculated with VolatileCalc (Newman and Lowenstern, 2002).

Figure 6. H_2O distribution profiles from the sample edge toward the core of the cylinder for series #1 glasses decompressed to different P_f from 150 to 25 MPa. Average H_2O concentration data given in Table 5. (a) H_2O supersaturation vs. distance plot. H_2O supersaturation is defined relative to the H_2O solubility for each P_f (Lesne et al., 2011b) as: H_2O supersaturation = glass H_2O concentration – H_2O solubility for each P_f. The dashed horizontal line (H_2O supersaturation = 0) represents the solubility values for each P_f. Note that two profiles are available for 25 MPa P_f charge. The H_2O distribution profile for sample D10#1 (P_f = 50 MPa) is illustrated in (b).

Figure 7. Typical coalescence structures frozen in sample S+D38#1 decompressed to 25 MPa P_f. Inter-bubble melt films (IBFs) are thinned by stretching (a), bending (b), and dimpling (c, d) (see also Castro et al., 2012; Martel and Iacono-Marziano, 2015). See Table 4 for experimental conditions.

Figure 8. H_2O (a) and CO_2 (b) concentrations in post-decompression glasses (Table 5) plotted as a function of the vesicularity V^d (expressed as vol% bubbles, Tables 3 and 4). In (a), only data for series #1 and #2 glasses are shown and data for series #2 and #3 in (b). Black symbols: series #1 glasses; gray symbols: series #2 glasses; white symbols: series #3 glasses. Rectangles: glasses decompressed to 150 MPa P_f (final pressure); triangles: glasses decompressed to 100 MPa P_f; squares: glasses decompressed to 50 MPa P_f; diamonds: glasses decompressed to 25 MPa P_f. Dashed horizontal lines: pure H_2O (a) and CO_2 (b) solubilities for each P_f (Lesne et al., 2011a, b). Error bars (standard deviations, Table 5) are indicated within the data points.

Figure 9. Cumulative *BND* plots. Bubble size distributions (BSD) expressed as log-log plots of bubble number density (BND_{melt}, in mm^{-3}) vs. bubble volume for all post-decompression glasses from this study. For each glass sample, the bubble population is characterized by a range of bubble size (expressed as diameters in Tables 3 and 4) and a bubble number density value (Tables 3; 4). Each point along the distribution curve corresponds to the number of bubbles with a volume strictly larger than a given volume. (a) Series #1 glasses, (b) series #2 glasses, (c) series#3 glasses. Rectangles:

glasses decompressed to 150 MPa P_f (final pressure); triangles: glasses decompressed to 100 MPa P_f; squares: glasses decompressed to 50 MPa P_f; diamonds: glasses decompressed to 25 MPa P_f. The continuous lines are power law fits and the continuous curves are exponential fits, both regressed with Excel software. α is the power law exponent.

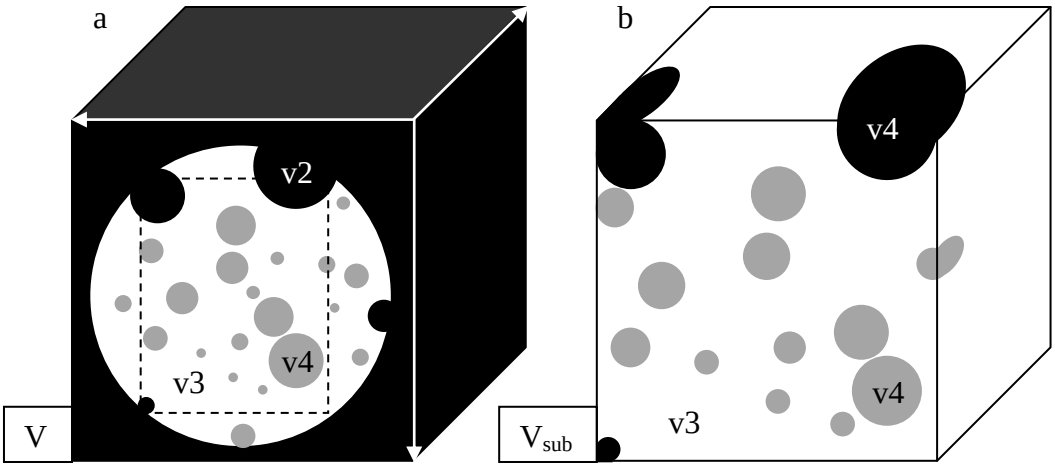

Le Gall and Pichavant. Fig. 1

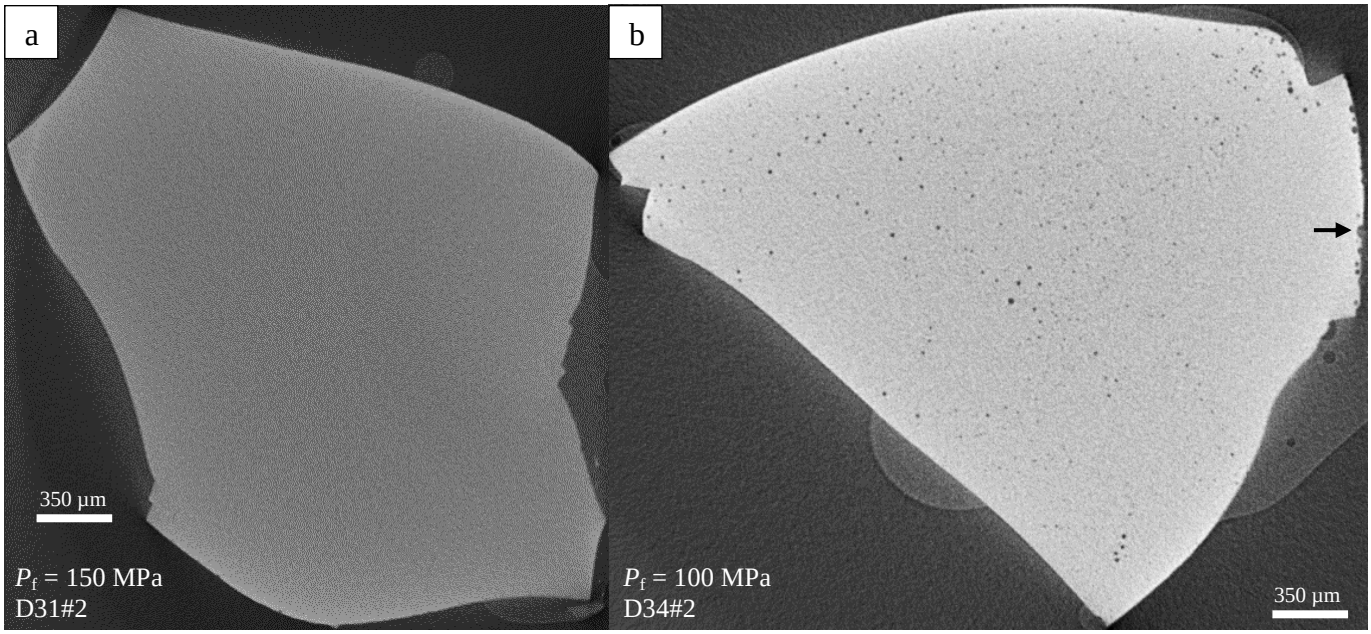

Le Gall and Pichavant. Fig. 2

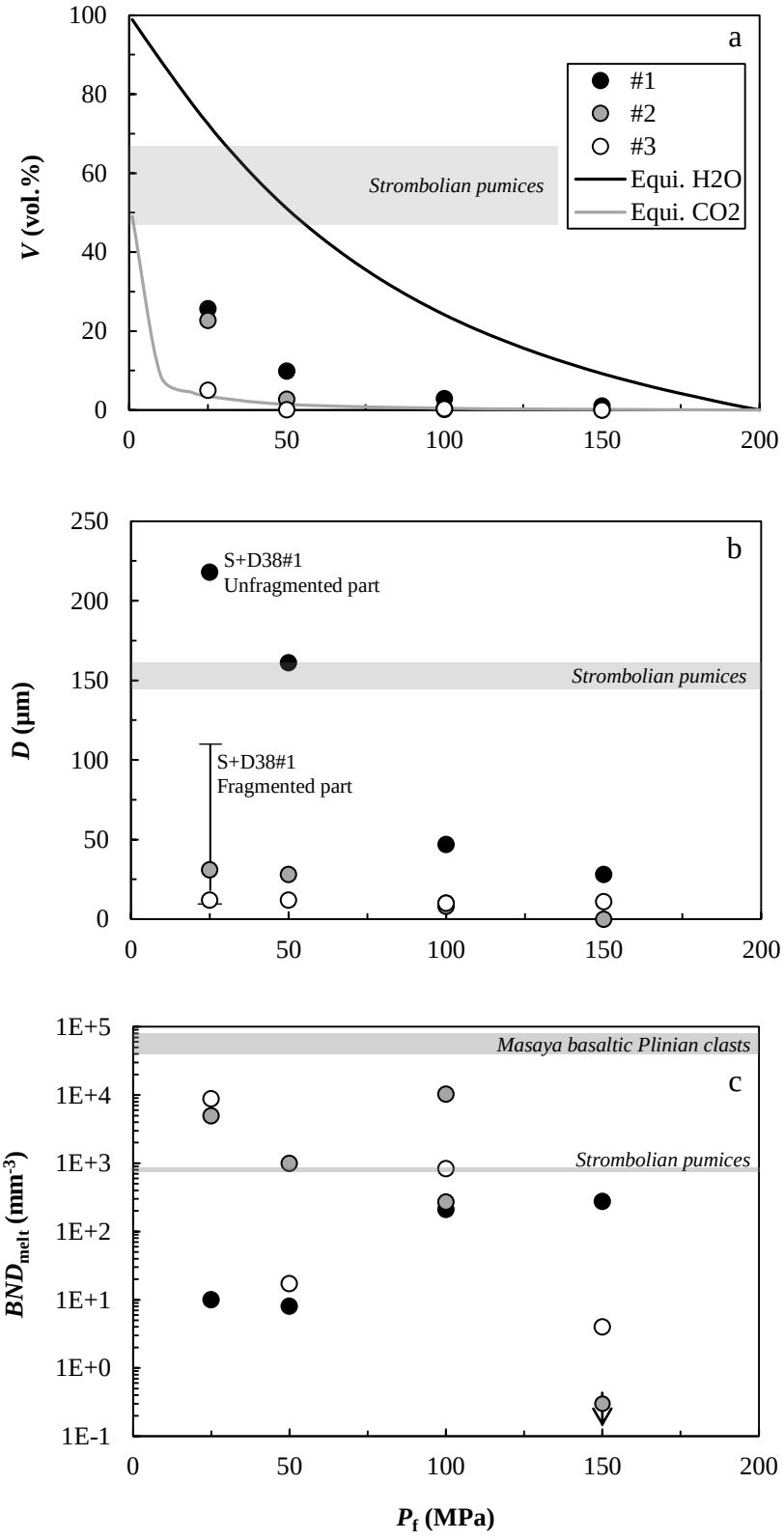

Le Gall and Pichavant. Fig. 3

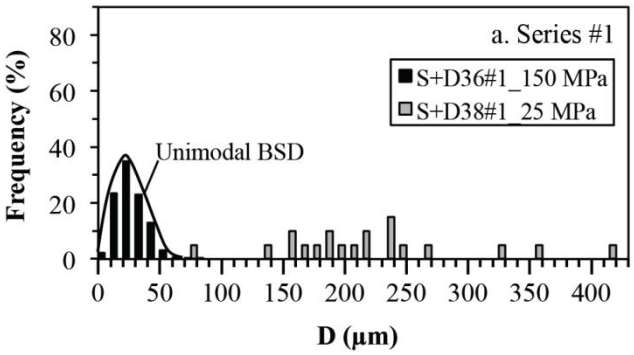

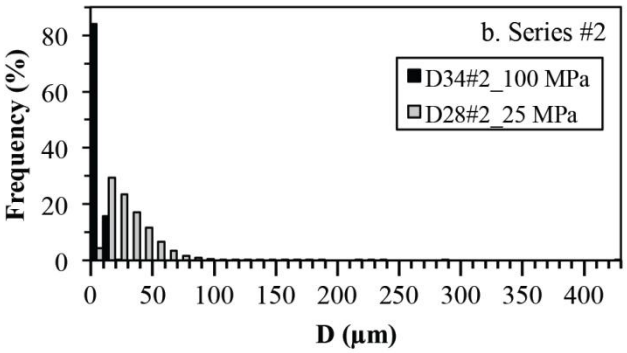

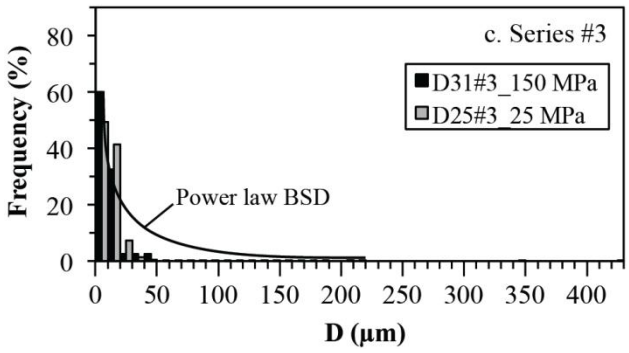

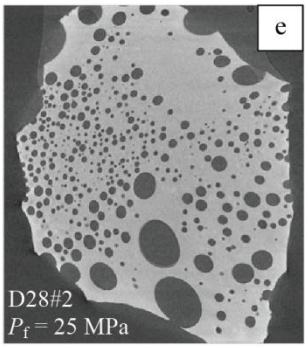

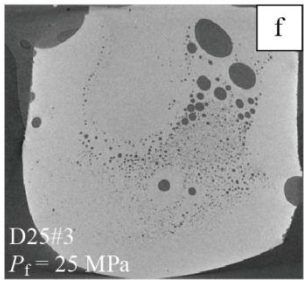

Le Gall and Pichavant. Fig. 4

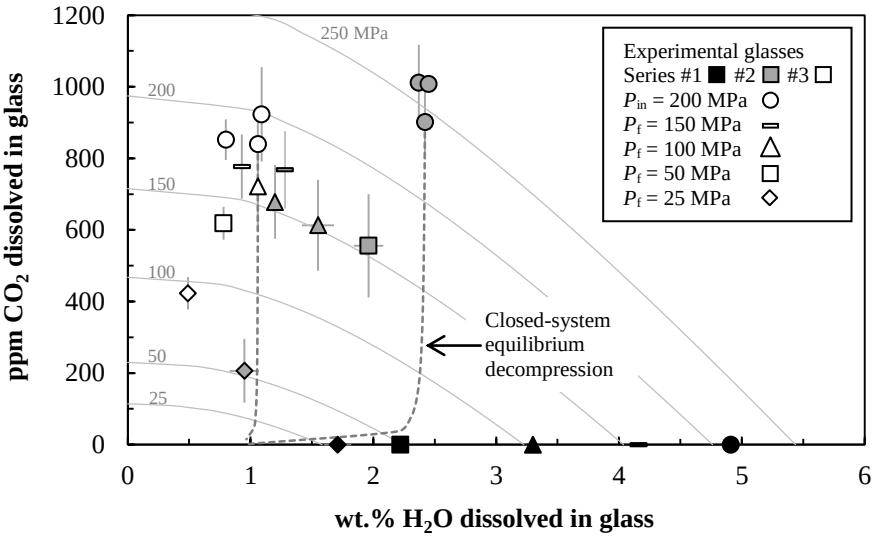

Le Gall and Pichavant. Fig. 5

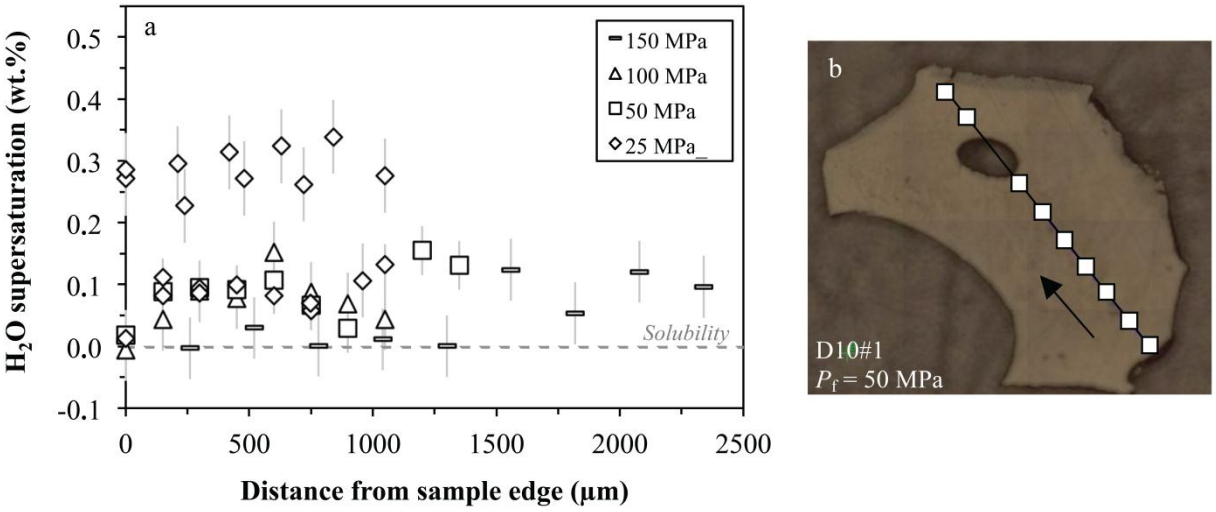

Le Gall and Pichavant. Fig. 6

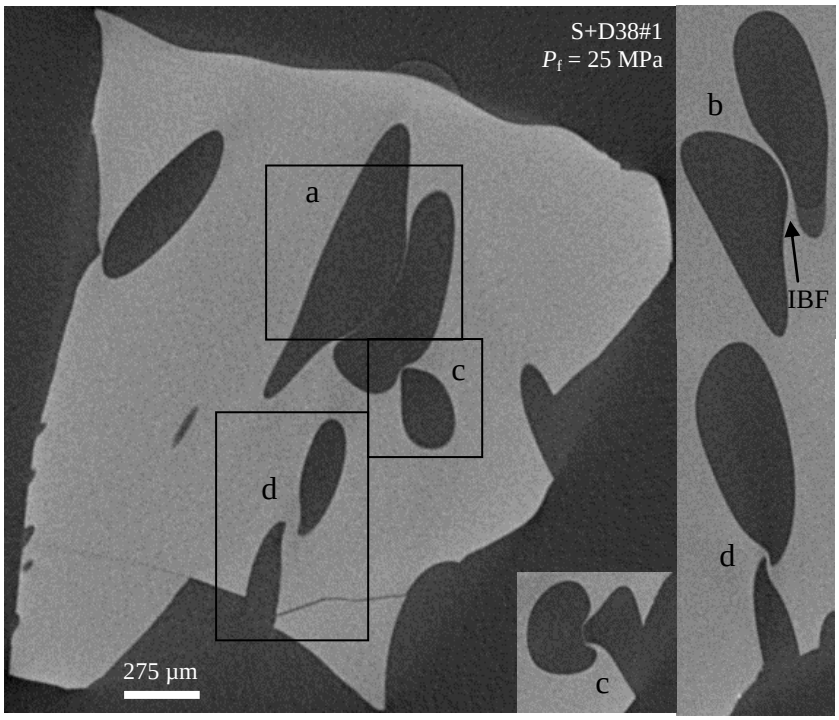

Le Gall and Pichavant. Fig. 7

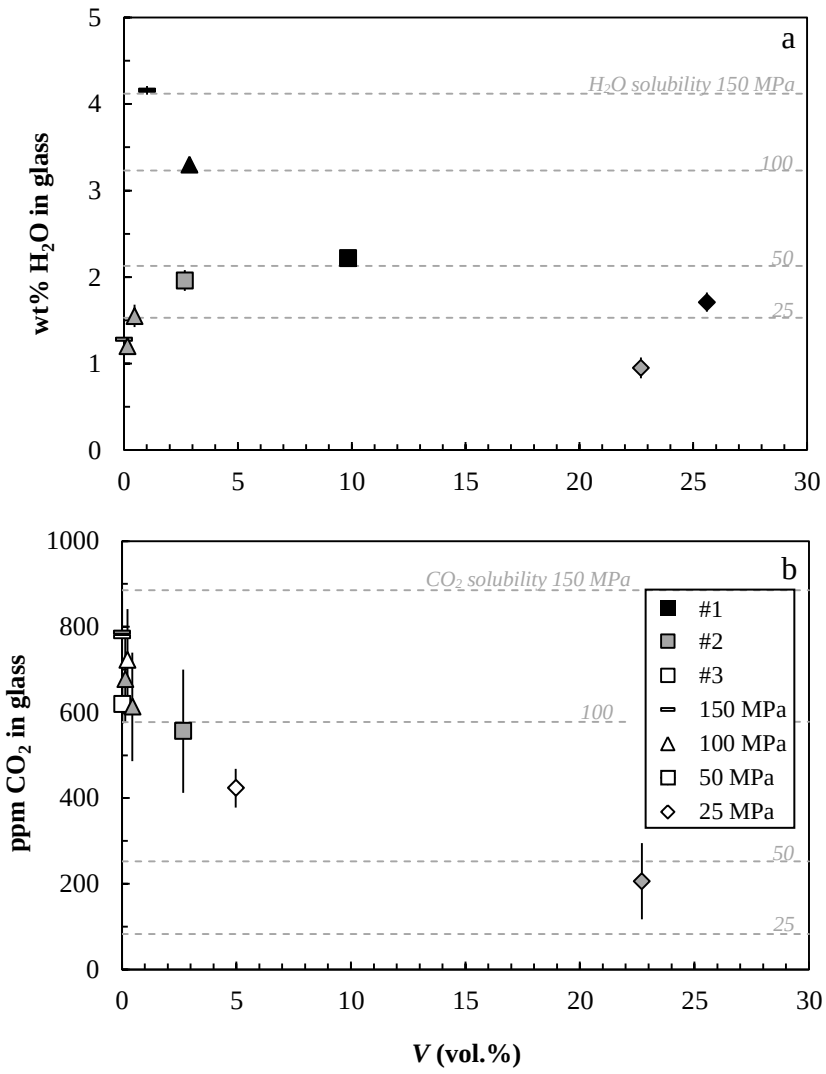

Le Gall and Pichavant. Fig. 8

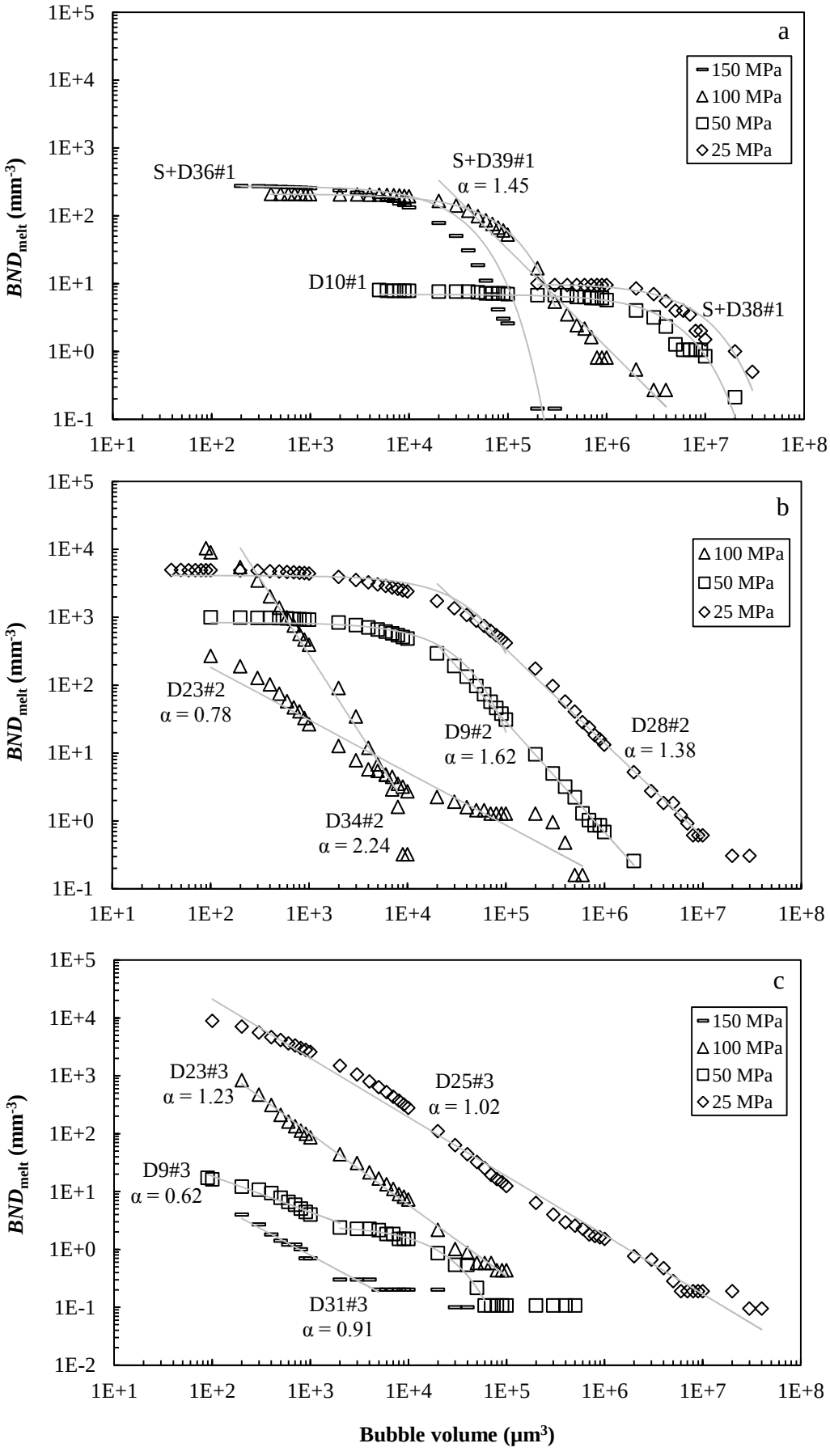

Le Gall and Pichavant. Fig. 9

Table 1. Composition of PST-9 golden pumice and starting glass

Label	PST-9[a]	Glass[b] (*n* = 54)
SiO_2	49.4	50.9 (3)[c]
TiO_2	0.79	0.81 (8)
Al_2O_3	15.75	15.99 (28)
Fe_2O_3	1.3	nd
FeO	6.5	7.7 (6)
MnO	0.15	0.16 (8)
MgO	7.96	7.21 (41)
CaO	12.73	12.34 (24)
Na_2O	2.27	2.39 (9)
K_2O	1.85	1.90 (12)
P_2O_5	0.43	0.55 (17)
Cr_2O_3	–	0.03 (4)
NiO	–	0.05 (6)
Total	99.1	97.4 (10)

[a] Whole-rock analysis (from Di Carlo et al., 2006). Major elements (wt.%) analyzed by inductively coupled plasma atomic emission spectrometry (ICP-AES); total includes LOI (loss of ignition) = 0.62 wt.%; trace elements analyzed by inductively coupled plasma mass spectrometry (ICP-MS; Cr 259 ppm; Ni 75 ppm; Ba 920 ppm; La 45 ppm; Eu 2.0 ppm; Lu 0.3 ppm). Analysis performed at the Centre de Recherches Pétrographiques et Géochimiques (CRPG, Nancy, France).

[b] Electron microprobe analysis (normalized to 100%) of PST-9 glass, with all Fe reported as FeO; oxides are in wt.%.

[c] One standard deviation in terms of last digit.

n: number of analyses.

nd: not determined.

Table 2. Synthesis experiments

Run	XH_2O_{in}	*T* (°C)	*P* (MPa)	*t* (min)	H_2O glass (wt.%)	CO_2 glass (ppm)
Volatile: H_2O (#1)						
S9#1	1	1200	201.8	2795	4.91 (1)	0 (0)
Volatile: H_2O+CO_2 (#2)						
S6#2	0.56	1200	202.2	2760	2.37 (1)	1011 (106)
S13#2	0.58	1200	201.5	2878	2.45 (2)	1008 (21)
S16#2	0.59	1200	201.8	2873	2.42 (3)	901 (104)
Volatile: H_2O+CO_2 (#3)						
S6#3	0	1200	202.2	2760	0.80 (3)	852 (57)
S13#3	0	1200	201.5	2878	1.09 (3)	923 (132)
S16#3	0	1200	201.8	2873	1.06 (1)	840 (64)

XH_2O_{in} = initial molar H_2O / (H_2O + CO_2) in the charge.
T: run temperature; *P*: run pressure; *t*: duration of the synthesis experiment.

Table 3. Decompression experiments: run conditions and textural information

Sample	Starting glass	P_{in} (MPa)	P_f (MPa)	t_{ramp} (s)	|dP/dt| (kPa/s)	Bubble 3D characteristics										
						n	pk. size (µm)	range (µm)	D (µm)	BND[a] (mm^{-3})	BND_{melt}[b] (mm^{-3})	S (µm)	V[c] (vol.%)	V[d] (vol.%)	$V_{Equi.\ H2O}$ (vol.%)	$V_{Equi.\ CO2}$ (vol.%)
Volatile: H_2O (#1)																
D10#1	S9#1	200	50	1928	78	38	–	22–368	161	7.8	8.1	309	2.93	9.85	51.0	
Volatile: H_2O+CO_2 (#2)																
D31#2	S16#2	200	150	642	78	0	–	–	0	0.0	0.0	–	0.00	0.00	9.22	0.17
D23#2	S13#2	200	100	1344	78	1692	7	7–109	10	269	269	96	0.07	0.15	24.1	0.47
D34#2	S13#2	200	100	1344	78	32212	6	6–27	8	10297	10331	28	0.32	0.46	24.1	0.47
D9#2	S6#2	200	50	1928	78	11609	23	6–169	28	970	991	62	2.19	2.67	51.0	1.48
D28#2	S16#2	200	25	2372	78	16187	16	4–424	31	4069	4935	36	17.5	22.7	72.5	3.47
Volatile: H_2O+CO_2 (#3)																
D31#3	S16#3	200	150	642	78	40	8	8–42	11	4.0	4.0	391	0.00	0.00	9.22	0.17
D23#3	S13#3	200	100	1344	78	5768	7	7–71	10	836	836	66	0.07	0.24	24.1	0.47
D9#3	S6#3	200	50	1928	78	160	6	6–102	12	17	17	96	0.01	0.02	51.0	1.48
D25#3	S13#3	200	25	2372	78	93103	8	6–425	12	8569	8799	30	2.60	4.97	72.5	3.47

P_{in} (initial pressure): pressure at the beginning of decompression ramp; P_f (final pressure): pressure at which the experiment was quenched; t_{ramp}: duration of the ramp; |dP/dt|: decompression rate ($=10^6(P_{in}-P_f)/(gdt_{ramp})$), with g = 9.81 m/s^2 and d = 2.65 kg/m^3.
X-ray microtomographic data acquired on entire charges (except V[d]).
n: number of bubbles counted in the analyzed volume.
pk. size: main peak diameter in bubble size distribution histograms.
range: total range of bubble diameters.
D: average bubble diameter.
[a] BND: bubble number density expressed in number of bubbles per mm^3 of the total sample (glass + bubbles).
[b] BND_{melt}: bubble number density per melt volume (without bubbles, following Proussevitch et al., 2007).
S: average spacing between bubbles calculated from BND_{melt} ($S = (3/4\pi BND_{melt})^{1/3}$; Lyakhovsky et al., 1996; Baker et al., 2006).
[c] V: vesicularity (volume fraction of bubbles, vol.%) measured from the total sample.
[d] V: vesicularity measured from representative sub-volumes.

$V_{Equi.H2O}$ and $V_{Equi.CO2}$: equilibrium vesicularities computed for the PST-9 composition considering the degassing of pure H_2O and pure CO_2, respectively (see text).

Table 4. Synthesis + Decompression experiments: run conditions and textural information

Sample	P_{in} (MPa)	t (min)	P_f (MPa)	t_{ramp} (s)	|dP/dt| (kPa/s)	Bubble 3D characteristics								
						n	pk. size (µm)	range (µm)	D (µm)	BND[a] (mm^{-3})	BND_{melt}[b] (mm^{-3})	S (µm)	V[c] (vol.%)	V[d] (vol.%)
Volatile: H_2O (#1)														
S+D36#1	202.0	41	150	642	78	1908	25	8–86	28	274	275	95	0.47	1.01
S+D39#1	202.2	54	100	1344	78	776	43	10–190	47	207	210	104	1.77	2.87
S+D38#1	202.2	60	25	2372	78	20	–	76–414	218	9.3	10	288	7.03	25.6

The synthesis + decompression experiments are divided in two steps: synthesis at P_{in} and decompression between P_{in} and P_f. P_{in} (initial pressure): pressure at the beginning of decompression ramp; t: duration of the synthesis step; P_f (final pressure): pressure at which the experiment was quenched; t_{ramp}: duration of the decompression step; |dP/dt|: decompression rate ($=10^6(P_{in}-P_f)/(gdt_{ramp})$), with g = 9.81 m/s^2 and d = 2.65 kg/m^3.

X-ray microtomographic data acquired on entire charges (except V^d).

Bubble 3D characteristics abbreviations as in Table 3.

S+D38#1 X-ray CT data concern the unfragmented part of the charge.

Table 5. FTIR data

Glass	n^a	Thickness (µm)	Absorbance 3530 cm^{-1}	H_2O (wt.%)	Absorbance 1515 cm^{-1}	CO_2 (ppm)
Synthesis experiments						
Volatile: H_2O (#1)						
S9#1	6	29 (2)[b]	1.337 (94)	4.91 (1)		
Volatile: H_2O+CO_2 (#2)						
S6#2	5	31 (1)	0.698 (34)	2.37 (1)	0.070 (9)	1011 (106)
S13#2	7	42 (2)	0.976 (44)	2.45 (2)		
	7	52 (5)			0.118 (13)	1008 (21)
S16#2	6	32 (2)	0.734 (50)	2.42 (3)	0.065 (11)	901 (104)
Volatile: H_2O+CO_2 (#3)						
S6#3	7	149 (1)	1.147 (48)	0.80 (3)	0.287 (18)	852 (57)
S13#3	8	111 (5)	1.168 (75)	1.09 (3)		
	5	62 (4)			0.129 (21)	923 (132)
S16#3	8	48 (3)	0.496 (34)	1.06 (1)	0.092 (12)	840 (64)
Decompression experiments						
Volatile: H_2O (#1)						
D10#1	9	72 (5)	1.523 (85)	2.22 (4)		
Volatile: H_2O+CO_2 (#2)						
D31#2	10	55 (5)	0.675 (69)	1.28 (5)	0.098 (20)	786 (108)
D23#2	5	84 (1)	0.973 (19)	1.20 (3)		
	7	68 (4)			0.105 (18)	678 (103)
D34#2	7	118 (5)	1.752 (132)	1.55 (13)		
	11	47 (3)			0.066 (16)	613 (127)
D9#2	12	58 (2)	1.059 (92)	1.91 (15)	0.088 (15)	668 (120)
	13	56 (1)	1.074 (50)	2.00 (6)	0.057 (8)	452 (65)
	av.			1.96 (12)		556 (144)
D28#2	9	61 (6)	0.566 (84)	0.95 (12)	0.029 (13)	206 (89)

Volatile: H_2O+CO_2 (#3)						
D31#3	11	152 (8)	1.384 (90)	0.93 (1)	0.269 (37)	777 (90)
D23#3	10	133 (7)	1.365 (73)	1.06 (2)	0.219 (43)	722 (119)
D9#3	8	171 (1)	1.291 (65)	0.78 (4)	0.239 (19)	619 (46)
D25#3	7	73 (4)	0.350 (40)	0.49 (4)		
	6	123 (9)			0.118 (14)	423 (45)
Synthesis+Decompression experiments						
Volatile: H_2O (#1)						
S+D36#1	10	38 (5)	1.480 (184)	4.16 (5)		
S+D39#1	8	58 (1)	1.801 (49)	3.30 (5)		
S+D38#1	11	54 (3)	0.932 (58)	1.80 (6)		
	10	102 (7)	1.590 (92)	1.61 (3)		
	av.			1.71 (11)		

D9#2 and S+D38#1 analyzed in duplicate. Average H_2O and CO_2 concentrations (av.) and standard deviations are reported. These are calculated by using all analytical spots.

[a] Number of analytical spots.

[b] One standard deviation in terms of the last digit.

Chapitre iv

Effet de la vitesse d'ascension sur la nucléation homogène des bulles dans les systèmes basalte-H_2O et basalte-H_2O-CO_2 : Implications pour le volcan Stromboli

Résumé

L'ensemble d'expériences de décompression faisant l'objet de ce chapitre a été réalisé afin de quantifier l'effet de la vitesse d'ascension sur la nucléation homogène des bulles (H_2O, CO_2) dans les liquides basaltiques. L'ascension de liquides basaltiques analogues à ceux du Stromboli et contenant soit de l'H_2O pure soit des mélanges H_2O-CO_2 comme volatils dissous a été simulée. La ponce PST-9, émise lors d'une éruption paroxysmale du Stromboli, a été utilisée comme matériel de départ.

Les verres de départ ont été saturés en H_2O et en H_2O-CO_2 à 1200°C et 200 MPa (P_{in}), puis décomprimés à un taux de 39 kPa/s (ou 1,5 m/s) entre 200 et 25 MPa (P_f). Les résultats de cet ensemble d'expériences sont comparés aux expériences décomprimées au taux de 78 kPa/s (ou 3 m/s, Chapitre iii). Comme au Chapitre iii, les verres ont été caractérisés texturalement (vésicularités, nombre et taille des bulles) et chimiquement (teneur en volatils dissous).

La nucléation homogène des bulles (H_2O, CO_2) intervient pour des pressions de sursaturation $\leq$ 50 MPa. Dans le système basalte-H_2O, deux événements de nucléation homogène des bulles sont observés, le premier et le plus important à haute pression (200–150 MPa) et le second à basse pression (50–25 MPa). Le second événement de nucléation intervient juste au-dessous du niveau de fragmentation. Il semble résulter d'un stade de sursaturation en H_2O des liquides basaltiques à basse pression. En présence de CO_2, la nucléation homogène des bulles est continue, les événements de nucléation se succédant au cours de la décompression. La coalescence des bulles est observée dans les systèmes avec et sans CO_2, notamment entre 100 et 50 MPa. Les liquides hydratés dégazent à l'équilibre chimique jusqu'à 100 MPa avant d'être sursaturés en H_2O à 60 et 50 MPa. En comparaison, les liquides contenant du CO_2 dégazent systématiquement hors équilibre ; leurs concentrations en CO_2 sont largement supérieures aux solubilités attendues. Un processus de fragmentation est observé à 25 MPa dans quelques charges dépourvues de CO_2, et il semble intimement lié au second événement de nucléation des bulles mis en évidence à basse pression. Les textures de nos verres contenant de l'H_2O et du CO_2 reproduisent certains aspects des textures (densités numériques de bulles, tailles, formes et distributions des bulles) ainsi que de la chimie (concentrations en volatils résiduelles) des verres naturels du Stromboli. Certains paramètres texturaux (tailles des bulles et distributions, densités numériques de bulles)

peuvent être utilisés pour contraindre la durée d'ascension des ponces Stromboliennes depuis leur région source à la surface (de 43 à 128 min).

Effect of ascent rate on homogeneous bubble nucleation in the system basalt-H_2O-CO_2: Implications for Stromboli volcano

Nolwenn Le Gall[1, 2, 3] · **Michel Pichavant**[1, 2, 3]

[1] Université d'Orléans, ISTO, UMR 7327, 45071, Orléans, France
[2] CNRS/INSU, ISTO, UMR 7327, 45071, Orléans, France
[3] BRGM, ISTO, UMR 7327, BP 36009, 45060, Orléans, France

Abstract High pressure and temperature decompression experiments were performed to simulate the ascent of H_2O- and H_2O-CO_2-bearing basaltic melts from the deeper to the shallower part of the Stromboli magmatic system. A well-studied "golden" pumice produced during an intermediate to a large-scale paroxysm was used as starting material. Volatile-bearing glasses were synthesized at an oxygen fugacity (fO_2) ranging from NNO–1.4 to +0.9, 1200°C and 200 MPa. The resulting crystal and bubble-free glasses were then isothermally (1200°C) decompressed to final pressures ranging between 200 and 25 MPa, at a linear ascent rate of 1.5 m/s (or 39 kPa/s) prior to be rapidly quenched. Textures of post-decompression glasses which were characterized by X-ray CT result from different mechanisms of degassing that include bubble nucleation, growth and coalescence, as well as fragmentation. Homogeneous bubble nucleation occurs for supersaturation pressures (difference between saturation pressure and pressure at which bubbles start to form homogeneously, ΔP_{HoN}) ≤ 50 MPa. In the CO_2-free melts, homogeneous nucleation occurs as two distinct events, the first and most important at high P_f (200–150 MPa) and the second at low P_f (50–25 MPa) near the fragmentation level. In contrast, in the CO_2-bearing melts, multiple events of homogeneous bubble nucleation occur over a substantial P_f interval along the decompression path. Bubble coalescence occurs in both H_2O- and H_2O-CO_2-bearing melts and is the more strongly marked between 100 and 50 MPa P_f. The CO_2-free melts follow equilibrium degassing until 100 MPa P_f and are slightly supersaturated at 60 and 50 MPa P_f, thus providing the driving force for the second bubble nucleation event. In comparison, disequilibrium degassing occurs systematically in the CO_2-bearing melts which retain high CO_2 concentrations. Fragmentation was observed in some CO_2-free charges decompressed to 25 MPa P_f and is intimately associated with the occurrence of the second bubble nucleation event. Textures of H_2O-CO_2-bearing glasses reproduce certain critical aspects of the Stromboli natural textures (*BND*s, bubble sizes, shapes and distributions) and chemistries (residual volatile concentrations).

Average bubble sizes, BSD and *BND* data are used together to constrain "golden" pumice magma ascent from their source region in 43 to 128 min.

Keywords Basalt . Stromboli . Volatiles . Magma degassing . Nucleation . Gas bubbles . Fragmentation

1. Introduction

Water and carbon dioxide, which are the two main volatile components dissolved in basalt magmas, control the physical processes involved in volcanic eruptions (e.g. Cashman and Sparks, 2013). As magma ascends to the Earth's surface, pressure decreases and this causes exsolution of the dissolved volatiles from the supersaturated melt. Accordingly, gas bubbles nucleate, grow and coalesce as magma continues to ascend. The evolution of the gas phase within the volcanic conduit is thought to govern the eruptive behavior. The gas phase can either remain as bubbles within the melt ("closed-system" degassing) or escape from the magma ("open-system" degassing). The former (rapid magma ascent) would lead to explosive behavior and the latter (slow magma ascent) to effusive behavior (e.g. Gonnermann and Manga, 2005, 2007). As an illustration, Stromboli volcano (Italy) is, among other basaltic volcanoes, characterized by a variety of eruptive styles ranging from lava flows, mild Strombolian explosions to more violent explosions. Such a variety is thought to be controlled by the kinetics of magma vesiculation (bubble nucleation, growth and coalescence) and fragmentation, as well as by changes in magma ascent rate (Woods and Koyaguchi, 1994; Sparks, 2003; Edmonds, 2008).

Studies of when and how gas bubbles form and separate from magma are needed to better understand whether a volcanic eruption is effusive or explosive (Edmonds, 2008). Volcanic magma degassing, corresponding to the loss of dissolved volatiles, can be studied from different approaches. The first, including petrological studies and phase equilibria experiments, aims at determining the volatile compositions and concentrations in magma prior to significant degassing (Edmonds, 2008) (e.g. Bertagnini et al., 2003; Métrich et al., 2005; Di Carlo et al., 2006; Métrich et al., 2010; Pichavant et al., 2009, 2011). Volatile solubility models (e.g. Newman and Lowenstern, 2002; Papale et al., 2006; Iacono-Marziano et al., 2012) play an important role. The second, including textural and geochemical studies,

deal with the exsolved, integrated products of degassing (Edmonds, 2008) (e.g. Mangan and Cashman, 1996; Gaonac'h et al., 1996; Lautze and Houghton, 2007; Polacci et al., 2006, 2008, 2009; Burton et al., 2007; Allard, 2010; Aiuppa et al., 2010a, 2011). In addition, numerical models are becoming available to simulate the physical (textures) and chemical (volcanic gases, volatile solubilities) evolution of gas bubbles and melt during degassing (e.g. Blower et al., 2001, 2002; Toramaru, 2006; Burgisser et al., 2015). However, none of these two main approaches are completely satisfactory. Volatile solubility models as well as the interpretation of volcanic gas data assume gas-melt equilibrium degassing of basaltic magmas, while recent experiments (Pichavant et al., 2013; Le Gall and Pichavant, 2015a) have reported the possibility of disequilibrium degassing during ascent and decompression of CO_2-bearing basaltic melts. There are also problems and disagreements associated with the interpretation of textural and chemical data in natural eruption products (Gaonac'h et al., 1996; Blower et al., 2001, 2002; Edmonds, 2008).

In complement to these two main approaches, high pressure and temperature decompression experiments (e.g. Mangan and Sisson, 2000; Mourtada-Bonnefoi and Laporte, 2002; 2004; Mangan and Sisson, 2005; Iacono-Marziano et al., 2007; Cluzel et al., 2008; Gardner and Ketcham, 2011) have the advantage to simulate the vesiculation process during magma ascent. Therefore, in an attempt to assist in the interpretation of textural and chemical data collected on basaltic eruptive products, we performed experimental simulations of the ascent and degassing of H_2O- and H_2O-CO_2-bearing Stromboli melts. The run products were texturally and chemically characterized to model the behavior of the major volatiles (H_2O, CO_2) during decompression, and in particular to assess the effect of ascent rate on the degassing kinetics. Our results bring direct constraints on degassing processes at Stromboli (Aeolian Islands, Italy) which is one representative example of explosive basaltic volcanoes (Rosi et al., 2013). It is also a very well-studied system and melt inclusion data (e.g. Métrich et al., 2010; Bertagnini et al., 2003; Métrich et al., 2005, 2010) and gas measurements (e.g. Burton et al., 2007; Aiuppa et al., 2010a, b, 2011; La Spina et al., 2013) are available, as well as equilibrium gas-melt computations and experimental solubilities of H_2O and CO_2 (Newman and Lowenstern, 2002; Shishkina et al., 2010; Lesne et al., 2011a, b) among other types of information, to enable detailed comparison to be made between experimental and natural products.

2. Volcanological background

Stromboli is a basaltic volcano located in the Aeolian Islands, Italy. It is well known for its persistent explosive activity established 1300–1700 years ago (Rosi et al., 2000). This normal activity, which consists of rhythmic, mild to moderate explosions lasting a few seconds (e.g. Rosi et al., 2013) is associated with a continuous degassing dominated by H_2O, CO_2 and SO_2 (Aiuppa et al., 2010a). Every 10–20 min, scoriaceous lapilli and bombs, ash and lithic blocks are ejected to heights of a few tens to hundreds of meters above the summit craters (Rosi et al., 2000; Bertagnini et al., 2003; Francalanci et al., 2004). According to Burton et al. (2007), such explosions result from the buoyant rise of deep-sourced (< 3 km) gas slugs. This normal Strombolian activity can be suddenly interrupted by lava flows, and by violent explosions of variable scale defined as Strombolian paroxysms (Mercalli, 1907; Rosi et al., 2013). Paroxysms range from small-scale (Métrich et al., 2005; Bertagnini et al., 2008; Rosi et al., 2013), also designated as "major explosions" (Barberi et al., 1993), to large-scale, the latter often called paroxysms for simplicity (Bertagnini et al., 2011; Rosi et al., 2013). These more violent explosions occur at a rate from 1.7 episodes per year (Rosi et al., 2013) to 1–10 episodes per century (Pichavant et al., 2009). During these highly energetic events, fallouts of meter-sized bombs and blocks, gas and ash, are produced and ejected up to a few kilometers from the vents.

These three types of eruptive activity at Stromboli are fed by two distinct magmas: a volatile-poor black scoria and a volatile-rich yellowish pumice (designated as "golden" pumice; Métrich et al., 2001; Bertagnini et al., 2003, 2008). The former, that supplies normal Strombolian activity and lava flows, is highly porphyritic (~50 vol.% crystals of plagioclase, clinopyroxene and olivine; Landi et al., 2004; Pichavant et al., 2011). In contrast, the latter, commonly produced during the paroxysms, has low porphyricity (~10 vol.% crystals of clinopyroxene, olivine and plagioclase; e.g. Francalanci et al., 2004; Pichavant et al., 2011). The present-day feeding system is thought to comprise a shallow reservoir hosting the black scoria magmas, recharged with the periodic arrival of "golden" pumice magmas from a deeper crustal reservoir (Pichavant et al., 2009; Métrich et al., 2010; Pichavant et al., 2011). Both magmas are often intermingled, and crystals in the "golden" pumices mainly come from the black scoria because of syn-eruptive mingling between the two magma types (e.g. Di Carlo et al., 2006).

Strombolian paroxysms constitute a serious hazard for inhabitants and visitors, due to their high intensity and potential to strike inhabited areas (Rosi et al., 2013). Development of the monitoring system since the 2002–2003 crisis now allows to daily collect a large body of geochemical and geophysical data (e.g. Ripepe and Harris, 2008; Rosi et al., 2013). Continuous measurements of CO_2 and SO_2 emissions have evidenced significant changes in the chemical composition of the gases between quiescent, passive degassing and eruptions (Burton et al., 2007; Aiuppa et al., 2009, 2010a, b, 2011; La Spina et al., 2013). Concerning Strombolian paroxysms, these appear systematically preceded by medium-term (days to weeks) increases of CO_2 fluxes (Aiuppa et al., 2010a, b, 2011). Two main models have been proposed to explain these observations. According to Bertagnini et al. (2003) and Métrich et al. (2001, 2005, 2010), the more violent explosions would be generated by the rapid ascent, decompression and fragmentation of a volatile-rich, low-porphyritic magma ("golden" pumice) batch. Alternatively, Allard (2010) suggests that such events would result from the bursting of CO_2-rich gas slugs generated at 8–10 km depth. In addition, Pichavant et al. (2013) has proposed that Strombolian paroxysms would be driven by explosive degassing and fragmentation of CO_2-oversaturated melts produced as a result of disequilibrium degassing during ascent.

3. Experimental methods

Two types of experiments were performed: synthesis and decompression. The synthesis experiments were conducted to generate the bubble-free H_2O- and H_2O-CO_2-bearing basaltic melts to be used in the decompression experiments, in order to simulate their ascent.

3.1. Scaling of the decompression experiments

Experimental conditions (P, T, basaltic composition, dissolved H_2O/CO_2, ascent rate and fO_2) were scaled against Stromboli. In this way, the initial pressure (P_{in} = 200 MPa) chosen in the decompression experiments is consistent with the depth of the storage region of "golden" pumice melts (around 7.5 km, Di Carlo et al., 2006; Pichavant et al., 2009; Métrich et al., 2010). Final pressures (P_f = 200–25 MPa) correspond to different heights in the volcanic conduit. The temperature (T = 1200°C and kept constant) was chosen to be above the

liquidus of "golden" pumice melts, on the basis of previous phase equilibrium experiments (Di Carlo et al., 2006; Pichavant et al., 2009). All experiments were performed with the same basaltic composition representative of "golden" pumice melts involved in the present-day activity at Stromboli (Francalanci et al., 1989, 1993, 2004; Di Carlo et al., 2006). The pre-decompression ranges of volatile concentrations (0.71–4.94 wt.% H_2O, 818–1094 ppm CO_2) investigated overlap with the H_2O and CO_2 concentrations in Stromboli melt inclusions (e.g. Métrich et al, 2010). Concerning the ascent rate, there is a large uncertainty on Stromboli. On the one hand, an ascent rate of 3 mm/s (Calvari et al., 2011) implies that "golden" magmas would ascend from 7–8 km depth in about 1 month. This seems much too slow since "golden" pumices lack microlites which implies ascent durations of a maximum of 10 h (Di Carlo et al., 2006; Pichavant et al., 2011). On the other hand, an ascent velocity of 32 m/s has been proposed from Stromboli melt viscosity data (Misiti et al., 2009), implying an ascent time of only a few minutes from 7–8 km depth. In this study an average ascent rate value of 1.5 m/s was investigated more in line with the petrological constraints (< 10 h). This value is in the average of ascent rates determined for Vulcanello shoshonite magmas (0.27–3.2 m/s; Vetere et al., 2007), a system closely similar to that of Stromboli (Pichavant et al., 2013). Concerning the redox state, oxidizing redox conditions around ΔNNO = +0.5 (where NNO is the nickel-nickel oxide buffer) were determined for the near-liquidus evolution of "golden" pumice melts (Di Carlo et al., 2006; Pichavant et al., 2009) and this fO_2 range was imposed in our decompression experiments.

3.2. Starting material

The starting material used for the experiments is a high-K basalt from a paroxysmal explosion (PST-9 "golden" pumice, Di Carlo et al., 2006; Pichavant et al., 2009, 2011). The whole-rock composition of this pumice sample is shown in Table 1. PST-9 is highly vesicular (~60 vol.% vesicles) and slightly porphyritic (~11 vol.%; Pichavant et al., 2011), within the range of other pumices. A homogeneous starting glass was obtained by crushing the PST-9 pumice and melting the fine powder at 1400°C, 1 atm, during 3 hours, in a Pt crucible (Table 1). The resulting crystal- and bubble-free glass was then cored to cylinders with a diameter of 2.5 and, less frequently, 5 mm and typical lengths around 10 and 6 mm, respectively. The 5 mm diameter was tested to explore the influence of sample size on bubble nucleation and also to increase the capsule void space.

For the synthesis experiments (Table 2), the glass cylinders were loaded into capsules (1.5–3 cm length, 2.5 or 5 mm internal diameter, 0.2 wall thickness) made of $Au_{80}Pd_{20}$. Such a metal composition was used to minimize iron loss during the experiments (Di Carlo et al., 2006; Pichavant et al., 2009). Distilled water and carbon dioxide as silver oxalate ($Ag_2C_2O_4$) were used as volatile sources. Three different proportions of H_2O and CO_2 were introduced in the capsules, corresponding to XH_2O_{in} (molar H_2O / (H_2O + CO_2)) = 1 (series #1: only H_2O dissolved in glass, no CO_2 present), 0.25–0.56 (series #2: H_2O and CO_2 both dissolved in glass, high dissolved H_2O/CO_2) and 0 (series #3: H_2O and CO_2 both dissolved in glass, low dissolved H_2O/CO_2, see below for the origin of H_2O). For the 5 mm diameter cores, only XH_2O_{in} = 1 conditions were investigated, because homogenization of melt CO_2 concentrations would have required a prohibitively long experimental duration (Zhang and Ni, 2010). In one of the synthesis experiments (S5, Table 2), a separate Ni-NiPd sensor capsule was included for the determination of the experimental fH_2. It consisted of two pellets of NiPd metal mixtures (with different Ni/Pd ratio) plus NiO, placed in a Pt capsule in the presence of excess H_2O (Taylor et al., 1992).

For the decompression experiments (Table 3), the synthesized volatile-bearing glass cores (2.5 or 5 mm in diameter and about 4 mm long) were fitted into $Au_{80}Pd_{20}$ capsules without further addition of volatiles. Capsules of identical internal diameter (2.5 and 5 mm) but variable lengths (from 1 to 5 cm for the capsules decompressed to the lowest pressures) were used to accommodate gas expansion during decompression.

Capsules were weighed before and after welding to ensure that no leaks occurred.

3.3. Equipment

All experiments were carried out in an internally heated pressure vessel (IHPV), working vertically and equipped with a rapid-quench device. The vessel was pressurized with Ar-H_2 mixtures obtained by sequential loading of H_2 and Ar at room temperature (Scaillet et al., 1992). The synthesis and decompression experiments were performed with an initial H_2 pressure of 1 bar and experimental fH_2 measured in one run with a redox sensor (see above). Then, Ar was pumped into the IHPV up to the pressure needed to attain the final target conditions (Pichavant et al., 2013). Total pressure was recorded continuously by a transducer calibrated against a Heise gauge with an accuracy of ± 20 bars. The capsules were placed

together in a sample holder made of an alumina tube and suspended by a thin Pt wire in a molybdenum furnace having a 2–3 cm long hotspot. Temperature was measured using two S-type thermocouples placed along the length of the capsules and recorded continuously (uncertainty ± 5°C) with a Eurotherm controller. Near-isothermal conditions (gradient < 2–3°C/cm) were maintained in the sample holder. At the end of the synthesis and decompression experiments, the Pt suspension wire was fused electrically, allowing the sample holder to fall into the cold part of the vessel, leading to a cooling rate of about 100°C/sec (Di Carlo et al., 2006).

3.4. Run procedure

All synthesis and decompression experiments were performed independently from each other.

The synthesis experiments were performed at 200 MPa and 1200°C (Table 2), which are conditions known to be above the PST-9 liquidus on the basis of previous phase equilibrium experiments (Di Carlo et al., 2006; Pichavant et al., 2009). Up to four capsules (one for each series# plus the sensor capsule) were placed together in the IHPV for duration of about 40 hours. According to H_2O and CO_2 melt diffusion calculations (Zhang and Ni, 2010), initial experiments have shown that such a duration is sufficient to attain an equilibrium distribution of dissolved H_2O and CO_2 in the 2.5 mm diameter melt cores (Le Gall and Pichavant, 2015a). For the 5 mm diameter melt core, a run duration of 24 hours was long enough to dissolve water and attain an equilibrium distribution. The synthesized crystal- and bubble-free glasses were used as starting materials in the decompression experiments (Table 3).

Each decompression run included up to three capsules (one for each series#, Table 3). The experiments were conducted at a constant temperature of 1200°C, from an initial pressure (P_{in}) of 200 MPa to final pressures (P_f) ranging between 200 (no decompression) and 25 MPa. The 5 mm diameter glass cylinder was decompressed to 60 MPa P_f. All runs began with a step of approximately one hour at 200 MPa and 1200°C, to re-equilibrate the starting volatile-bearing glasses. Pressure was then released manually to P_f at a decompression rate of 39 kPa/s (or 1.5 m/s taking a rock density of 2.65 kg/m^3), which leads to decompression durations of

20–75 min depending on P_f. Immediately after attainment of P_f, decompression charges were rapid-quenched (within ~1–2 s) to freeze the glass textures and chemistries.

After the quench, capsules were weighted to check for leaks and then opened.

4. Analytical methods

4.1. Sample preparation

After each synthesis experiment, a part of the glass cylinder (one for each series#) was analyzed by IR spectroscopy to check for the homogeneity of H_2O and CO_2 concentrations and distributions. To do so, sections were cut perpendicularly to the long axis of the glass cylinders, double-polished and analyzed.

After the decompression experiments, the glass cylinders were carefully removed from their capsules. Their texture was studied by X-ray microtomography (the analysis is performed on the entire charge). Then, the glasses were subdivided into several sections, again cut perpendicularly to the cylinder long axis. One of these sections (or several sections when numerous analyses were needed) was double-polished for the determination of volatile concentrations dissolved in the glass, by IR spectroscopy. Another section was embedded into epoxy resin and polished for scanning electron microscope (SEM) observations.

The metallic pellets in the sensor capsule were also recovered, mounted in epoxy resin, and then analyzed by electron microprobe.

4.2. Textural analyses

We used the Phoenix Nanotom 180 at ISTO, Orléans to perform X-ray computed tomography (X-ray CT) analyses of each post-decompression charge. Between 1000 and 1100 projection images were collected from the 360° rotation of the samples, using a tungsten filament and either a molybdenum (most of the time) or a tungsten (more rarely) target. During the acquisition of the X-ray CT scans, the glass cylinders were mounted on carbon fiber rods with thermoplastic adhesive. Operating voltages ranged from 90 to 110 kV, with filament currents of 58–170 µA. Voxel edge lengths ranged between 2.78 and 6.77 µm, and they represent the minimum bubble sizes that can be detected. Reconstruction of the

projections into a stack of grayscale images was performed with a Phoenix program (datos|x reconstruction). Then, a complete three-dimensional reconstruction of the sample was produced using the ImageJ software package (Abràmoff et al., 2004). This allows the determination of the textural parameters (individual bubble volume, individual bubble size *D* calculated from volume assuming a spherical shape, bubble number density *BND* calculated from the total number of bubbles per unit volume of melt, average spacing between bubbles *S* and vesicularity *V*, Table 3), following the procedure described in Le Gall and Pichavant (2015a). Image analysis was performed either on entire X-ray CT dataset (V^c determination, Table 3) or on four representative sub-volumes of each sample (V^d determination, Table 3). A particular case needed to be made for charge D24#1 (Fig. 1c) which contains a population of very large interconnected bubbles opened toward the exterior of the charge and counted as voids (v2 in Le Gall and Pichavant, 2015a), whose sizes and number densities were estimated from two-dimensional tomographic slices.

For comparison with the vesicularities measured in our run products, theoretical vesicularities generated from equilibrium degassing were computed for the PST-9 melt composition, as detailed in Le Gall and Pichavant (2015a). Two end-member cases were considered corresponding to the equilibrium degassing of pure H_2O and pure CO_2 gas, respectively.

A limited number of samples were examined by scanning electron microscopy (SEM), to check for the presence of bubbles which cannot be detected by X-ray CT because of their size (< 4 µm). SEM images were collected using the MIRA3 TESCAN FEG instrument at ISTO, Orléans. An accelerating voltage of 15–25 kV was applied.

4.3. Glass volatile concentrations

H_2O and CO_2 contents in the samples were determined by Fourier transform infrared spectroscopy (FTIR). We used a Nicolet 6700 spectrometer and a Continuµm FT-IR microscope, together with an IR source, a KBr beamsplitter and a MCT/A detector (mercury, cadmium, tellurium). Punctual analyses and concentration profiles, to control the homogeneity of the starting glass cores and the distribution of the volatiles, were performed with a 50 µm diameter spot. FTIR spectra were acquired between 650 and 7000 cm^{-1} on

doubly polished samples (18–207 µm) from 128 scans collected at a resolution of 4 cm^{-1}. H_2O and CO_2 concentrations (C, wt.%) were calculated from the Beer-Lambert law, as (e.g. Métrich et al., 2004):

$$C = \frac{100AM}{\varepsilon \rho e} \text{ (Eq. 1)}$$

where A is the absorbance (measured at 3530 cm^{-1} for H_2O and at 1515 cm^{-1} for CO_2), M the molar mass of the species ($g.mol^{-1}$), ε the molar absorptivity ($L.mol^{-1}.cm^{-1}$), ρ the glass density ($g.cm^{-3}$), and e the sample thickness (cm) measured with an optical microscope.

Absorbance of the 3530 cm^{-1} total H_2O band was measured with a straight base line, and that of the 1515 cm^{-1} carbonate ions band was determinate by subtracting a spectrum obtained on a glass with no dissolved volatiles. For H_2O we considered a ε of 64 $L.mol^{-1}.cm^{-1}$ (Dixon et al., 1995) and for CO_2, we calculated a ε of 363 $L.mol^{-1}.cm^{-1}$ from the equation of Dixon and Pan (1995), as ε^{1525}=451-342 [Na/(Ca+Na)]. Densities of the experimental glasses were calculated using the method of Richet et al. (2000), using the measured density of the anhydrous starting glass (ρ = 2.747 ± 0.001). With this method we consider only the amount of water dissolved in the glass and assume that the quantity of CO_2 dissolved does not significantly affect densities (Lange, 1994; Bourgue and Richet, 2001; Lesne et al., 2011a).

Equilibrium gas-melt computations (volatile solubilities as a function of P-T conditions, isobaric solubility curves and closed-system degassing paths) were calculated with the VolatileCalc model of Newman and Lowenstern (2002), for a basalt with 49 wt.% SiO_2. H_2O and CO_2 contents in glasses from the synthesis experiments and from the series #1 decompression experiments (see in Fig. 5a) were also compared with the recent experimental solubilities of Lesne et al. (2011a, b) and Shishkina et al. (2010), determined for a pressure of 200 MPa and a temperature of 1200–1250°C.

Electron microprobe analyses of metallic sensor phases were performed with the Cameca SX-50 at Orléans. Analyses were carried out under an acceleration voltage of 20 kV, counting times of 10 s, and a sample current of 20 nA.

5. Experimental results

5.1. Redox conditions

The mole fraction of Ni in the alloy phase of the sensor capsule (X_{Ni}) indicated a fH_2 of 9 bar. This translates to fO_2 conditions in the synthesis experiments ranging from NNO–1.4 (series #3), NNO+0.1 (series #2) to NNO+0.9 (series #1) depending on the H_2O concentrations (and thus the fH_2O) in the three experimental series (NNO is the fO_2 of the Ni-NiO equilibrium at the *P-T* of interest). The fO_2 conditions determined for series #1 and #2 melts are close to the fO_2 around NNO+0.5 determined for the near-liquidus evolution of "golden" pumice melts (Di Carlo et al., 2006). It is worth noting that the fO_2 determined for series #3 melts is more reduced, because of the lower melt H_2O concentrations (and so lower fH_2O) measured in this series (see below).

5.2. H_2O and CO_2 concentrations in starting glasses

The volatile contents of the crystal- and bubble-free glasses from the synthesis experiments (hereafter designated as pre-decompression glasses) are presented in Table 2. No concentration gradients of either H_2O or CO_2 were observed on FTIR profiles from capsule walls towards glass cores. If the standard deviations and analytical errors for the volatile concentration measurements (± 0.1 wt.% for H_2O and ± 100 ppm for CO_2) are considered, the pre-decompression glasses have homogeneous H_2O and CO_2 concentrations.

Starting glasses divide into three compositional groups consistent with the synthesis conditions (Table 2). Series #1 glasses contain about 4.92 ± 0.02 wt.% dissolved H_2O and no CO_2. Water-saturated conditions were confirmed in series #1 charges by the presence of water bubbles hissing out from the capsules during their opening (Lesne et al., 2011b). The H_2O concentration measured in sample S8#1 is clearly lower (2.53 ± 0.05 wt.%, Table 2) and thus appears anomalous, being excluded from the average. Actually, H_2O loss occurred in this charge during the experiment. Series #2 glasses have between 1.95 to 2.37 wt.% H_2O and from 818 to 1011 ppm CO_2 (Table 2). As in the series #1 glasses, a charge has a clearly lower H_2O content (0.58 wt.%, S4#2). This deviation is related to an analytical problem since the glass decompressed to $P_f = P_{in}$ = 200 MPa from S4#2 (D3#2 charge) contains 2.45 wt.% H_2O (Tables 3 and 5). In spite of multiple checks, the analytical problem persisted. Therefore, the H_2O content of charge S4#2 is estimated below to 2.5 wt.%. Apart from S4#2, the series #2

volatile concentrations are within the range of melt inclusions in Stromboli "golden" pumices (H_2O = 1.8–3.4 wt.%, CO_2 = 894–1689 ppm; Métrich et al., 2001; Bertagnini et al., 2003; Métrich et al., 2010). Although water was not initially added in series #3 capsules (XH_2O_{in} = 0, Table 2), this volatile component was found dissolved in all series #3 pre-decompression glasses (concentration range: 0.71–1.12 wt.%, Table 2). Glass CO_2 concentrations are of the order of 850–1100 ppm. H_2O is generated through the reduction of the Fe^{3+} of the melt during synthesis, because of the pressurization of the vessel with H_2. The reduction reaction can be written (e.g. Lesne et al., 2011a):

$$Fe_2O_{3(melt)} + H_{2(vap/melt)} = 2FeO_{(melt)} + H_2O_{(melt)} \quad \text{(Eq. 2)}$$

Part of the water may also come from the silver oxalate used as the CO_2 source, as mentioned by Lesne et al. (2011a), reaction (Eq. 2) being insufficient to account for the measured H_2O contents of series #3 glasses.

The dissolved H_2O and CO_2 concentrations in all compositional series are in agreement with the experimental solubilities found in basaltic melts equilibrated at 200 MPa, 1200–1250°C (Shishkina et al., 2010; Lesne et al., 2011a, b).

5.3. Textures of post-decompression glasses: qualitative observations

Charges from the decompression experiments (hereafter designated as post-decompression glasses) were generally recovered as glassy blocks. Exceptions are provided by the series #1 charges decompressed to 25 MPa which yielded a range of textures totally different from all the other charges from this paper. Bubbly glass fragments, foams (Fig. 1c) and in one case a glass powder were observed in the 5 series #1 charges decompressed to 25 MPa P_f (Table 4). All post-decompression glasses were crystal-free. The absence of crystals was checked by optical microscopy on the doubly polished sections prepared for FTIR and also by SEM. Tiny oxide crystals (Ti-bearing magnetite, Di Carlo et al., 2006; Pichavant et al., 2009; Pichavant et al., 2013) occur in some charges but always in very small amounts. Some charges show evidence for bubble nucleation on those Fe–Ti oxides (Le Gall and Pichavant, 2015b). However, this was observed only for a negligible proportion of nucleated bubbles.

Two main types of post-decompression glasses were distinguished on the basis of textures observed in the core of the samples. The *first* type corresponds to bubble-free glasses (Fig. 1a). It concerns D3#1 and D3#3 samples (Table 3). Although the interior of these glasses is completely devoid of bubbles, D3#1 charge exhibits a thin (< 50 µm, Fig. 1a) bubbly rim resulting from heterogeneous nucleation on the inner wall of the capsule (e.g. Mourtada-Bonnefoi and Laporte, 2002). The *second* type of post-decompression glasses is characterized by a nucleated core with a homogeneous texture (Fig. 1b). Three distinct zones can be identified in these glasses: (1) a bubbly rim (generally up to ~300 µm, e.g. in the order of 150–200 µm in D24#3 sample, Fig. 1b) at the glass-capsule interface, followed by (2) a bubbly-free zone (depleted in volatiles), and (3) a core with uniformly spaced bubbles having variable sizes, from a few micrometers up to 266 µm (range of bubble diameters, Table 3). Given the uniform spatial distribution of bubbles and the absence of crystals (hence of possible nucleation sites), we interpret the textures of type 2 post-decompression glasses to result from homogeneous bubble nucleation. Charge D1#2 is characterized by a somewhat heterogeneous distribution of relatively large bubbles (6–60 µm, Table 3). However, SEM imaging revealed the presence of a large population of smaller (< 5 µm) bubbles, homogeneously distributed within the charge. This seems to be the case of charges D1#3 and D2#3 although no check of the presence of numerous small bubbles was performed by SEM.

Note that texture of D3#2 sample is particular. It contains a few large bubbles (10 bubbles with an average size of 40 µm, Table 3) although it was quenched at 200 MPa without decompression. The presence of these bubbles may reflect an excess of the fluid phase (early excess fluid-phase bubbles), as observed by Lensky et al. (2006), or correspond to trapped air bubbles.

Otherwise, the interior of all post-decompression glasses is devoid of bubbles until P_f = 150 MPa, and bubbles are absent in series #1 and #3 experiments decompressed to $P_f = P_{in} = P_{synthesis}$ = 200 MPa.

5.4. Textures of post-decompression glasses: quantitative observations

Textural information about the decompression experiments are given in Tables 3 and 4 and depicted in Fig. 2–4.

Vesicularities range from 0 to 71.2 vol.% (series #1), 0.01 to 13.8 vol.% (series #2) and from 0 to 9.25 vol.% (series #3). It is worth noting that the series #1 charge (D24#1) yielding 71.2 vol.% is part of the texturally different 25 MPa P_f charges (Table 4). This charge yielded a highly vesicular foam that was found extruded out of the capsule (Fig. 1c). However, this unusual texture is not the result of capsule failure as detailed below, and is considered to be representative of the evolution from 50 to 25 MPa P_f in series #1 charges. Consequently, the data from charge D24#1 are given full consideration. Another series #1 charge (D8#1) is also worth being detailed since it was performed with a pre-decompression melt having a H_2O concentration ~50% lower than all the other series #1 charges. D8#1 was decompressed to 25 MPa P_f and yielded a vesicularity of 1.45 vol.% which cannot be directly compared with the data for the other series #1 charges. For this reason, D8#1 is plotted with a different symbol on Fig. 2.

In general, vesicularity increases with decreasing P_f from 200 to 25 MPa (Fig. 2a, Tables 3 and 4), especially between P_f = 50 and 25 MPa. Besides the dependence on P_f, vesicularities are a function of the volatile series since the highest vesicularities are for the H_2O-rich glasses (series #1). For example, when decreasing the melt H_2O content at constant P_f (25 MPa, Fig. 2a), V decreases from 71.2 (series #1) to 13.8 (series #2) to 9.7 (series #3) vol.%. Vesicularities for series #1 are lower than theoretical vesicularities calculated from equilibrium degassing, except the point at 25 MPa P_f which plots on the theoretical curve. The series #2 data plot intermediate between the two theoretical vesicularity curves whereas the series #3 glasses plot close to the theoretical curve for CO_2 degassing (Fig. 2a).

Average bubble diameters in series #1 range from 8 to 741 µm. Charge D24#1 (P_f = 25 MPa, Fig. 1c) is characterized by two distinct bubble populations with sizes ranging from 9 µm to 1.8 mm. The first population has an average bubble size of 17 µm and the second of 741 µm (Fig. 2b). In comparison with the other series #1 glasses, sample D8#1 (P_f = 25 MPa) deviates from the general behavior since bubble sizes are lower on average (28 µm) as a result of its lower pre-decompression melt H_2O concentration. For the series #2 samples, D ranges from 13 to 74 µm and from 6 to 18 µm for the series #3. Note that sample D3#2 (P_f = 200 MPa) shows relatively large bubbles (40 µm) despite P_f = P_{in} = 200 MPa, probably a consequence of heterogeneous bubble nucleation (Le Gall and Pichavant, 2015b). For the three series, bubble diameter generally increases with decreasing P_f from 200 to 25 MPa (Fig. 2b, Table 3). The average bubble diameter is also dependent on the concentration of dissolved volatiles. The larger bubble sizes are for the H_2O-rich series #1 post-decompression glasses

(741 µm at 25 MPa P_f), decreasing with lowering the melt H_2O content (69–74 µm for series #2 and 16–18 µm for series #3).

Bubble size distributions (BSDs) are analyzed from histograms based on the average diameter of the bubbles (Fig. 3) and from cumulative distributions of volumetric classes (Fig. 4), constructed for each series. Two main distributions were distinguished in Fig. 4, exponential and power law. Regressions were performed with the Excel software. Very good fits were generally obtained, yielding $R^2 > 0.99$ for more than 50% charges. Series #1 glasses are initially (at P_f = 150 MPa) characterized by bubbles sizes ranging between 4 and 46 µm (D30#1, Fig. 3a, Table 3), leading to a power law bubble size distribution with an exponent of 1.91 (Figs. 3a and 4a). Then, from P_f = 100 to 50 MPa bubbles become larger (40–200 µm, D5#1) and multiple peaks occur in the histogram (Fig. 3a), corresponding to exponential distributions (Fig. 4a). At P_f = 25 MPa, the two bubble populations in D24#1 charge have sizes of 9–56 µm and 400–1800 µm, respectively (Fig. 3a). The former exhibits a mixed power law–exponential distribution and the latter a power law with exponents of 0.63 and 0.50, respectively (Fig. 4a). Series #2 glasses have bubble sizes from 6–60 µm at 150 MPa P_f (D1#2, Fig. 3b, Table 3) to 15–48 µm at 100 MPa (D2#2, Table 3), both fitted by power law distributions with exponents of 0.49 and 2.22, respectively (Fig. 4b). Upon decreasing P_f, bubble sizes become larger (24–175 µm, D8#2, P_f = 25 MPa, Fig. 3b and Table 3), yielding mixed power law–exponential distributions (Fig. 4b). In fact, two types of distributions can be recognized in the charges decompressed to P_f = 50 and 25 MPa: the small to medium sized bubbles can be fitted by an exponential function whereas the larger bubbles are best described by a power law with an exponent of 0.78–1.96. Series #3 post-decompression glasses have numerous small bubbles (< 10 µm, Fig. 3c) at 150 MPa P_f (range: 7–57 µm, D1#3, Table 3). Upon lowering P_f to 25 MPa, the bubbles become a little larger (8–135 µm, D24#3, Table 3), and the maximum is shifted to 10–20 µm (Fig. 3c). The BSDs are characterized by both power law and exponential shapes (Fig. 4c). For example, glasses decompressed to P_f = 150 and 50 MPa (D1#3 and D5#3, Fig. 4c) are best described by exponential functions, while the three duplicated glasses decompressed to 100 MPa P_f can be described by either power law functions (D2#3 and D18#3, Fig. 4c) or a combination of both (D16#3, Fig. 4c) as the two samples decompressed to 25 MPa P_f (D8#3 and D24#3, Fig. 4c). It is worth noting that two charges with exponential distributions yielded relatively poor fits (Fig. 4c): D1#3 (P_f = 150 MPa, R^2 = 0.88) and D24#3 (P_f = 25 MPa, R^2 = 0.94 for the small-to-medium bubble sizes).

Bubble number densities (BND_{melt}, Table 3 and Fig. 2c) range from about 10^0 to 10^2 mm^{-3} (series #2), 10^3 mm^{-3} (series #1) and 10^4 mm^{-3} (series #3). Upon decreasing P_f, *BND*s of series #1 glasses generally decrease, from 10^3 (150 MPa, D30#1) to 10^0 mm^{-3} (50 MPa, D5#1). Nevertheless, two *BND* increases are observed along the decompression path, the first and largest between 200 (0 mm^{-3}, D3#1) and 150 MPa and the second from 50 to 25 (10^0–10^1 mm^{-3}, D24#1) MPa. In contrast, the series #2 and #3 glasses have *BND*s generally increasing from 200 (10^0 and 0 mm^{-3}, D3#2 and D3#3) to 25 (10^2 and 10^4 mm^{-3}, D8#2 and D24#3) MPa. Nevertheless, in both glass series there are a few exceptions characterized by *BND* decreases, for example between P_f = 150 and 100 MPa for one series #3 charge and between P_f = 100 and 50 MPa for one series #2 and also one series #3 charges (Fig. 2c).

5.5. H_2O and CO_2 concentrations in post-decompression glasses

H_2O and CO_2 concentrations in post-decompression glasses are presented in Table 5 and shown in Fig. 5. Series #1 glasses have H_2O contents ranging from 4.91 wt.% (D3#1, P_f = 200 MPa) to 1.52 wt.% (D8#1, P_f = 25 MPa). Thus, a general decrease of the concentration of dissolved H_2O is observed when decreasing P_f (Fig. 5a). Considering the analytical uncertainties (Fig. 5a, Table 5), the H_2O contents of series #1 glasses are in good agreement with H_2O solubilities determined by Lesne et al. (2011b), with the exception of two glasses decompressed to P_f = 60 (D22#1) and 50 (D5#1) MPa which have H_2O concentrations exceeding solubilities (H_2O supersaturations of 0.2–0.35 and 0.3 wt.% absolute for D22#1 and D5#1, respectively, Fig. 6). In addition, in these two series #1 charges, H_2O concentrations are close to solubilities near the glass-capsule interface and become higher in the core of the glass cylinder (Fig. 6). The fact that the increase of the H_2O concentration toward the core is more progressive in the charge with the larger diameter (D22#1, 5 mm) is consistent with a mechanism of diffusive motion of H_2O inside the melt toward the gas phase.

Series #2 post-decompression glasses have H_2O concentrations ranging between 2.45 and 0.82 wt.% and CO_2 concentrations ranging from 850 to 550 ppm (Table 5). Both their H_2O and CO_2 contents progressively decrease with P_f (Fig. 5b). However, the drop in H_2O and CO_2 concentrations is nonlinear with P_f. For example, the glass decompressed to 50 MPa has a much lower H_2O content (0.82 wt.%, D5#2) than the glasses decompressed to 25 MPa (1.60 wt.%, D6#2 and D8#2), and a higher CO_2 content (775 ppm) than the two glasses decompressed to 150 (754 ppm, D1#2) and 100 MPa (732 ppm, D2#2). Degassing trajectories

in our experiments are different from closed-system equilibrium decompression trends, in that there is a marked drop of H_2O content for a comparatively slight CO_2 decrease. All post-decompression glasses retain elevated CO_2 concentrations, since the data points plot well above their respective gas-melt saturation isobars. For example, measured CO_2 contents in the glasses decompressed to 25 MPa (550–558 ± 62–76 ppm, D6#2 and D8#2) largely exceed the calculated value (< 50 ppm).

Series #3 glasses have H_2O contents ranging between 0.69 and 0.95 wt.% and CO_2 contents ranging from 873 to 461 ppm (Table 5). Post-decompression glass CO_2 concentrations progressively decrease from 873 (D1#3, P_f = 150 MPa), 699–540 (D2#3, D16#3 and D18#3, P_f = 100 MPa), 626 (D5#3, P_f = 50 MPa) to 513–461 ppm (D8#3 and D24#3, P_f = 25 MPa), at approximately constant melt H_2O contents (Table 5 and Fig. 5c). Taken globally, the data points follow degassing trajectories that are nearly vertical, as are the theoretical equilibrium closed-system decompression paths. However, the decompressed glasses retain CO_2 contents that are well above equilibrium values. For example, at P_f = 25 MPa the equilibrium CO_2 concentration is < 100 ppm while our samples contain 461–513 ± 80–94 ppm CO_2 (D8#3, D24#3, Table 5).

6. Interpretation and discussion of experimental observations

6.1. Supersaturation pressures required for homogeneous bubble nucleation

The homogeneous nature of bubble nucleation in our experiments is supported by the lack of crystals to serve as nucleation sites in the melts, as well as by the textural homogeneity of our post-decompression glasses which is clearly expressed by the absence of spatial variation of the bubble number density and average bubble size (Mourtada-Bonnefoi and Laporte, 2002).

From our decompression experiments, we can determine the supersaturation pressure required to trigger homogeneous bubble nucleation ΔP_{HoN}, which is defined as the difference between the saturation pressure (P_{sat} = P_{in}, except in charge D8#1 considered apart) and the final pressure (P_f) at which bubbles begin to form homogeneously. In each post-decompression glass series, we observed a transition from a bubble-free glass core (but for series #2 the presence of heterogeneously nucleated bubbles at P_f = 200 MPa is reminded) at a high P_f to a nucleated glass core at a lower P_f. As previously mentioned, in series #1 post-

decompression glasses, bubbles are absent at P_f = 200 MPa (D3#1, Table 3 and Fig. 1a). They appear uniformly distributed in the melts from P_f = 150 MPa (D30#1, Table 3), suggesting that homogeneous bubble nucleation takes place between 200 and 150 MPa P_f, hence a ΔP_{HoN} ≤ 50 MPa. The series #1 D8#1 sample made from a pre-decompression melt with a low H_2O concentration yields a ΔP_{HoN} of 40–45 MPa by taking a P_{sat} of 65–70 MPa (Lesne et al., 2011b). Overall a critical supersaturation pressure of 45 MPa maximum is determined for the series #1 melts. This ΔP_{HoN} value is consistent with that found by Le Gall and Pichavant (ΔP_{HoN} << 50 MPa, 2015a) in their faster decompression rate experiments. This range of ΔP_{HoN} value is less than recorded for more evolved melts (60–150 MPa; Mangan and Sisson, 2000; Mourtada-Bonnefoi and Laporte, 2004; Mangan and Sisson, 2005; Iacono-Marziano et al., 2007; Gardner and Ketcham, 2011), reinforcing the idea that bubble nucleation takes place at low supersaturations in hydrous basaltic melts (Le Gall and Pichavant, 2015a).

The series #2 melts contain a few heterogeneously nucleated bubbles at P_f = 200 MPa (D3#2, Table 3). At P_f = 150 MPa, the D1#2 glass contain small (main peak diameter of 6–7 µm) bubbles. Only 15 bubbles were detected by X-ray CT because their size is hardly higher than the instrumental spatial resolution. Yet, SEM imaging revealed the presence of a population of small (< 6 µm) uniformly distributed bubbles, suggesting that an event of homogenous nucleation takes place between 200 and 150 MPa P_f. Therefore, a ΔP_{HoN} of 50 MPa maximum is inferred for the series #2 melts. This value is less than found for similar compositions in the study of Le Gall and Pichavant (ΔP_{HoN} < 100 MPa, 2015a) performed at a faster decompression rate. Pichavant et al. (2013) found a supersaturation pressure of 150 MPa maximum in their experiments performed on compositions similar to our series #2 melts. However, no data were given for P_f > 50 MPa, and so it cannot be excluded that, in their decompression experiments, homogeneous bubble nucleation would start at pressures > 50 MPa, leading to ΔP_{HoN} << 150 MPa.

Series #3 post-decompression glasses are bubble-free at P_f = 200 MPa (D3#3, Table 3). We observed small (main peak diameter of 8 µm) bubbles in the glass core decompressed to P_f = 150 MPa (D1#3, Table 3). The number of bubbles analyzed by X-ray CT is very small (8 bubbles) presumably because of their small size. However, they indicate an event of homogenous bubble nucleation between 200 and 150 MPa P_f. From this observation, a ΔP_{HoN} of 50 MPa maximum is also inferred for the series #3 melts. This ΔP_{HoN} value is the same as found for similar compositions in the study of Le Gall and Pichavant (2015a) performed at a faster decompression rate. For comparison, a critical supersaturation pressure of 200 ± 100

MPa was found by Lensky et al. (2006) for CO_2 bubbles in a synthetic mafic melt decompressed from 1.5 GPa, larger than determined here for series #2 and #3 melts. However, it is worth specifying that Lensky et al. (2006) worked on nominally H_2O-free melts. The range of supersaturations ($\Delta P_{HoN} \leq 50$ MPa) found in our series #2 and #3 melts is less than recorded for the nucleation of H_2O-CO_2 bubbles in more evolved melts (160–350 MPa, Mourtada-Bonnefoi and Laporte, 2002).

Because the range of supersaturation pressures required for homogeneous nucleation is essentially the same ($\Delta P_{HoN} \leq 50$ MPa) for each glass series, it is difficult from our data to quantify the effects of H_2O and CO_2 on ΔP_{HoN}, as proposed for melts more evolved than basalts (Mourtada-Bonnefoi and Laporte, 2002). In addition, our experimental results confirm previous observations and conclusions on the fact that ΔP_{HoN} values ≤ 50 MPa are specific to basaltic compositions, and that bubble nucleation takes place at low supersaturations in H_2O- and H_2O-CO_2-bearing basaltic melts (Le Gall and Pichavant, 2015a).

Surface tensions (σ) have been calculated (Appendix) by taking the supersaturation pressures determined for each series and our measured experimental nucleation rates. The supersaturation pressures are given as maxima, hence the calculated surface tensions are upper limits. Computations give σ values ranging from 0.054 (series #1) to 0.059 $N.m^{-1}$ (series #2 and #3). For comparison, Le Gall and Pichavant (2015a) obtained surfaces tensions of 0.058 (series #1), 0.059 (series #3) and 0.091 (series #2) $N.m^{-1}$ for the same melt compositions and volatile concentrations. The differences observed for series #1 and #2 melts are related to differences in supersaturation pressures between the two studies. In the same way, Pichavant et al. (2013) found a σ of 0.18 $N.m^{-1}$ maximum for compositions as our series #2 melts. This maximum is higher than determined here, but again consistent with their higher supersaturation pressures ($\Delta P_{HoN} < 150$ MPa). Surface tensions from this study and Le Gall and Pichavant (2015a) are lower than the values found by Khitarov et al. (1979): 0.1 to 0.4 $N.m^{-1}$ for basaltic melts at 1200°C and 100–500 MPa, the lowest end of the range corresponding to hydrous compositions.

6.2. Physical mechanisms of degassing and textures

In this section, we discuss the physical mechanisms of degassing occurring in our decompression experiments, from nucleation, growth and coalescence of gas bubbles, up to fragmentation. Emphasis is placed on textural differences between the three glass series.

6.2.1. *Vesicularities*

The three series of post-decompression glasses have vesicularities which generally increase upon decompression (i.e. upon decreasing P_f). It is worth reminding that, for all glass series, the increase in vesicularity is the most strongly marked between P_f = 50 and 25 MPa (Fig. 2a). Nevertheless, the series #2 measured vesicularities are lower than expected for a closed-system degassing. It is also the case of the series #1 glasses decompressed up to 50 MPa P_f whose measured vesicularities remain very low (< 3%) well below the equilibrium values. However, it is recalled that the series #1 25 MPa P_f D24#1 charge has a very high vesicularity of 71.2%, slightly above the range of vesicularities for Strombolian pumices (47 and 67%, Polacci et al., 2006). The general increase in vesicularity observed upon decreasing P_f is consistent with a mechanism of progressive melt vesiculation associated with decompression. However, diffusive volatile outgassing from the melts must also take place. This is demonstrated in particular by the series #1 samples which have, on the one hand, low vesicularities and, on the other hand, glass H_2O concentrations near solubilities.

6.2.2. *Nucleation events*

The melt vesiculation mechanism observed in our experiments results from different sub-processes that include bubble nucleation, growth, coalescence and collapse, as well as fragmentation. Textural evidence (bubble size distributions and bubble number densities) can be used to distinguish between single vs. multiple bubble nucleation events (or pulses) in our experiments. In series #1 post-decompression glasses, a large increase of *BND* is first observed from P_f = 200 (BND_{melt} = 0 mm^{-3}) to 150 (BND_{melt} = 1325 mm^{-3}, Table 3, Fig. 2c) MPa, implying that an event of homogeneous bubble nucleation takes place. Then, there is a general decrease of *BND* with decreasing P_f from 150 to 50 (BND_{melt} = 1.33 mm^{-3}) MPa. This trend reflects a mechanism of bubble coalescence combined with diffusive H_2O outgassing from the melt. This interpretation is supported by the small number (5) of bubbles in the charge decompressed to 50 MPa (D5#1) and the very low (< 3%) vesicularities measured up

to 50 MPa P_f. In addition, textural differences exist between the two charges of different diameter decompressed to P_f = 60 (D22#1) and 50 (D5#1) MPa. The 5 mm diameter charge contains much more bubbles (149), and accordingly has a higher vesicularity (2.1%) than the 2.5 mm diameter charge (5 bubbles and 0.3% vesicularity). This suggests that, with a higher diameter charge, diffusive H_2O outgassing from the melt is limited. Although we do not observe *BND* stabilization (which would mark by a horizontal line in Fig. 2c and would reflect the end of a nucleation event), the absence of small (< 10 µm) newly formed bubbles from 100 to 50 MPa P_f testifies to the end of the first nucleation event. This is also suggested by the exponential distributions of bubble sizes from P_f = 100 to 50 MPa (Fig. 4a) which are indicative of an absence of small bubbles. Below 50 MPa, an additional increase of *BND* is observed, suggesting that a second nucleation event takes place between 50 and 25 MPa P_f. This is supported by the small newly formed bubbles in D24#1 as revealed both by X-ray CT and microscopic textural observations (1st population with main peak diameter 10 µm, Fig. 1c). It is also worth emphasizing that the 4 other charges decompressed to 25 MPa P_f contain a population of small bubbles (Table 4). The mechanism of bubble nucleation observed in series #1 melts is thus discontinuous and restricted to two narrow P_f intervals (200–150 and 50–25 MPa).

In series #2 glasses, a general increase of the *BND* is observed from P_f = 200 (BND_{melt} = 1.15 mm^{-3}) to 100 (BND_{melt} = 104 mm^{-3}, Table 3, Fig. 2c) MPa which corresponds to the beginning of a homogeneous bubble nucleation mechanism. It is worth noting that the early event of heterogeneous bubble nucleation observed in charge D3#2 (P_f = 200 MPa) leads to a small number (10) of bubbles and, accordingly, to a low but nonzero *BND*. Below 100 MPa, we observe a decrease of *BND* (BND_{melt} = 19.2 mm^{-3}, D5#2, P_f = 50 MPa) which is interpreted to reflect a mechanism of bubble coalescence, and a possible outgassing of volatiles from the melt. As a result, the number of bubbles is reduced from 665 (D2#2, P_f = 100 MPa) to 114 (D5#2, P_f = 50 MPa). At the same time, bubble sizes give evidence for the appearance of small (< 10 µm) newly formed bubbles, indicating the occurrence of secondary nucleation events. The evolution below 50 MPa and down to 25 MPa P_f is marked by an increase of the *BND* which is interpreted as the continuation of the same nucleation process.

In series #3 melts, an increase of *BND* is observed from P_f = 200 (BND_{melt} = 0 mm^{-3}) to 150 MPa (BND_{melt} = 4.38 mm^{-3}, Table 3, Fig. 2c) which corresponds to the beginning of a homogeneous bubble nucleation mechanism. Below 150 MPa, three cases were observed, either a continuous increase of the *BND* (D18#3), a decrease of the *BND* (D2#3) or a near-

steady evolution of the *BND* (D16#3). The first case suggests the continuation of the same nucleation process below 150 MPa. This interpretation is supported by an increase in the number of bubbles from 8 (P_f = 150 MPa, D1#3) to 2042 (P_f = 100 MPa, D18#3), by the appearance of small (main peak size of 6 µm, Table 3) newly formed bubbles and by the power law distribution of the bubble sizes (Fig. 4c) which suggests that small bubbles are continuously appearing. The second case is interpreted to reflect a mechanism of bubble coalescence. However, numerous small (< 5 µm) bubbles could not be measured in D2#3 and, so, its *BND* is underestimated. The third case corresponds to a *BND* stabilization which reflects the end of a nucleation event and the beginning of bubble growth and coalescence. In this sense, the BSD of charge D16#3 evolves to a mixed power law–exponential relation which indicates a decrease in the number of small newly formed bubbles and an increase in the number of larger bubbles (Fig. 4c). Below 100 MPa and down to 50 MPa P_f, two new situations are possible, either an increase of the *BND* (continuous bubble nucleation) or a decrease of the *BND* (bubble coalescence). In any case, the evolution below 50 MPa and down to 25 MPa P_f is marked by an increase of *BND*s which is interpreted as the continuation of the same nucleation process and the occurrence of secondary nucleation events.

We conclude to a major difference in the mechanism of bubble nucleation between series #1, on the one hand, and series #2 and #3, on the other hand, as observed in the experiments of Le Gall and Pichavant (2015a). In H_2O-rich melts, two distinct events of bubble nucleation occur in narrow P_f intervals (the first at high pressure and the second at low pressure). In contrast, in CO_2-bearing melts, a single mechanism of continuous bubble nucleation takes place over a substantial P_f interval along the decompression path, leading to multiple bubble nucleation events.

6.2.3. *Bubble coalescence*

Textural evidence (decrease of the *BND* and common coalescence structures) can be used as indicators of bubble coalescence process in our experiments. Common coalescence structures were generally not observed in the three glass series (compare with Le Gall and Pichavant, 2015a). Therefore, evidence for coalescence mainly comes from decrease of *BND*s and bubble numbers and possibly from the increase in bubble sizes. The series #1 post-decompression glasses are characterized by a general decrease of the *BND* from P_f = 150 to 50 MPa (Fig. 2c). This decrease is associated with a reduction in the number of bubbles from

8350 (D30#1, P_f = 150 MPa) to 5 (D5#1, P_f = 50 MPa) and with a large increase of the average bubble size (Fig. 2b), suggesting that both bubble growth and coalescence take place in series #1 melts. In fact, a few coalescence structures (dimpling, Castro et al., 2012) were observed in the charge decompressed to P_f = 60 MPa (D22#1). In addition, the evolution of the bubble size distribution from power law to exponential indicates the presence of larger bubbles interpreted to result from coalescence (Figs. 3a and 4a). Therefore, as observed in the experiments of Le Gall and Pichavant (2015a), bubble coalescence starts very early along the decompression path in series #1 glasses. It is worth mentioning that the charge decompressed to 25 MPa P_f (D24#1) present numerous coalescence structures (dimpling, bending and stretching; Castro et al., 2012; Martel and Iacono-Marziano, 2015; Le Gall and Pichavant, 2015a) involving particularly large (up to 1.8 mm) bubbles (Fig. 1c). This suggests that the mechanism of bubble coalescence continues below 50 MPa and until 25 MPa P_f.

In series #2 glasses, the decrease of *BND* observed between 100 and 50 MPa P_f (Fig. 2c) provides evidence for the occurrence of a bubble coalescence mechanism. In this way, the number of bubbles decreases from 665 (D2#2, P_f = 100 MPa) to 114 (D5#2, P_f = 50 MPa). Increases in the average and the main bubble sizes are, however, hidden by the superimposition of a bubble nucleation process which continuously generates small (< 10 µm) bubbles and contributes to reduce bubble sizes.

In series #3 glasses, two decreases of *BND* are observed, the first between 150 and 100 MPa P_f and the second between 100 and 50 MPa P_f, both interpreted as evidence for coalescence. However, it is worth mentioning that the observed *BND* evolutions for the different charges at 100 and 50 MPa P_f indicate that coalescence is not systematic. We interpret these differences from one charge to the other at a given P_f to reflect variations in distances between bubbles. For example, the average distance between bubbles in charges D2#3 (734 µm) and D16#3 (385 µm) is larger than in charge D18#3 (101 µm), all at P_f = 100 MPa. This would make bubble interactions upon further decompression progressively more difficult in charges such as D2#3, D16#3 than in D18#3.

We conclude that, in series #2 and #3 glasses, coalescence occurs as bubbles continue to nucleate and the space between neighboring bubbles is sufficiently small. For the three glass series, bubble coalescence is the more strongly marked in the same pressure range (between 100 and 50 MPa P_f), as observed in faster decompression rate experiments (Le Gall and Pichavant, 2015a).

6.2.4. *Bubble size distributions*

Each of the three glass series shows a different evolution of the bubble size distribution (Figs. 3 and 4). With decreasing P_f, the BSD of series #1 glasses evolve from a power law (D30#1, P_f = 150 MPa, Figs. 3a and 4a), exponential (D2#1, D22#1 and D5#1, P_f = 100–50 MPa, Fig. 4a) and then to a mixed power law–exponential distribution which is specific of the 25 MPa P_f D24#1 charge. The power law BSD (which was not found in the faster decompression rate experiments, Le Gall and Pichavant, 2015a) is interpreted to reflect ongoing bubble nucleation and bubble growth. The fact that the small (volumes < 200 μm^3) bubbles are not fitted by the power law, suggests that the nucleation process is close to its end. The exponential distributions are interpreted to indicate a mechanism of bubble coalescence that goes along without further bubble nucleation. The mixed power law–exponential BSD observed at 25 MPa is due to the occurrence of the second bubble nucleation event. The increase in the number of bubbles and sizes when compared to the 50 MPa charge requires either fast bubble growth or a combination of bubble growth and coalescence, possibly promoted by rapid gas expansion between 50 and 25 MPa.

Series #2 glasses are characterized by a continuous evolution from a power law (D1#2 and D2#2, P_f = 150 and 100 MPa, Figs. 3b and 4b) to mixed power law–exponential distributions (D5#2, D6#2 and D8#2, P_f = 50 and 25 MPa, Fig. 4b) upon decreasing P_f. This transition is consistent with a mechanism of bubble growth dominated by coalescence, taking place between P_f = 100 and 50 MPa, as well as by a lowering in the bubble nucleation rate.

Series #3 glasses are characterized by power law, exponential and mixed power law–exponential bubble size distributions (Figs. 3c and 4c). Exponential distributions first were not found in series #2 and second appear at different P_f in series #3 samples. We interpret this type of BSD to reflect the pre-dominant influence of bubble growth, bubble nucleation playing a relatively minor role. Bubble coalescence would become more important in the case of mixed power law–exponential distributions.

We conclude that power law, exponential and mixed power law–exponential bubble size distributions are observed in all glass series, with the exception of the series #2 glasses which lack exponential BSDs.

6.2.5. *Fragmentation*

A process of magma fragmentation was observed in a total of three series #1 charges decompressed to 25 MPa P_f (Table 4). D19#1 was recovered entirely as a fine (< 500 µm) glass powder and S+D40#1 partially so. D12#1 yielded coarse (< 1.5 mm) glass fragments. Two other 25 MPa P_f series #1 charges were unfragmented but yielded strongly unusual textures (extruded foam for D24#1 and extruded dense block for D27#1). Capsule failure was observed systematically in the series #1 charges decompressed to 25 MPa, occurring in four out of the five charges performed under these conditions, despite capsules having lengths up to 5 cm to accommodate gas expansion during decompression. However, capsule failure and fragmentation are not always associated since the capsule of the fragmented D19#1 charge did not fail. When capsules failed, failures were systematically found around the melt cylinders and never in void spaces. Both fragmented and unfragmented charges contain a population of small bubbles (Table 4). Therefore, melt fragmentation in our experiments is intimately associated with the occurrence of the second event of bubble nucleation characterized for charge D24#1. Our experimental observations thus strengthen the proposal (Massol and Koyaguchi, 2005) that late nucleation of gas bubbles in the conduit triggers fragmentation. Although detailed discussion of the fragmentation mechanism is outside the scope of this paper, our observations (presence of small bubbles, capsule failures) are consistent with fragmentation being driven by high internal pressures inside the newly formed bubbles (Zhang, 1999; Massol and Koyaguchi, 2005).

6.3. Equilibrium vs. disequilibrium degassing

Chemical equilibrium is reached or approached in the H_2O-only melts (series #1). On the one hand, glasses decompressed to P_f = 200, 150, 100 and 25 MPa have H_2O concentrations in agreement with their respective solubilities, and thus follow an equilibrium degassing trend (Fig. 5a). On the other hand, deviation from equilibrium is encountered in glasses decompressed to P_f = 60 and 50 MPa (D22#1 and D5#1) which have H_2O concentrations in excess compared to their respective equilibrium solubilities (Fig. 6). H_2O supersaturations of the order of 0.2–0.35 wt.% absolute were found in these two glasses. This indicates the possibility of near- or slight non-equilibrium degassing in the H_2O-only melts, which would provide the driving force for the nucleation of the second bubble population observed at 25 MPa. However, and despite chemical equilibrium being approached, textural

equilibrium is not attained in the series #1 melts which have vesicularities lower than expected from equilibrium degassing (Fig. 2a). This demonstrates that, in order to achieve chemical equilibrium, H_2O can be lost diffusively from the melts during decompression, either toward the gas-melt capsule interface, as suggested by the H_2O distribution profiles measured in D22#1 and D5#1 charges (Fig. 6), or toward the gas bubbles present inside the glass cylinder.

In contrast, disequilibrium degassing occurs systematically in the CO_2-bearing melts (series #2 and #3). CO_2 is retained within these melts at elevated concentration levels (Fig. 5b, c). In parallel, H_2O is lost in significant amounts, especially in series #2 glasses. The combination of high melt CO_2 concentrations and significant H_2O losses generates a disequilibrium degassing trend. Such a deviation from a closed-system equilibrium decompression trend was previously observed in the experiments of Pichavant et al. (2013) and Le Gall and Pichavant (2015a). For series #2, glass CO_2 concentrations are weakly negatively correlated with vesicularities and positively correlated with *BND*s. As discussed by Pichavant et al. (2013) and Le Gall and Pichavant (2015a), equilibrium degassing in CO_2-bearing melts need both numerous and large bubbles, i.e. high vesicularities, which is the case neither in our series #2 nor in our series #3 post-decompression glasses.

6.4. Effect of decompression rate on degassing mechanisms

Previous experiments on hydrated rhyolites and phonolites (Mangan and Sisson, 2000; Mourtada-Bonnefoi and Laporte, 2004; Iacono-Marziano et al., 2007; Cluzel et al., 2008) have demonstrated strong variations in bubble number density, bubble size and vesicularity with decompression rates, as anticipated on the basis of numerical simulations (Toramaru, 1995, 2006). In line with these observations, below we compare our experimental products with those from the experiments of Le Gall and Pichavant (2015a) performed at a higher decompression rate of 78 kPa/s (or 3 m/s), under the same conditions and on similar compositions than in our three glass series. For the series #2 glasses, we extend the comparison with the experimental products from the experiments of Pichavant et al. (2013) performed at lower decompression rates (17 and 27 kPa/s, or 0.64 and 1.03 m/s) under similar conditions and compositions.

First, a positive correlation between bubble number density and decompression rate (dP/dt) is generally observed. For a given P_f, the experiments decompressed the most rapidly have the highest *BND*s. This is illustrated in particular by the data for the series #2 glasses (Fig. 7a). Note that for this series the data points for the two slowest decompression rates (17 and 27 kPa/s) are for 1150°C experiments, whereas experiments for the two fastest decompression rates (39 and 78 kPa/s) are performed at 1200°C. For the series #1 glasses, a negative trend appears for P_f = 150 MPa. For the series #3 glasses, the correlation between *BND* and dP/dt is either neutral or slightly positive. The general positive correlation found in this study is consistent with previous results on rhyolitic systems (e.g. Mourtada-Bonnefoi and Laporte, 2004; Cluzel et al., 2008). However, our experimental results show more variability. For a given decompression rate, no stationary *BND* value is reached and *BND* depends in a complex way on P_f (Fig. 2c; Le Gall and Pichavant, 2015a). This is because *BND* values in basaltic melts do not reflect only the nucleation step but rather the combination between nucleation and growth (coalescence) processes. In addition, in our CO_2-bearing basaltic melts nucleation occurs as a continuous process over a wide P_f range. Two distinct bubble nucleation events were also identified in our CO_2-free melts which implies a *BND* variation as a function of P_f. Application of *BND*s to infer magma ascent rates (Toramaru, 2006) needs caution in the case of basaltic melts.

Average bubble diameters for the three glass series show little variations with dP/dt > 25 kPa/s. The 25 MPa P_f data points have D slightly negatively correlated with dP/dt whereas the trends for the 50 MPa P_f range from negative to slightly positive. Note that the 39 kPa/s 25 MPa P_f series #1 charge is the one with two populations of bubbles of markedly different sizes. Below 25 MPa P_f, significant variations in bubble diameters are observed for the series #2 compositions at 1150°C (Fig. 7b). This is interpreted to reflect the predominant role of bubble growth since bubble growth and maybe coalescence would be favored by lowering dP/dt (e.g. Mangan and Sisson, 2000). Vesicularities for series #2 glasses are constant or generally slightly decrease with decreasing dP/dt (Fig. 7c). These variations reflect the combined influences of the bubble diameter (whose increase below 25 kPa/s contributes to a vesicularity increase) and of the *BND* (whose decrease with decreasing dP/dt contributes to lowering the number of bubbles).

Previous work in rhyolitic systems has suggested a very small effect of decompression rate on nucleation pressure (Mourtada-Bonnefoi and Laporte, 2004; Cluzel et al., 2008). In our experiments on basaltic compositions, a significant difference in nucleation pressure is

found in the case of our series #2 glasses. ΔP_{HoN} is lower (≤ 50 MPa, this study) at 39 than at 78 (< 100 MPa, Le Gall and Pichavant, 2015a) kPa/s. This difference in nucleation pressure cannot be attributed to heterogeneous bubble nucleation since D1#2 (Table 3) was examined by SEM. It is possible that the higher ΔP_{HoN} measured at 78 kPa/s results from a higher glass CO_2 concentration (901 ± 104 ppm, Le Gall and Pichavant, 2015a) than in D1#2 (818 ± 111 ppm, Table 3). For our CO_2-free series #1 glasses, bubble nucleation occurs at 150 MPa for both decompression rates (ΔP_{HoN} << 50 MPa). Nevertheless, the 39 kPa/s 150 MPa P_f sample has a higher *BND* and a lower average bubble diameter (8 µm, Table 3) than the equivalent sample decompressed at 78 kPa/s (28 µm, Le Gall and Pichavant, 2015a). These observations would be consistent with bubbles nucleating slightly earlier along the decompression ramp at 78 than at 39 kPa/s.

7. Volcanological implications

7.1. Comparison between experimental and Strombolian textural parameters

Despite the fact that our experimental products do not simulate the last stages of degassing near the surface and post-fragmentation processes, the comparison of bubble textures in our H_2O-CO_2-bearing melts decompressed at 39 kPa/s (or 1.5 m/s, series #2 from this study) and in Strombolian explosive samples can provide insights on degassing processes occurring in the Stromboli volcanic conduit. The comparison focuses on pumices from paroxysmal explosive activity, as well as on scoriae from normal explosive activity (Polacci et al., 2006, 2009) although it is clear that the two systems correspond to two contrasted degassing regimes. At P_f = 25 MPa (i.e. at the pressure corresponding to the shallower depth in our experiments), the series #2 charges show a narrow range of bubble sizes ranging from 21–24 µm to 175–179 µm (Table 3). For comparison, the pumice samples have a similar minimum bubble size (21–23 µm) but a larger maximum bubble size around 1 mm (Polacci et al., 2009). From our results, the smaller bubbles would result from a mechanism of continuous nucleation. The absence of bubbles < 10 µm in pumices suggests that nucleation ended before magma fragmentation. The large bubble sizes in pumices would result from a combination of growth and coalescence processes in the conduit. These large bubbles have spherical to subspherical shapes. Coalescence is limited during paroxysmal activity as shown by the lack of connected bubbles in both our series #2 melts and in pumice samples. In

contrast, connected bubbles occur in scoriae in the form of large coalescing bubbles from 0.5 up to 1.2 mm (Polacci et al., 2009).

The series #2 glasses have vesicularities which extend up to 13.8%, i.e. well below the vesicularities measured in Strombolian eruptive products. For comparison, vesicularities of pumices range from 47 to 67% (Polacci et al., 2006; Fig. 2a) and those of scoriae range between 24 and 78% (Polacci et al., 2006, 2008, 2009). Nevertheless, because a rapid vesicularity increase is observed between 50 and 25 MPa P_f, it is reasonable to expect that vesicularities typical of Strombolian explosive products can be attained by extrapolating the data to $P_f << 25$ MPa, i.e. by postulating a fragmentation level shallower than ~1 km.

Strombolian pumices have bubble number densities (6–9.10^2 mm^{-3}, Polacci et al., 2009; Fig. 2c) higher by 0.5 order of magnitude than the series #2 melts at 25 MPa P_f (up to 2.10^2 mm^{-3}, Fig. 2c). Nevertheless, the *BND*s measured in series #2 are in the same range as the *BND*s measured in scoriae (1–4.6.10^2 mm^{-3}, Polacci et al., 2009). It is reminded here that the bubble nucleation process is continuous in our series #2 melts and that CO_2-supersaturated melt compositions are obtained at 25 MPa P_f. This suggests the possibility that additional bubble nucleation can take place below 25 MPa, which would result in experimental *BND* becoming closer to the range found in pumices.

BSDs in both our series #2 melts and pumice samples (Fig. 4b) can be fitted by mixed power law–exponential distribution, with power law exponents of 1.51 and 1.96 (this study) and up to 1.4 (Polacci et al., 2009). In contrast, the BSDs of scoriae follow power law trends with exponents of 1 ± 0.2 (Bai et al., 2008; Polacci et al., 2009). From our results, the mixed power law–exponential distributions found in Strombolian pumices would be indicative of a system where growth and coalescence are superimposed on a continuous bubble nucleation mechanism, as the system evolves toward equilibrium (compare with Polacci et al., 2009). The power law distributions found in scoriae would also result from a combination of continuous bubble nucleation and coalescence, in agreement with previous interpretation (Polacci et al., 2009). The decrease in the power law exponent between pumices and scoriae reflects the pre-dominant influence of coalescence in the latter than in the former.

Series #2 melts decompressed between 200 and 25 MPa have CO_2 and H_2O concentrations both in the range of Stromboli embayments and melt inclusions data (Fig. 8). Series #2 melts from this study and decompressed at a faster rate (Le Gall and Pichavant,

2015a) overlap. The agreement between the experimental and analytical data strongly suggests that the natural Stromboli degassing trend is simulated (Pichavant et al., 2013).

We conclude that our decompression experiments on series #2 melts either reproduce or approach certain critical aspects of the natural textures (*BND*s, bubble sizes, shapes and distributions) and chemistries (residual volatile concentrations) of Stromboli explosive basaltic eruptions. The main differences between experimental and natural products concern the maximum bubble sizes and the vesicularities (both lower in the experiments), but the range of natural characteristics is expected to be approached in experiments at P_f below 25 MPa.

7.2. Implications for the dynamics of magma ascent at Stromboli volcano

Timescales of magma ascent at Stromboli are poorly constrained yet this is a critical point for volcanic risk mitigation. On the one hand, slow geophysically derived ascent rates (3 mm/s, Calvari et al., 2011) have been proposed. On the other hand, the petrologic constraints lead to ascent rates for volatile-rich magmas at the origin of paroxysms (Bertagnini et al., 2003, Métrich et al., 2005) that are much shorter of the order of minutes to hours (< 10 h). In this context, Polacci et al. (2009) used the experimental data of Baker et al. (2006) and Bai et al. (2008) to suggest time constraints of the order to minutes to hours to evolve from power law to mixed power law–exponential bubble size distributions. In our experiments, such a transition was observed to take place at a minimum pressure of 50 MPa both for a decompression rate of 1.5 (this study) and 3 m/s (Le Gall and Pichavant, 2015a). This implies that timescales of 32 (3 m/s) to 64 (1.5 m/s) minutes maximum would be needed to start producing mixed power law–exponential BSDs. These texturally based constraints are in the lower range of timescales estimated from petrological studies.

Additional constraints are provided by the *BND* data (Fig. 7a). The range of natural *BND*s in Strombolian pumices is bracketed by experiments from this study, Le Gall and Pichavant (2015a) and Pichavant et al. (2013). In detail, the 3 m/s experiments on series #2 melts produce *BND*s that exceed the natural values. Note, however, that the associated bubble sizes are far too small compared to pumices. Taking 3 m/s as an upper range of ascent rates, timescales of 43 min for “golden” pumice magma to ascend from their source region at 7–8 km depth to the surface are obtained. The 1.5 m/s experiments do not yield *BND*s as the

natural values, but higher *BND*s are expected below 25 MPa P_f. Therefore, an 1.5 m/s ascent rate also seems plausible, corresponding to a timescale of 86 min for "golden" pumice magma ascent. The 1 m/s experiments produce *BND*s very close to the natural range both at 25 and 50 MPa P_f. From this decompression rate and below, we begin to observe a decrease of *BND* with decreasing P_f, interpreted to reflect the pre-dominant influence of bubble growth. Below 1 m/s (0.64 m/s), experimental *BND*s are lower than natural values. Both the 1 and 0.64 m/s 25 MPa P_f samples are characterized by equilibrium degassing, implying that the driving force for increasing *BND*s has been lost. We therefore propose 1 m/s as the lower end of the range of ascent rates at Stromboli, corresponding to ascent timescales of 128 min.

8. Conclusions

We have performed high pressure and temperature (1200°C) experiments to simulate the ascent and degassing of H_2O- and H_2O-CO_2-bearing basaltic melts from 200 to 25 MPa, at a decompression rate of 1.5 m/s. Pre-decompression melts with three volatile compositions were investigated: pure H_2O (series #1), H_2O/CO_2 (series #2) and H_2O poor/CO_2 (series #3). Experimental products were characterized texturally and chemically and compared with natural products from Stromboli. The main conclusions are the following:

(1) Bubbles begin to form homogeneously for supersaturation pressures (ΔP_{HoN}) ≤ 50 MPa in the three series.

(2) For series #1 melts, the mechanism of bubble nucleation is discontinuous taking place in two narrow P_f intervals (200–150 MPa and 50–25 MPa) and leading to two distinct bubble nucleation events.

(3) For the CO_2-bearing melts, the mechanism of bubble nucleation is continuous and takes place over a substantial P_f interval along the decompression path. This leads to multiple bubble nucleation events.

(4) Post-nucleation mechanisms, including growth and coalescence, lead to larger bubble sizes and vesicularities, and lower *BND*s. Bubble coalescence is the most strongly marked between 100 and 50 MPa P_f.

(5) Bubble size distributions in experimental products yield power law, exponential and mixed power law–exponential patterns. Differences in BSD between melt series and P_f reflect to different extents the influence of bubble nucleation, growth and coalescence.

(6) Melt fragmentation occurred in a total of three H_2O-rich charges decompressed to 25 MPa P_f and is intimately associated with the occurrence of the second event of bubble nucleation.

(7) The series #1 melts degas at equilibrium until 100 MPa P_f and show slight supersaturations at 60 and 50 MPa P_f. Disequilibrium degassing is systematic in the CO_2-bearing melts which are highly CO_2-supersaturated. The trend of CO_2-rich and H_2O-poor melts recorded in Stromboli natural glasses is reproduced upon decompression of series #2 melts.

(8) Series #2 decompression textures (*BND*s, bubble sizes, shapes and distributions) and chemistries (residual volatile concentrations) approach certain critical characteristics of the natural products from Stromboli.

(9) Average bubble sizes, BSD and *BND* data are combined to constrain the timescales of "golden" pumice magma ascent from their source region. Results range from 43 to 128 min, which emphasizes the short time spans of signals precursory to paroxysms at Stromboli.

Appendix

Surface tensions (σ) have been calculated from our supersaturation pressures (ΔP_{HoN}) and nucleation rates (J) computed from our measured bubble number densities and decompression timescales, using the expression of the critical degree of supersaturation ΔP_{HoN} given by e.g. Hurwitz and Navon (1994), Mourtada-Bonnefoi and Laporte (2002). To do this, the parameter J_0 which is given by (e.g. Mourtada-Bonnefoi and Laporte, 2004):

$$J_0 = \frac{(2\Omega_L n_0^2 D)}{a_0 \left(\frac{\sigma}{kT}\right)^{1/2}} \text{ (Eq. 2)},$$

where Ω_L is the volume of water molecules in the liquid ($\Omega_L = 3.10^{-29}$ m^3), n_0 is the number of water molecules per unit volume of liquid, a_0 is the mean distance between water molecules ($a_0 \approx n_0^{-1/3}$) and D is the water diffusivity in the liquid, has been estimated. D is taken from the equation of Zhang and Ni (2010) which takes into consideration the effects of H_2O content and temperature. n_0 is defined as $6.02 \times 10^{23} X_m \rho_{liq}/m$, where 6.02×10^{23} is the Avogadro number, X_m is the mass fraction of molecular water in the liquid, ρ_{liq} is the liquid density (2650 kg/m^3), and m is the molar mass of water (0.018 kg/mol). Ω_L and X_m parameters are poorly constrained in basalt melts and we have used the values given by Mourtada-Bonnefoi and Laporte (2004), determined for rhyolitic liquids. Checks were performed to evaluate their influence on the calculated results and found to be small (< 0.001 N.m^{-1}). In the same way, the choice of the D equation leads to very small (< 0.001 N.m^{-1}) differences in σ.

References

Abràmoff, M.D., Magalhães, P.J., and Ram, S.J. (2004) Image processing with ImageJ. Biophotonics international, 11, 36–43.

Aiuppa, A., Bertagnini, A., Métrich, N., Moretti, R., Di Muro, A., Liuzzo, M., and Tamburello, G. (2010a) A model of degassing for Stromboli volcano. Earth and Planetary Science Letters, 295, 195–204 (DOI:10.1016/j.epsl.2010.03.040).

Aiuppa, A., Burton, M., Caltabiano, T., Giudice, G., Guerrieri, S., Liuzzo, M., Murè, F., and Salerno, G. (2010b) Unusually large magmatic CO_2 gas emissions prior to a basaltic paroxysm: CO_2 gas emissions prior to a paroxysm. Geophysical Research Letters, 37, L17303 (DOI:10.1029/2010GL043837).

Aiuppa, A., Burton, M., Allard, P., Caltabiano, T., Giudice, G., Gurrieri, S., Liuzzo, M., and Salerno, G. (2011) First observational evidence for the CO_2-driven origin of Stromboli's major explosions. Solid Earth, 2, 135–142 (DOI:10.5194/se-2-135-2011).

Aiuppa, A., Federico, C., Giudice, G., Giuffrida, G., Guida, R., Gurrieri, S., Liuzzo, M., Moretti, R., and Papale, P. (2009) The 2007 eruption of Stromboli volcano: Insights from real-time measurement of the volcanic gas plume CO_2/SO_2 ratio. Journal of Volcanology and Geothermal Research, 182, 221–230 (DOI:10.1016/j.jvolgeores.2008.09.013).

Allard, P. (2010) A CO_2-rich gas trigger of explosive paroxysms at Stromboli basaltic volcano, Italy. Journal of Volcanology and Geothermal Research, 189, 363–374 (DOI:10.1016/j.jvolgeores.2009.11.018).

Bai, L., Baker, D.R., and Rivers, M. (2008) Experimental study of bubble growth in Stromboli basalt melts at 1 atm. Earth and Planetary Science Letters, 267, 533–547 (DOI:10.1016/j.epsl.2007.11.063).

Baker, D.R., Lang, P., Robert, G., Bergevin, J.-F., Allard, E., and Bai, L. (2006) Bubble growth in slightly supersaturated albite melt at constant pressure. Geochimica et cosmochimica acta, 70, 1821–1838.

Barberi, F., Rosi, M., and Sodi, A. (1993) Volcanic hazard assessment at Stromboli based on review of historical data. Acta Vulcanologica, 3, 173–187.

Bertagnini, A., Roberto, A., and Pompilio, M. (2011) Paroxysmal activity at Stromboli: lessons from the past. Bulletin of Volcanology, 73, 1229–1243 (DOI:10.1007/s00445-011-0470-3).

Bertagnini, A., Métrich, N., Landi, P., and Rosi, M. (2003) Stromboli volcano (Aeolian Archipelago, Italy): An open window on the deep-feeding system of a steady state basaltic volcano. Journal of Geophysical Research, 108 (B7), 2336 (DOI:10.1029/2002JB002146).

Bertagnini, A., Métrich, N., Francalanci, L., Landi, P., Tommasini, S., and Conticelli, S. (2008) Volcanology and magma geochemistry of the present-day activity: constraints on the feeding system. In: Calvari, S., Inguaggiato, S., Puglisi, G., Ripepe, M., Rosi, M. (Eds.) Learning from Stromboli. American Geophysical Union, Washington, Geophysical Monograph, 182, 19–38.

Blower, J.D., Keating, J.P., Mader, H.M., and Phillips, J.C. (2001) Inferring volcanic degassing processes from vesicle size distributions. Geophysical Research Letters, 28, 347–350.

Blower, J.D., Keating, J.P., Mader, H.M., and Phillips, J.C. (2002) The evolution of bubble size distributions in volcanic eruptions. Journal of Volcanology and Geothermal Research, 120, 1–23.

Bottinga, Y., and Javoy, M. (1990) MORB degassing: Bubble growth and ascent. Chemical Geology, 81, 255–270.

Bourgue, E., and Richet, P. (2001) The effects of dissolved CO_2 on the density and viscosity of silicate melts: a preliminary study. Earth and Planetary Science Letters, 193, 57–68.

Burgisser, A., Alletti, M., and Scaillet, B. (2015) Simulating the behavior of volatiles belonging to the C–O–H–S system in silicate melts under magmatic conditions with the software D-Compress. Computers & Geosciences, 79, 1–14.

Burton, M., Allard, P., Mure, F., and La Spina, A. (2007) Magmatic Gas Composition Reveals the Source Depth of Slug-Driven Strombolian Explosive Activity. Science, 317, 227–230 (DOI:10.1126/science.1141900).

Calvari, S., Spampinato, L., Bonaccorso, A., Oppenheimer, C., Rivalta, E., and Boschi, E. (2011) Lava effusion–A slow fuse for paroxysms at Stromboli volcano? Earth and Planetary Science

Letters, 301, 317–323.
Cashman, K.V., and Sparks, R.S.J. (2013). How volcanoes work: A 25 year perspective. Geological Society of America Bulletin, 125, 664–690.
Castro, J.M., Burgisser, A., Schipper, C.I., and Mancini, S. (2012) Mechanisms of bubble coalescence in silicic magmas. Bulletin of volcanology, 74, 2339–2352.
Cluzel, N., Laporte, D., Provost, A., and Kannewischer, I. (2008) Kinetics of heterogeneous bubble nucleation in rhyolitic melts: implications for the number density of bubbles in volcanic conduits and for pumice textures. Contributions to Mineralogy and Petrology, 156, 745–763 (DOI:10.1007/s00410-008-0313-1).
Di Carlo, I., Pichavant, M., Rotolo, S.G., and Scaillet, B. (2006). Experimental Crystallization of a High-K Arc Basalt: the Golden Pumice, Stromboli Volcano (Italy). Journal of Petrology, 47, 1317–1343 (DOI:10.1093/petrology/egl011).
Dixon, J.E., and Pan, V. (1995) Determination of the molar absorptivity of dissolved carbonate in basanitic glass. American Mineralogist, 80, 1339–1342.
Dixon, J.E., Stolper, E.M., and Holloway, J.R. (1995). An experimental study of water and carbon dioxide solubilities in mid-ocean ridge basaltic liquids. Part I: calibration and solubility models. Journal of Petrology, 36, 1607–1631.
Edmonds, M. (2008) New geochemical insights into volcanic degassing. Philosophical Transactions of the Royal Society A: Mathematical, Physical and Engineering Sciences, 366, 4559–4579 (DOI:10.1098/rsta.2008.0185).
Francalanci, L., Manetti, P., and Peccerillo, A. (1989) Volcanological and magmatological evolution of Stromboli volcano (Aeolian Islands): the roles of fractional crystallization, magma mixing, crustal contamination and source heterogeneity. Bulletin of Volcanology, 51, 355–378.
Francalanci, L., Tommasini, S., and Conticelli, S. (2004) The volcanic activity of Stromboli in the 1906–1998 AD period: mineralogical, geochemical and isotope data relevant to the understanding of the plumbing system. Journal of Volcanology and Geothermal Research, 131, 179–211 (DOI:10.1016/S0377-0273(03)00362-7).
Francalanci, L., Taylor, S.R., McCulloch, M.T., and Woodhead, J.D. (1993) Geochemical and isotopic variations in the calc-alkaline rocks of Aeolian arc, southern Tyrrhenian Sea, Italy: constraints on magma genesis. Contributions to Mineralogy and Petrology, 113, 300–313.
Gaonac'h, H., Stix, J., and Lovejoy, S. (1996) Scaling effects on vesicle shape, size and heterogeneity of lavas from Mount Etna. Journal of Volcanology and Geothermal Research, 74, 131–153.
Gardner, J.E., and Ketcham, R.A. (2011) Bubble nucleation in rhyolite and dacite melts: temperature dependence of surface tension. Contributions to Mineralogy and Petrology, 162, 929–943 (DOI:10.1007/s00410-011-0632-5).
Gonnermann, H., and Manga, M. (2005) Nonequilibrium magma degassing: Results from modeling of the ca. 1340 A.D. eruption of Mono Craters, California. Earth and Planetary Science Letters, 238, 1–16 (DOI:10.1016/j.epsl.2005.07.021).
Gonnermann, H.M., and Manga, M. (2007) The fluid mechanics inside a volcano. Annual Review of Fluid Mechanics, 39, 321–356.
Iacono-Marziano, G., Schmidt, B.C., and Dolfi, D. (2007) Equilibrium and disequilibrium degassing of a phonolitic melt (Vesuvius AD 79 "white pumice") simulated by decompression experiments. Journal of Volcanology and Geothermal Research, 161, 151–164 (DOI:10.1016/j.jvolgeores.2006.12.001).
Iacono-Marziano, G., Morizet, Y., Le Trong, E., and Gaillard, F. (2012) New experimental data and semi-empirical parameterization of H_2O–CO_2 solubility in mafic melts. Geochimica et Cosmochimica Acta, 97, 1–23 (DOI:10.1016/j.gca.2012.08.035).
Khitarov, N.I., Lebedev, E.B., Dorfman, A.M., Bagdasarov, N.S., 1979. Effect of temperature, pressure and volatiles on the surface tension of molten basalt. Geochemistry International 16, 78–86.
La Spina, A., Burton, M.R., Harig, R., Mure, F., Rusch, P., Jordan, M., and Caltabiano, T. (2013) New insights into volcanic processes at Stromboli from Cerberus, a remote-controlled open-path FTIR scanner system. Journal of Volcanology and Geothermal Research, 249, 66–76.
Le Gall, N., and Pichavant, M. (2015a, to be submitted) Homogeneous bubble nucleation in H_2O- and H_2O-CO_2-bearing basaltic melts: results of high temperature decompression experiments.

Le Gall, N., and Pichavant, M. (2015b, to be submitted) Heterogeneous bubble nucleation on Fe–Ti oxides in H_2O- and H_2O-CO_2-bearing basaltic melts.

Landi, P., Métrich, N., Bertagnini, A., and Rosi, M. (2004) Dynamics of magma mixing and degassing recorded in plagioclase at Stromboli (Aeolian Archipelago, Italy). Contributions to Mineralogy and Petrology, 147, 213–227 (DOI:10.1007/s00410-004-0555-5).

Lange, R.A. (1994) The effect of H_2O, CO_2, and F on the density and viscosity of silicate melts. In Mineralogical Society of America Reviews in Mineralogy, 30, 331–369.

Lautze, N.C., and Houghton, B.F. (2007) Linking variable explosion style and magma textures during 2002 at Stromboli volcano, Italy. Bulletin of Volcanology, 69, 445–460.

Lensky, N.G., Niebo, R.W., Holloway, J.R., Lyakhovsky, V., and Navon, O. (2006) Bubble nucleation as a trigger for xenolith entrapment in mantle melts. Earth and Planetary Science Letters, 245, 278–288.

Lesne, P., Scaillet, B., Pichavant, M., and Beny, J.-M. (2011a). The carbon dioxide solubility in alkali basalts: an experimental study. Contributions to Mineralogy and Petrology, 162, 153–168.

Lesne, P., Scaillet, B., Pichavant, M., Iacono-Marziano, G., and Beny, J.-M. (2011b) The H_2O solubility of alkali basaltic melts: an experimental study. Contributions to Mineralogy and Petrology, 162, 133–151.

Lyakhovsky, V., Hurwitz, S., and Navon, O. (1996) Bubble growth in rhyolitic melts: experimental and numerical investigation. Bulletin of Volcanology, 58,19–32.

Mangan, M.T., and Cashman, K.V. (1996) The structure of basaltic scoria and reticulite and inferences for vesiculation, foam formation, and fragmentation in lava fountains. Journal of Volcanology and Geothermal Research, 73, 1–18.

Mangan, M., and Sisson, T. (2000) Delayed, disequilibrium degassing in rhyolite magma: decompression experiments and implications for explosive volcanism. Earth and Planetary Science Letters, 183, 441–455.

Mangan, M., and Sisson, T. (2005) Evolution of melt-vapor surface tension in silicic volcanic systems: Experiments with hydrous melts. Journal of Geophysical Research, 110, B01202.

Martel, C., and Iacono-Marziano, G. (2015) Timescales of bubble coalescence, outgassing, and foam collapse in decompressed rhyolitic melts. Earth and Planetary Science Letters, 412, 173–185.

Massol, H., and Koyaguchi, T. (2005) The effect of magma flow on nucleation of gas bubbles in a volcanic conduit. Journal of volcanology and geothermal research, 143, 69–88.

Mercalli, G. (1907) Vulcani attivi della Terra. Ulrico Hoepli.

Métrich, N., Bertagnini, A., and Di Muro, A. (2010) Conditions of magma storage, degassing and ascent at Stromboli: new insights into the volcano plumbing system with inferences on the eruptive dynamics. Journal of Petrology, 51, 603–626.

Métrich, N., Bertagnini, A., Landi, P., and Rosi, M. (2001) Crystallization driven by decompression and water loss at Stromboli volcano (Aeolian Islands, Italy). Journal of Petrology, 42, 1471–1490.

Métrich, N., Allard, P., Spilliaert, N., Andronico, D., and Burton, M. (2004) 2001 flank eruption of the alkali-and volatile-rich primitive basalt responsible for Mount Etna's evolution in the last three decades. Earth and Planetary Science Letters, 228, 1–17.

Métrich, N., Bertagnini, A., Landi, P., Rosi, M., and Belhadj, O. (2005) Triggering mechanism at the origin of paroxysms at Stromboli (Aeolian Archipelago, Italy): the 5 April 2003 eruption. Geophysical Research Letters, 32, L103056 (DOI:10.1029).

Misiti, V., Vetere, F., Mangiacapra, A., Behrens, H., Cavallo, A., Scarlato, P., and Dingwell, D.B. (2009) Viscosity of high-K basalt from the 5th April 2003 Stromboli paroxysmal explosion. Chemical Geology, 260, 278–285.

Mourtada-Bonnefoi, C.C., and Laporte, D. (2002) Homogeneous bubble nucleation in rhyolitic magmas: an experimental study of the effect of H_2O and CO_2. Journal of Geophysical Research, 107, ECV 2-1–EVC 2-19 (DOI:10.1029/2001JB000290).

Mourtada-Bonnefoi, C.C., and Laporte, D. (2004) Kinetics of bubble nucleation in a rhyolitic melt: an experimental study of the effect of ascent rate. Earth and Planetary Science Letters, 218, 521–537.

Newman, S., and Lowenstern, J.B. (2002) VolatileCalc: a silicate melt–H_2O–CO_2 solution model written in Visual Basic for Excel. Computers & Geosciences, 28, 597–604.

Papale, P., Moretti, R., and Barbato, D. (2006) The compositional dependence of the saturation surface of H_2O+CO_2 fluids in silicate melts. Chemical Geology, 229, 78–95.

Pichavant, M., Pompilio, M., D'Oriano, C., and Di Carlo, I. (2011) Petrography, mineralogy and geochemistry of a primitive pumice from Stromboli: implications for the deep feeding system. European Journal of Mineralogy, 23, 499–517.

Pichavant, M., Di Carlo, I., Le Gac, Y., Rotolo, S.G., and Scaillet, B. (2009) Experimental constraints on the deep magma feeding system at Stromboli volcano, Italy. Journal of Petrology, 50, 601–624.

Pichavant, M., Di Carlo, I., Rotolo, S.G., Scaillet, B., Burgisser, A., Le Gall, N., and Martel, C., 2013. Generation of CO_2-rich melts during basalt magma ascent and degassing. Contributions to Mineralogy and Petrology, 166, 545–561.

Polacci, M., Baker, D.R., Bai, L., and Mancini, L. (2008) Large vesicles record pathways of degassing at basaltic volcanoes. Bulletin of Volcanology, 70, 1023–1029.

Polacci, M., Baker, D.R., Mancini, L., Tromba, G., and Zanini, F. (2006) Three-dimensional investigation of volcanic textures by X-ray microtomography and implications for conduit processes. Geophysical Research Letters, 33, L13312 (DOI:10.1029/2006GL026241).

Polacci, M., Baker, D.R., Mancini, L., Favretto, S., and Hill, R.J. (2009) Vesiculation in magmas from Stromboli and implications for normal Strombolian activity and paroxysmal explosions in basaltic systems. Journal of Geophysical Research, 114, B01206 (DOI:10.1029/2008JB005672).

Proussevitch, A.A., Sahagian, D.L., and Tsentalovich, E.P. (2007) Statistical analysis of bubble and crystal size distributions: Formulations and procedures. Journal of Volcanology and Geothermal Research, 164, 95–111.

Richet, P., Whittington, A., Holtz, F., Behrens, H., Ohlhorst, S., and Wilke, M. (2000) Water and the density of silicate glasses. Contributions to Mineralogy and Petrology, 138, 337–347.

Ripepe, M., and Harris, A.J. (2008) Dynamics of the 5 April 2003 explosive paroxysm observed at Stromboli by a near-vent thermal, seismic and infrasonic array. Geophysical Research Letters, 35, L07306 (DOI:10.1029/2007GL032533).

Rosi, M., Bertagnini, A., and Landi, P. (2000) Onset of the persistent activity at Stromboli volcano (Italy). Bulletin of Volcanology, 62, 294–300.

Rosi, M., Pistolesi, M., Bertagnini, A., Landi, P., Pompilio, M., and Di Roberto, A. (2013) Stromboli volcano, Aeolian Islands (Italy): present eruptive activity and hazards. Geological Society, London, Memoirs 37, 473–490.

Scaillet, B., Pichavant, M., Roux, J., Humbert, G., and Lefèvre, A. (1992) Improvements of the Shaw membrane technique for measurement and control of fH_2 at high temperatures and pressures. American Mineralogist, 77, 647–655.

Shishkina, T.A., Botcharnikov, R.E., Holtz, F., Almeev, R.R., and Portnyagin, M.V. (2010) Solubility of H_2O-and CO_2-bearing fluids in tholeiitic basalts at pressures up to 500MPa. Chemical Geology, 277, 115–125.

Sparks, R.S.J. (2003) Dynamics of magma degassing. Geological Society, London, Special Publications, 213, 5–22.

Taylor, J.R., Wall, V.J., and Pownceby, M.I. (1992) The calibration and application of accurate redox sensors. American Mineralogist, 77, 284–295.

Toramaru, A. (1995) Numerical study of nucleation and growth of bubbles in viscous magmas. Journal of Geophysical Research, 100, 1913–1931.

Toramaru, A. (2006) BND (bubble number density) decompression rate meter for explosive volcanic eruptions. Journal of Volcanology and Geothermal Research, 154, 303–316.

Vetere, F., Behrens, H., Misiti, V., Ventura, G., Holtz, F., De Rosa, R., and Deubener, J. (2007) The viscosity of shoshonitic melts (Vulcanello Peninsula, Aeolian Islands, Italy): insight on the magma ascent in dikes. Chemical Geology, 245, 89–102.

Woods, A.W., and Koyaguchi, T. (1994) Transitions between explosive and effusive eruptions of silicic magmas. Nature 370, 641–644.

Zhang, Y. (1999) A criterion for the fragmentation of bubbly magma based on brittle failure theory. Nature, 402, 648–650.

Zhang, Y., and Ni, H. (2010) Diffusion of H, C, and O components in silicate melts. Reviews in Mineralogy and Geochemistry, 72, 171–225.

Figure captions

Figure 1. Representative types of textures of post-decompression glass samples. (a) Tomographic slice of sample D3#1 decompressed to $P_f = P_{in}$ = 200 MPa, showing a bubble-free core and a thin (< 50 µm) bubbly rim indicated by black arrows. (b) Tomographic slice of sample D24#3 decompressed to 25 MPa P_f, showing three distinct zones: (1) a thick (150–200 µm) bubbly rim indicated by a black arrow, (2) a bubble-free zone depleted in volatiles delimited by a double black arrow and (3) a core with numerous homogeneously distributed bubbles. (c) Tomographic slice of sample D24#1 decompressed to 25 MPa P_f, characterized by two distinct bubble populations. The inset gives a close-up view of the small bubbles which correspond to the first bubble population. See Table 3 for details about the experimental conditions and textural results.

Figure 2. (a) Vesicularity *V*, (b) average bubble diameter *D* and (c) bubble number density per unit volume of melt BND_{melt} plotted as a function of final pressure P_f for the post-decompression glasses of this study. Experimental data in Tables 3. The three glass series are distinguished, series #1: black circles; series #2; gray circles; series #3: white circles. The series #1 charge D8#1 is plotted with a different symbol (black diamond) since it started from a pre-decompression melt with a H_2O concentration ~50% lower than all the other series #1 charges. In (a), equilibrium vesicularities (thick black and gray lines) calculated for pure H_2O and CO_2 degassing respectively (see text) are shown for comparison with the experimental data. Both the first and the second bubble populations of sample D24#1 (Table 3) are plotted in (b) and (c). The *V*, *D* and BND_{melt} values for Strombolian pumices (data from Polacci et al., 2006, 2009) are shown for comparison with the experimental data points.

Figure 3. Evolution of the bubble size distribution (BSD) during decompression within each glass series. (a) Series #1, (b) series #2, (c) series #3 post-decompression glasses. For each glass series, two post-decompression glass samples are detailed, one representative of the early and the other of the late stage of the nucleation process. Note that for series #1 glasses, the D24#1 charge is also detailed. For each post-decompression glass sample, histograms show frequencies (normalized to 100%) of diameters of individual bubbles in the population (or the two populations for charge D24#1) using size classes of 10 µm each. In (b), the power law BSD curve represents a fit to the data for charge D1#2 in order to illustrate an example of power law distribution. The average bubble diameter of the populations is given in Table 3. Details about experimental conditions and other textural data in Table 3.

Figure 4. Bubble size distributions (BSD) expressed as log-log plots of bubble number density (BND_{melt}, in mm^{-3}) vs. bubble volume for all post-decompression glasses from this study. For each glass sample, the bubble population is characterized by a range of bubble size (expressed as diameters in Table 3) and a bubble number density value (Table 3). Each point along the distribution curve corresponds to the number of bubbles with a volume strictly larger than indicated. (a) Series #1 glasses, (b) series #2

glasses and (c) series #3 glasses. Rectangles: glasses decompressed to 150 MPa P_f (final pressure); triangles: glasses decompressed to 100 MPa P_f; crosses; glass decompressed to 60 MPa P_f; squares: glasses decompressed to 50 MPa P_f; diamonds: glasses decompressed to 25 MPa P_f. The inset in (a) shows the bubble size distributions of the two bubble populations in charge D24#1. The gray continuous lines are power law fits and the gray continuous curves are exponential fits, both regressed with Excel software. α is the power law exponent. The bubble volume distribution (black continuous line and curve) of a pumice sample from Polacci et al. (2009, Str50403 from a paroxysmal explosion at Stromboli) is given in (b) for comparison with the experimental BSDs.

Figure 5. H_2O and CO_2 concentrations in pre- and post-decompression glasses. (a) Plot of series #1 H_2O concentrations as a function of final pressure P_f. H_2O solubilities are computed using the Lesne et al. (2011b) regression equation. They define the closed-system equilibrium decompression path (black continuous line). H_2O vs. CO_2 concentrations in series #2 and #3 glasses are shown in (b) and (c) respectively. Circles: pre-decompression glasses synthesized at 200 MPa P_{in} (initial pressure); crosses: glasses decompressed to 200 MPa P_f (final pressure); rectangles: glasses decompressed to 150 MPa P_f; triangles: glasses decompressed to 100 MPa P_f; squares: glasses decompressed to 50 MPa P_f; diamonds: glasses decompressed to 25 MPa P_f. In (b) the symbol color refers to the synthesis experiments, either S3 (black), S6 (gray) or S4 (white, Table 2). Error bars (standard deviations, Table 5) are indicated on the data points. The thin continuous lines are fluid-melt equilibrium saturation isobars (25–250 MPa) and the dashed curves are equilibrium decompression paths calculated for some series #2 and series #3 glasses assuming closed-system behavior. Equilibrium fluid-melt calculations were performed with VolatileCalc (Newman and Lowenstern, 2002).

Figure 6. FTIR profiles of H_2O concentrations from the sample edge toward the core of the cylinder for series #1 glasses decompressed to different P_f from 150 to 25 MPa (note that the 25 MPa data points are for the D8#1 charge performed with a low H_2O concentration pre-decompression melt). Average H_2O concentration data are given in Table 5. H_2O solubilities (at pressures of 150–25 MPa, dashed horizontal lines) come from Lesne et al. (2011b).

Figure 7. (a) Bubble number density per unit volume of melt BND_{melt}, (b) average bubble diameter D and (c) vesicularity V plotted as a function of decompression rate for the series #2 glasses. Textural data from this study (dP/dt = 39 kPa/s, Table 3) are compared with data from Le Gall and Pichavant (2015a, dP/dt = 78 kPa/s) and from Pichavant et al. (2013, dP/dt = 17 and 27 kPa/s). The BND, D and V values for Strombolian pumices (data come from Polacci et al., 2006, 2009) are shown for comparison. The gray continuous lines are P_f isobars drawn for P_f = 100, 50 and 25 MPa.

Figure 8. H_2O and CO_2 contents in natural glasses from Stromboli (data from Métrich et al., 2010) and comparison with experimental series #2 glasses from this study (39 kPa/s,

Table 5) and from Le Gall and Pichavant (2015a, 78 kPa/s). Stromboli glasses plotted include melt inclusions (MI) and embayments (Emb.) from pumices and scoriae. Experimental glasses include pre- (circles) and post-decompression glasses (squares). The closed system equilibrium degassing trend (dashed curve) is calculated using VolatileCalc (Newman and Lowenstern, 2002).

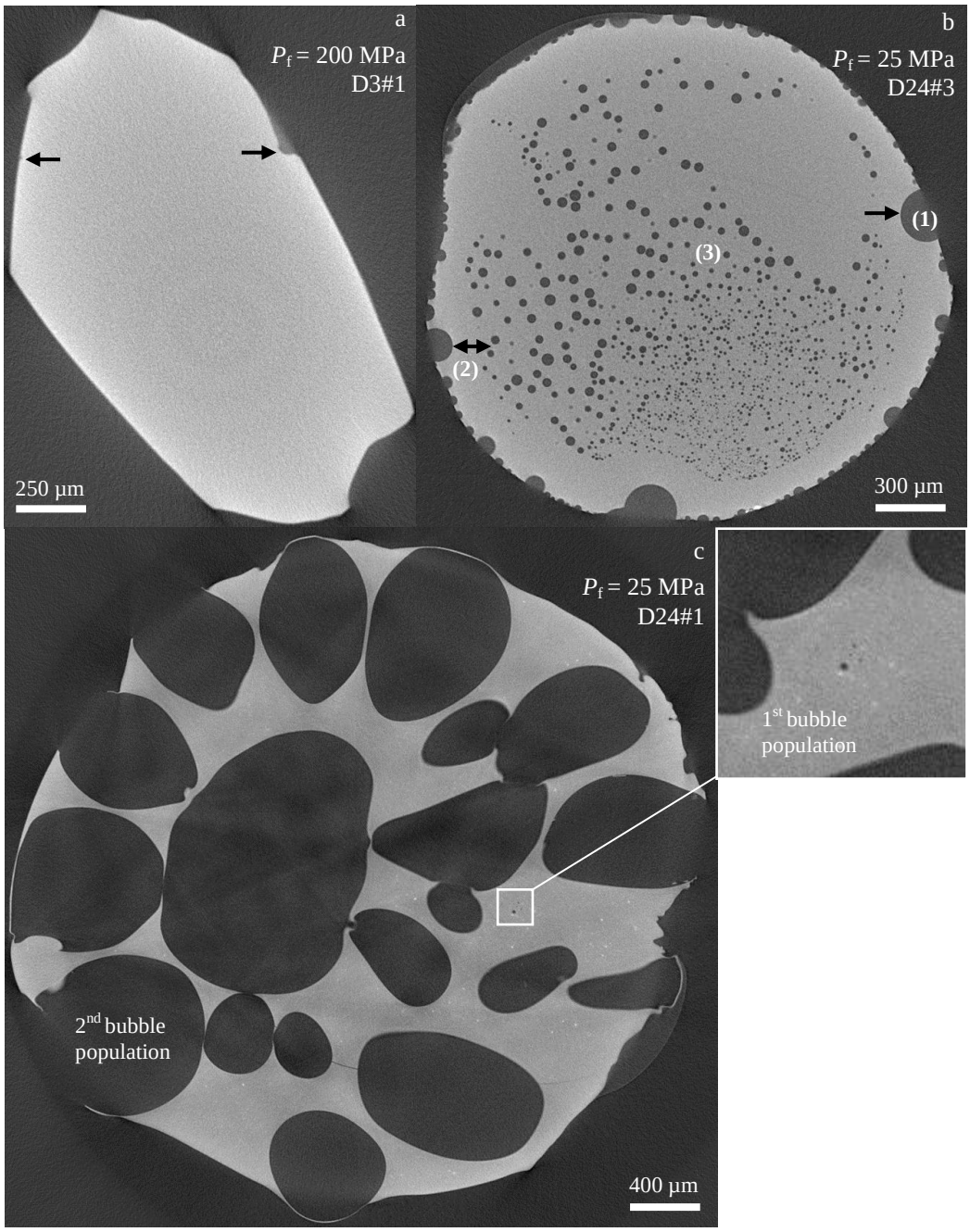

Le Gall and Pichavant. Fig. 1

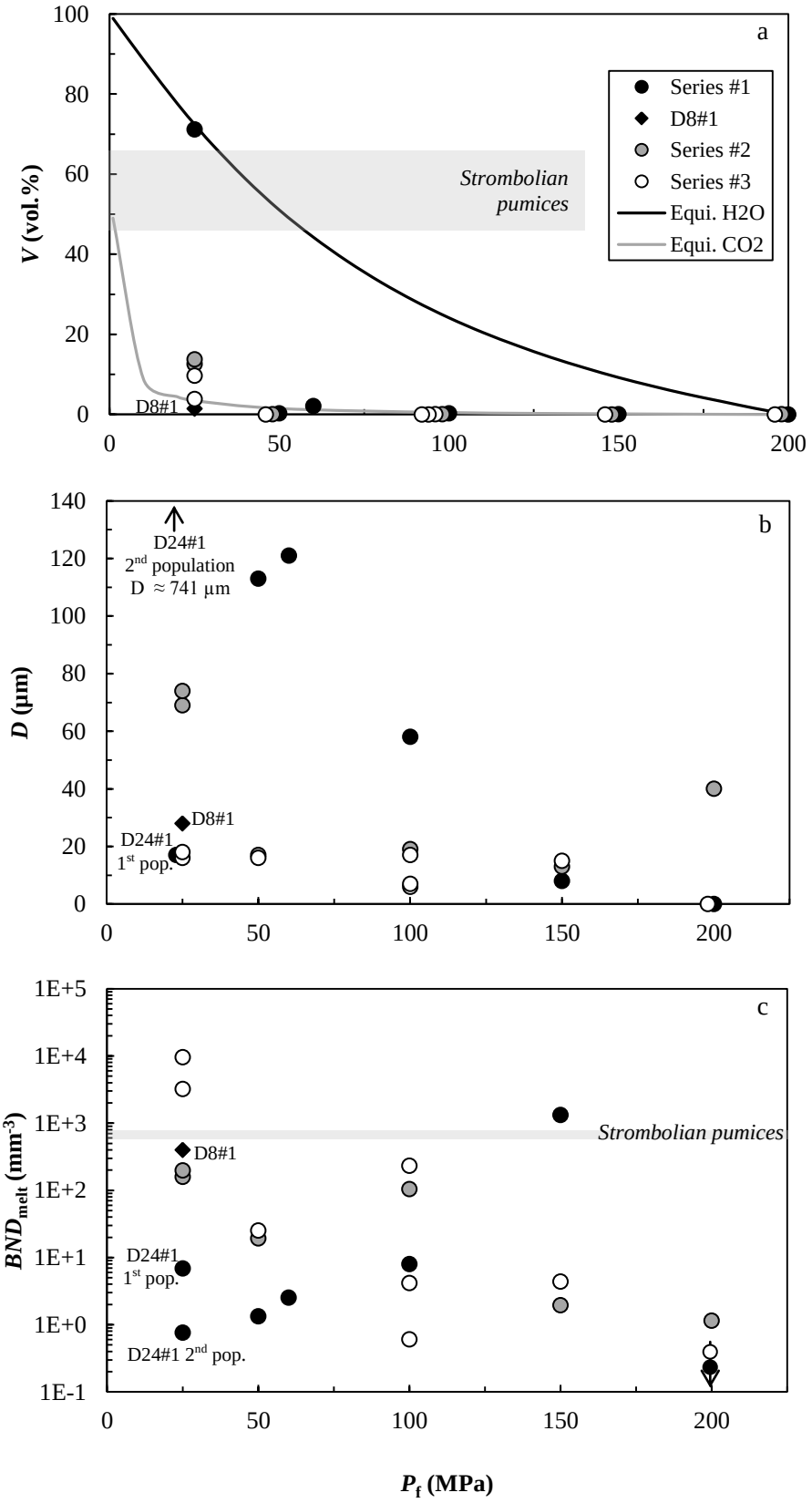

Le Gall and Pichavant. Fig. 2

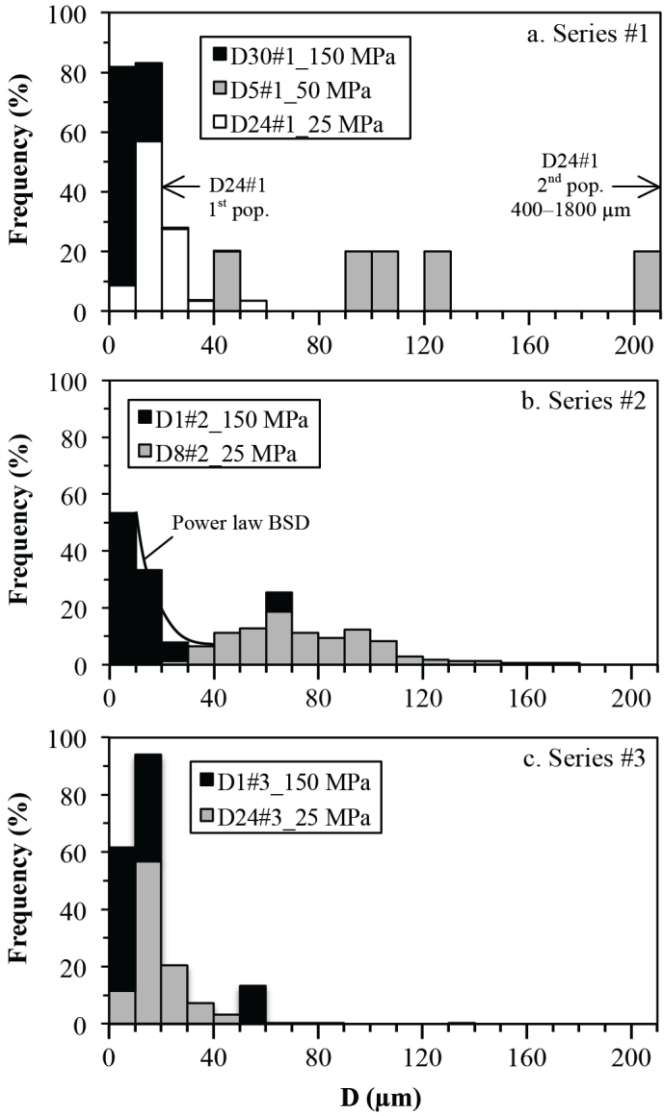

Le Gall and Pichavant. Fig. 3

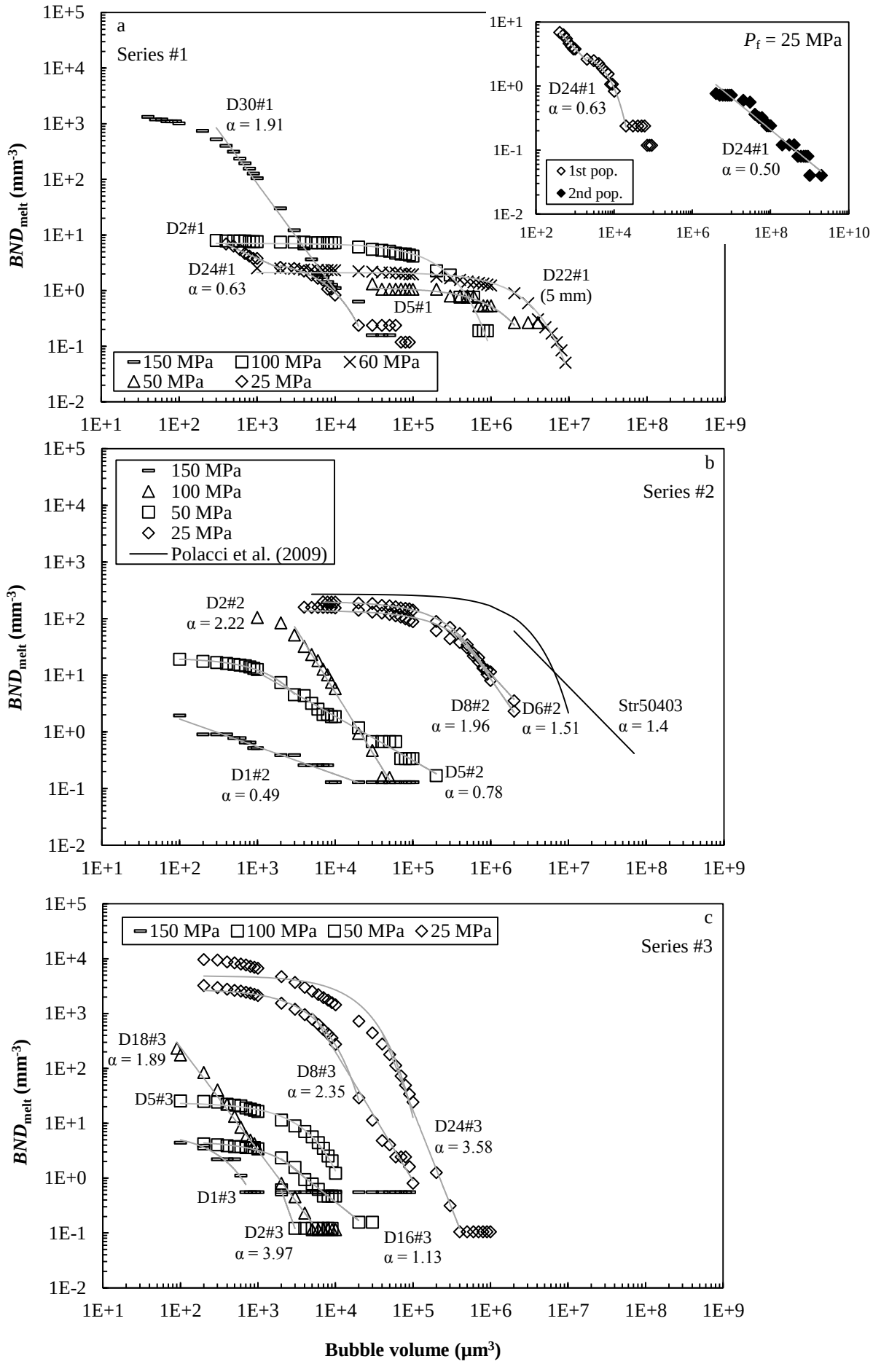

Le Gall and Pichavant. Fig. 4

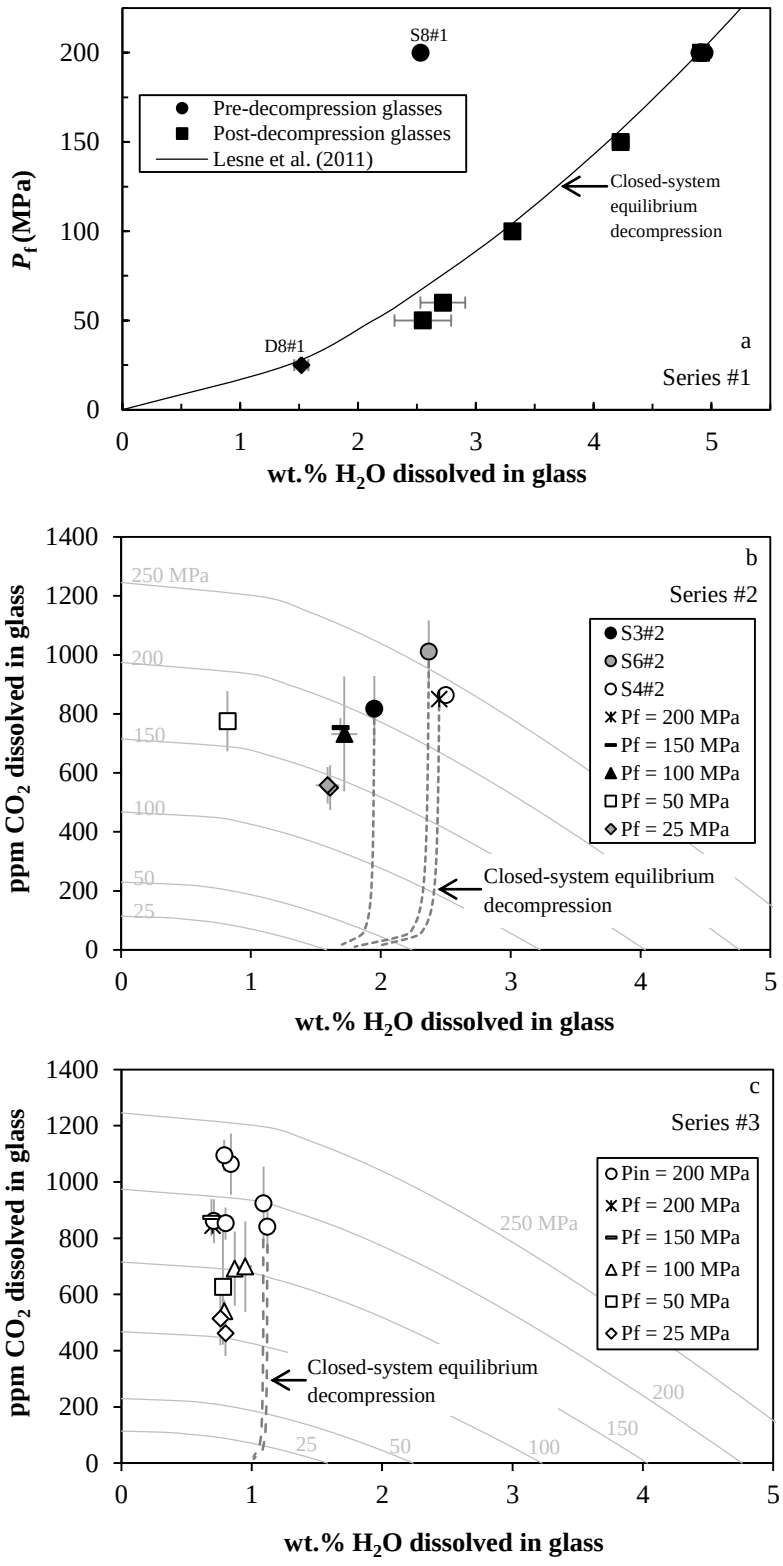

Le Gall and Pichavant. Fig. 5

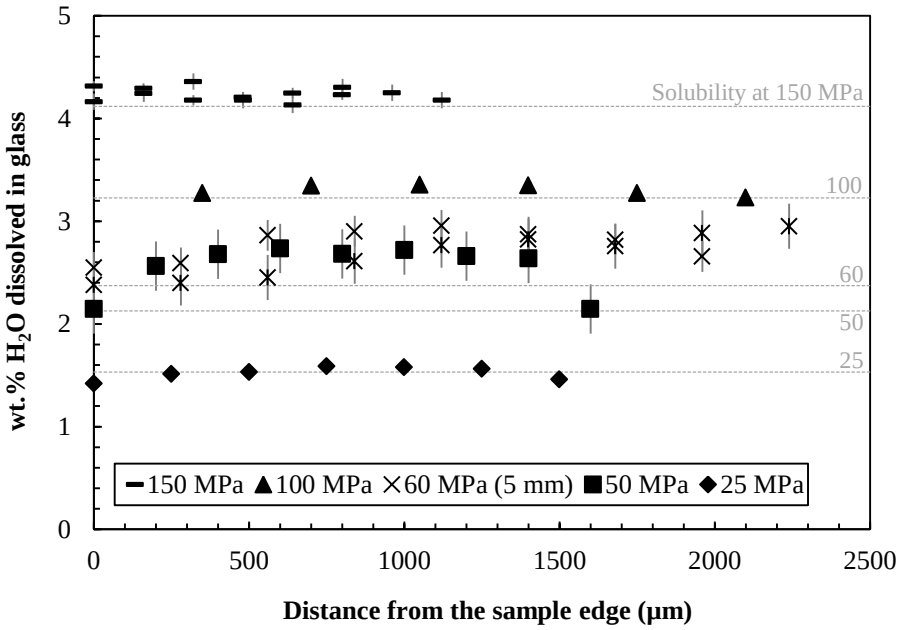

Le Gall and Pichavant. Fig. 6

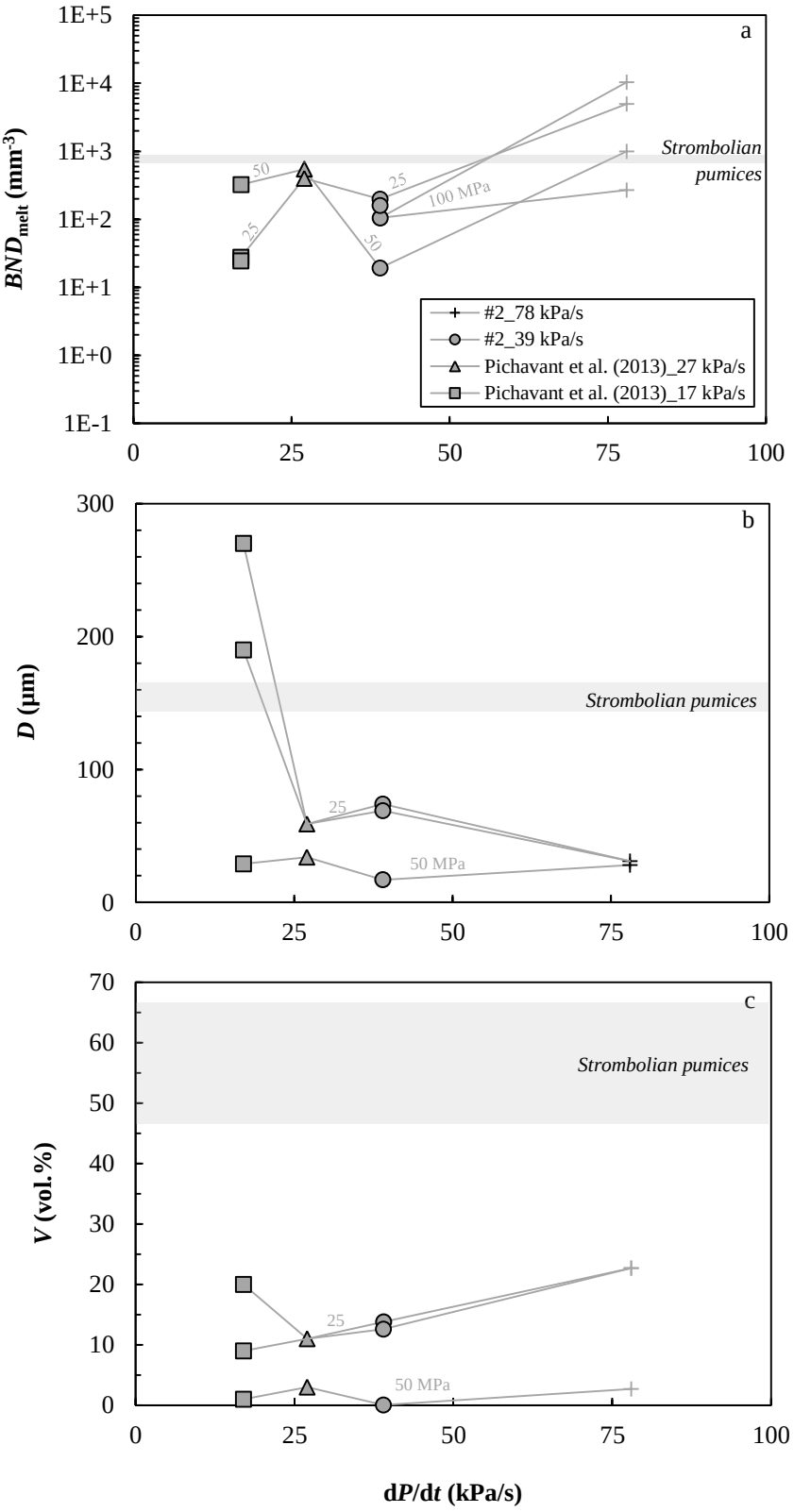

Le Gall and Pichavant. Fig. 7

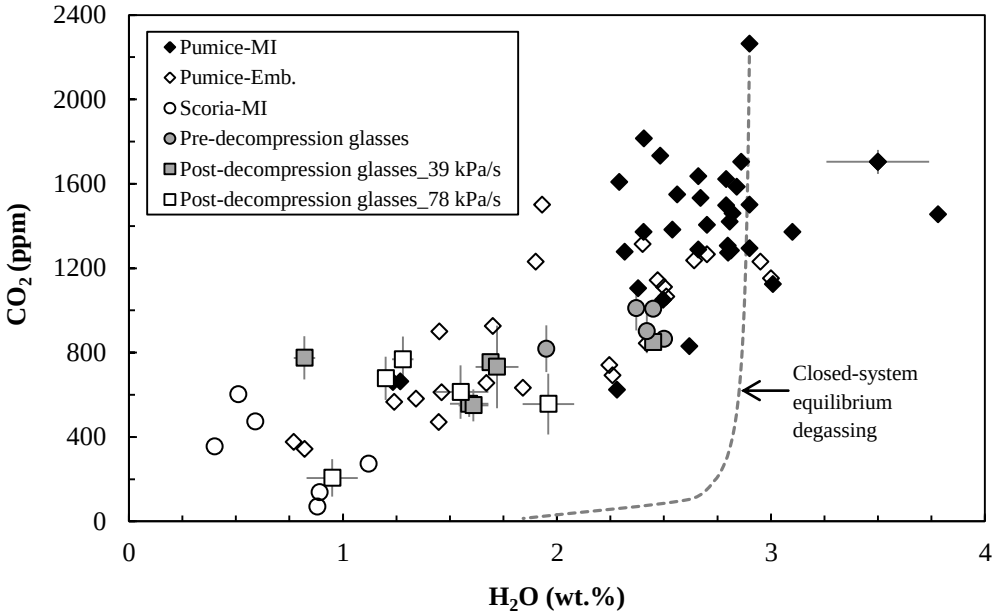

Le Gall and Pichavant. Fig. 8

Table 1. Composition of PST-9 golden pumice and starting glass

Label	PST-9[a]	Glass[b] (*n* = 54)
SiO_2	49.4	50.9 (3)[c]
TiO_2	0.79	0.81 (8)
Al_2O_3	15.75	15.99 (28)
Fe_2O_3	1.3	nd
FeO	6.5	7.7 (6)[d]
MnO	0.15	0.16 (8)
MgO	7.96	7.21 (41)
CaO	12.73	12.34 (24)
Na_2O	2.27	2.39 (9)
K_2O	1.85	1.90 (12)
P_2O_5	0.43	0.55 (17)
Cr_2O_3	–	0.03 (4)
NiO	–	0.05 (6)
Total	99.1	97.4 (10)

Oxides are in wt.%.

[a] Whole-rock analysis performed at CRPG, Nancy, France (from Di Carlo et al., 2006).

[b] Electron microprobe analysis (normalized to 100%) of PST-9 glass (from Le Gall and Pichavant, 2015a), *n*: number of analyses.

[c] One standard deviation in terms of last digit.

[d] Total Fe as FeO.

nd: not determined.

Table 2. Synthesis experiments

Run	XH_2O_{in}	*T* (°C)	*P* (MPa)	*t* (min)	H_2O glass (wt.%)	CO_2 glass (ppm)
Volatile: H_2O (#1)						
S3#1	1	1200	202.2	2793	4.91 (3)	0 (0)
S4#1	1	1200	203.1	2509	4.93 (5)	0 (0)
S5#1	1	1200	202.8	2985	4.94 (4)	0 (0)
S6#1	1	1200	202.2	2760	4.90 (1)	0 (0)
S8#1	1	1200	203.8	4198	2.53 (5)	0 (0)
S11#1	1	1200	202.1	2900	4.90 (3)	0 (0)
S14#1	1	1200	201.9	1465	4.91 (1)	0 (0)
S16#1	1	1200	201.8	2873	4.90 (2)	0 (0)
Volatile: H_2O+CO_2 (#2)						
S3#2	0.25	1200	202.2	2793	1.95 (1)	818 (111)
S4#2	0.55	1200	203.1	2509	*0.58 (1)	864 (17)
S6#2	0.56	1200	202.2	2760	2.37 (1)	1011 (106)
Volatile: H_2O+CO_2 (#3)						
S3#3	0	1200	202.2	2793	1.12 (1)	840 (92)
S4#3	0	1200	203.1	2509	0.71 (1)	860 (78)
S5#3	0	1200	202.8	2985	0.84 (4)	1063 (109)
S6#3	0	1200	202.2	2760	0.80 (3)	852 (57)
S8#3	0	1200	203.8	4198	0.79 (1)	1094 (56)
S13#3	0	1200	201.5	2878	1.09 (3)	923 (132)

S11 synthesis from Le Gall and Pichavant (2015b)
XH_2O_{in} = initial molar H_2O / (H_2O + CO_2) in the charge.
T: run temperature; *P*: run pressure; *t*: duration of the synthesis experiment.
*~ 2.50 wt.% H_2O (see text for explanations).

Table 3 Decompression experiments: run conditions and textural information

Sample	Starting glass	P_{in} (MPa)	P_f (MPa)	t_{ramp} (s)	$\lvert dP/dt \rvert$ (kPa/s)	Bubble 3D characteristics										
						n	pk. size (µm)	range (µm)	*D* (µm)	*BND*[a] (mm^{-3})	BND_{melt}[b] (mm^{-3})	*S* (µm)	*V*[c] (vol.%)	*V*[d] (vol.%)	$V_{Equi.\ H2O}$ (vol.%)	$V_{Equi.\ CO2}$ (vol.%)
Volatile: H_2O (#1)																
D3#1	S5#1	200	200	0	39	0	–	–	0	0.00	0.00	–	0.00	0.00	0.00	
D30#1	S16#1	200	150	1284	39	8350	6	4–46	8	1324	1325	56	0.06	0.05	9.22	
D2#1	S3#1	200	99.8	2568	39	42	29	9–120	58	7.97	7.98	310	0.14	0.28	24.1	
D22#1	S14#1	200	60	3649	39	149	–	15–266	121	2.51	2.52	456	0.45	2.10	44.3	
D5#1	S4#1	200	50	3840	39	5	–	40–200	113	1.33	1.33	564	0.17	0.31	51.0	
D8#1	S8#1	200	25	4488	39	567	27	7–73	28	397	400	84	0.64	1.45	72.5	
D19#1	S6#1	200	25	4488	39	nd	nd	nd	nd	nd	nd	nd	nd	nd	72.5	
D24#1[e]	S11#1	200	25	4488	39	58	10	9–56	17	6.89	6.89	326	0.00	71.2	72.5	
D24#1[f]	S11#1	200	25	4488	39	> 28	nd	400–1800	741	0.65	0.76	680	0.00	71.2	72.5	
Volatile: H_2O+CO_2 (#2)																
D3#2	S4#2	200	200	0	39	10	19	6–141	40	1.15	1.15	592	0.02	0.05	0.00	0.00
D1#2	S3#2	200	149.9	1284	39	15	6–7	6–60	13	1.95	1.95	497	0.00	0.01	9.22	0.17
D2#2	S3#2	200	99.8	2568	39	665	15	15–48	19	104	105	132	0.04	0.10	24.1	0.47
D5#2	S4#2	200	50	3840	39	114	15	6–73	17	19.2	19.2	232	0.01	0.04	51.0	1.48
D6#2	S6#2	200	25	4488	39	179	53	21–179	69	152	159	115	4.70	12.6	72.5	3.47
D8#2	S6#2	200	25	4488	39	171	61, 97	24–175	74	186	198	107	5.82	13.8	72.5	3.47
Volatile: H_2O+CO_2 (#3)																
D3#3	S4#3	200	200	0	39	0	–	–	0	0.00	0.00	–	0.00	0.00	0.00	0.00
D1#3	S3#3	200	149.9	1284	39	8	8	7–57	15	4.38	4.38	379	0.01	0.00	9.22	0.17
D2#3	S3#3	200	99.8	2568	39	5	5	5–8	6	0.60	0.60	734	0.00	0.04	24.1	0.47
D16#3	S6#3	200	100	2568	39	27	13	8–39	17	4.18	4.18	385	0.00	0.02	24.1	0.47
D18#3	S13#3	200	100	2568	39	2042	6	6–28	7	231	231	101	0.01	0.01	24.1	0.47
D5#3	S5#3	200	50	3840	39	270	13	7–31	16	25.1	25.1	212	0.01	0.01	51.0	1.48

D8#3	S8#3	200	25	4488	39	4029	9	7–59	16	3183	3220	42	1.15	3.87	72.5	3.47
D24#3	S13#3	200	25	4488	39	91765	12	8–135	18	9016	9549	29	5.59	9.25	72.5	3.47

P_{in} (initial pressure): pressure at the beginning of decompression ramp; P_f (final pressure): pressure at which the experiment was quenched; t_{ramp}: duration of the ramp; $|dP/dt|$: decompression rate ($=10^6(P_{in}-P_f)/(gdt_{ramp})$), with g = 9.81 m/s^2 and d = 2.65 kg/m^3.
nd: not determined
X-ray microtomographic data acquired on entire charges (except V^d).
n: number of bubbles counted in the analyzed volume.
pk. size: main peak diameter in bubble size distribution histograms.
range: total range of bubble diameters.
D: average bubble diameter.
[a] *BND*: bubble number density expressed in number of bubbles per mm^3 of the total sample (glass + bubbles).
[b] BND_{melt}: bubble number density per melt volume (without bubbles, following Proussevitch et al., 2007).
S: average spacing between bubbles calculated from BND_{melt} ($S = (3/4\pi BND_{melt})^{1/3}$; Lyakhovsky et al., 1996; Baker et al., 2006).
[c] *V*: vesicularity (volume fraction of bubbles, vol.%) measured from the total sample.
[d] *V*: vesicularity measured from representative sub-volumes.
[e] Textural data on the first bubble population of D24#1 charge.
[f] Textural data on the second bubble population of D24#1 charge.
$V_{Equi.H2O}$ and $V_{Equi.CO2}$: equilibrium vesicularities computed for the PST-9 composition considering the degassing of pure H_2O and pure CO_2, respectively (see text).

Table 4. Texture range of the 25 MPa P_f series #1 charges

Charge	PST-9 starting material	Capsule length (cm)	Capsule after experiment	Glass after experiment	Bubble texture	Interpretation capsule	Interpretation charge	Bubbles (vol.%)
D12#1	Cylinder	3.5	Swollen around sample, weight gain, perforated around sample	Large blocks inside and outside the capsule	Bubbles (< 2– > 100 µm)	Sample causes capsule failure	Coarsely fragmented	nd
D19#1	Cylinder	4	Unswollen, no weight change, unperforated	Glass powder inside the capsule	Bubbles (< 4 – > 200 µm)	No capsule failure	Finely fragmented	nd
D24#1	Cylinder	4	Entirely swollen, weight gain, perforated around sample	Foam leaked outside the capsule (3–4 mm diameter)	Highly vesicular	Sample causes capsule failure	Unfragmented	71.2
D27#1	Cylinder	5	Unswollen, weight ?, perforated around sample	Dense block flown outside the capsule	Bubbles (< 11 – 46 µm)	Sample causes capsule failure	Unfragmented	0.00
S+D40#1	Powder	4.5	Swollen around sample, weight gain	Foam and powder inside the capsule	Highly vesicular, slug	Sample causes capsule failure	Partially fragmented	High

Experimental conditions: T = 1200°C; P_{in} = 200 MPa; P_f = 25 MPa; t_{ramp} = 4488 s; $|dP/dt|$ = 39 kPa/s.
nd: not determined.

Table 5. FTIR data

Glass	n^a	Thickness (µm)	Absorbance 3530 cm^{-1}	H_2O (wt.%)	Absorbance 1515 cm^{-1}	CO_2 (ppm)
Synthesis experiments						
Volatile: H_2O (#1)						
S3#1	4	37 (2)[b]	1.697 (92)	4.91 (3)		
S4#1	4	38 (3)	1.776 (155)	4.93 (5)		
S5#1	5	22 (2)	1.038 (86)	4.94 (4)		
S6#1	5	37 (1)	1.707 (46)	4.90 (1)		
S8#1	8	21 (3)	0.512 (76)	2.53 (5)		
S14#1	10	31 (1)	1.437 (61)	4.91 (1)		
S16#1	7	31 (5)	1.429 (225)	4.90 (2)		
Volatile: H_2O+CO_2 (#2)						
S3#2	5	65 (7)	1.209 (142)	1.95 (1)	0.123 (28)	818 (111)
S4#2	7	161 (2)	0.913 (23)	*0.58 (1)	0.316 (5)	864 (17)
S6#2	5	31 (1)	0.698 (34)	2.37 (1)	0.070 (9)	1011 (106)
Volatile: H_2O+CO_2 (#3)						
S3#3	5	33 (4)	0.351 (45)	1.12 (1)	0.065 (8)	840 (92)
S4#3	5	149 (1)	1.022 (23)	0.71 (1)	0.289 (26)	860 (78)
S5#3	10	34 (3)	0.274 (38)	0.84 (4)	0.082 (15)	1063 (109)
S6#3	7	149 (1)	1.147 (48)	0.80 (3)	0.287 (18)	852 (57)
S8#3	8	128 (11)	0.975 (84)	0.79 (1)	0.317 (39)	1094 (56)
S13#3	8	111 (5)	1.168 (75)	1.09 (3)	0.129 (21)	923 (132)
Decompression experiments						
Volatile: H_2O (#1)						
D3#1	4	38 (6)	1.738 (276)	4.91 (2)		
D30#1	14	18 (3)	0.718 (121)	4.23 (7)		
D2#1	6	41 (4)	1.294 (136)	3.31 (5)		
D22#1	17	59 (6)	1.534 (130)	2.72 (19)		

D5#1	9	37 (5)	0.918 (179)	2.55 (24)		
D8#1	7	37 (2)	0.540 (43)	1.52 (6)		
Volatile: H_2O+CO_2 (#2)						
D3#2	3	89 (5)	2.084 (120)	2.45 (2)		
	3	49 (6)			0.094 (13)	850 (9)
D1#2	10	27 (13)	0.768 (214)	1.69 (3)		
	3	161 (0)			0.275 (12)	754 (32)
D2#2	4	28 (0)	0.467 (32)	1.72 (10)		
	7	151 (8)			0.251 (75)	732 (195)
D5#2	7	128 (0)	1.015 (56)	0.82 (5)	0.225 (30)	775 (102)
D6#2	6	57 (5)	0.883 (123)	1.59 (9)		
	6	191 (20)			0.240 (46)	558 (62)
D8#2	5	116 (0)	1.794 (74)	1.61 (7)	0.145 (20)	550 (76)
Volatile: H_2O+CO_2 (#3)						
D3#3	5	132 (13)	0.899 (87)	0.70 (1)		
	2	102 (8)			0.195 (23)	843 (28)
D1#3	6	122 (3)	0.812 (43)	0.69 (3)	0.241 (22)	873 (65)
D2#3	5	31 (4)	0.261 (41)	0.87 (2)	0.049 (15)	691 (132)
D16#3	9	207 (20)	1.586 (171)	0.79 (1)	0.251 (15)	540 (41)
D18#3	5	45 (8)	0.415 (73)	0.95 (5)	0.073 (26)	699 (161)
D5#3	6	160 (0)	1.209 (99)	0.78 (6)	0.227 (74)	626 (204)
D8#3	8	160 (0)	1.181 (45)	0.76 (3)	0.186 (34)	513 (94)
D24#3	12	98 (14)	0.765 (138)	0.80 (5)	0.103 (27)	461 (80)

[a] Number of analytical spots.

[b] One standard deviation in terms of the last digit.

*~ 2.50 wt.% H_2O (see text for explanations).

Chapitre v

Nucléation hétérogène des bulles dans les systèmes basalte-H_2O et basalte-H_2O-CO_2

Résumé

Dans ce chapitre, rédigé sous la forme d'un article, est présenté un ensemble d'expériences de décompression mené dans les systèmes basalte-H_2O et basalte-H_2O-CO_2. La présence d'oxydes Fe–Ti en proportions variables dans les charges expérimentales permet de tester le rôle de cette phase cristalline sur le processus de nucléation hétérogène des bulles dans les liquides basaltiques.

Les verres basaltiques issus du Stromboli (composition PST-9) ont été synthétisés à 1200°C et 200 MPa, sous des conditions "oxydantes" (NNO+2,3 à +4,3) et "intermédiaires" (NNO+0,9 à +1,7), produisant des verres saturés en H_2O (4,90% pds) et en H_2O-CO_2 (0,97–2,45% pds) avec différentes quantités d'oxydes Fe–Ti. Les verres ont ensuite été décomprimés jusqu'à 150–25 MPa avec des taux de 39 et 78 kPa/s (ou 1,5 et 3 m/s, respectivement), puis rapidement trempés.

Une association texturale entre les bulles et les oxydes Fe–Ti a été révélée par microtomographie par rayons X, et interprétée comme indiquant un processus de nucléation hétérogène des bulles sur les oxydes. Seuls les oxydes Fe–Ti apparaissent comme des sites de nucléation efficaces, alors que les cristaux silicatés (olivine, clinopyroxène) ne semblent avoir aucun rôle. Bien qu'un processus de nucléation hétérogène soit présent, une nucléation homogène des bulles intervient aussi dans les verres expérimentaux, et elle conduit à des pressions de sursaturation comparables dans les liquides hydratés (< 50 MPa) et dans ceux contenant de l'H_2O et du CO_2 (< 100 MPa). Dans les liquides pauvres en H_2O et riches en CO_2, ΔP_{HeN} (< 175 MPa, nucléation hétérogène) est supérieur à ΔP_{HoN} (< 50 MPa, nucléation homogène), ce qui implique que l'influence des oxydes Fe–Ti sur la nucléation des bulles est globalement mineure et décroit avec le rapport CO_2/H_2O de la bulle de gaz. Au cours de la décompression, l'équilibre chimique est atteint dans les liquides hydratés. Au contraire, les liquides contenant du CO_2 dégazent systématiquement hors équilibre, quelles que soient la présence et l'abondance des oxydes Fe–Ti. La densité numérique de cristaux d'oxydes n'influence ni le diamètre ni la densité numérique des bulles. Nos résultats tendent à démontrer que la nucléation hétérogène des bulles est d'importance limitée dans les liquides basaltiques communs, et que la nucléation des bulles pourrait être majoritairement homogène.

Heterogeneous bubble nucleation on Fe–Ti oxides in H_2O- and H_2O-CO_2-bearing basaltic melts

Nolwenn Le Gall[1, 2, 3] · **Michel Pichavant**[1, 2, 3]

[1] Université d'Orléans, ISTO, UMR 7327, 45071, Orléans, France
[2] CNRS/INSU, ISTO, UMR 7327, 45071, Orléans, France
[3] BRGM, ISTO, UMR 7327, BP 36009, 45060, Orléans, France

Abstract We have performed high pressure and temperature decompression experiments to evaluate the importance of heterogeneous bubble nucleation on Fe–Ti oxides in common basaltic melts. H_2O-saturated (4.90 wt.% H_2O, CO_2-free) and H_2O-CO_2-bearing (0.97–2.45 wt.% H_2O, 773–847 ppm CO_2) glasses were synthesized at 1200°C and 200 MPa, under "oxidizing" (NNO+2.3 to +4.3) and "intermediate" conditions (NNO+0.9 to +1.7). This resulted in bubble-free glasses containing different amounts of Ti-bearing magnetite crystals, which were then decompressed to a final pressure between 150 and 25 MPa, at a constant ascent rate of 1.5 or 3 m/s (39 and 78 kPa/s, respectively), and rapidly quenched. Examination of the run products by X-ray micro-CT reveals a preferential textural association between bubbles and Fe–Ti oxide crystals, interpreted to indicate heterogeneous bubble nucleation. This behavior is unique to Fe–Ti oxides, as silicate crystals (olivine, clinopyroxene) appear to show no preferential textural association with gas bubbles. Both heterogeneous and homogeneous nucleation occur together in experimental products. This leads to comparable supersaturation pressures (difference between saturation pressure and pressure at which heterogeneous and homogeneous nucleation are observed, ΔP_{HeN} and ΔP_{HoN} respectively) in H_2O-only melts (< 50 MPa), as well as in H_2O-CO_2-bearing melts (< 100 MPa). In the H_2O-poor, CO_2-bearing melts, ΔP_{HeN} (< 175 MPa) is higher than ΔP_{HoN} (< 50 MPa), suggesting that the role of Fe–Ti oxides on bubble nucleation decreases in magnitude with the CO_2/H_2O ratio of the gas phase. Chemical equilibrium is reached during decompression of the H_2O-only melts whereas disequilibrium degassing occurs systematically for the CO_2-bearing melts, irrespective of the presence and abundance of Fe–Ti oxides. The crystal number density influences neither the bubble diameter nor the bubble number density. Our results tend to demonstrate that in common basaltic melts heterogeneous bubble nucleation is limited and bubble nucleation is for the most part homogeneous.

Keywords Heterogeneous nucleation . Basalt . Degassing . Ti-magnetite . Volatiles

1. Introduction

Bubble formation in magmas starts with a nucleation process (Bottinga and Javoy, 1990) which is basically an energy exchange process (Mangan et al., 2004a). When the melt becomes supersaturated in volatiles (mainly H_2O and CO_2 in basalts), e.g. during decompression, a separate gas phase forms to maintain chemical equilibrium (Navon and Lyakhovsky, 1998). However, bubble nucleation is energetically costly and it can be either heterogeneous (e.g. Hurwitz and Navon, 1994; Gardner et al., 1999; Gardner and Denis, 2004; Mangan et al., 2004b; Gardner, 2007; Cluzel et al., 2008) or homogeneous (e.g. Mourtada-Bonnefoi and Laporte, 1999, 2002, 2004; Gardner and Ketcham, 2011). Heterogeneous bubble nucleation occurs in the presence of discontinuities in the melt, such as on crystals faces and at corners (Mangan et al., 2004a), while homogeneous bubble nucleation occurs spontaneously in a melt free of any heterogeneities. The energy needed for the formation of a bubble-melt interface (ΔF) depends on whether nucleation is heterogeneous or homogeneous (Massol and Koyaguchi, 2005). According to the classical theory of nucleation, in the case of homogeneous nucleation, this energy is (e.g. Hurwitz and Navon, 1994):

$$\Delta F = \frac{16\pi\sigma^3}{3\Delta P^2} \quad \text{(Eq. 1)}$$

where ΔF is the Helmholtz free energy required for the formation of a bubble-melt interface, σ is the surface tension between melt and bubble, and ΔP is the supersaturation pressure required for bubble nucleation.

In the case of heterogeneous nucleation, the activation energy for bubble nucleation on a crystal face is reduced by a factor ϕ and becomes (e.g. Hurwitz and Navon, 1994):

$$\Delta F = \frac{16\pi\sigma^3\phi}{3\Delta P^2} \quad \text{(Eq. 2)}$$

where ϕ is a geometric factor which depends on the wetting angle (θ) between the bubble and the crystal (Gardner and Denis, 2004; Cluzel et al., 2008):

$$\phi = \frac{(2 - \cos\theta)(1 + \cos\theta)^2}{4} \quad \text{(Eq. 3)}$$

The wetting angle (θ) is defined by the surface tensions of the bubble-crystal (σ_{BC}), bubble-melt (σ_{BM}) and crystal-melt (σ_{CM}) interfaces (e.g. Navon and Lyakhovsky, 1998):

$$\cos\theta = \frac{(\sigma_{BC} - \sigma_{CM})}{\sigma_{BM}} \quad \text{(Eq. 4)}$$

Since the surface tension of the bubble-crystal interface (σ_{BC}) is lower than that of the bubble-melt interface (σ_{BM}), bubbles can nucleate more easily when crystalline heterogeneities are present in the melt. The activation energy (ΔF) and, accordingly, the supersaturation pressure (ΔP) required for heterogeneous bubble nucleation would be reduced. This has been confirmed in previous decompression experiments (Hurwitz and Navon, 1994; Gardner et al., 1999; Gardner and Denis, 2004; Mangan et al., 2004b; Gardner, 2007; Cluzel et al., 2008) which have shown that, in magnetite-bearing rhyolitic and dacitic melts, the nucleation of H_2O bubbles is triggered at low ΔP < 5–35 MPa. For comparison, higher ΔP of 60–150 MPa (Mangan and Sisson, 2000, 2005; Mourtada-Bonnefoi and Laporte, 2004; Gardner and Ketcham, 2011) are needed for homogeneous nucleation to occur in rhyolitic and dacitic melts. Nevertheless, not all crystalline phases were found to facilitate bubble nucleation. Heterogeneous bubble nucleation takes place principally on Fe–Ti oxides, biotite, zircon and apatite, but was observed neither on plagioclase nor on quartz (Hurwitz and Navon, 1994; Mangan et al., 2004a, b). According to Hurwitz and Navon (1994), heterogeneous bubble nucleation mainly depends on surface tension (reflected in the wetting angle θ) as well as on crystal roughness (reflected in the geometric factor ϕ); the presence of corners facilitates nucleation (Sigsbee, 1969; Navon and Lyakhovsky, 1998).

In natural systems, crystals present in the magma are expected to serve as heterogeneous bubble nucleation sites. However, as stated above, not all crystals can be efficient sites for heterogeneous bubble nucleation. There are also examples where the proportion of crystals present in the magma is low. Therefore, the importance of heterogeneous bubble nucleation as a mechanism requires careful evaluation. Presently, no experimental study is available on heterogeneous bubble nucleation in basaltic melts.

Recent decompression experiments on basaltic melts have stressed the possibility of disequilibrium degassing when homogeneous bubble nucleation does not take place or is such

that bubbles cannot grow to sizes large enough (Pichavant et al., 2013; Le Gall and Pichavant, 2015a, b). Application of these experimental results to natural cases however requires that the influence of crystals on bubble nucleation in basaltic melts is known. Here, we report results of heterogeneous nucleation experiments performed in H_2O- and H_2O-CO_2-bearing basaltic melts. Run products were texturally and chemically characterized to assess whether the presence of Fe–Ti oxide crystals has an influence on bubble nucleation and more generally to evaluate the importance of heterogeneous bubble nucleation in basaltic magmas.

2. Experimental methods

The influence of crystals on heterogeneous bubble nucleation was assessed by performing decompression experiments on basaltic melts containing different amounts of Fe–Ti oxides. To do so, pre-decompression charges with different amounts of Fe–Ti oxides were synthesized. This was obtained by varying the fO_2 during synthesis. In this paper, synthesis experiments were performed under respectively "oxidizing" and "intermediate" conditions. This was obtained by varying the fH_2 in the synthesis experiment, as described below. Results from those experiments are completed by data from decompression experiments under "reducing" conditions from Le Gall and Pichavant (2015a, b).

2.1. Preparation of starting glasses

The starting materials for the decompression experiments were bubble-free volatile-bearing glasses prepared from a basaltic pumice from Stromboli volcano, Italy (PST-9 "golden" pumice, Di Carlo et al., 2006; Pichavant et al., 2009, 2011; Table 1). PST-9 is highly vesicular and poorly crystallized, consisting of 89 vol.% glass, 8 vol.% clinopyroxene, 1–2 vol.% olivine, 1–2 vol.% plagioclase phenocrysts plus minor amounts of Fe–Ti oxides (Di Carlo et al., 2006; Pichavant et al., 2011). No microlites are present (Pichavant et al., 2011). The pumice sample was hand crushed to a fine powder, and then fused at 1 atm, 1400°C in a Pt crucible for 3 hours, yielding a homogeneous glass whose composition was checked by electron microprobe (Table 1). The crystal- and bubble-free glass was then cored into cylinders (2.5 mm in diameter and about 10 mm long).

For the synthesis experiments (Table 2), the glass cylinders were loaded into $Au_{80}Pd_{20}$ capsules of up to 3.5 cm height, 2.5 mm inner diameter and 2.9 mm outer diameter. Such a metal composition was used to minimize iron loss from the sample (Di Carlo et al., 2006; Pichavant et al., 2009). Distilled water and carbon dioxide as silver oxalate ($Ag_2C_2O_4$) were added to generate volatile-bearing melts. Three volatile compositions were investigated by introducing different proportions of H_2O and CO_2 in the capsules, corresponding to XH_2O_{in} (molar H_2O / (H_2O + CO_2)) of 1 (series #1: only H_2O dissolved in glass, no CO_2 present), 0.55–0.57 (series #2: H_2O and CO_2 both dissolved in glass, high dissolved H_2O/CO_2) and 0 (series #3: H_2O and CO_2 both dissolved in glass, low dissolved H_2O/CO_2, see below for the origin of H_2O).

For the decompression experiments (Table 3), 3–4 mm long volatile-bearing glass cylinders from the synthesis experiments were fitted into $Au_{80}Pd_{20}$ capsules of identical inner (2.5 mm) and outer (2.9 mm) diameters but variable heights (1–4 cm) to accommodate gas expansion. Capsules were welded shut with no volatile added, resulting in low proportions of free fluid in the decompression charges.

These capsules were weighted before and after welding, and then placed in an oven to ensure that no water was lost.

2.2. Equipment

Experiments were conducted in a rapid-quench internally heated pressure vessel (IHPV) operated in a vertical position. To control the redox conditions, the IHPV was pressurized with either pure argon or gas mixtures made of Ar and H_2. When experiments were performed using pure Ar as the pressure medium (synthesis run S10, Table 2; decompression runs D12, D13, D14 and D15, Table 3), "oxidizing" redox conditions were imposed (NNO+2.3 to +4.3, see below) as a result of the low intrinsic fH_2 prevailing inside the vessel when pressurized with pure Ar. In contrast, one synthesis (run S11, Table 2) and two decompression experiments (runs D16 and D18, Table 3) were pressurized with Ar-H_2 mixtures, H_2 and Ar being loaded sequentially in the vessel (Scaillet et al., 1992). In those three experiments, a pressure of 1 bar H_2 was initially applied. Then, Ar was pumped into the vessel up to the pressure needed to attain the final target conditions, generating "intermediate" redox conditions (NNO+0.9 to +1.7, see below).

Pressure was measured using a Heise pressure gauge, precise to ± 20 bars. Up to four capsules were run simultaneously (one for each series# plus a sensor capsule in the synthesis experiments, see below). These were loaded in a sample holder made of alumina which was hanged by a thin Pt wire in the hot spot of a molybdenum furnace. Temperature was measured using two S-type thermocouples placed along the 2–3 cm hot spot zone and recorded continuously with a Eurotherm controller to ± 5°C. Temperature differences between the top and the bottom of the capsules were always less than 10°C. Experiments were ended by drop-quenching. The capsules instantly fall in the cold part of the vessel following the flowing of an electrical current through the Pt suspension wire. Quenching was nearly isobaric and occurred within a few seconds (~100°C.s^{-1}, Di Carlo et al., 2006).

2.3. Run procedure

Synthesis and decompression experiments were performed independently from each other, allowing a systematic characterization of the samples before decompression.

The synthesis experiments (Table 2) were performed at 200 MPa and 1200°C, corresponding to conditions above the PST-9 liquidus on the basis of previous phase equilibrium experiments (Di Carlo et al., 2006; Pichavant et al., 2009). Run durations were more than 40 hours to ensure attainment of equilibrium distribution of dissolved H_2O and CO_2 in the cores, according to previous experiments (Le Gall and Pichavant, 2015a, b) and in agreement with H_2O and CO_2 melt diffusion data (Zhang and Ni, 2010).

The decompression experiments were conducted at a constant temperature of 1200°C, from an initial pressure (P_{in}) of 200 MPa to final pressures (P_f) of 150, 100 and 25 MPa. All P_f were investigated for the "oxidizing" fO_2 (and its reference "reducing" counterpart), and only a P_f of 100 MPa for the "intermediate" fO_2. All runs began with an approximately one-hour dwell at 200 MPa, to re-equilibrate the pre-synthesized glass cylinders. Pressure was then dropped manually at the constant decompression rates of either 39 or 78 kPa/s, leading to decompression durations of 21–75 min. The corresponding ascent velocities (1.5 and 3 m/s, respectively, taking a rock density of 2.65 kg/m^3) are consistent with literature data for ascent of basaltic magmas (Vetere et al., 2007; Le Gall and Pichavant, 2015b).

In all experiments, charges were rapid-quenched immediately after attainment of the desired final pressure, to freeze the glass textures and chemistries.

After quenching, the charges were weighed to verify that no leaks occurred.

2.4. Control of redox conditions

Since redox conditions were varied by imposing different fH_2, each synthesis experiment (Table 2) included a separate Ni–NiPd sensor capsule to measure the experimental fH_2. This consisted of two pellets of NiPd metal mixtures (with different Ni/Pd ratio) plus NiO, placed in a Pt capsule together with excess H_2O (Taylor et al., 1992). The decompression experiments were performed without sensor capsules added since run times would be too short to equilibrate the NiPd alloy. The redox conditions imposed during synthesis are assumed to be kept unchanged during decompression.

After the synthesis experiment, the composition (mole fraction Ni, X_{Ni}) of the alloy phase was measured by electron microprobe, and the fO_2 of the sensor capsule determined (Taylor et al., 1992; Pownceby and O'Neill, 1994). The fH_2 of the experiment (since fH_2 is identical for all charges) is then calculated from the H_2O dissociation equilibrium, using the fO_2 of the sensor capsule, the dissociation constant of H_2O (K_w; Robie et al., 1979) and the fugacity of pure H_2O at 200 MPa and 1200°C ($fH_2O°$; Ferry and Baumgartner, 1987; Holloway, 1987; Papale, 1997; Di Carlo et al., 2006). The fO_2 of the different charges depends on their H_2O content, expressed as aH_2O (or fH_2O), and thus varies within charges for a given synthesis experiment. To determine the fO_2 of each charge, fH_2O was calculated from the dissolved H_2O contents of the synthesized melts (determined by IR spectroscopy), using the thermodynamic model for H_2O solution in multicomponent melts of Burnham (1979, see Di Carlo et al., 2006; Pichavant et al., 2009). Alloy compositions (X_{Ni}) and the fH_2 for each synthesis experiment are given in Table 2.

3. Analytical techniques

3.1. Sample preparation

After the synthesis experiment, the glass cylinder was divided into two parts, one to serve as starting material in the decompression experiments and the other to be analyzed for its volatile content and distribution. To do so, sections were cut perpendicular to the long axis

of the cylinder and double-polished. Volatile concentrations were determined by Fourier transform infrared spectroscopy (FTIR).

After the decompression experiments, the glass cylinders were carefully extracted from the capsules and first analyzed by X-ray microtomography, the analysis being performed on the entire charge. The cylinders were then submitted to additional analyses on sections cut perpendicular to their long axes. One section (or several sections when numerous analyses were needed) was used to measure dissolved volatile contents by FTIR. Another section was mounted in epoxy resin and polished for scanning electron microscope (SEM) observations.

The metallic pellets in the sensor capsules were also recovered, embedded into epoxy, and then analyzed by electron microprobe.

3.2. Textural analyses

Textures of experimental charges were analyzed by X-ray micro-computed tomography (X-ray micro-CT). The Nanotom 180 instrument by GE Sensing, phoenix|x-ray at ISTO, Orléans, was used. Projection images were recorded from the 360° rotation of the samples, using a tungsten filament and either a molybdenum (most of the time) or a tungsten (more rarely) target. During data acquisition, the glass cylinders were mounted on carbon fiber rods with thermoplastic adhesive. Operating voltages ranged from 90 to 110 kV, with filament currents of 59–170 µA. Voxel sizes ranged between 2.81 and 4.72 μm^3. This spatial resolution was insufficient for detecting the smaller bubbles and crystals (diameter < 6 µm). Reconstruction of the tomographic slices into an image stack of the sample was performed with a Phoenix program. The reconstructed two-dimensional image slices were then stacked and processed using the ImageJ software package (Abràmoff et al., 2004), producing a complete three-dimensional reconstruction of the sample (Polacci et al., 2006). Bubble numbers (*n*, Table 3), diameters calculated from the measured volumes assuming spherical shapes (*D*, Table 3) and densities (number of bubbles per unit volume of sample/melt *BND* and BND_{melt}, Table 3) and vesicularities (volume fraction of bubbles *V*, Table 3) were determined from those stacked volume images. Vesicularities were determined either on the total volume sample (V^c determination, Table 3) or on four representative sub-volumes (V^d determination, Table 3). In addition to vesicularities, crystal number densities (number of Fe–Ti oxide crystals per unit volume of melt CND_{melt}, Table 3) were also determined on one or

more representative sub-volumes. To do so, each image sub-stack was segmented using manual thresholding; the Fe–Ti oxides were separated from the glass plus bubbles. Following segmentation, the volume of these crystals was measured using the 3D Object Counter plugin (Bolte and Cordelières, 2006); the volume of each Fe–Ti oxide was separated and counted. Then, the procedure was repeated to determine the volume of bubbles present in each sub-volume; the bubbles being separated from the glass plus oxides. This allows obtaining the volume of melt (for CND_{melt} determination). The average spacing between bubbles S was also calculated (Table 3). Additional details of the image analysis procedure can be found in Le Gall and Pichavant (2015a).

For comparison with the vesicularities measured in our run products, theoretical equilibrium vesicularities were computed as detailed in Le Gall and Pichavant (2015a). Two end-member cases were considered corresponding to the equilibrium degassing of pure H_2O and pure CO_2 gas, respectively.

All decompressed charges were analyzed by scanning electron microscopy (SEM) for the observation of bubbles which cannot be detected by X-ray micro-CT because of their small size. To do so, the MIRA3 TESCAN FEG instrument at ISTO, Orléans, was used with an accelerating voltage of either 15 or 25 kV. We also attempted to complement the X-ray micro-CT data on oxide-bubble relationships from SEM observations. However, no oxides could be found exposed at the surface of our polished sections.

3.3. Volatile concentrations

Concentrations and spatial distributions of H_2O (total water) and CO_2 (carbonate) dissolved in glasses were determined using infrared spectroscopy at ISTO, Orléans. We used a Nicolet 6700 spectrometer attached to a Continuμm IR microscope, together with an IR light, a KBr beamsplitter and a liquid nitrogen cooled MCT/A detector. IR spectra were acquired between 650 and 7000 cm^{-1} on doubly polished samples 23–169 μm thick. From 4 to 11 spots (aperture 50 μm) were made on each glass, allowing us to check the homogeneity of H_2O and CO_2 contents. Absorption spectra were acquired for 128 scans with a resolution of 4 cm^{-1}. Volatile concentrations (C, wt.%) were calculated from the Beer-Lambert law:

$$C = \frac{100AM}{\varepsilon \rho e} \quad \text{(Eq. 5)}$$

where A is the molar absorbance (measured from peak heights at 3530 cm^{-1} for H_2O and at 1515 cm^{-1} for CO_2), M the molar mass of the volatile species ($g.mol^{-1}$), ε the molar absorption coefficient ($L.mol^{-1}.cm^{-1}$), ρ the glass density ($g.cm^{-3}$), and e the sample thickness (cm).

Absorbance of the 3530 cm^{-1} total H_2O band (H_2O_{mol} + OH^-) was measured with a straight base line between ~3800 and ~2500 cm^{-1}. Absorbance of the 1515 cm^{-1} carbonate ions band was determinate by subtracting a spectrum obtained on a glass starting without dissolved H_2O and CO_2. For H_2O we considered a ε of 64 $L.mol^{-1}.cm^{-1}$ determined for basaltic alkaline glass (Dixon et al., 1995), and for CO_2 we calculated a ε of 363 $L.mol^{-1}.cm^{-1}$ from the Dixon and Pan equation (1995), as ε^{1525}=451-342 [Na/(Ca+Na)]. Sample thickness was measured microscopically to within 1–2 µm. Densities of experimental glasses were determined from the density of the volatile-free starting glass measured at room conditions (ρ = 2.747 ± 0.001), and then propagating the influence of the dissolved volatile species (Richet et al., 2000). Only H_2O was considered to affect glass densities and the influence of CO_2 was neglected (Lange, 1994; Bourgue and Richet, 2001; Lesne et al., 2011a).

All equilibrium gas-melt computations (H_2O and CO_2 solubilities as a function of P-T conditions, saturation isobars and closed-system decompression paths) were calculated with the silicate melt-H_2O-CO_2 model (VolatileCalc) of Newman and Lowenstern (2002), for a basalt with 49 wt.% SiO_2. H_2O and CO_2 contents dissolved in starting glasses were also compared with the recent experimental solubilities of Lesne et al. (2011a, b) and Shishkina et al. (2010), determined at 200 MPa and 1200–1250°C.

The metallic pellets in the sensor capsules were analyzed by electron microprobe (Cameca SX-50 of the joint BRGM–CNRS facility at Orléans) under conditions of 20 kV acceleration voltage, 20 nA sample current, and 10 s counting times.

4. Experimental results

4.1. Synthesis experiments

All glasses from the synthesis experiments (hereafter designated as pre-decompression glasses) were bubble-free. The presence of scattered oxide crystals (Ti-bearing magnetite, Di Carlo et al., 2006; Pichavant et al., 2009; Pichavant et al., 2013) with sizes sometimes up to 20–30 µm (Fig. 1a) was ascertained from X-ray micro-CT observations performed on one synthesis charge (S11#2, "intermediate"). All the other oxide micro-CT observations were performed on the post-decompression charges.

When pressurized with pure Ar (run S10, Table 2; also decompression runs D12, D13, D14 and D15, Table 3), the mole fraction of Ni in the alloy (X_{Ni}) indicated a fH_2 of 0.2 bar. This translates to oxygen fugacity (fO_2) conditions ranging from NNO+2.3 (series #3) to NNO+4.3 (series #1) depending on the H_2O contents (and thus the fH_2O) in the different capsules (NNO is the fO_2 of the Ni–NiO equilibrium at 1200°C and 200 MPa). This fO_2 range will be designated below as "oxidizing" (Table 2). When pressurized with Ar–H_2 mixtures (run S11, Table 2; also decompression runs D16 and D18, Table 3), a fH_2 of 3.7 bar was determined, corresponding to fO_2 conditions ranging between NNO+0.9 (series #2) and NNO+1.7 (series #1) designated below as "intermediate" (Table 2).

Volatile contents are reported in Tables 2 and 4. In accordance with the synthesis conditions, three compositional groups of pre-decompression glasses are distinguished: series #1 (4.90 wt.% H_2O, no CO_2), series #2 (2.43–2.45 wt.% H_2O, 778–847 ppm CO_2) and series #3 (0.97 wt.% H_2O, 773 ppm CO_2). Although H_2O was not introduced in the series #3 capsules, it was found to be present as a dissolved component. H_2O (0.97 wt.%) probably comes from the silver oxalate used as the CO_2 source, but it may also have been generated through the reduction of the Fe^{3+} of the melt by H_2 coming from the pressurizing gas mixture. It is worth noting that the oxidized and intermediate charges have comparable H_2O and CO_2 concentrations in each glass series.

No gradients in H_2O and CO_2 contents were found in pre-decompression glasses, indicating that run durations (>40h) were long enough to completely homogenize the volatile concentrations in the melts. Furthermore at 200 MPa, which corresponds to the saturation pressure, H_2O and CO_2 concentrations agree well with experimental solubilities (Shishkina et al., 2010; Lesne et al., 2011a, b).

4.2. Decompression experiments

All decompressed glasses (hereafter designated as post-decompression glasses) were recovered as glassy blocks containing different amounts of Fe–Ti oxides inherited from their synthesis conditions. Although the data overlap between the three redox series, there is a general positive correlation between oxide *CND*s in post-decompression samples and synthesis fO_2 conditions. The charges from the "oxidizing" syntheses have *CND*s between 2.53 and 61.7 mm^{-3} and the "intermediate" between 4.18 and 26.5 mm^{-3} (Table 3). In addition, decompression charges obtained by Le Gall and Pichavant (2015a, b) on the same starting melt compositions but under less oxidizing fO_2 (NNO–1.4 to +0.9, designated below as "reducing") will be used below as references for charges almost free of Fe–Ti oxides, having *CND*s between 0.68 and 12.4 mm^{-3} (Table 3).

In addition to the presence of Fe–Ti oxide crystals, the post-decompression glasses contain various amounts and types of bubbles. Four types of bubbles can be distinguished (Fig. 1b). *Type 1* appears at the melt-capsule interface. It results from heterogeneous bubble nucleation at the contact with the capsule wall (e.g. Mangan and Sisson, 2000; Gonnermann and Gardner, 2013). These bubbles range in size from a few micrometers up to about 500 µm. *Type 2* corresponds to bubbles that have become detached from the capsule wall because of crowding (Mangan and Sisson, 2000). They also result from heterogeneous nucleation along the contact. These bubbles occur inside the glass but remain close to the glass cylinder rim. They can be large (diameter up to about 400 µm) as a result of growth from early during the decompression ramp. Note that type 1 and 2 bubbles are surrounded by a region devoid of bubbles that reflects local volatile depletion. In comparison, type 3 and 4 bubbles are found nucleating in the core of the glass sample. *Type 3* bubbles are systematically attached to the Fe–Ti oxide crystals and appear to wet oxide crystal faces (Fig. 1b, c). In contrast, *type 4* bubbles show no preferential textural association with Fe–Ti oxides (Fig. 1b–d); their spatial distribution in the charge is uniform. We interpret these textural observations to indicate heterogeneous and homogeneous nucleation, respectively, for the type 3 and 4 bubbles. Both types of bubbles have diameters varying from 6 to 200 µm, the large bubbles corresponding to early nucleation events (at relatively high pressure along the decompression ramp) and so to long timescales for bubble growth, and the small bubbles to late nucleation events and short growth durations.

The preferential relation between Fe–Ti oxides and bubbles is clearly apparent on X-ray micro-CT slices (Fig. 1b, c). However, even when Fe–Ti oxides are present bubbles are not found always systematically attached to them; many oxides lack a preferential association

with bubbles. For example, the series #3 150 MPa P_f charge D15#3 contains Fe–Ti oxides, yet bubbles appear to have nucleated without any preferential relation with these crystals (Fig. 1d). The rare bubbles present are unrelated to the presence of Fe–Ti oxides and formed by homogeneous nucleation. In that charge the distribution of the 7–21 µm bubbles is somewhat heterogeneous (Table 3, Fig. 1d). However, SEM imaging revealed the presence of a large population of smaller (< 7 µm) bubbles, homogeneously distributed within the charge and with no relation with the Fe–Ti oxides present.

4.3. Quantitative textural observations

The textural characteristics (vesicularities, *V*; bubble diameters, *D*; bubble number densities, *BND*s) are given in Table 3 and reported as a function of crystal number densities (*CND*s) for the different volatile series decompressed to either 150, 100 or 25 MPa P_f (Fig. 2).

Vesicularities at 150 (Fig. 2a) and 100 (Fig. 2b) MPa P_f are very low (≤ 0.76 vol.%) in all volatile series. At 25 MPa P_f (Fig. 2c), vesicularities increase to a maximum of 22.7 vol.%. Note that vesicularities for series #1 and #2 are lower than theoretical vesicularities calculated from equilibrium degassing of H_2O and H_2O-CO_2 (Fig. 2a–c). In comparison, the series #3 glasses plot close to the theoretical curve for CO_2 degassing (Fig. 2a, c). No dependence is observed between vesicularity and *CND*. The higher vesicularity observed in charge D28#2 (*CND* = 3.53 mm^{-3}, "reducing") compared to the others at 25 MPa P_f (*CND* range: 2.53–40.4 mm^{-3}) is not correlated with a higher *CND*. Theoretically, one would expect a positive dependency between vesicularity and *CND* in case heterogeneous nucleation is important (since nucleation would start earlier along the decompression ramp), but this is not what is observed.

Average bubble diameters at 150 MPa P_f (Fig. 2d) are essentially the same in volatile series #1 (8–19 µm) and #3 (9–15 µm). At 100 MPa P_f (Fig. 2e), an increase in bubble sizes is observed in the series #1 glasses which have higher bubble diameters (58–70 µm) than the series #2 glasses (13–20 µm). The same type of dependence of bubble size with volatile concentrations is also observed at 25 MPa P_f (Fig. 2f) between series #2 (25–31 µm) and #3 glasses (10–12 µm) decompressed at 78 kPa/s. Note that for a given *CND*, the 39 kPa/s have slightly higher *D* values than the 78 kPa/s series #3 samples (Fig. 2f). The data show no general dependence between bubble diameter and *CND*. Theoretically, if nucleation is

facilitated on crystals faces, bubbles would nucleate earlier along the decompression ramp which would give more time for bubble growth. This would result in a positive correlation between the number of sites for heterogeneous nucleation and *D*. However, our data show only a slight positive relation at 150 and maybe at 100 MPa P_f for the series #1 glasses. Charge D15#1 (*CND* = 12.7 mm^{-3}, "oxidizing") has a higher *D* than charge D30#1 (*CND* = 1.62 mm^{-3}, "reducing").

Results show that experimental *BND*s (3.51–9549 mm^{-3}) are generally larger (by up to several orders of magnitude) than *CND*s (0.68–61.7 mm^{-3}). This suggests that *BND* values are not determined by *CND*s (otherwise *CND* and *BND* values would be approximately equal). It is worth noting that our textural observations indicate that a maximum of one bubble can be associated with one oxide (Fig. 1b, c). The case of several bubbles heterogeneously nucleated on the same oxide was not encountered. Charges D15#3, D16#1, D16#2 and D1#3 have similar or lower *BND* than *CND* values. However, in three of those charges no textural evidence for heterogeneous bubble nucleation was found (Table 3), which demonstrates that *BND* and *CND* values are unrelated. At 100 and 25 MPa P_f, the three volatile series have comparable *BND* values irrespective of *CND*s (Fig. 2g–i). The 150 MPa P_f series #1 charges make an exception. Charge D30#1 (*CND* = 1.62 mm^{-3}, "reducing") has a much higher *BND* than charge D15#1 (*CND* = 12.7 mm^{-3}, "oxidizing"). The negative dependency observed between *BND* and *CND* for those two charges is unexpected (since a higher number of sites for heterogeneous nucleation would imply a higher number of bubbles). However, it is possible that charge D15#1 nucleated much earlier along the decompression ramp (between 200 and 150 MPa because of heterogeneous nucleation) than D30#1 and that post-nucleation processes (growth, coalescence) also started earlier in the former than in the latter charge. This would lead to attribute a tentative effect of heterogeneous nucleation on *BND* data for series #1 charges decompressed to 150 MPa.

4.4. Volatile contents in post-decompression glasses

Series #1 post-decompression glasses have near-equilibrium H_2O concentrations (D30#1, "reducing", 4.23 wt.% H_2O, D15#1, "oxidizing", 4.18 wt.% H_2O both at 150 MPa P_f; D18#1 and D16#1, "intermediate", 3.28 and 3.26 wt.% H_2O, 100 MPa P_f), i.e. their glass H_2O contents are close to solubility values calculated from VolatileCalc (Newman and

Lowenstern, 2002) for each P_f (Fig. 3). Thus, a general decrease of the melt H_2O content is observed when decreasing pressure.

In contrast, series #2 and #3 post-decompression glasses contain volatile concentrations that differ from theoretical concentrations calculated assuming closed-system equilibrium degassing (Le Gall and Pichavant, 2015a, b; Fig. 3). This disequilibrium degassing behavior is marked in all charges by a decrease in H_2O concentration compared to the expected degassing trend and by CO_2 concentrations that largely exceed solubilities (the latter calculated for each P_f isobar and keeping the H_2O concentration of the glass constant). As an example of excess CO_2, one of the two series #2 25 MPa P_f glasses (D13#2, "oxidizing") has a CO_2 content (647 ppm) much higher than the value calculated on the 25 MPa isobar at the H_2O concentration of the glass (~100 ppm).

Series #3 post-decompression glasses have H_2O concentrations ranging from 0.80 (D24#3, "reducing", 25 MPa P_f, 461 ppm CO_2) to 0.41 wt.% (D12#3, "oxidizing", 25 MPa P_f, 319 ppm CO_2) and CO_2 concentrations between 770 (D15#3, "oxidizing", 150 MPa P_f, 0.56 wt.% H_2O) and 319 ppm (D12#3, "oxidizing", 25 MPa P_f, 0.41 wt.% H_2O, Table 4). Upon decreasing P_f, melt CO_2 concentrations decrease progressively along nearly vertical degassing trends close to the theoretical ones (Fig. 3). It is worth noting that one charge (D15#3, "oxidizing", P_f = 150 MPa) has a CO_2 concentration (770 ppm CO_2) close to the 150 MPa isobar. However, most post-decompression glasses keep CO_2 concentrations that plot above their respective gas-melt saturation isobars. For example, the 25 MPa P_f glasses have CO_2 contents (319–564 ppm) largely above the 25 MPa isobar if the H_2O concentration of the glasses is kept constant.

It is worth noting that disequilibrium degassing is encountered irrespective of redox conditions imposed during synthesis, i.e. for the "oxidizing", "intermediate" and "reducing" charges. In order to evaluate the influence of heterogeneous nucleation on glass volatile concentrations, excess concentrations of dissolved CO_2 (ΔCO_2) are plotted as a function of *CND*s for the three P_f (Fig. 4). ΔCO_2 is calculated as the difference between the CO_2 concentration of the post-decompression glass and the CO_2 solubility value determined on the appropriate P_f isobar (Newman and Lowenstern, 2002) keeping the H_2O concentration of the glass constant. Previous decompression experiments have emphasized that equilibrium degassing in CO_2-bearing basaltic melts needs both numerous and large bubbles (Le Gall and Pichavant, 2015a, b). Therefore, if heterogeneous nucleation on Fe–Ti oxides is important, a

negative correlation would be expected between ΔCO_2 and *CND* because, theoretically, for a given P_f, heterogeneous nucleation would increase the number and size of bubbles. Instead at 25 MPa, the data show a positive correlation between these two parameters. At 150 and 100 MPa, no correlation is observed (Fig. 4). We therefore conclude to the absence of influence of crystals on the attainment of equilibrium CO_2 concentrations.

5. Interpretation and discussion of experimental observations

5.1. Heterogeneous vs. homogeneous bubble nucleation

Our experiments bear textural evidence for both (1) heterogeneous and (2) homogeneous bubble nucleation. (1) The heterogeneous nature of bubble nucleation in our post-decompression glasses is demonstrated by the remarkable textural association between bubbles and Fe–Ti oxide crystals (Fig. 1b, c), the latter serving as nucleation sites for gas bubbles. In addition to heterogeneous nucleation within the melt (*type 3* bubbles), we also observed heterogeneous bubble nucleation taking place at the melt-capsule interface (*types 1* and *2* bubbles, Fig. 1b). (2) The homogenous nature of bubble nucleation in our post-decompression glasses is evidenced by the occurrence of bubbles uniformly distributed inside the melt and showing no textural association with Fe–Ti oxide crystals (*type 4* bubbles, Fig. 1b–d). Therefore, homogeneous nucleation can occur even in presence of Fe–Ti oxide crystals.

From our decompression experiments, the supersaturation pressures required for either heterogeneous (ΔP_{HeN}) or homogeneous (ΔP_{HoN}) bubble formation, i.e. the difference between the saturation pressure ($P_{sat} = P_{in}$) and the final pressure (P_f) at which bubbles begin to nucleate, can be determined. It is worth reminding that bubbles are absent from the pre-decompression glasses (P_{in} = 200 MPa, Fig. 1a).

In series #1 post-decompression glasses, bubbles are found nucleating on the surface of Fe–Ti oxides from P_f = 150 MPa (D15#1, “oxidizing”, Fig. 1c and Table 3), but there are also numerous bubbles nucleating spontaneously in the melt (Fig. 1c). *Type 1* bubbles also appear heterogeneously at the capsule wall from P_f = 150 MPa. This suggests that both heterogeneous and homogeneous bubble nucleation occurs between 200 and 150 MPa P_f. Therefore, supersaturation pressures of 50 MPa maximum (ΔP_{HeN} and ΔP_{HoN} both < 50 MPa) are inferred for the H_2O-rich, CO_2-free, series #1 melts. The ΔP_{HeN} value appears higher than

recorded by Hurwitz and Navon (< 1–5 MPa, 1994) and Gardner and Denis (< 20 MPa, 2004) for rhyolitic melts, as well as by Mangan et al. (35 ± 5 MPa, 2004b) for dacitic melts. Nevertheless, in view of our relatively large P_f step (50 MPa), our ΔP_{HeN} value is a maximum. The ΔP_{HoN} value is consistent with previous results: Le Gall and Pichavant (2015a, b) observed that in almost crystal-free basaltic melts bubbles nucleate in response to small amounts of volatile supersaturation, i.e. for a low ΔP_{HoN} << 50 MPa. Therefore, Fe–Ti oxides appear to be relatively efficient sites for bubble nucleation in basaltic melts, consistent with the experimental results of Hurwitz and Navon (1994), Gardner and Denis (2004) and Gardner (2007) for more evolved melts. Given our relatively large P_f step, our experiments do not allow the influence of the presence of Fe–Ti oxide crystals on nucleation pressure to be documented in detail.

In series #2 post-decompression glasses, we mainly observed homogeneously nucleated bubbles at P_f = 100 MPa (D14#2, "oxidizing", D16#2 and D18#2, "intermediate", Table 3), leading to a ΔP_{HoN} < 100 MPa, a value consistent with results for nearly crystal-free basaltic melts (Le Gall and Pichavant, 2015a, b). The same charges also contain a minor proportion of bubbles heterogeneously nucleated on the surface of Fe–Ti oxide crystals (Table 3) and at the melt-capsule interface, thus leading to a ΔP_{HeN} < 100 MPa. It is worth noting that no data exist for P_f > 100 MPa and, so, it cannot be excluded that bubble nucleation would start at pressures > 100 MPa, which would make our measured ΔP_{HeN} and ΔP_{HoN} maximum values.

In series #3 post-decompression glasses, bubbles begin to form homogeneously from P_f = 150 MPa (D15#3, "oxidizing", Fig. 1d and Table 3), corresponding to a ΔP_{HoN} < 50 MPa. Only 8 bubbles were detected by X-ray micro-CT because their size is hardly higher than the instrumental spatial resolution. Nevertheless, SEM imaging revealed the presence of a population of small (< 7 µm) uniformly distributed bubbles. It is worth noting that, although oxide crystals are present in D15#3 charge, bubbles are systematically not attached to their faces (Fig. 1d) and, so, there is no evidence that bubble nucleation is favored (and thus takes place at a higher pressure) in presence of Fe–Ti oxide crystals. Only at P_f = 25 MPa (D12#3 and 13#3, "oxidizing", Table 3) some bubbles were found attached to the faces of Fe–Ti oxides (Fig. 1b). The possibility that heterogeneous nucleation occurs at relatively high P_f along the decompression ramp but becomes obliterated at lower pressures can be ruled out because, if this would be the case, (1) the heterogeneous nucleation texture should be preserved and (2) bubble growth should be observed. In contrast, *type 1* bubbles begin to form

at the capsule-melt interface from P_f = 150 MPa (D15#3, Fig. 1d). Therefore, the data lead to a ΔP_{HeN} < 50 MPa but we emphasize that the influence of Fe–Ti oxide crystals and capsule is different. The delayed influence of Fe–Ti oxides on heterogeneous bubble nucleation, as found in our experiments, contrast with results of Masotta et al. (2014) who found a ΔP_{HeN} of 18 MPa in basaltic melts containing 13 ppm H_2O and 101 ppm CO_2.

We conclude that, in H_2O-only melts (series #1) Fe–Ti oxides appear as favorable sites for heterogeneous nucleation. Both homogeneous and heterogeneous nucleation processes occur from P_f = 150 MPa, leading to ΔP_{HeN} and ΔP_{HoN} < 50 MPa. In contrast, in H_2O-poor, CO_2-bearing melts (series #3), homogenous bubble nucleation is the first process taking place from P_f = 150 MPa (ΔP_{HoN} < 50 MPa), being followed by heterogeneous bubble nucleation on Fe–Ti oxides at a much lower P_f (25 MPa). In H_2O-CO_2-bearing melts (series #2), both heterogeneous and homogeneous bubble nucleation occurs at P_f = 100 MPa, leading to ΔP_{HeN} and ΔP_{HoN} < 100 MPa. Our results tend to suggest a dependence of the role of Fe–Ti oxides with the dissolved volatile composition (H_2O/CO_2 ratio). Bubbles composed predominantly of CO_2 seem to nucleate less efficiently on faces of Ti-bearing magnetite than H_2O-rich bubbles. It is possible that a difference in σ_{BC} (Eq. 4) between H_2O-rich and CO_2-rich bubbles explains the differential wetting properties of the gas phase on the surface of Fe–Ti oxides. Hurwitz and Navon (1994) explained the high efficiency of this mineral group by the low surface tension of the oxide-bubble interface (σ_{BC}) and the rough morphology of the crystals. This result is consistent with our own observations: neither clinopyroxene nor olivine was found as preferential sites for heterogeneous bubble nucleation (Pichavant et al., 2013).

5.2. Equilibrium vs. disequilibrium degassing

Our results show that chemical equilibrium is reached in the H_2O-only melts. Overall, series #1 glasses decompressed to P_f = 150 and 100 MPa have H_2O concentrations in agreement with their respective equilibrium solubilities (Fig. 3). The two 150 MPa charges plot slightly above the reference isobar yet they contain evidence for heterogeneous bubble nucleation on oxides (Table 3). In contrast, the two 100 MPa glasses, which do not reveal a preferential bubble-oxide association, have H_2O concentrations very close to the solubility. This suggests that in series #1 charges, the occurrence of heterogeneous nucleation has no significant influence on the H_2O concentration of the post-decompression glasses. Despite chemical equilibrium being reached, it is worth noting that series #1 glasses have

vesicularities lower than expected from equilibrium degassing (Fig. 2a, b). This suggests that, in order to achieve chemical equilibrium, H_2O is lost diffusively from the melt towards the gas phase (gas bubbles and capsule-melt interface) during decompression (Le Gall and Pichavant, 2015a, b). Although clear evidence for H_2O diffusion in our series #1 glasses is lacking, the very low (4) number of bubbles present in charge D16#1 (P_f = 100 MPa, "intermediate") would reflect diffusive H_2O outgassing from the melt, as observed in the experiments of Le Gall and Pichavant (2015b) performed at the same decompression rate.

In contrast, disequilibrium degassing is systematically encountered in the CO_2-bearing melts (series #2 and #3), irrespective of redox conditions imposed during synthesis, i.e. for the "oxidizing", "intermediate", as well as for the "reducing" charges. It is worth emphasizing that most series #2 and #3 charges display the bubble-oxide association. Only two 150 MPa P_f charges from series #3 lack evidence for heterogeneous nucleation (Fig. 3). Most series #2 and #3 post-decompression glasses retain CO_2 at elevated concentration levels. The 150 MPa P_f series #3 glass (D15#3, "oxidizing") that lack heterogeneous nucleation are the only charges among series #2 and #3 to approach solubility (Fig. 3), which underlines that heterogeneous nucleation plays no role in the attainment of gas-melt equilibrium. At the same time, H_2O is lost in significant amounts, generating degassing trends that are in marked contrast with theoretical equilibrium closed-system decompression trends (Fig. 3). This behavior has been previously observed in the experiments of Pichavant et al. (2013) and Le Gall and Pichavant (2015a, b) in basaltic melts that are almost free of Fe–Ti oxides. Thus, our results demonstrate the possibility of generating disequilibrium degassing trends in CO_2-bearing basaltic melts even when Fe–Ti oxide crystals are present to assist bubble nucleation. Disequilibrium degassing would persist if silicate crystals are present instead of Fe–Ti oxides since neither clinopyroxene nor olivine has influence on bubble nucleation (Pichavant et al., 2013).

6. Volcanological implications

6.1. Heterogeneous bubble nucleation in basaltic magmas

Although our experimental results clearly document the possibility of heterogeneous nucleation of bubbles on Fe–Ti oxide crystals in basaltic melts, it is important to evaluate in practice the importance of this process in natural systems.

First, the experimental data from this study emphasize the need for Fe–Ti oxides to be present to promote heterogeneous bubble nucleation. Textural evidence presented in this paper clearly shows that heterogeneous bubble nucleation on Fe–Ti oxides can take place. Conversely, clinopyroxene and olivine-bearing charges produced in previous decompression experiments (Pichavant et al., 2013) do not suggest an influence of silicate crystals on bubble nucleation. Our conclusions regarding (1) the role of Fe–Ti oxides on heterogeneous nucleation in basaltic magmas and (2) the lack of influence of silicate crystals are thus similar to those previously drawn (Hurwitz and Navon, 1994; Gardner and Denis, 2004) for rhyolitic magmas.

Second, natural basaltic magmas can have commonly a low crystallinity, as illustrated for example by pumice samples from Stromboli (~11 vol.% clinopyroxene, olivine and plagioclase phenocrysts, Pichavant et al., 2011), and by products from the Etna 122 BC (1–10 vol.% plagioclase plus minor clinopyroxene, olivine and Fe–Ti oxide phenocrysts, Sable et al., 2006), Tarawera 1886 (< 0.5 vol.% phenocrysts, Sable et al., 2009) and Masaya (< 1–4 vol.% plagioclase and clinopyroxene plus very rare olivine phenocrysts, Costantini et al., 2010) Plinian eruptions. Among phenocryst assemblages, the proportion of Fe–Ti oxides in those products never exceed a few vol.%. Basalt crystallization experiments demonstrate a correlation between the proportion of Fe–Ti oxides and the experimental fO_2 (e.g. Pichavant et al., 2002; Berndt et al., 2005). For the most oxidized basaltic magmas (~NNO+3), proportions of Fe–Ti oxides reach a maximum of a few vol.% (e.g. Pichavant et al., 2002; Berndt et al., 2005). This severely restricts the proportion of Fe–Ti oxides and, so, the number of sites available for heterogeneous bubble nucleation in basaltic magmas. In the case of Stromboli pumices, Fe–Ti oxides have been found as inclusions in clinopyroxene; they never occur in isolation in the groundmass (Di Carlo, 2006). In comparison with proportions of Fe–Ti oxides, typical vesicularities in basaltic pumices can reach > 50 vol.% (Polacci et al., 2009; Sable et al., 2009; Costantini et al., 2010; Pichavant et al., 2011), which emphasizes that bubble nucleation must be for the most part of homogeneous nature. It is worth noting that Fe–Ti oxides can be also part of the groundmass assemblage and sometimes form an important fraction of microlites (up to 8 vol.% of the microlite assemblage in Etna clasts, Sable et al., 2006, and up to 17 vol.% in Masaya clasts, Costantini et al., 2010). However, it is rare to observe bubbles wetting microlites (e.g. Costantini et al., 2010), one possible explanation being that their crystallization correspond to a late, volatile-poor, evolutionary stage. Textural observations of basaltic eruption products generally confirm our experimental

conclusions that silicate phenocrysts do not serve as nucleation sites for bubbles (Sable et al., 2006; Lautze and Houghton, 2007).

We conclude to the possibility of heterogeneous bubble nucleation to occur but emphasize that the importance of this process is limited by the low (a few vol.% maximum) proportion of Fe–Ti oxides phenocrysts that can be present in basaltic magmas.

6.2. Influence of Fe–Ti oxide crystals on degassing mechanisms

In our experiments, similar supersaturation pressures for heterogeneous (ΔP_{HeN}) and homogenous bubble nucleation (ΔP_{HoN}) were found in the H_2O-only series #1 melts (< 50 MPa), as well as in the H_2O-CO_2-bearing series #2 melts (< 100 MPa). In the H_2O-poor, CO_2-bearing, series #3 melts, a ΔP_{HoN} (< 50 MPa) much lower than ΔP_{HeN} (< 175 MPa) was found for heterogeneous bubble nucleation on Fe–Ti oxides. Although the influence of Fe–Ti oxide crystals on the supersaturation pressure (or on the nucleation pressure) was not documented in detail (because of our relatively large P_f step), our results suggest that it is minimal in basaltic melts. Thus, the formation of a gas phase in an ascending H_2O-CO_2-bearing basaltic magma should not be greatly facilitated by Fe–Ti oxide crystallization.

Our experimental data show that the crystal number density affects neither the bubble diameter nor the bubble number density. Increasing the abundance of Fe–Ti oxides is generally not accompanied by an increase in bubble size, except at 150 and maybe at 100 MPa P_f for the series #1 glasses (Fig. 2d, e). In addition, increasing the number of Fe–Ti oxides (i.e. the number of nucleation sites) does not generally increase the bubble number density (Fig. 2g–i). The fact that experimental *BND*s (3.51–9549 mm^{-3}) are generally larger (by up to several orders of magnitude) than *CND*s (0.68–61.7 mm^{-3}) stresses the restricted effect of Fe–Ti oxide crystals on bubble nucleation and, in general, the minor importance of heterogeneous bubble nucleation. Our observations reveal that most bubbles lack a textural association with Fe–Ti oxides and, so, that nucleation is not restricted to preferential sites at crystal surfaces. This establishes the dominant role of homogeneous bubble nucleation in common basaltic melts.

7. Conclusions

High pressure and temperature (1200°C) decompression experiments were performed to evaluate the importance of heterogeneous bubble nucleation on Fe–Ti oxides in basaltic magmas. Compared to previous studies about heterogeneous bubble nucleation (Hurwitz and Navon, 1994; Gardner et al., 1999; Gardner and Denis, 2004; Mangan et al., 2004b; Gardner, 2007; Cluzel et al., 2008), this study is the first to provide systematic information on basaltic compositions. Ascent and degassing of H_2O and H_2O-CO_2-bearing basaltic melts were simulated from 200 to 25 MPa, at a decompression rate of either 1.5 or 3 m/s and in presence of different amounts of Fe–Ti oxides. Run products were texturally and chemically characterized, and compared with natural basaltic products. The main conclusions are the following:

(1) Textural evidence of heterogeneous bubble nucleation on Fe–Ti oxides has been documented. Conclusions drawn previously (Hurwitz and Navon, 1994; Gardner and Denis, 2004; Gardner, 2007) about the preferential role of Fe–Ti oxides in promoting heterogeneous bubble nucleation can be extended to basaltic melts.

(2) The experimental data of Pichavant et al. (2013) and the textural observations on natural basaltic products (Sable et al., 2006; Lautze and Houghton, 2007) both concur to suggest no influence of silicate crystals (olivine, clinopyroxene) on heterogeneous bubble nucleation.

(3) Both heterogeneous and homogeneous nucleation was found to occur together in our experiments. This leads to comparable ΔP_{HeN} (corresponding to heterogeneous nucleation on crystals) and ΔP_{HoN} (corresponding to homogeneous nucleation) in the series #1 melts (< 50 MPa, H_2O-only) as well as in the series #2 melts (< 100 MPa, H_2O-CO_2-bearing). The influence of Fe–Ti oxide crystals on the supersaturation pressure (or on the nucleation pressure) is minimal in basaltic melts.

(4) In the series #3 melts (H_2O-poor, CO_2-bearing) ΔP_{HeN} (< 175 MPa) is higher than ΔP_{HoN} (< 50 MPa). This suggests that the role of Fe–Ti oxides on bubble nucleation decreases in magnitude with the CO_2/H_2O ratio of the gas bubble.

(5) The H_2O-only melts (series #1) follow a degassing behavior close to equilibrium whereas the CO_2-bearing melts systematically show disequilibrium degassing. Highly CO_2-supersaturated melts were produced during decompression irrespective of the presence and abundance of Fe–Ti oxides.

(6) There is systematic influence of the crystal number density neither on the bubble diameter nor on the bubble number density.

(7) Our results globally lead to conclude that heterogeneous bubble nucleation is limited and that bubble nucleation should be for the most part homogeneous in common basaltic melts.

References

Abràmoff, M.D., Magalhães, P.J., Ram, S.J., 2004. Image processing with ImageJ. Biophotonics International 11, 36–43.

Bai, L., Baker, D.R., Polacci, M., Hill, R. J., 2011. In-situ degassing study on crystal-bearing Stromboli basaltic magmas: Implications for Stromboli explosions: Geophysical Research Letters 38, L17309, doi: 10.1029/2011GL048540.

Baker, D.R., Lang, P., Robert, G., Bergevin, J.-F., Allard, E., Bai, L., 2006. Bubble growth in slightly supersaturated albite melt at constant pressure. Geochimica et Cosmochimica Acta 70, 1821–1838.

Berndt, J., Koepke, J., Holtz, F., 2005. An Experimental Investigation of the Influence of Water and Oxygen Fugacity on Differentiation of MORB at 200 MPa. Journal of Petrology 46, 135–167. doi:10.1093/petrology/egh066

Bolte, S., Cordelières, F.P., 2006. A guided tour into subcellular colocalization analysis in light microscopy. Journal of Microscopy 224, 213–232.

Bottinga, Y., Javoy, M., 1990. MORB degassing: Bubble growth and ascent. Chemical Geology 81, 255–270.

Bourgue, E., Richet, P., 2001. The effects of dissolved CO_2 on the density and viscosity of silicate melts: a preliminary study. Earth and Planetary Science Letters 193, 57–68.

Burnham, C.W., 1979. The importance of volatile constituents. In: Yoder, H.S. (Eds.), The evolution of the igneous rocks (Fiftieth anniversary perspectives), Princeton University Press, Princeton, 439–482.

Cluzel, N., Laporte, D., Provost, A., Kannewischer, I., 2008. Kinetics of heterogeneous bubble nucleation in rhyolitic melts: implications for the number density of bubbles in volcanic conduits and for pumice textures. Contributions to Mineralogy and Petrology 156, 745–763. doi:10.1007/s00410-008-0313-1

Costantini, L., Houghton, B.F., Bonadonna, C., 2010. Constraints on eruption dynamics of basaltic explosive activity derived from chemical and microtextural study: the example of the Fontana Lapilli Plinian eruption, Nicaragua. Journal of Volcanology and Geothermal Research 189, 207–224.

Di Carlo, I., Pichavant, M., Rotolo, S.G., Scaillet, B., 2006. Experimental Crystallization of a High-K Arc Basalt: the Golden Pumice, Stromboli Volcano (Italy). Journal of Petrology 47, 1317–1343. doi:10.1093/petrology/egl011

Dixon, J.E., Pan, V., 1995. Determination of the molar absorptivity of dissolved carbonate in basanitic glass. American Mineralogist 80, 1339–1342.

Dixon, J.E., Stolper, E.M., Holloway, J.R., 1995. An experimental study of water and carbon dioxide solubilities in mid-ocean ridge basaltic liquids. Part I: calibration and solubility models. Journal of Petrology 36, 1607–1631.

Ferry, J.M., Baumgartner, L., 1987. Thermodynamic models of molecular fluids at the elevated pressures and temperatures of crustal metamorphism. Reviews in Mineralogy and Geochemistry 17, 323–365.

Gardner, J., 2007. Heterogeneous bubble nucleation in highly viscous silicate melts during

instantaneous decompression from high pressure. Chemical Geology 236, 1–12. doi:10.1016/j.chemgeo.2006.08.006
Gardner, J.E., Denis, M.-H., 2004. Heterogeneous bubble nucleation on Fe-Ti oxide crystals in high-silica rhyolitic melts. Geochimica et Cosmochimica Acta 68, 3587–3597. doi:10.1016/j.gca.2004.02.021
Gardner, J.E., Ketcham, R.A., 2011. Bubble nucleation in rhyolite and dacite melts: temperature dependence of surface tension. Contributions to Mineralogy and Petrology 162, 929–943. doi:10.1007/s00410-011-0632-5
Gardner, J.E., Hilton, M., Carroll, M.R., 1999. Experimental constraints on degassing of magma: isothermal bubble growth during continuous decompression from high pressure. Earth and Planetary Science Letters 168, 201–218.
Gonnermann, H.M., Gardner, J.E., 2013. Homogeneous bubble nucleation in rhyolitic melt: Experiments and nonclassical theory. Geochemistry, Geophysics, Geosystems 14, 4758–4773.
Holloway, J.R., 1987. Igneous fluids. Reviews in Mineralogy and Geochemistry 17, 211–233.
Hurwitz, S., Navon, O., 1994. Bubble nucleation in rhyolitic melts: Experiments at high pressure, temperature, and water content. Earth and Planetary Science Letters 122, 267–280.
Le Gall, N., Pichavant, M., 2015a (to be submitted). Homogeneous bubble nucleation in H_2O- and H_2O-CO_2-bearing basaltic melts: results of high temperature decompression experiments.
Le Gall, N., Pichavant, M., 2015b (to be submitted). Effect of ascent rate on homogeneous bubble nucleation in the system basalt-H_2O-CO_2: Implications for Stromboli volcano.
Lange, R.A., 1994. The effect of H_2O, CO_2, and F on the density and viscosity of silicate melts. Reviews in Mineralogy and Geochemistry 30, 331–369.
Lautze, N.C., Houghton, B.F., 2007. Linking variable explosion style and magma textures during 2002 at Stromboli volcano, Italy. Bulletin of Volcanology 69, 445–460.
Lesne, P., Scaillet, B., Pichavant, M., Beny, J.-M., 2011a. The carbon dioxide solubility in alkali basalts: an experimental study. Contributions to Mineralogy and Petrology 162, 153–168.
Lesne, P., Scaillet, B., Pichavant, M., Iacono-Marziano, G., Beny, J.-M., 2011b. The H_2O solubility of alkali basaltic melts: an experimental study. Contributions to Mineralogy and Petrology 162, 133–151.
Lyakhovsky, V., Hurwitz, S., Navon, O., 1996. Bubble growth in rhyolitic melts: experimental and numerical investigation. Bulletin of Volcanology 58, 19–32.
Mangan, M.T., Sisson, T., 2000. Delayed, disequilibrium degassing in rhyolite magma: decompression experiments and implications for explosive volcanism. Earth and Planetary Science Letters 183, 441–455.
Mangan, M.T., Sisson, T., 2005. Evolution of melt-vapor surface tension in silicic volcanic systems: Experiments with hydrous melts. Journal of Geophysical Research 110, B01202. doi:10.1029/2004JB003215
Mangan, M.T., Mastin, L., Sisson, T., 2004a. Gas evolution in eruptive conduits: combining insights from high temperature and pressure decompression experiments with steady-state flow modeling. Journal of Volcanology and Geothermal Research 129, 23–36.
Mangan, M.T., Sisson, T.W., Hankins, W.B., 2004b. Decompression experiments identify kinetic controls on explosive silicic eruptions. Geophysical Research Letters 3:L08605. doi:10.1029/2004GL019509
Masotta, M., Ni, H., Keppler, H., 2014. In situ observations of bubble growth in basaltic, andesitic and rhyodacitic melts. Contributions to Mineralogy and Petrology 167, 976.
Massol, H., Koyaguchi, T., 2005. The effect of magma flow on nucleation of gas bubbles in a volcanic conduit. Journal of Volcanology and Geothermal Research 143, 69–88.
Mourtada-Bonnefoi, C.C., Laporte, D., 1999. Experimental study of homogeneous bubble nucleation in rhyolitic magmas. Geophysical Research Letters 26, 3505–3508.
Mourtada-Bonnefoi, C.C., Laporte, D., 2002. Homogeneous bubble nucleation in rhyolitic magmas: an experimental study of the effect of H_2O and CO_2. Journal of Geophysical Research 107 (B4). doi:10.1029/2001JB00290
Mourtada-Bonnefoi, C.C., Laporte, D., 2004. Kinetics of bubble nucleation in a rhyolitic melt: an experimental study of the effect of ascent rate. Earth and Planetary Science Letters 218, 521–537.

Navon, O., Lyakhovsky, V., 1998. Vesiculation processes in silicic magmas. In: Gilbert, J.S. & Sparks, R.S.J. (Eds.) The Physics of Explosive Volcanic Eruptions. Geological Society, London, Special Publications 145, 27–50.

Newman, S., Lowenstern, J.B., 2002. VolatileCalc: a silicate melt–H_2O–CO_2 solution model written in Visual Basic for Excel. Computers & Geosciences 28, 597–604.

Papale, P., 1997. Modeling of the solubility of a one-component H_2O or CO_2 fluid in silicate liquids. Contributions to Mineralogy and Petrology 126, 237–251.

Pichavant, M., Martel, C., Bourdier, J.-L., Scaillet, B., 2002. Physical conditions, structure, and dynamics of a zoned magma chamber: Mount Pelée (Martinique, Lesser Antilles Arc). Journal of Geophysical Research 107 (B5), 2093. doi:10.1029/2001JB000315

Pichavant, M., Pompilio, M., D'Oriano, C., Di Carlo, I., 2011. Petrography, mineralogy and geochemistry of a primitive pumice from Stromboli: implications for the deep feeding system. European Journal of Mineralogy 23, 499–517.

Pichavant, M., Di Carlo, I., Le Gac, Y., Rotolo, S.G., Scaillet, B., 2009. Experimental constraints on the deep magma feeding system at Stromboli volcano, Italy. Journal of Petrology 50, 601–624.

Pichavant, M., Di Carlo, I., Rotolo, S.G., Scaillet, B., Burgisser, A., Le Gall, N., Martel, C., 2013. Generation of CO_2-rich melts during basalt magma ascent and degassing. Contributions to Mineralogy and Petrology 166, 545–561.

Polacci, M., Baker, D.R., Mancini, L., Tromba, G., Zanini, F., 2006. Three-dimensional investigation of volcanic textures by X-ray microtomography and implications for conduit processes. Geophysical Research Letters 33, L13312. doi:10.1029/2006GL026241

Polacci, M., Baker, D.R., Mancini, L., Favretto, S., Hill, R.J., 2009. Vesiculation in magmas from Stromboli and implications for normal Strombolian activity and paroxysmal explosions in basaltic systems. Journal of Geophysical Research 114, B01206. doi:10.1029/2008JB005672

Pownceby, M.I., O'Neill, H.S.C., 1994. Thermodynamic data from redox reactions at high temperatures. III. Activity-composition relations in Ni-Pd alloys from EMF measurements at 850–1250 K, and calibration of the NiO+ Ni-Pd assemblage as a redox sensor. Contributions to Mineralogy and Petrology 116, 327–339.

Proussevitch, A.A., Sahagian, D.L., Tsentalovich, E.P., 2007. Statistical analysis of bubble and crystal size distributions: Formulations and procedures. Journal of Volcanology and Geothermal Research 164, 95–111.

Richet, P., Whittington, A., Holtz, F., Behrens, H., Ohlhorst, S., Wilke, M., 2000. Water and the density of silicate glasses. Contributions to Mineralogy and Petrology 138, 337–347.

Robie, R. A., Hemingway, B. S., Fisher, J. R., 1979. Thermodynamic properties of minerals and related substances at 298.15 K and 1 bar (10^5 pascals) pressure and at higher temperatures. US Geological Survey, Bulletin 1452.

Sable, J.E., Houghton, B.F., Del Carlo, P., Coltelli, M., 2006. Changing conditions of magma ascent and fragmentation during the Etna 122 BC basaltic Plinian eruption: evidence from clast microtextures. Journal of Volcanology and Geothermal Research 158, 333–354.

Sable, J.E., Houghton, B.F., Wilson, C.J.N., Carey, R.J., 2009. Eruption mechanisms during the climax of the Tarawera 1886 basaltic Plinian eruption inferred from microtextural characteristics of the deposits. Studies in volcanology. The legacy of George Walker. Geological Society, London, 129–154.

Scaillet, B., Pichavant, M., Roux, J., Humbert, G., Lefèvre, A., 1992. Improvements of the Shaw membrane technique for measurement and control of fH_2 at high temperatures and pressures. American Mineralogist 77, 647–655.

Shishkina, T.A., Botcharnikov, R.E., Holtz, F., Almeev, R.R., Portnyagin, M., 2010. Solubility of H_2O-and CO_2-bearing fluids in tholeiitic basalts at pressures up to 500MPa. Chemical Geology 277, 115–125.

Sigsbee, R.A., 1969. Vapor to condensed-phase heterogeneous nucleation. Nucleation. Zettlemoyer AC (Eds.). New York, Marcel Dekker, 151–224.

Taylor, J.R., Wall, J., Pownceby, M.I., 1992. The calibration and application of accurate redox sensors. American Mineralogist 77, 284–295.

Vetere, F., Behrens, H., Misiti, V., Ventura, G., Holtz, F., De Rosa, R., Deubener, J., 2007. The

viscosity of shoshonitic melts (Vulcanello Peninsula, Aeolian Islands, Italy): insight on the magma ascent in dikes. Chemical Geology 245, 89–102.
Zhang, Y., Ni, H., 2010. Diffusion of H, C, and O components in silicate melts. Reviews in Mineralogy and Geochemistry 72, 171–225.

Figure captions

Figure 1. Slices through X-ray microtomographic volumes of a pre-decompression (a) and three post-decompression (b, c, d) charges showing representative types of textures. (a) Sample S11#2 synthesized at 202.1 MPa containing scattered Fe–Ti oxide crystals (Ox). (b) Sample D12#3 decompressed to 25 MPa, at 39 kPa/s showing four bubble types (see text for description and interpretation). (c) Sample D15#1 decompressed to 150 MPa showing bubble either attached (*type 3*) or not (*type 4*) to the Fe–Ti oxide crystals. (d) Sample D15#3 decompressed to 150 MPa showing bubbles systematically unattached (*type 4*) to the Fe–Ti oxide crystals. See Tables 2 and 3 for details about the experimental conditions and textural results.

Figure 2. (a–c) Vesicularity *V*, (d–f) average bubble diameter *D* and (g–i) bubble number density BND_{melt} plotted as a function of crystal number density CND_{melt} for the post-decompression glasses; "oxidizing", "intermediate" and "reducing" charges are plotted with the same symbol. The data are shown for three final pressures, 150 MPa (a, d, g), 100 MPa (b, e, h) and 25 MPa (c, f, i). Open squares: series #1 glasses; open diamonds: series #2 glasses; open triangles: series #3 glasses. The data are for a decompression rate (dP/dt) of 39 kPa/s except when stated otherwise (asterisks: dP/dt = 78 kPa/s). In (a–c), equilibrium vesicularities (thick black and gray lines) calculated respectively for pure H_2O and CO_2 degassing (see text) are shown for comparison with the experimental data.

Figure 3. H_2O vs. CO_2 concentrations in post-decompression glasses from series #1 (black symbols), #2 (gray symbols) and #3 (white symbols). Circles: pre-decompression glasses synthesized at 200 MPa; rectangles: glasses decompressed to 150 MPa; triangles: glasses decompressed to 100 MPa; diamonds: glasses decompressed to 25 MPa. The data are for a decompression rate (dP/dt) of 39 kPa/s except when stated otherwise (asterisks: dP/dt = 78 kPa/s). The "oxidizing", "intermediate" and "reducing" charges are plotted with the same symbol. Charges with no evidence for heterogeneous bubble nucleation (Table 3) are indicated with a black arrow. For all the other charges, at least one case of bubble-oxide textural association was found. Error bars (standard deviations, Table 4) are indicated on the data points. The 25–250 MPa gas-melt saturation isobars (thin continuous lines labeled with pressure) and the closed-system equilibrium decompression trajectories (dashed curves) are calculated using VolatileCalc (for 49 wt.% SiO_2, Newman and Lowenstern, 2002).

Figure 4. Excess concentration of dissolved CO_2 (ΔCO_2, see text for definition) plotted as a function of crystal number density CND_{melt}. (a) P_f = 150 MPa, (b) P_f = 100 MPa, (c) P_f = 25 MPa. Open squares: series #2 post-decompression glasses; open diamonds: series #3 post-decompression glasses; "oxidizing", "intermediate" and "reducing" charges are plotted with the same symbol. The data are for a decompression rate (dP/dt) of 39 kPa/s except when stated otherwise (asterisks: dP/dt = 78 kPa/s). See Table 4 for CO_2 concentrations and Table 3 for *CND* data.

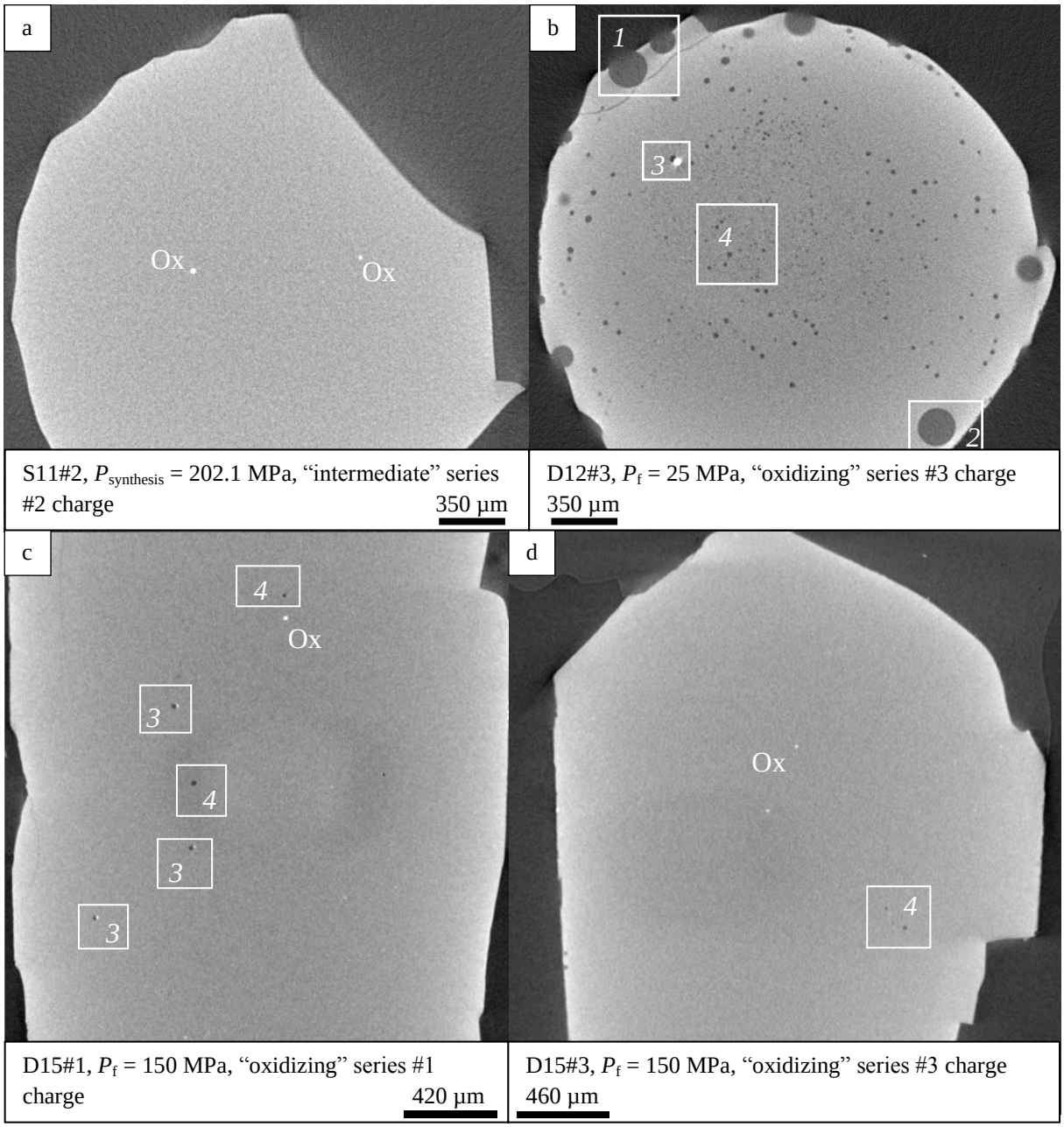

S11#2, $P_{synthesis}$ = 202.1 MPa, “intermediate” series #2 charge 350 µm

D12#3, P_f = 25 MPa, “oxidizing” series #3 charge 350 µm

D15#1, P_f = 150 MPa, “oxidizing” series #1 charge 420 µm

D15#3, P_f = 150 MPa, “oxidizing” series #3 charge 460 µm

Le Gall and Pichavant. Fig. 1

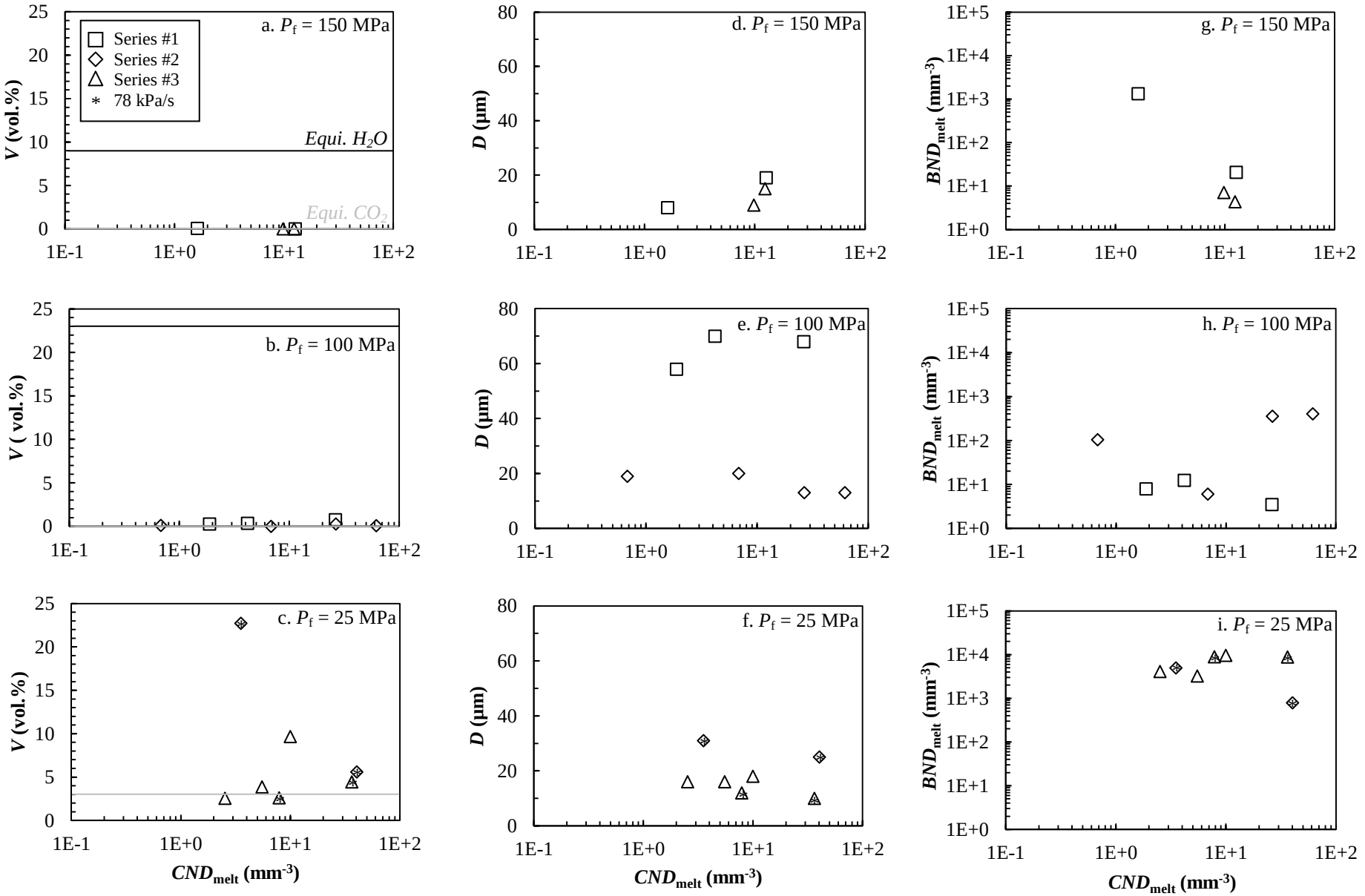

Le Gall and Pichavant. Fig. 2

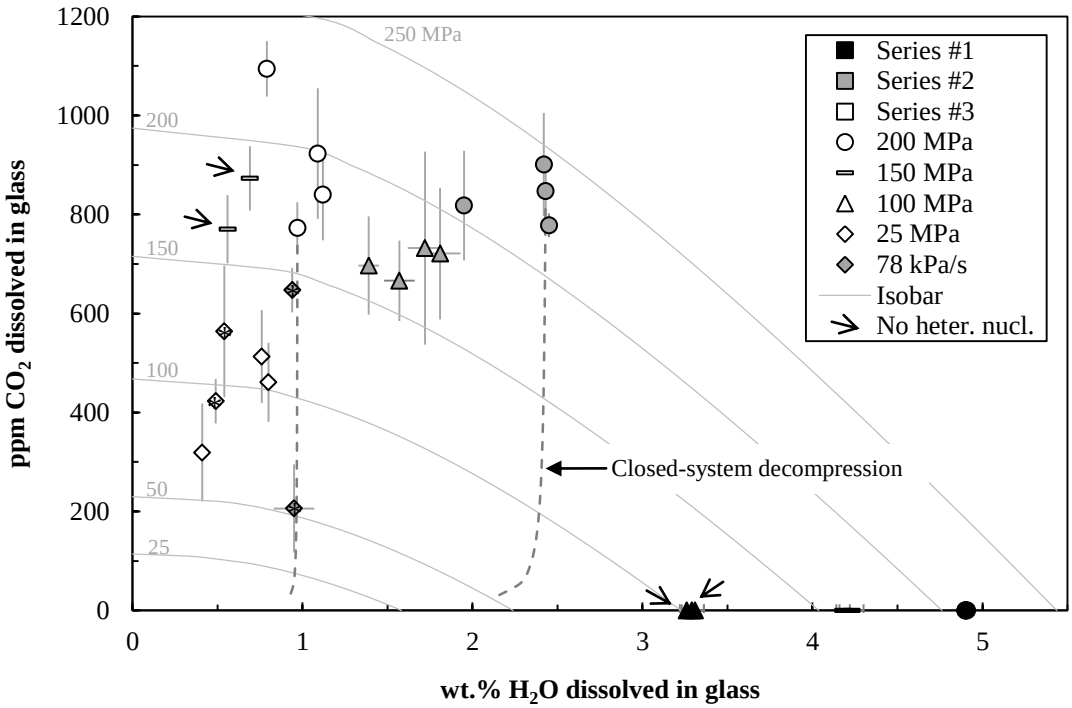

Le Gall and Pichavant. Fig. 3

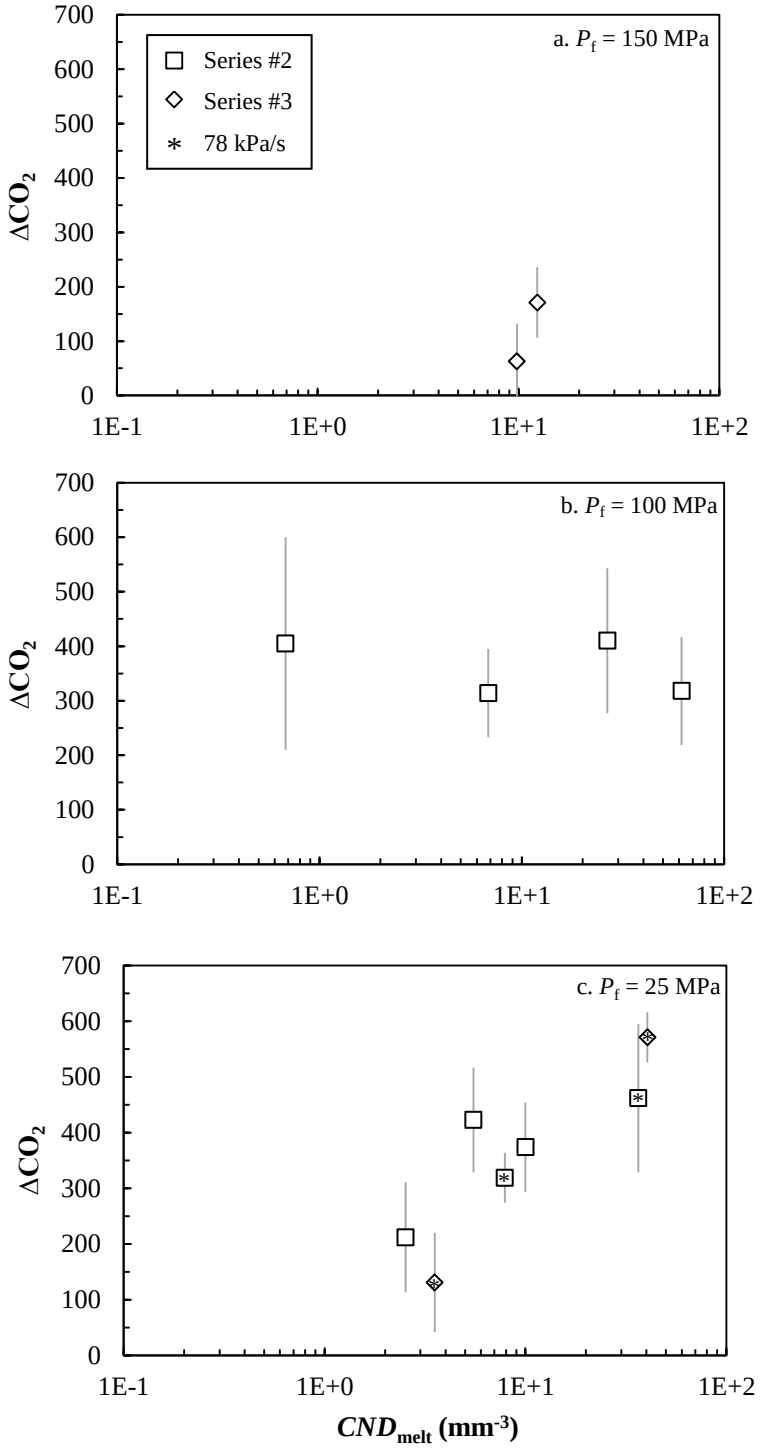

Le Gall and Pichavant. Fig. 4

Table 1. Composition of PST-9 golden pumice and starting glass

Label	PST-9[a]	Glass[b] (*n* = 54)
SiO_2	49.4	50.9 (3)[c]
TiO_2	0.79	0.81 (8)
Al_2O_3	15.75	15.99 (28)
Fe_2O_3	1.3	nd
FeO	6.5	7.7 (6)[d]
MnO	0.15	0.16 (8)
MgO	7.96	7.21 (41)
CaO	12.73	12.34 (24)
Na_2O	2.27	2.39 (9)
K_2O	1.85	1.90 (12)
P_2O_5	0.43	0.55 (17)
Cr_2O_3	–	0.03 (4)
NiO	–	0.05 (6)
Total	99.1	97.4 (10)

Oxides are in wt.%.

[a] Whole-rock analysis performed at CRPG, Nancy, France (from Di Carlo et al., 2006).

[b] Electron microprobe analysis (normalized to 100%) of PST-9 glass (from Le Gall and Pichavant, 2015a), *n*: number of analyses.

[c] One standard deviation in terms of last digit.

[d] Total Fe as FeO.

nd: not determined.

Table 2. Synthesis experiments

Charge	XH_2O_{in}	H_2O melt (wt.%)	CO_2 melt (ppm)	aH_2O[1]	log fO_2	ΔNNO
"Oxidizing" conditions						
Run S10, 1200°C, 201.0 MPa, 40.4h, fH_2=0.2 bar, X_{Ni}=0.03						
Volatile: H_2O (#1)						
S10#1	1	4.90 (2)	–	0.99	–3.36	+4.3
Volatile: H_2O+CO_2 (#2)						
S10#2	0.57	2.43 (2)	847 (51)	0.41	–4.14	+3.6
Volatile: H_2O+CO_2 (#3)						
S10#3	0	0.97 (4)	773 (52)	0.10	–5.40	+2.3
"Intermediate" conditions						
Run S11, 1200°C, 202.1 MPa, 48.3h, fH_2=3.7 bar, X_{Ni}=0.27						
Volatile: H_2O (#1)						
S11#1	1	4.90 (3)	–	0.99	–6.05	+1.7
Volatile: H_2O+CO_2 (#2)						
S11#2	0.55	2.45 (4)	778 (24)	0.41	–6.81	+0.9

XH_2O_{in} = initial molar H_2O / (H_2O + CO_2) in the charge.
Melt H_2O and CO_2 contents by FTIR, standard deviations in parentheses.
[1]aH_2O calculated from H_2O melt using the model of Burnham (1979) and melt composition from Table 1; X_{Ni} is mole fraction of Ni in the alloy phase of the sensor; log fO_2 calculated from experimental fH_2 and fO_2 (determined from aH_2O); ΔNNO = log fO_2 – log fO_2 of the NNO buffer calculated at experimental P and T (Pownceby and O'Neill, 1994).

Table 3. Decompression experiments: run conditions and textural information

Charge	Starting glass	P_{in} (MPa)	P_f (MPa)	t_{ramp} (s)	|dP/dt| (kPa/s)	Bubble 3D characteristics												
						n	pk. size (µm)	range (µm)	D (µm)	BND[a] (mm^{-3})	BND_{melt}[b] (mm^{-3})	S (µm)	V[c] (vol.%)	V[d] (vol.%)	$V_{Equi.\ H2O}$ (vol.%)	$V_{Equi.\ CO2}$ (vol.%)	CND_{melt}[e] (mm^{-3})	Heter. nucl.
"Oxidizing" conditions																		
Volatile: H_2O (#1)																		
D15#1	S10#1	200	150	1284	39	302	17	7–37	19	20.8	20.8	225	0.01	0.02	9.22	–	12.7	×
Volatile: H_2O+CO_2 (#2)																		
D14#2	S10#2	200	100	2568	39	3594	8	7–105	13	406	407	84	0.15	0.08	24.1	0.47	61.7	×
D13#2	S10#2	200	25	2372	78	9048	17	6–435	25	772	783	67	1.52	5.57	72.5	3.47	40.4	×
Volatile: H_2O+CO_2 (#3)																		
D15#3	S10#3	200	150	1284	39	8	7	7–21	9	7.15	7.15	322	0.00	0.00	9.22	0.17	9.82	
D12#3	S10#3	200	25	4488	39	56626	11	10–407	16	3986	4063	39	1.88	2.55	72.5	3.47	2.53	×
D13#3	S10#3	200	25	2372	78	66576	8	6–195	10	8687	8762	30	0.85	4.44	72.5	3.47	36.4	×
"Intermediate" conditions																		
Volatile: H_2O (#1)																		
D16#1	S10#1	200	100	2568	39	4	–	40–102	68	3.51	3.51	408	0.08	0.76	24.1	–	26.3	
D18#1	S11#1	200	100	2568	39	177	–	13–161	70	12.5	12.5	267	0.35	0.55	24.1	–	4.18	×
Volatile: H_2O+CO_2 (#2)																		
D16#2	S10#2	200	100	2568	39	59	19-20	11–29	20	6.03	6.03	341	0.00	0.00	24.1	0.47	6.84	×
D18#2	S11#2	200	100	2568	39	5494	9	9–78	13	359	359	87	0.06	0.26	24.1	0.47	26.5	×
"Reducing" conditions*																		
Volatile: H_2O (#1)																		
D30#1	S16#1	200	150	1284	39	8350	6	4–46	8	1324	1325	56	0.06	0.05	9.22	–	1.62	×
D2#1	S3#1	200	99.8	2568	39	42	29	9–120	58	7.97	7.98	310	0.14	0.28	24.1	–	1.88	
Volatile: H_2O+CO_2 (#2)																		
D2#2	S3#2	200	99.8	2568	39	665	15	15–48	19	104	105	132	0.04	0.10	24.1	0.47	0.68	×
D28#2	S16#2	200	25	2372	78	16187	16	4–424	31	4069	4935	36	17.5	22.7	72.5	3.47	3.53	×

Volatile: H_2O+CO_2 (#3)																		
D1#3	S3#3	200	149.9	1284	39	8	8	7–57	15	4.38	4.38	379	0.01	0.00	9.22	0.17	12.4	
D8#3	S8#3	200	25	4488	39	4029	9	7–59	16	3183	3220	42	1.15	3.87	72.5	3.47	5.51	×
D24#3	S13#3	200	25	4488	39	91765	12	8–135	18	9016	9549	29	5.59	9.25	72.5	3.47	10.0	×
D25#3	S13#3	200	25	2372	78	93103	8	6–425	12	8569	8799	30	2.60	4.97	72.5	3.47	7.89	×

P_{in} (initial pressure): pressure at the beginning of decompression ramp; P_f (final pressure): pressure at which the experiment was quenched; t_{ramp}: duration of the ramp; $|dP/dt|$: decompression rate ($=10^6(P_{in}-P_f)/(gdt_{ramp})$), with g = 9.81 m/s^2 and d = 2.65 kg/m^3.
*Data from decompression experiments under "reducing" conditions from Le Gall and Pichavant (2015a, b).
X-ray microtomographic data acquired on entire charges (except for V^d and CND_{melt}).
n: number of bubbles counted in the analyzed volume.
pk. size: main peak diameter in bubble size distribution histograms.
range: total range of bubble diameters.
D: average bubble diameter.
[a] *BND*: bubble number density expressed in number of bubbles per mm^3 of the total sample (glass + bubbles).
[b] BND_{melt}: bubble number density per melt volume (without bubbles, following Proussevitch et al., 2007).
S: average spacing between bubbles calculated from BND_{melt} ($S = (3/4\pi BND_{melt})^{1/3}$; Lyakhovsky et al., 1996; Baker et al., 2006).
[c] *V*: vesicularity (volume fraction of bubbles, vol.%) measured from the total sample.
[d] *V*: vesicularity measured from representative sub-volumes.
$V_{Equi.H2O}$ and $V_{Equi.CO2}$: equilibrium vesicularities computed for the PST-9 composition considering the degassing of pure H_2O and pure CO_2, respectively (see text).
[e] CND_{melt}: crystal number density expressed in number of Fe–Ti oxide crystals per melt volume (without oxides and bubbles).
Heter. nucl. (Heterogeneous nucleation): charge wherein at least one bubble nucleated on Fe–Ti oxides.

Table 4. FTIR data

Glass	n[a]	Thickness (μm)	Absorbance 3530 cm^{-1}	H_2O (wt.%)	Absorbance 1515 cm^{-1}	CO_2 (ppm)
Synthesis experiments						
"Oxidizing" conditions						
Volatile: H_2O (#1)						
S10#1	5	30 (3)[b]	1.392 (126)	4.90 (2)		
Volatile: H_2O+CO_2 (#2)						
S10#2	5	67 (2)	1.546 (37)	2.43 (2)		
	6	141 (3)			0.272 (21)	847 (51)
Volatile: H_2O+CO_2 (#3)						
S10#3	5	150 (3)	1.415 (85)	0.97 (4)	0.263 (18)	773 (52)
"Intermediate" conditions						
Volatile: H_2O (#1)						
S11#1	10	23 (2)	1.077 (96)	4.90 (3)		
Volatile: H_2O+CO_2 (#2)						
S11#2	8	51 (3)	1.197 (79)	2.45 (4)		
	6	128 (6)			0.226 (17)	778 (24)
"Reducing" conditions						
Volatile: H_2O (#1)						
S3#1	4	37 (2)	1.697 (92)	4.91 (3)		
S16#1	7	31 (5)	1.429 (225)	4.90 (2)		
Volatile: H_2O+CO_2 (#2)						
S3#2	5	65 (7)	1.209 (142)	1.95 (1)	0.123 (28)	818 (111)
S16#2	6	32 (2)	0.734 (50)	2.42 (3)	0.065 (11)	901 (104)
Volatile: H_2O+CO_2 (#3)						
S3#3	5	33 (4)	0.351 (45)	1.12 (1)	0.065 (8)	840 (92)
S8#3	8	128 (11)	0.975 (84)	0.79 (1)	0.317 (39)	1094 (56)
S13#3	8	111 (5)	1.168 (75)	1.09 (3)	0.129 (21)	923 (132)

Decompression experiments

"Oxidizing" conditions

Volatile: H_2O (#1)

D15#1	8	34 (3)	1.340 (114)	4.18 (4)		

Volatile: H_2O+CO_2 (#2)

D14#2	11	141 (4)	1.902 (124)	1.39 (6)	0.224 (36)	697 (99)
D13#2	9	166 (0)	1.514 (75)	0.94 (5)	0.243 (17)	647 (45)

Volatile: H_2O+CO_2 (#3)

D15#3	9	169 (7)	0.921 (79)	0.56 (3)	0.295 (36)	770 (69)
D12#3	8	45 (5)	0.176 (20)	0.41 (1)	0.032 (8)	319 (99)
D13#3	8	132 (5)	0.688 (47)	0.54 (2)	0.170 (44)	564 (133)

"Intermediate" conditions

Volatile: H_2O (#1)

D16#1	7	53 (3)	1.646 (95)	3.26 (3)		
D18#1	7	35 (2)	1.082 (63)	3.28 (2)		

Volatile: H_2O+CO_2 (#2)

D16#2	5	56 (22)	0.849 (350)	1.57 (9)		
	4	64 (12)			0.096 (16)	666 (81)
D18#2	6	48 (12)	0.903 (187)	1.81 (12)	0.085 (28)	721 (133)

"Reducing" conditions

Volatile: H_2O (#1)

D30#1	14	18 (3)	0.718 (121)	4.23 (7)		
D2#1	6	41 (4)	1.294 (136)	3.31 (5)		

Volatile: H_2O+CO_2 (#2)

D2#2	4	28 (0)	0.467 (32)	1.72 (10)		
	7	151 (8)			0.251 (75)	732 (195)
D28#2	9	61 (6)	0.566 (84)	0.95 (12)	0.029 (13)	206 (89)

Volatile: H_2O+CO_2 (#3)

D1#3	6	122 (3)	0.812 (43)	0.69 (3)	0.241 (22)	873 (65)

D8#3	8	160 (0)	1.181 (45)	0.76 (3)	0.186 (34)	513 (94)
D24#3	12	98 (14)	0.765 (138)	0.80 (5)	0.103 (27)	461 (80)
D25#3	7	73 (4)	0.350 (40)	0.49 (4)		
	6	123 (9)			0.118 (14)	423 (45)

S3 to S16: glass synthesis experiments; D1 to D28: glass decompression experiments.

[a] Number of analytical spots.

[b] One standard deviation in terms of the last digit.

Chapitre vi

Partage du soufre entre liquide et gaz lors de l'ascension et du dégazage d'un magma basaltique contenant les volatils C-H-O-S

Résumé

L'ensemble d'expériences de décompression présenté dans ce chapitre a pour but d'étudier l'évolution de la phase volatile (H_2O, CO_2, S) lors de la remontée d'un magma basaltique. L'influence du soufre sur les processus physiques et chimiques du dégazage et la distribution du soufre entre le liquide basaltique et la phase gazeuse (ou fluide) ont été particulièrement étudiés.

Des liquides basaltiques d'une composition naturelle du Stromboli (ponce PST-9) ont été synthétisés à pression (200 MPa) et température (1200°C) constantes, avant d'être immédiatement décomprimés jusqu'à des pressions finales (P_f) comprises entre 150 et 25 MPa, et rapidement trempés. Deux taux de décompression ont été appliqués : 39 et 78 kPa/s (ou 1,5 et 3 m/s). Les expériences ont été menées en conditions oxydantes (NNO+1,1) afin que tout le soufre dissous dans la phase liquide soit présent sous forme sulfatée (S^{6+}). Les verres expérimentaux ont été analysés par microsonde électronique pour S et par spectroscopie infrarouge pour H_2O et CO_2.

Après synthèse, les verres contiennent 2,72 ± 0,02% pds H_2O, 1291 ± 85 ppm CO_2 et 1535 ± 369 ppm S, dans la gamme des inclusions vitreuses des ponces du Stromboli. Dans certaines charges, une association texturale entre les bulles et les sulfures de fer (FeS) présents dans le liquide est observée, témoignant d'un processus de nucléation hétérogène des bulles qui reste toutefois d'importance limitée. Les bulles commencent à nucléer de façon hétérogène pour des pressions de sursaturation $\Delta P_{HeN} \leq 1$ MPa, et de façon homogène pour $\Delta P_{HoN} < 50$ MPa (ΔP_{HeN} et ΔP_{HoN} sont les différences entre la pression de saturation et les pressions de nucléation hétérogène et homogène, respectivement). Les vésicularités sont comprises entre 0,6 et 45 vol%, et elles augmentent avec la baisse de pression. Une micro poche de gaz ("gas slug") est présente dans une charge décomprimée à 25 MPa, résultant de la coalescence de bulles ainsi que d'une séparation physique quasi-complète entre gaz et liquide. Au cours de la décompression, les pertes en H_2O et S des liquides sont plus importantes qu'attendues lors d'un dégazage à l'équilibre. Au contraire, de fortes concentrations en CO_2, bien plus élevées que les solubilités, persistent dans les verres après décompression. Le trajet de dégazage des volatils enregistré par les verres naturels du Stromboli est étroitement simulé par nos expériences. L'ajout de soufre n'affecte ni le comportement de H_2O, ni celui du CO_2, au cours du dégazage magmatique ; le CO_2 est le volatil dont le comportement dévie le plus de l'équilibre. La composition de la phase fluide exsolvée, calculée par bilan de masse,

montre que les deux rapports molaires H_2O/CO_2 et CO_2/SO_2 augmentent légèrement avec une diminution de P_f pour les deux taux de décompression étudiés. Le coefficient de partage du soufre entre fluide et liquide ($D_S^{fl/liq}$ = 129–228) n'est influencé ni par le taux de décompression, ni par la pression finale. Les rapports molaires H_2O/CO_2 et CO_2/SO_2 de la phase fluide expérimentale reproduisent tous deux les faibles valeurs mesurées au Stromboli lors du dégazage passif. Les rapports H_2O/CO_2 associés à l'activité explosive sont eux aussi reproduits de manière satisfaisante. Au contraire, les rapports CO_2/SO_2 associés aux éruptions normales et majeures sont bien plus élevés que dans nos expériences. Cependant, nos données pour la série de verres décomprimés à 78 kPa/s suggèrent que de plus fortes valeurs de CO_2/SO_2 pourraient être atteintes à P_f << 25 MPa. Nos observations expérimentales supportent un modèle de dégazage explosif de liquides sursaturés en CO_2 à basse pression pour générer les paroxysmes éruptifs au Stromboli. Nos données ont aussi des implications pour l'interprétation des mesures de gaz en sortie de conduit.

Sulfur partitioning between melt and fluid during degassing of ascending C-O-H-S-bearing basaltic magma: an experimental study

Nolwenn Le Gall[1, 2, 3] · **Michel Pichavant**[1, 2, 3] · **Ida Di Carlo**[1, 2, 3] · **Bruno Scaillet**[1, 2, 3]

[1] Université d'Orléans, ISTO, UMR 7327, 45071, Orléans, France
[2] CNRS/INSU, ISTO, UMR 7327, 45071, Orléans, France
[3] BRGM, ISTO, UMR 7327, BP 36009, 45060, Orléans, France

Abstract We present high pressure and temperature decompression experiments to constrain the degassing of volatiles (H_2O, CO_2, S) and the fluid-melt partitioning of S in ascending basaltic magma. Volatile-bearing (2.72 ± 0.02 wt.% H_2O, 1291 ± 85 ppm CO_2, 1535 ± 369 ppm S) Stromboli melts were synthesized at constant pressure (200 MPa) and temperature (1200°C) prior to be immediately decompressed to final pressures (P_f) ranging from 150 to 25 MPa, and then rapidly quenched. Continuous decompressions were conducted at rates of 39 and 78 kPa/s (corresponding to ascent velocities of 1.5 and 3 m/s). Experiments were performed under oxidizing conditions (fO_2: NNO+1.1) so that all sulfur occurs as sulfate (S^{6+}) in the melt. Experimental glasses were analyzed by electron microprobe (S) and IR spectroscopy (H_2O, CO_2). A preferential textural association between bubbles and iron sulfides present in the melt interpreted to indicate heterogeneous bubble nucleation, is revealed in a few charges. Bubbles start to nucleate heterogeneously for supersaturation pressures $\Delta P_{HeN} \leq 1$ MPa and to nucleate homogeneously for $\Delta P_{HoN} < 50$ MPa (ΔP_{HeN} and ΔP_{HoN} are the difference between the saturation pressure and the nucleation pressure, respectively). Vesicularities range from 0.6 to 45 vol.%, increasing with decreasing P_f. A micro gas slug is present in one 25 MPa P_f charge, indicating bubble coalescence and bubble-melt physical separation. During decompression, H_2O and S are lost from the melt more importantly than expected from equilibrium degassing, while CO_2 is retained at elevated concentration levels in the melt. The volatile degassing trend recorded by Stromboli natural glasses is closely experimentally simulated. S addition does not affect the degassing behavior of H_2O and CO_2; the latter appearing to be the component that deviates the more strongly from equilibrium. The composition of the exsolved fluid phase, calculated by mass balance, shows that both the H_2O/CO_2 and CO_2/SO_2 molar ratios slightly increase with decreasing P_f

for the two ascent rates investigated. The sulfur partition coefficient between fluid and melt ($D_S^{fl/m}$ = 129–228) is greatly influenced neither by the decompression rate nor by P_f. The experimental H_2O/CO_2 and CO_2/SO_2 fluid molar ratios both reproduce the lower ranges of gas ratios measured at Stromboli for quiescent magma degassing. The H_2O/CO_2 gas ratios associated with explosive activity are also satisfactorily reproduced. In contrast, the CO_2/SO_2 accompanying the normal and major explosions are much higher than in our experiments. However, our results for the 78 kPa/s glass series suggest the possibility of still higher CO_2/SO_2 values at P_f << 25 MPa. Our experimental observations support a model of low pressure explosive degassing of CO_2-rich melts to generate Strombolian paroxysms. They also have implications for the interpretation of the geochemistry of volcanic fluids.

Keywords Decompression experiments . Basalt . Magma degassing . Sulfur . Melt-vapor partitioning . Stromboli

1. Introduction

Volcanic eruptions induce changes in geochemical observables (composition and flux of volcanic gases; e.g. Aiuppa and Federico, 2004; Burton et al., 2007; Allard et al., 2008; Aiuppa et al., 2009, 2010a, b, 2011; Allard, 2010; La Spina et al., 2013) whose record and interpretation in terms of eruption precursors is critical for volcanic risk mitigation (Saccorotti et al., 2014). Interpretation of geochemical measurements is based on the assumption that degassing occurs at equilibrium (e.g. Burgisser and Scaillet, 2007; Burton et al., 2007), while recent experiments (Pichavant et al., 2013; Le Gall and Pichavant, 2015a, b, c) have reported the possibility of disequilibrium degassing during ascent and decompression of CO_2-bearing basaltic melts. Therefore, interpreting the geochemistry of magmatic fluids is a difficult task which stresses the need for additional data and models to more fully understand the degassing behavior of ascending basaltic magma.

Volatiles play an important role in the monitoring and forecasting of eruptions, especially sulfur which is the third component present in volcanic gases (after H_2O and CO_2). This is understandable as the measurement of S emissions and fluxes is relatively easy (Stoiber et al., 1983; Saccorotti et al., 2014). Several studies have reported correlations between S time series in volcanic gases and type and intensity of volcanic activity

(Malinconico, 1979; McGee and Sutton, 1994; Allard et al., 1994; Saccorotti et al., 2014). Increases in SO_2 flux prior to explosive eruptions have been frequently documented at intermediate to silicic volcanoes (e.g. at Pinatubo, Philippines, Daag et al., 1996, and Tungurahua volcanoes, Ecuador, Hidalgo et al., 2013; Saccorotti et al., 2014), and interpreted as near-surface manifestations of degassing mechanisms occurring at depth. In basaltic systems, transition from effusive to highly explosive activity is occasionally observed. In that case, violent explosions are systematically preceded by a phase of increasing CO_2/SO_2 ratio and CO_2 flux, as documented at Etna (Aiuppa et al., 2007) and at Stromboli (Aiuppa et al., 2009, 2010b, 2011) volcanoes. The origin of such changes in gas ratios and fluxes, although debated, has been often attributed to deep CO_2-rich volatile fluxes in the volcano plumbing system (CO_2-flushing models, Allard, 2010; Aiuppa et al., 2010a, 2011). Critical in the interpretations is the knowledge of the partitioning of the various volatile species (CO_2, S) between basaltic melt and fluid as a function of pressure (Moretti and Papale, 2004; Burton et al., 2007; Aiuppa et al., 2009; Allard, 2010).

During decompression of volatile-bearing melts, volatile degassing is controlled by the partitioning of volatile components between melt and gas. In recent experiments (Pichavant et al., 2013; Le Gall and Pichavant, 2015a, b, c), CO_2 was found to be preferentially partitioned in the melt until high vesicularities are reached, i.e. until the latest stages of degassing. This disequilibrium behavior, favored by short gas-melt interface and volatile diffusion distances (Pichavant et al., 2013), contrasts with the equilibrium model that is classically assumed (e.g. Dixon et al., 1995; Dixon and Stolper, 1995). This study aims at further experimentally testing mechanisms of basaltic magma degassing by considering sulfur-bearing systems. Although a critical component of the magmatic gas phase, S has been largely excluded from experimental degassing simulations mainly because it is a difficult element to work with. In basaltic systems, partitioning of S between fluid and melt has been investigated by Moune et al. (2009), Beermann (2010), Lesne et al. (2011c), Fiege et al. (2015), and also reviewed by Webster and Botcharnikov (2011). Experiments have been performed at 1050–1250°C, 25–400 MPa, and at fO_2 ranging from NNO–2 to NNO+3.2. These studies have shown that S partitioning is highly sensitive to fO_2 (Beermann, 2010; Fiege et al., 2015) and compositional effects (Lesne et al., 2011c), as well as potentially sensitive to P (Lesne et al., 2011c) and T (Fiege et al., 2015). Fiege et al. (2015) investigated the influences of melt MgO, H_2O and Cl contents on S partitioning. Their conclusions for H_2O and Cl contrast with those of Moune et al. (2009) for H_2O and of Beermann (2010) for Cl which document strong influences of those

chemical parameters on S partitioning. The only study were disequilibrium S partitioning between fluid and melt was encountered is that of Fiege et al. (2015), a behavior consistent with the low reported S diffusivity in silicate melts (Freda et al., 2005).

In this paper, we report continuous decompression experiments performed to simulate the ascent and degassing of H_2O-CO_2-S-bearing basaltic melts. Experimental conditions simulate those potentially encountered during paroxysmal events that occur at explosive basaltic volcanoes. The experiments model the degassing behavior of sulfur (and also of CO_2 and H_2O) and aim to assist in the interpretation of geochemical observables. The study is backed up by gas data available in particular at Stromboli (Aeolian Islands, Italy) which serves both as a reference example of explosive basaltic volcano and as a source of data (glass inclusions and volcanic gases) for comparison with our experimental results.

2. Experimental techniques

This study builds upon previous decompression experiments performed on H_2O and H_2O-CO_2-bearing basaltic melts (Le Gall and Pichavant, 2015a, b, c). The introduction of sulfur necessitated to modify several critical aspects of the experimental and analytical methods (starting composition, source of volatiles, containers, physical state of the starting material, i.e. glass powder vs. glass core, use of 2D images instead of 3D micro-CT data). *Synthesis* experiments were carried out first to adjust the H_2O, CO_2 and S concentrations in the pre-decompression melts to the volatile concentrations of the Stromboli melt inclusions. Then, *decompression* experiments were performed by combining in the same experiment the synthesis and decompression steps. This enables to reduce experimental durations, thus limiting problems of capsule failure which were found to be particularly severe in this study.

2.1. Starting material and capsule preparation

A poorly crystallized, high-K basaltic pumice from Stromboli was used as starting material (sample PST-9, Di Carlo et al., 2006; Pichavant et al., 2009, 2011). The composition of this golden pumice, ejected during a paroxysmal explosion, is representative of the magma at depth (49.4 wt.% SiO_2, 7.96 wt.% MgO, 1.85 wt.% K_2O, Table 1) in the Stromboli plumbing system. The sample was crushed to a fine powder and then fused in air at 1400°C in

a Pt crucible for 3 hours. The resulting glass was crushed again and 1% of iron (as Fe_2O_3) was added to generate a Fe-enriched mixture prepared to compensate for Fe loss to the Pt capsule (Brugier et al., 2015). The glass-Fe_2O_3 mixture was then melted under the same conditions as above. The resulting iron-enriched glass was powdered (~10–50 µm) and a glass chip was set aside for electron microprobe analysis, to ensure that Fe was homogeneously distributed. Glass compositions are given in Table 1.

Between 30 and 100 mg of powdered iron-enriched basalt glass, distilled water, carbon dioxide as oxalic acid dihydrate ($C_2H_2O_4.2H_2O$), and sulfur as elemental S were loaded into Pt capsules (2.5 mm inner diameter, 0.2 mm wall thickness, 30–45 mm length). Such a metal composition has the disadvantage of reacting with Fe from the charge, but possesses the advantage of being less sensitive to S compared to AuPd which can produce S-bearing alloys (Pichavant et al., 2006) and corrode capsules (Lesne, 2008; Webster and Botcharnikov, 2011). CO_2 addition as $C_2H_2O_4.2H_2O$ avoids using $Ag_2C_2O_4$ (silver oxalate) which can form silver sulfides (Ag_2S; Lesne, 2008; Webster and Botcharnikov, 2011). Although the use of powders can contribute to the formation of bubbles during synthesis, the use of cylinders as starting materials (Le Gall and Pichavant, 2015a, b, c) proved impossible in presence of sulfur because homogenization of the S (and also of the H_2O and CO_2) distribution in the melt requires durations largely exceeding the lifetime of the capsules. Indeed, in 72 h synthesis experiments, S was found to corrode the capsule walls by forming platinum sulfides, hereafter designated as PtS ($Pt_{84–85}S_{15–16}$, wt.% basis, Fig. 1a), which systematically led to capsules failure. Therefore, the use of glass powders and short (~1 h) synthesis durations (nevertheless sufficient to achieve a homogeneous distribution of S, H_2O and CO_2 in the melt), were adopted.

The proportions of H_2O, CO_2 and S introduced in the Pt capsules were adjusted to match the pre-eruptive volatile concentrations analyzed in Stromboli pumice glass inclusions (Métrich et al., 2001; Bertagnini et al., 2003; Métrich et al., 2010). To do so, H_2O, CO_2 and S were loaded in proportions ranging from XH_2O_{in} (initial molar H_2O / (H_2O + CO_2)) and XCS_{in} (initial molar CO_2 / (CO_2 + S)) of 0.51–0.64 and 0.45–0.59, respectively. All capsules were welded shut and weighed before and after the experiments, to ensure that no volatile loss occurred.

2.2. Apparatus and run procedure

Experiments were performed in an internally heated pressure vessel (IHPV) operated in a vertical position and equipped with a drop quench set up. Ar–H_2 gas mixtures were used as the pressurizing medium and to control the redox conditions. Experiments were run with an initially applied pressure of 1 bar H_2. Argon was then pumped into the vessel up to the pressure needed to attain the final target conditions (Pichavant et al., 2013). Determinations of experimental fH_2 have not been performed specifically for this study, for example using Ni–Pd oxygen sensors (Taylor et al., 1992; Di Carlo et al., 2006). Instead, we use fH_2 measurements made from Ni–NiPd sensors in companion experiments performed in the same autoclave and under the same P–T–fH_2 conditions (Le Gall and Pichavant, 2015b). They yield log fO_2 = NNO+1.08 (NNO is the fO_2 of the Ni–NiO equilibrium at 200 MPa and 1200°C) for synthesis experiments of this study.

Pressure was measured using a pressure transducer calibrated against a Heise gauge, to ± 20 bars. The capsule (one for each run) was placed in a sample holder made of an alumina tube, itself hold in the 2–3 cm long hotspot of a molybdenum furnace by a Pt wire. Temperature was measured to ± 5°C using two thermocouples (type S) placed along the length of the capsule. Near-isothermal conditions (gradient < 2–3°C/cm) were maintained in the sample holder. Experiments were drop quenched in a few seconds (Di Carlo et al., 2006). The Pt suspension wire was fused electrically, allowing the sample holder to fall into the cold part of the IHPV.

Synthesis experiments were performed at 200 MPa and 1200°C, which are conditions known to be above the liquidus of the golden pumice sample PST-9 on the basis of previous phase equilibrium experiments (Di Carlo et al., 2006; Pichavant et al., 2009). Just one capsule was placed in the IHPV for a short duration of about one hour, according to the diffusion rates of H_2O, CO_2 and especially S which is much slower (Freda et al., 2005; Zhang and Ni, 2010). In *decompression* experiments, following the one-hour synthesis step at 200 MPa, 1200°C, pressure was decreased manually from an initial pressure (P_{in}) of 200 MPa to final pressures (P_f) ranging from 150 to 25 MPa. Fast rates of 39 and 78 kPa/s (1.5 and 3m/s, respectively, taking a rock density of 2.65 kg/m^3) were applied, leading to decompression durations of 20–75 min and 10–40 min, respectively, depending on P_f. Decompression charges were rapid-quenched immediately after attainment of P_f.

Capsules were removed from the IHPV, checked that they remained sealed during the experiments and then carefully opened. The presence of a vapor phase was confirmed by a

characteristic sound when puncturing the capsule and the release of water from the capsules during opening.

3. Analytical techniques

3.1. Sample preparation

After the synthesis and the decompression experiments, the glasses (pre- and post-decompression glasses, respectively) were subdivided into several parts for analytical purposes. Note that in the decompression experiments, only compositions of post-decompression glasses are known (compositions of glasses produced after the synthesis step have not been determined). One part (or several parts when numerous analyses were needed) was doubly-polished for volatile (H_2O, CO_2) analysis by IR spectroscopy. Another part (or small glass fragments) was embedded into epoxy resin and polished for electron microprobe analysis and scanning electron microscope (SEM) textural observations.

3.2. Textures

Textures of experimental charges were observed on a Tescan Mira3 XMU Field Emission Scanning Electron Microscope (FESEM) instrument with a working distance of 3780–13.6 mm and an accelerating voltage of 25 kV. SEM images were collected at ISTO, Orléans, and the images (one for each sample) analyzed to determine vesicularity. Vesicularity is determined from an average of 4 values obtained by counting the surfaces of glass and bubbles present on the image. This was performed using the ImageJ Voxel Counter plugin (Abràmoff et al., 2004). The image was subdivided manually in order to exclude the void space of the segmented SEM image.

3.3. Major elements and sulfur

Experimental glasses were analyzed, using a SX FIVE CAMECA electron microprobe at ISTO, Orléans. The following analytical conditions were applied: 15 kV accelerating voltage, 6 nA beam current, 10 s counting time on peak and a defocused beam of 5 µm diameter. A ZAF correction procedure was applied. Glasses were analyzed for major elements

and S, assuming that S is predominantly present as S^{+6} (SO_4^{2-}) since conditions are relatively oxidizing (ΔNNO > 1; Jugo et al., 2010; Witham et al., 2012). Barite ($BaSO_4$, sulfate) standard was used for sulfur calibration. To check for homogeneity, multiple analyses and traverses (n = 27–44) were performed for each glass sample. The S determinations were validated by analyzing two synthetic secondary glass standards prepared in this study and whose S contents were known from wet chemical techniques (CRPG, Nancy). Comparable concentrations were obtained by both methods, the electron microprobe data yielding values within 5% relative of the wet chemical data. Multiple analyses (n = 243) of one secondary glass standard (S = 3583 ppm) yielded a standard deviation of 300 ppm which is taken below as the analytical error on sulfur. A few capsules were also analyzed to characterize the phases produced as a result of the interactions between the charges and Pt capsules. Modified analytical conditions were applied: 15 or 20 kV accelerating voltage, 20 nA beam current and a focused beam of 1 µm diameter.

3.4. H_2O and CO_2

Water and carbon contents (the latter as carbonate groups CO_3^{2-}) in quenched glasses were determined by IR spectroscopy. A Nicolet 6700 spectrometer coupled to a Continuµm FT-IR microscope and equipped with an IR source, a KBr beamsplitter and a liquid nitrogen cooled MCT/A detector was used. To check the distribution of volatiles in the experimental glasses, 1D profiles were performed using a 50x50 µm square aperture. Spectra were accumulated for 128 scans at a resolution of 4 cm^{-1} on doubly polished glass chips, with thicknesses varying between 33 and 144 µm. Sample thickness was measured with an optical microscope to a precision of 1–2 microns. H_2O and CO_2 concentrations were calculated with Beer's law from absorbance spectra peaks at 3530 and 1515 cm^{-1}, respectively. To eliminate oscillation effects and maximize the 1515 cm^{-1} band, thicker samples were prepared. Absorbance of the 3530 cm^{-1} total H_2O band was measured with a straight base line. That of the 1515 cm^{-1} carbonate ions band was determined by subtracting the spectrum of a glass without volatiles and of the same thickness. For H_2O we considered a ε of 64 $L.mol^{-1}.cm^{-1}$ (Dixon et al., 1995) and for CO_2, we calculated a ε of 363 $L.mol^{-1}.cm^{-1}$ from the Dixon and Pan equation (1995), as ε^{1525}=451-342 [Na/(Ca+Na)]. Densities of experimental glasses were determined from the density of the volatile-free starting glass measured using a Mettler balance equipped with a density accessory kit (ρ = 2.747 ± 0.001) and considering a partial

molar volume of H_2O of 12 cm^3/mol (Richet et al., 2000). Only the influence of dissolved H_2O on the glass density was considered and the effects of CO_2 and S both assumed negligible (Lange, 1994; Bourgue and Richet, 2001; Lesne et al., 2011a). Analytical errors on the determined H_2O and CO_2 concentrations are 0.1 wt.% and 100 ppm, respectively.

3.5. Fluid phase

The composition of the exsolved vapor phase in both the synthesis and decompression capsules was determined by mass balance. To do so, the amounts of silicate glass and volatiles (H_2O, CO_2, S) initially loaded in the capsule, as well as their concentrations in the experimental melts, must be known. In addition, we also considered in the calculations the additional amount of H_2O produced by the reduction of Fe^{3+} with H_2 from the pressurizing medium, via the following reaction (e.g. Lesne et al., 2011a):

$$Fe_2O_{3melt} + H_{2vap} = 2FeO_{melt} + H_2O_{vap} \text{ (Eq. 1)}$$

The amount of H_2O produced via Eq. 1 (0.75 wt.% H_2O) was constrained from companion experiments (Le Gall and Pichavant, 2015a, b, c) and is consistent with previous estimations (Lesne et al., 2011c).

It is worth noting that sulfur is not uniquely distributed between melt and fluid. As mentioned above, sulfur was found to systematically react with the capsule to form platinum sulfides (PtS: $Pt_{84–85}S_{15–16}$, wt.% basis). The amount of PtS formed, estimated by mass balance, varies between experimental capsules. Between 23 and 51% of the sulfur initially introduced in the capsule is sequestered in PtS phases (Table 2). The mass balance calculation of the gas phase composition takes into consideration the amount of sulfur locked as PtS. Results are expressed in wt.% H_2O, CO_2 and S which are then converted to mol% H_2O, CO_2 and SO_2.

Sulfur is also present in a few charges as iron sulfides, but their abundance is always very low and these phases were not considered in the mass balance calculations.

3.6. Fluid-melt equilibrium computations

Equilibrium gas-melt computations (H_2O, CO_2 and S solubilities as a function of P–T conditions, isobaric solubility curves and closed-system equilibrium decompression paths) were modeled with the software D-Compress (Burgisser et al., 2015), for a PST-9 basaltic melt.

4. Experimental results

4.1. Charge-capsule interactions

Iron and sulfur from the melt were found to systematically react with the container Pt capsule. As expected (Brugier et al., 2015), the use of a Fe pre-enriched starting glass (Table 1) minimized Fe loss from the charges which ranges from –5 to –16% (Table 2). In general, Fe loss was found to increase with experimental duration. The glass from the shortest experiment has a Fe loss of –6% (S19 from the synthesis experiment) while the two glasses from the longest runs have Fe losses of –16 (S+D37) and –12% (S+D40), among the highest (Table 2). Sulfur was found to be sequestered in platinum sulfides (1–25 µm in size, Fig. 1a), forming a nearly continuous rim in the inner wall of the capsule. The PtS phases are Fe-poor (maximum 0.19 wt.% Fe) yet they coexist with a FePt alloy (~5 wt.% Fe) which is almost S-free (maximum 0.6 wt.% S). Iron sulfides (identified by SEM) also occur in the melt, in most cases forming very small (< 10 µm) phases.

4.2. Textural observations

All experimental charges were recovered as single glassy blocks. The absence of silicate and oxide crystals was checked by optical microscopy on the doubly polished sections prepared for FTIR and also by SEM.

In the synthesis experiment, the glass S19 (hereafter designated as the pre-decompression glass) contains a few small (≤ 6.5 µm) bubbles together with small (≤ 6 µm) iron sulfides, localized in the sample center (Fig. 1b, c). Bubbles are found to be attached to the iron sulfides (Fig. 1c), in a textural relation similar to that described for heterogeneous bubble nucleation on Fe–Ti oxides (Le Gall and Pichavant, 2015c). A bubbly rim is present at the glass-capsule interface (< 85 µm, Fig. 1b), representing the space filled by the free gas phase in the capsule (Pichavant et al., 2013).

In the decompression experiments, all glasses (hereafter designated as post-decompression glasses) contain various amounts of bubbles. Vesicularities range from 0.6 to 45 vol.% (Table 2), increasing with decreasing P_f. Given the general absence of crystals (hence of possible nucleation sites, Le Gall and Pichavant, 2015c) and the uniform spatial distribution of bubbles, we interpret the textures of the 39 and 78 kPa/s series glasses to result from homogeneous bubble nucleation. Iron sulfides are present in two 78 kPa/s series glasses decompressed to P_f = 100 (S+D34, Fig. 1d) and 50 MPa (S+D35) but without systematic textural association with bubbles, indicating that heterogeneous bubble nucleation plays a minor role in this study (Le Gall and Pichavant, 2018c). However, heterogeneous bubble nucleation occurs on the inner wall of the capsule (e.g. Mourtada-Bonnefoi and Laporte, 2002), being marked by a bubbly rim of small (< 10–70 µm) bubbles. One charge (S+D38) is characterized by the occurrence of a very large (~1670 µm) bubble open to the free gas phase, similar to a micro gas slug (Fig. 2a).

4.3. Volatile contents of experimental glasses

Volatile contents are reported in Tables 3 and 4. The glass from the synthesis experiment contains 2.72 ± 0.02 wt.% H_2O, 1291 ± 85 ppm CO_2 and 1535 ± 369 ppm S, in the range of melt inclusions in Stromboli golden pumices (1.8–3.4 wt.% H_2O, 894–1689 ppm CO_2 and 1520–2450 ppm S, Métrich et al., 2001; Bertagnini et al., 2003 Métrich et al., 2010).

If standard deviations are compared with analytical errors for H_2O (± 0.1 wt.%), CO_2 (± 100 ppm) and S (± 300 ppm), the pre-decompression glass has homogeneous H_2O and CO_2 concentrations and a sub-homogeneous S concentration. FTIR profiles reveal a homogeneous distribution of H_2O and CO_2 in the glass; near-rim H_2O and CO_2 concentrations are identical within error to values measured in the center of the glassy block. In the S-free system, a solubility of 1170 ± 277 ppm CO_2 was experimentally determined by Lesne et al. (2011a) at a pressure of 205.9 MPa. In the S-bearing system, Lesne (2008) found a S concentration of 5865 ± 78 ppm in experiments on a K-enriched PST-9 melt performed under conditions more oxidizing than in this study.

Glasses from the 39 kPa/s decompression experiments have 2.58 to 1.31 wt.% H_2O, 1238 to 315 ppm CO_2 and 1384 to 965 ppm S (Tables 3 and 4). A general decrease of dissolved H_2O and CO_2 contents is observed with decreasing P_f (Fig. 3a). The glass

decompressed to 150 MPa P_f (2.85 wt.% H_2O and 1238 ppm CO_2, S+D32) has the highest H_2O and CO_2 concentrations and the glass decompressed to 25 MPa P_f (1.31 wt.% H_2O and 315 ppm CO_2, S+D40) has the lowest H_2O and CO_2 concentrations. Sulfur concentrations progressively decrease with decreasing P_f (Fig. 3b).

In the 78 kPa/s series, the post-decompression glasses have 2.30 to 1.39 wt.% H_2O, 1264 to 290 ppm CO_2 and 1121 to 730 ppm S (Tables 3 and 4). As in the 39 kPa/s series, a general decrease of melt H_2O and CO_2 contents is observed with decreasing P_f (Fig. 3a). With lowering pressure, the amount of S dissolved in the 78 kPa/s series melts remains almost constant between 150 and 50 MPa P_f and then decreases below 50 MPa down to 25 MPa P_f (Fig. 3b). In detail, a slight increase in dissolved S is observed between 100 and 50 MPa P_f, possibly related to the dissolution of iron sulfides in the melt.

Volatile concentrations of post-decompression glasses are compared with theoretical equilibrium values computed with D-Compress (Burgisser et al., 2015). A test of the software was first performed by calculating the S concentration of a PST-9 melt (with 2.72 wt.% H_2O and 1220 ppm CO_2) equilibrated at 1200°C, 200 MPa, NNO+1.08. The calculated concentration (1537 ppm S) is almost identical to the S concentration of the pre-decompression glass. In a second step, the H_2O, CO_2, S concentrations were calculated along a closed-system decompression path from 200 to 25 MPa, and the results are shown separately for H_2O-CO_2 and H_2O-S on Fig. 3a and 3b, respectively. The decompression paths are calculated for different initial fO_2 conditions. Different initial gas fractions were tested, the results shown being for an initial gas fraction of 0.05 wt.% defined on the basis of the mass balance calculation results for the synthesis charge S19.

The experimental H_2O-CO_2 trends for the 39 and 78 kPa/s glass series are in marked contrast with the closed-system equilibrium decompression trend computed with D-Compress (Burgisser et al., 2015; Fig. 3a). On the one hand, there is an important H_2O loss at high pressures (100–150 MPa) that is not observed in the theoretical trend and, on the other hand, the post-decompression glasses keep CO_2 concentrations that plot well above their respective gas-melt saturation isobars (150–25 MPa). An important effect of the gas fraction on the theoretical decompression path appears in the calculations (not shown on Fig. 3a). Conversely, the calculated decompression path is insensitive to changes in redox conditions (not shown on Fig. 3a). In comparison with the H_2O-CO_2 trends, the experimental H_2O-S trends show a closer agreement with the closed-system equilibrium degassing paths (Fig. 3b).

Yet, an important fraction of H_2O is lost at high pressures (experimental data points plot left to their corresponding isobars) and S losses appear more important than theoretically expected (experimental data points plot below the theoretical degassing curves). Significant drops in S melt concentrations below 150 MPa were also observed in equilibrium (Lesne et al., 2011c) and decompression (Fiege et al., 2015) experiments on basaltic melts. Our results do not show an important influence of the gas fraction on the position of the theoretical decompression path (not shown on Fig. 3b). On the other hand, the calculations are very sensitive to changes in redox conditions (Fig. 3b). Increasing the initial fO_2 to NNO+1.5 shifts the theoretical decompression path towards higher S concentrations, i.e. away from the experimental data points. Conversely, slightly lower S melt concentrations (~1000 ppm) are calculated upon lowering the initial fO_2 to NNO–0.5 (while slightly varying the H_2O and CO_2 melt concentrations), but the computation of the degassing trajectory is impossible under these conditions.

4.4. Composition of experimental fluids

The composition of gas exsolved in the decompression experiments are given in Table 3 and shown in Fig. 4. There is little influence of the decompression rate on the gas phase composition. Experimental fluids are predominantly composed of H_2O and CO_2 with SO_2 as a subordinate component. The gas phase evolves from CO_2-dominant (at 200 MPa P_f) to H_2O-dominant (below 150 MPa P_f) in both glass series. The concentration of H_2O (mol% H_2O, Fig. 4a and Table 3) generally increases with decreasing P_f, from 33 mol% (200 MPa P_f) to 55 and 63 mol% in the 39 and 78 kPa/s series, respectively (25 MPa P_f). In detail, however, the H_2O concentration decreases between 100 and 50 MPa in the 39 kPa/s series and remains almost constant between 150 and 50 MPa in the 78 kPa/s series.

In contrast, both the concentrations of CO_2 and S (mol% CO_2 and mol% SO_2, Fig. 4b, c and Table 3) generally decrease upon lowering P_f. The CO_2 concentration ranges from 42 mol% (200 MPa P_f) to 28 mol% (25 MPa P_f) while the SO_2 concentration ranges from 25 mol% (200 MPa P_f) to 18 and 9 mol% in the 39 and 78 kPa/s series, respectively (25 MPa P_f). In detail, however, there are slight increases in CO_2 concentration between 100 and 50 MPa P_f in the 39 kPa/s series and between 50 and 25 MPa P_f in the 78 kPa/s series (Fig. 4b). Slight increases in mol% SO_2 are also observed between 100 and 50 MPa in the 39 kPa/s series and between 150 and 50 MPa in the 78 kPa/s series (Fig. 4c).

The experimental trends for both H_2O and CO_2 fluid concentrations are qualitatively reproduced with D-Compress (Burgisser et al., 2015) which predicts an increase and a decrease of mol% H_2O and mol% CO_2, respectively (Fig. 4a, b). In contrast, D-Compress calculates very low mol% SO_2 (the D-Compress curve is almost indistinguishable from the y axis, Fig. 4c) that slightly increase with decreasing P_f, i.e. opposite to the experimental trends.

4.5. Sulfur partitioning

Sulfur distribution between melt and fluid is reported as the partition coefficient $D_S^{fl/m} = S_{fluid}/S_{melt}$; S_{fluid} and S_{melt} being the concentrations (in wt.%) of sulfur in the fluid and in the melt, respectively. S_{fluid} was determined via mass balance calculations (see above). The estimated error on $D_S^{fl/m}$ is ± 30%. $D_S^{fl/m}$ generally increases with decreasing P_f, although moderately ($D_S^{fl/m}$ = 129–228, Fig. 5 and Table 3). In detail (Fig. 5a), in the 78 kPa/s series $D_S^{fl/m}$ increases regularly from 147 (150 MPa P_f) to 228 (50 MPa P_f), before decreasing up to 147 (25 MPa P_f). In the 39 kPa/s series, $D_S^{fl/m}$ first decreases slightly from 147 (150 MPa P_f) to 129 (100 MPa P_f), before increasing up to 209 (25 MPa P_f). However, the magnitude of the above $D_S^{fl/m}$ variations with pressure is less than the measurement error. Note that at 100 and 50 MPa P_f, $D_S^{fl/m}$ is higher for the 78 kPa/s series than for the 39 kPa/s series (up to 1.4 times higher at 100 MPa P_f). However, it is the opposite at 25 MPa P_f and at 150 MPa P_f, similar $D_S^{fl/m}$ are found in both glass series. This demonstrates no systematic correlation between $D_S^{fl/m}$ and the decompression rate. Our $D_S^{fl/m}$ values are in good agreement with the results of Beermann (2010, $D_S^{fl/m}$ = 200) and Fiege et al. (2015, $D_S^{fl/m}$ = 181, Fig. 5b). The data of Lesne et al. (2011c) show a strong pressure dependency ($D_S^{fl/m}$ values change by nearly 3 orders of magnitude) that is not confirmed in this study.

5. Discussion

5.1. Bubble textures

Our experimental textures bear evidence for the occurrence of both (1) heterogeneous and (2) homogeneous bubble nucleation. (1) The heterogeneous nature of bubble nucleation in our glasses is evidenced by the textural association between bubbles and iron sulfides (Fig. 1c, d). However, iron sulfides do not occur in all decompression charges and, even when present, bubbles are not found always systematically attached to them. This indicates the

minor role played by heterogeneous bubble nucleation in this study. (2) The homogenous nature of bubble nucleation in our post-decompression glasses is evidenced by the occurrence of bubbles uniformly distributed within the melt and showing no sulfide-bubble relationships.

The supersaturation pressure required for either heterogeneous (ΔP_{HeN}) or homogeneous (ΔP_{HoN}) bubble nucleation, i.e. the difference between the saturation pressure ($P_{sat} = P_{in}$) and the final pressure (P_f) at which bubbles begin to form, can be determined from our decompression experiments. Bubbles are found nucleating on the surface of iron sulfides in the pre-decompression glass which leads to a ΔP_{HeN} value in principle $\leq$ 1 MPa. However, as emphasizes above, iron sulfides are not present in all decompression runs, being found in two charges decompressed at 78 kPa/s (S+D34, 100 MPa P_f, and S+D35, 50 MPa P_f). At P_f = 150 MPa and below, we observe numerous uniformly distributed bubbles in glass cores from both series, leading to ΔP_{HoN} < 50 MPa. Although sulfur is present in our melts, this ΔP_{HoN} value is consistent with that found in sulfur-free basaltic melts containing only H_2O and CO_2 as dissolved volatiles (ΔP_{HoN} < 50 MPa, series #2 melts, Le Gall and Pichavant, 2015b). This suggests that sulfur has no large influence on the homogeneous nucleation pressure.

An evolution in the bubble shape is observed with decreasing pressure. At P_f = 150 MPa, bubbles from both glass series are spherical. Bubbles (at least the largest) begin to elongate from P_f = 100 MPa. Bubble elongation is strongly marked in the 78 kPa/s series at 50 MPa P_f and in both glass series at 25 MPa P_f (Fig. 2). For comparison, natural bubble textures at Stromboli exhibit a population of small to intermediate, tube-shaped vesicles interpreted to result from the coalescence of smaller bubbles (Polacci et al., 2006). Coalescence structures (Castro et al., 2012; Le Gall and Pichavant, 2015a) were indeed observed in two of our 78 kPa/s series post-decompression glasses (S+D35, P_f = 50 MPa, and S+D38, P_f = 25 MPa, Fig. 2). Therefore, bubble elongation indicates that coalescence of growing bubbles is taking place, but also that bubbles move upward relative to melt in the capsule (Iacono-Marziano et al., 2007). Both processes are thought to be at the origin of the generation of the micro bubbly slug (Vergniolle and Jaupart, 1986) observed in sample S+D38 (Fig. 2a).

5.2. Comparison with glass inclusions

Volatile concentrations in our experimental glasses are compared with the data for the Stromboli glass inclusions (Métrich et al., 2010; Fig. 6). The Stromboli natural glasses are characterized by H_2O and CO_2 contents that deviate from the theoretical closed-system equilibrium degassing trend (Fig. 6a); H_2O is lost in significant amounts and CO_2 retained at elevated concentration levels. Previous experiments performed to simulate the ascent and degassing of H_2O-CO_2-bearing basalt melts, from 200 to 25 MPa (Pichavant et al., 2013; Le Gall and Pichavant, 2015b), have closely simulated such "unexpected" evolutions of the melt H_2O and CO_2 concentrations. Our data in the S-bearing system also show a good correlation between experimental (from both glass series) and glass inclusion H_2O and CO_2 concentrations (Fig. 6a). In addition, there is a very good match between the H_2O and S contents measured in our run products and those of Stromboli glass inclusions (Fig. 6b). This confirms that the degassing processes that control the evolution of the melt volatile concentrations during magma ascent are closely approached in our decompression experiments. More in detail, both the natural and experimental glass data evolve along trends similar to the theoretical closed-system equilibrium degassing trend (Fig. 6b). However, significant differences exist since both H_2O and S appear to be lost more importantly than expected. This implies a behavior of S fundamentally different from that of CO_2 (Fig. 6a) although this conclusion needs confirmation because calculation of the CO_2 and S melt concentrations in D-Compress are coupled (Burgisser et al., 2015).

We conclude that our decompression experiments (at both rates of 39 and 78 kPa/s) reasonably simulate the melt volatile concentrations during basaltic magma ascent at Stromboli.

5.3. Comparison with volcanic gases

Below, we extend the comparison between our experiments and the Stromboli volcanic system to the fluid/gas phase composition. Time series for volcanic gas compositions are available at Stromboli (Aiuppa and Federico, 2004; Burton et al., 2007; Allard et al., 2008; Aiuppa et al., 2009, 2010a, b; Allard, 2010; Aiuppa et al., 2011; La Spina et al., 2013). They show that the composition of gases emitted from the summit craters changes before major explosions and paroxysms, allowing the possibility of using such changes as an indication of deep magma recharge in the plumbing system (Allard, 2010; Aiuppa et al., 2010a, b, 2011). Time variability for both CO_2/SO_2 and H_2O/CO_2 molar ratios has been

evidenced, especially a systematic and progressive increase in CO_2/SO_2 molar ratio some days to weeks prior to the paroxysmal explosions (Aiuppa et al., 2010a; La Spina et al., 2013).

During quiescent magma degassing, and so in-between Strombolian explosions, volcanic gases have high H_2O/CO_2 molar ratios (1.5–65, Aiuppa et al., 2010a; 6.1, Burton et al., 2007; Allard et al., 2008). The lower end of the range is reproduced experimentally from 150 MPa for the 39 kPa/s series and from 150–100 MPa for the 78 kPa/s (Fig. 7). However, the highest observed values (> 6) were not reproduced since the highest ratios experimentally measured are 2.3, irrespective of the glass series. Nevertheless, inspection of Fig. 7 suggest that H_2O/CO_2 molar ratios > 2.3, and possibly up to 10, would be likely for P_f < 25 MPa since an increase in H_2O/CO_2 is observed between 50 and 25 MPa in both glass series. During explosive magma degassing associated with the "normal" activity and the major explosions, H_2O/CO_2 are lower than during passive degassing (typically 1–3, Aiuppa et al., 2010a; 2.3–4.5, Burton et al., 2007; Allard et al., 2008), and well in the range of our experimental H_2O/CO_2 for P_f ranging from 150 to 25 MPa in both glass series.

The H_2O/CO_2 and CO_2/SO_2 molar ratios are anticorrelated and, so, quiescent emissions are characterized by low CO_2/SO_2 which range from 1.6 to 12 (Allard et al., 2008; Aiuppa et al., 2009; Allard, 2010). The lower end of the CO_2/SO_2 range is reproduced experimentally for 150 to 25 MPa P_f in both glass series. However, higher CO_2/SO_2 occur in the 78 kPa/s glass series at 25 MPa P_f (CO_2/SO_2 = 3.1) which suggest the possibility of still higher CO_2/SO_2 below 25 MPa P_f. In contrast, the explosions (both associated with the normal activity and the major explosions) correlate with the highest CO_2/SO_2 (> 10, up to 26 for major explosions; Allard et al., 1999; Burton et al., 2007; Aiuppa et al., 2009, 2010a, 2011; Allard, 2010). Such high CO_2/SO_2 values are never found in our experiments which yield a maximum CO_2/SO_2 of 3.1. The only way to reconcile the experimental and natural CO_2/SO_2 would be to consider magma degassing at P_f << 25 MPa, since a marked increase of the CO_2/SO_2 ratio (by a factor of 2.6) is observed between 50 and 25 MPa P_f in the 78 kPa/s glass series. In other words, our experimental results do not support the interpretation that an increase of the CO_2/SO_2 in volcanic gases reflects supply from deeper in the plumbing system (Allard, 2010; Aiuppa et al., 2011). The relatively low CO_2/SO_2 ratios found in our experiments is directly related to the fact that CO_2 is retained in the melt at elevated concentration levels, as a result of disequilibrium degassing and, this, until the last stages of magma ascent at low pressures (< 25 MPa). S does not seem to show a particular difficulty to

be exsolved (Fig. 6b) which, when combined with the behavior of CO_2, explains the minor influence of pressure (except at 25 MPa and below) on the CO_2/SO_2 ratio.

We conclude that our decompression experiments (at both rates of 39 and 78 kPa/s) reasonably simulate both the H_2O/CO_2 and CO_2/SO_2 molar ratios (from 150–100 to 25 MPa P_f) in the gas phase during quiescent magma degassing. Experimental H_2O/CO_2 also reasonably reproduce the natural H_2O/CO_2 measured during explosive magma degassing (from 150 to 25 MPa P_f). Our data for the 78 kPa/s glass series suggest that the high CO_2/SO_2 associated with the Strombolian paroxysms could be the result of a shallow magma degassing (P_f << 25 MPa).

5.4. A degassing model for Stromboli volcano

Strombolian paroxysms are phases of high CO_2 degassing (Aiuppa et al., 2011) which results in high CO_2/SO_2 in the gas plume. These energetic events have the peculiarity of being associated with the ejection, not only of a crystal-rich and nearly degassed black scoria which occupies the shallow reservoir (2–4 km, equivalent to 50–100 MPa; Métrich et al., 2010) and sustains the normal activity, but also of a poorly crystallized, highly vesicular, golden pumice residing in the deep feeding system (7–10 km, equivalent to 190–260 MPa; Pichavant et al., 2009; Métrich et al., 2010; Aiuppa et al., 2010a). Paroxysmal eruptions are thus characterized by specific conditions of basaltic magma ascent and degassing whose modalities remain debated. Two main models have been proposed to explain these specificities. The first (Allard, 2010) attributes a critical role to the fast ascent of CO_2-rich gas slugs of deep derivation. In the second model, eruptive paroxysms are driven by the rapid ascent and decompression of volatile-rich magma batches coming from the golden pumice reservoir (Métrich et al., 2001; Bertagnini et al., 2003; Métrich et al., 2005, 2010). Recently, it was proposed as an alternative hypothesis that paroxysms are driven by low pressure explosive degassing and fragmentation of CO_2-oversaturated melts generated as a result of disequilibrium degassing (Pichavant et al., 2013). Below, constraints from our experimental simulations (this study; Le Gall and Pichavant, 2015a, b, c) are integrated to reexamine the conditions of degassing associated with eruptive paroxysms.

According to Allard (2010), the golden pumice magma may originally coexist with a volumetrically abundant CO_2-rich gas phase (~2 wt.% CO_2, Burton et al., 2007; Allard, 2010;

Aiuppa et al., 2011) with high CO_2/SO_2 (> 60 at 10 km depth). This high gas content, coupled with a low golden pumice magma viscosity, would allow bubble-melt separation and accumulation of CO_2-rich bubbles at discontinuities in the plumbing system (Allard, 2010). Difficulties with this model of bubble foam growth and collapse concern the generation of gas pockets (since it requires bubble coalescence at depth, Burton et al., 2007; Aiuppa et al., 2011) and the control of the composition of the gas phase which needs to be CO_2-rich. Although early and, so, deep exsolution of CO_2 is classically assumed, our experiments (this study; Le Gall and Pichavant, 2015a, b, c) demonstrate that CO_2 is retained in the melt at 150–200 MPa. This is shown by CO_2 melt concentrations in post-decompression glasses that remain much higher than expected from equilibrium degassing (Fig. 3a; Le Gall and Pichavant, 2015a, b, c). In addition, the experimental data show that the gas phase is not CO_2-enriched at high pressure (Fig. 7). Furthermore, bubble coalescence is limited at depth (100–150 MPa) due to small bubble sizes and the long distances between them (Le Gall and Pichavant, 2015a, b). Our observations lead to propose the formation of gas slugs at pressures between 50 and 25 MPa, because this pressure range is associated with an increase in bubble diameter, bubble number density and vesicularity, all promoting bubble coalescence as observed in post-decompression products (Le Gall and Pichavant, 2015a, b). It is worth reminding that a micro gas slug is present in one 25 MPa P_f charge (Fig. 2a), which indicates the possibility of physical bubble-melt segregation. In addition, in this pressure range, an increase of the CO_2/SO_2 gas ratio is evidenced (Fig. 7). Although always lower than the maximum measured CO_2/SO_2 gas ratios, the experimental trends are suggestive of a strong increase of CO_2/SO_2 at P_f << 25 MPa. Therefore, these experimental observations are fully consistent with a shallow depth (2.7–0.8 km depth below crater vents, equivalent to 80–70 to 20 MPa, Burton et al., 2007) for the formation mechanisms (coalescence of smaller bubbles and gas-melt segregation) of gas slugs driving Strombolian explosions. In addition to volatile loss through vesiculation, diffusive H_2O outgassing from the melt, which is a significant process in our experiments between 100 and 50 MPa (especially at 1.5 m/s, Le Gall and Pichavant, 2015b), can also contribute to the exsolution of gases from the melt and their accumulation at structural discontinuities to promote the generation of large gas slugs.

Additional difficulties with the model of Allard (2010) concern the high initial magma CO_2 content postulated (~2 wt.%) which is supported by equilibrium computations whose applicability is questionable because of the possibility of disequilibrium degassing. Such a high magma CO_2 content would promote magma dehydration and shift glass inclusion

compositions along a CO_2-fluxing trend (Métrich et al., 2010). However, in our experiments with a very little excess fluid phase present (0.05 wt.% at 200 MPa), significant H_2O losses from the pre-decompression melt are associated with decompression, vesiculation and probably diffusion. Therefore, the CO_2-fluxing model is not necessary to account for magma dehydration. We also note that CO_2-fluxing would lead to extensive magma crystallization, yet golden pumices are nearly aphyric.

In comparison, there are numerous petrological and textural features of golden pumices that are consistent with a rapid magma ascent and degassing, as proposed by Bertagnini et al. (2003) and Métrich et al. (2001, 2005, 2010). Comparison between bubble and crystal textures of natural and experimental products allows timescales of golden pumice magma ascent to be constrained. First, bubble number densities and bubble diameters (Pichavant et al., 2013; Le Gall and Pichavant, 2015b) imply ascent rates of 1–3 m/s, higher than estimations based from olivine growth rates (0.05–0.55 m/s, Bertagnini et al., 2003; Aiuppa et al., 2010b). This leads to timescales of a few minutes to a few tenths of hours for golden pumice magma to ascend from the deep feeding system. Second, the crystallinity of the golden pumice magma argues for a rapid ascent. The absence (or scarcity, Métrich et al., 2010) of microlites in golden pumices limits ascent durations to a maximum of 10 h (Di Carlo et al., 2006; Pichavant et al., 2011). In addition, the lack of large coalesced bubbles in both natural (Polacci et al., 2009) and H_2O-CO_2-bearing experimental products (Le Gall and Pichavant, 2015a, b) is consistent with a very short travel time from the deep reservoir to the surface. In comparison, large vesicles resulting from coalescence processes are observed in scoriae (Polacci et al., 2009), attesting of a longer residence time in the shallow reservoir. The evolution of bubble size distributions from power law to mixed power law–exponential in both golden pumices and experimental products also suggest time constraints of the order of minutes to hours for the vesiculation process (Polacci et al., 2009; Le Gall and Pichavant, 2015b).

If the different petrological, textural and geochemical constraints are considered, the shallow degassing model (Pichavant et al., 2013) appears strengthened. In the frame of this model, the increase in CO_2 flux accompanying the major explosions (Aiuppa et al., 2010b) would reflect the explosive degassing and fragmentation of CO_2-oversaturated melts generated as a result of disequilibrium degassing during fast ascent of the golden pumice magma (Pichavant et al., 2013). The presence of CO_2-enriched melts at Stromboli is evidenced by natural glasses (melt inclusions and embayments, Métrich et al., 2010) whose

volatile concentrations have been satisfactorily simulated by our decompression experiments (at both ascent rates of 1.5 and 3 m/s, Fig. 6a; Le Gall and Pichavant, 2015b). The gradual increase in CO_2 degassing before paroxysms (on timescales typically of several days, Aiuppa et al., 2011) would reflect the progressive arrival of CO_2-enriched golden pumice magma batches from the deep storage zone (Pichavant et al., 2013). This magma recharge at shallow levels would thus explain the high CO_2/SO_2 ratios measured in the gas plume as a result of shallow (P_f << 25 MPa) golden pumice magma degassing. It is worth reminding that our experimental results for the fluid H_2O/CO_2 are in reasonable agreement with those measured at Stromboli during both quiescent and explosive magma degassing, although the highest H_2O/CO_2 associated with quiescent degassing are not reproduced (Fig. 7). The experimental H_2O/CO_2 are almost insensitive to pressure and therefore H_2O/CO_2 gas ratios associated with normal explosions (CO_2 signal) do not need to have a deep source. It is worth noting that highly vesicular golden pumice ash fragments are erupted during normal Strombolian explosions (D'Oriano et al., 2010), demonstrating that the golden pumice magma is continuously recharging (although at varying rates) the shallow plumbing system. We propose that the eruption intensity would depend on the magma supply rate (thus modifying processes of scoria-pumice syn-eruptive mingling in the shallow reservoir) and result from variable magma pressurization from the deep feeding system (Métrich et al., 2010).

6. Conclusions

Volatile-bearing (2.72 ± 0.02 wt.% H_2O, 1291 ± 85 ppm CO_2, 1535 ± 369 ppm S) Stromboli melts were continuously decompressed from 200 to P_f = 150–25 MPa, at both rates of 39 and 78 kPa/s, to simulate the fluid-melt partitioning of H_2O, CO_2 and S during basalt magma ascent and degassing. Melt volatile concentrations were measured by FTIR (H_2O, CO_2) and by electron microprobe (S) and experimental fluid compositions estimated by mass balance. Results were compared with glass inclusion and volcanic gas data available at Stromboli, as well as with bubble textures in pumices. The main conclusions are the following:

(1) A textural relation similar to that previously described for heterogeneous bubble nucleation on Fe–Ti oxides (Le Gall and Pichavant, 2015c) was found for iron sulfides. Bubbles begin to nucleate heterogeneously on the surface of iron sulfides for

supersaturation pressures (ΔP_{HeN}) ≤ 1 MPa and to nucleate homogeneously for ΔP_{HoN} < 50 MPa.

(2) Experimental trends of decreasing melt volatile concentrations with decreasing P_f were compared with a closed-system equilibrium degassing path computed with D-Compress (Burgisser et al., 2015). For both glass series, H_2O is lost in significant amounts at high pressure and CO_2 is retained at elevated concentration levels in the melt. Upon decompression, S losses from the melt are more important than theoretically expected with D-Compress. The volatile degassing trend recorded by Stromboli natural glasses is closely experimentally simulated.

(3) The addition of sulfur does not affect the degassing behavior of H_2O and CO_2 during decompression. Compared to theoretical degassing models, CO_2 is the component that deviates the more strongly from equilibrium behavior.

(4) The composition of experimental fluids is little influenced by the decompression rate. Both the H_2O/CO_2 and CO_2/SO_2 trends are weakly dependent on P_f, and both slightly increase with decreasing P_f.

(5) The sulfur partition coefficient between fluid and melt ($D_S^{fl/m}$) is greatly influenced neither by the decompression rate nor by the pressure. Our $D_S^{fl/m}$ values (129–228) are in good agreement with recent determinations for basaltic melts.

(6) All post-decompression glasses contain various amounts of bubbles with vesicularities ranging from 0.6 to 45 vol.%. A very large bubble similar to a micro gas slug occurred in a charge decompressed to 25 MPa, indicating coalescence of gas bubbles and bubble-melt segregation.

(7) Experimental H_2O/CO_2 molar ratios are in the lower range measured at Stromboli for quiescent magma degassing and reproduce satisfactorily the H_2O/CO_2 gas ratios associated with normal explosive activity. The decrease in H_2O/CO_2 during Strombolian explosions does not require a deep gas source.

(8) Experimental CO_2/SO_2 molar ratios reproduced the lower range measured at Stromboli for quiescent magma degassing and are distinctly lower than gas ratios associated with normal explosions. Our results for the 78 kPa/s glass series show a strong increase of

CO_2/SO_2 between 50 and 25 MPa P_f, suggesting the possibility of still higher values at << 25 MPa P_f that would approach those associated with explosive activity.

(9) Our experimental observations support a model of low pressure explosive degassing of CO_2-oversaturated melts to generate the explosive activity and paroxysms at Stromboli. They also have implications for the interpretation of geochemical and textural observables.

References

Abràmoff, M.D., Magalhães, P.J., Ram, S.J., 2004. Image processing with ImageJ. Biophotonics International 11, 36–43.

Aiuppa, A., Federico, C., 2004. Anomalous magmatic degassing prior to the 5th April 2003 paroxysm on Stromboli. Geophysical Research Letters 31, L14607. doi:10.1029/2004GL020458

Aiuppa, A., Bertagnini, A., Métrich, N., Moretti, R., Di Muro, A., Liuzzo, M., Tamburello, G., 2010a. A model of degassing for Stromboli volcano. Earth and Planetary Science Letters 295, 195–204. doi:10.1016/j.epsl.2010.03.040

Aiuppa, A., Burton, M., Caltabiano, T., Giudice, G., Guerrieri, S., Liuzzo, M., Murè, F., Salerno, G., 2010b. Unusually large magmatic CO_2 gas emissions prior to a basaltic paroxysm: CO_2 gas emissions prior to a paroxysm. Geophysical Research Letters 37, L17303. doi:10.1029/2010GL043837

Aiuppa, A., Burton, M., Allard, P., Caltabiano, T., Giudice, G., Gurrieri, S., Liuzzo, M., Salerno, G., 2011. First observational evidence for the CO_2-driven origin of Stromboli's major explosions. Solid Earth 2, 135–142. doi:10.5194/se-2-135-2011

Aiuppa, A., Moretti, R., Federico, C., Giudice, G., Gurrieri, S., Liuzzo, M., Papale, P., Shinohara, H., Valenza, M., 2007. Forecasting Etna eruptions by real-time observation of volcanic gas composition. Geology 35, 1115–1118.

Aiuppa, A., Federico, C., Giudice, G., Giuffrida, G., Guida, R., Gurrieri, S., Liuzzo, M., Moretti, R., Papale, P., 2009. The 2007 eruption of Stromboli volcano: Insights from real-time measurement of the volcanic gas plume CO_2/SO_2 ratio. Journal of Volcanology and Geothermal Research 182, 221–230. doi:10.1016/j.jvolgeores.2008.09.013

Allard, P., 2010. A CO_2-rich gas trigger of explosive paroxysms at Stromboli basaltic volcano, Italy. Journal of Volcanology and Geothermal Research 189, 363–374. doi:10.1016/j.jvolgeores.2009.11.018

Allard, P., Aiuppa, A., Loyer, H., 1999. Airborne determinations of gas and trace-metal fluxes in volcanic plumes of Mt. Etna and Stromboli. CEE Res. Contract ENV4-CT96-288, Monitoring Volcanic Risks by Remote Sensing, Final Rep., Bruxelles, Belgium (55 pp.).

Allard, P., Carbonnelle, J., Metrich, N., Loyer, H., Zettwoog, P., 1994. Sulphur output and magma degassing budget of Stromboli volcano. Nature 368, 326–330.

Allard, P., Aiuppa, A., Burton, M., Caltabiano, T., Federico, C., Salerno, G., La Spina, A., 2008. Crater gas emissions and the magma feeding system of Stromboli volcano. In: Calvari, S., Inguaggiato, S., Puglisi, G., Ripepe, M., Rosi, M. (Eds.), Learning from Stromboli: AGU Geophysics Monograph Series 182, 65–80.

Beermann, O., 2010. The solubility of sulfur and chlorine in H_2O-bearing dacites of Krakatau and basalts of Mt. Etna. PhD thesis, Leibniz University of Hanover.

Bertagnini, A., Métrich, N., Landi, P., Rosi, M., 2003. Stromboli volcano (Aeolian Archipelago, Italy): An open window on the deep-feeding system of a steady state basaltic volcano. Journal of Geophysical Research 108 (B7), 2336. doi:10.1029/2002JB002146

Bourgue, E., Richet, P., 2001. The effects of dissolved CO_2 on the density and viscosity of silicate

melts: a preliminary study. Earth and Planetary Science Letters 193, 57–68.
Brugier, Y.A., Alletti, M., Pichavant, M., 2015. Fe pre-enrichment: A new method to counteract iron loss in experiments on basaltic melts. American Mineralogist 100, 2106–2111. doi: 10.2138/am-2015-5166
Burgisser, A., Scaillet, B., 2007. Redox evolution of a degassing magma rising to the surface. Nature 445, 194–197.
Burgisser, A., Alletti, M., Scaillet, B., 2015. Simulating the behavior of volatiles belonging to the C–O–H–S system in silicate melts under magmatic conditions with the software D-Compress. Computers & Geosciences 79, 1–14.
Burton, M., Allard, P., Mure, F., La Spina, A., 2007. Magmatic Gas Composition Reveals the Source Depth of Slug-Driven Strombolian Explosive Activity. Science 317, 227–230. doi:10.1126/science.1141900
Castro, J.M., Burgisser, A., Schipper, C.I., Mancini, S., 2012. Mechanisms of bubble coalescence in silicic magmas. Bulletin of Volcanology 74, 2339–2352.
D'Oriano, C., Bertagnini, A., Pompilio, M., 2010. Ash erupted during normal activity at Stromboli (Aeolian Islands, Italy) raises questions on how the feeding system works. Bulletin of Volcanology 73, 471–477.
Daag, A.S., Tubianosa, B.S., Newhall, C.G., Tungol, N.M., Javier, D., Dolan, M.T., Delos Reyes, P.J, Arboleda, R.A., Martinez, M.M.A., Regalado, M.T.M., 1996. Monitoring sulphur dioxide emission at Mount Pinatubo. In: Newhall, C.G., Punongbayan, R.S. (Eds.) Fire and mud: eruptions and lahars of Mount Pinatubo, Philippines. University of Washington Press, Seattle, 409–414.
Di Carlo, I., Pichavant, M., Rotolo, S.G., Scaillet, B., 2006. Experimental crystallization of a high-K arc basalt: the golden pumice, Stromboli volcano (Italy). Journal of Petrology 47, 1317–1343.
Dixon, J.E., Pan, V., 1995. Determination of the molar absorptivity of dissolved carbonate in basanitic glass. American Mineralogist 80, 1339–1342.
Dixon, J.E., Stolper, E.M., 1995. An experimental study of water and carbon dioxide solubilities in mid-ocean ridge basaltic liquids. Part II: applications to degassing. Journal of Petrology 36, 1633–1646.
Dixon, J.E., Stolper, E.M., Holloway, J.R., 1995. An experimental study of water and carbon dioxide solubilities in mid-ocean ridge basaltic liquids. Part I: calibration and solubility models. Journal of Petrology 36, 1607–1631.
Fiege, A., Holtz, F., Behrens, H., Mandeville, C.W., Shimizu, N., Crede, L.S., Göttlicher, J., 2015. Experimental investigation of the S and S-isotope distribution between H_2O–S ± Cl fluids and basaltic melts during decompression. Chemical Geology 393, 36–54.
Freda, C., Baker, D.R., Scarlato, P., 2005. Sulfur diffusion in basaltic melts. Geochimica et Cosmochimica Acta 69, 5061–5069.
Hidalgo, S., Battaglia, J., Steele, A., Arellano, S., Bernard, B., Ruiz, M., Galle, B., 2013. Open and closed system eruptive dynamics at Tungurahua volcano constrained by SO_2 emission rate and seismo-acoustic intensity measurements. In: Proceeding IAVCEI 2013 Scientific Assembly, July 20-24, Kagoshima, Japan, Abstract 4A2_21-011.
Iacono-Marziano, G., Schmidt, B.C., Dolfi, D., 2007. Equilibrium and disequilibrium degassing of a phonolitic melt (Vesuvius AD 79 "white pumice") simulated by decompression experiments. Journal of Volcanology and Geothermal Research 161, 151–164. doi:10.1016/j.jvolgeores.2006.12.001
Jugo, P.J., Wilke, M., Botcharnikov, R.E., 2010. Sulfur K-edge XANES analysis of natural and synthetic basaltic glasses: Implications for S speciation and S content as function of oxygen fugacity. Geochimica et Cosmochimica Acta 74, 5926–5938.
La Spina, A., Burton, M.R., Harig, R., Mure, F., Rusch, P., Jordan, M., Caltabiano, T., 2013. New insights into volcanic processes at Stromboli from Cerberus, a remote-controlled open-path FTIR scanner system. Journal of Volcanology and Geothermal Research 249, 66–76.
Le Gall, N., Pichavant, M., 2015a (to be submitted). Homogeneous bubble nucleation in H_2O- and H_2O-CO_2-bearing basaltic melts: results of high temperature decompression experiments.
Le Gall, N., Pichavant, M., 2015b (to be submitted). Effect of ascent rate on homogeneous bubble nucleation in the system basalt-H_2O-CO_2: Implications for Stromboli volcano.

Le Gall, N., Pichavant, M., 2015c (to be submitted). Heterogeneous bubble nucleation on Fe–Ti oxides in H_2O- and H_2O-CO_2-bearing basaltic melts.

Lange, R.A., 1994. The effect of H_2O, CO_2, and F on the density and viscosity of silicate melts. Reviews in Mineralogy and Geochemistry 30, 331–369.

Lesne, P., 2008. Etude expérimentale de la solubilité des volatils C-H-O-S dans les basaltes alcalins italiens. Simulations numériques du dégazage chimique : application à l'Etna. Ph.D. thesis, Université d'Orléans.

Lesne, P., Scaillet, B., Pichavant, M., Beny, J.-M., 2011a. The carbon dioxide solubility in alkali basalts: an experimental study. Contributions to Mineralogy and Petrology 162, 153–168.

Lesne, P., Scaillet, B., Pichavant, M., Iacono-Marziano, G., Beny, J.-M., 2011b. The H_2O solubility of alkali basaltic melts: an experimental study. Contributions to Mineralogy and Petrology 162, 133–151.

Lesne, P., Kohn, S.C., Blundy, J., Witham, F., Botcharnikov, R.E., Behrens, H., 2011c. Experimental simulation of closed-system degassing in the system basalt–H_2O–CO_2–S–Cl. Journal of Petrology 52, 1737–1762.

Malinconico, L.L., 1979. Fluctuations in SO_2 emission during recent eruptions of Etna. Nature 278, 43–45.

McGee, K.A., Sutton, A.J., 1994. Eruptive activity at Mount St Helens, Washington, USA, 1984–1988: a gas geochemistry perspective. Bulletin of Volcanology 56, 435–446.

Métrich, N., Bertagnini, A., Di Muro, A., 2010. Conditions of magma storage, degassing and ascent at Stromboli: new insights into the volcano plumbing system with inferences on the eruptive dynamics. Journal of Petrology 51, 603–626.

Métrich, N., Bertagnini, A., Landi, P., Rosi, M., 2001. Crystallization driven by decompression and water loss at Stromboli volcano (Aeolian Islands, Italy). Journal of Petrology 42, 1471–1490.

Métrich, N., Bertagnini, A., Landi, P., Rosi, M., Belhadj, O., 2005. Triggering mechanism at the origin of paroxysms at Stromboli (Aeolian Archipelago, Italy): the 5 April 2003 eruption. Geophysical Research Letters 32, L103056. doi:10.1029

Moretti, R., Papale, P., 2004. On the oxidation state and volatile behavior in multicomponent gas–melt equilibria. Chemical Geology 213, 265–280.

Moune, S., Holtz, F., Botcharnikov, R.E., 2009. Sulphur solubility in andesitic to basaltic melts: implications for Hekla volcano. Contributions to Mineralogy and Petrology 157, 691–707.

Mourtada-Bonnefoi, C.C., Laporte, D., 2002. Homogeneous bubble nucleation in rhyolitic magmas: an experimental study of the effect of H_2O and CO_2. Journal of Geophysical Research 107 (B4). doi:10.1029/2001JB00290

Pichavant, M., Pompilio, M., D'Oriano, C., Di Carlo, I., 2011. Petrography, mineralogy and geochemistry of a primitive pumice from Stromboli: implications for the deep feeding system. European Journal of Mineralogy 23, 499–517.

Pichavant, M., Di Carlo, I., Le Gac, Y., Rotolo, S.G., Scaillet, B., 2009. Experimental constraints on the deep magma feeding system at Stromboli volcano, Italy. Journal of Petrology 50, 601–624.

Pichavant, M., Di Carlo, I., Rotolo, S.G., Scaillet, B., Burgisser, A., Le Gall, N., Martel, C., 2013. Generation of CO_2-rich melts during basalt magma ascent and degassing. Contributions to Mineralogy and Petrology 166, 545–561.

Polacci, M., Baker, D.R., Mancini, L., Favretto, S., Hill, R.J., 2009. Vesiculation in magmas from Stromboli and implications for normal Strombolian activity and paroxysmal explosions in basaltic systems. Journal of Geophysical Research 114, B01206. doi:10.1029/2008JB005672

Polacci, M., Baker, D.R., Mancini, L., Tromba, G., Zanini, F., 2006. Three-dimensional investigation of volcanic textures by X-ray microtomography and implications for conduit processes. Geophysical Research Letters 33, L13312. doi:10.1029/2006GL026241

Richet, P., Whittington, A., Holtz, F., Behrens, H., Ohlhorst, S., Wilke, M., 2000. Water and the density of silicate glasses. Contributions to Mineralogy and Petrology 138, 337–347.

Saccorotti, G., Iguchi, M., Aiuppa, A., 2014. In situ Volcano Monitoring: Present and Future. Volcanic Hazards, Risks and Disasters 169.

Stoiber, R.E., Malinconico, L.L., Williams, S.N., 1983. Use of the correlation spectrometer at volcanoes. Forecasting volcanic events 1, 425–444.

Taylor, J.R., Wall, V.J., Pownceby, M.I., 1992. The calibration and application of accurate redox sensors. American Mineralogist 77, 284–295.
Vergniolle, S., Jaupart, C., 1986. Separated two-phase flow and basaltic eruptions. Journal of Geophysical Research 91, 12842–12860.
Webster, J.D., Botcharnikov, R.E., 2011. Distribution of Sulfur Between Melt and Fluid in S-O-H-C-Cl-Bearing Magmatic Systems at Shallow Crustal Pressures and Temperatures. Reviews in Mineralogy and Geochemistry 73, 247–283. doi:10.2138/rmg.2011.73.9
Witham, F., Blundy, J., Kohn, S.C., Lesne, P., Dixon, J., Churakov, S.V., Botcharnikov, R., 2012. SolEx: a model for mixed COHSCl-volatile solubilities and exsolved gas compositions in basalt. Computers & Geosciences 45, 87–97.
Zhang, Y., Ni, H., 2010. Diffusion of H, C, and O components in silicate melts. Reviews in Mineralogy and Geochemistry 72, 171–225.

Figure captions

Figure 1. SEM images illustrating sulfur reactions with (a) the Pt capsule and with (b–d) iron from the melt. (a) Platinum sulfide formation in the inner wall of a Pt capsule in a 72 h 1200°C synthesis experiment (P_{in}: initial pressure = 200 MPa). (b) Small (≤ 6 μm) iron sulfides in synthesis charge S19 (200 MPa P_{in}). The black arrow underlines the presence of a bubbly rim at the glass-capsule interface. (c) Inset showing the preferential textural association between bubble and iron sulfide indicating heterogeneous bubble nucleation. (d) Textural relation between a large bubble and an iron sulfide in the S+D34 78 kPa/s series charge decompressed to 100 MPa P_f (final pressure). See Table 2 for details about the experimental conditions and textural results.

Figure 2. SEM images of S+D38 and S+D35 78 kPa/s series charges decompressed to 25 and 50 MPa P_f, respectively, showing typical coalescence textures. (a) A micro gas slug in charge S+D38 resulting from bubble coalescence and bubble-melt physical separation. (b), (c) Details of observed coalescence structures. See Table 2 for experimental conditions.

Figure 3. H_2O, CO_2 and S concentrations in pre- and post-decompression glasses, (a) H_2O vs. CO_2 concentrations, (b) H_2O vs. S concentrations. Experimental data from Tables 3 and 4. Black circle: starting (or pre-decompression) glass synthesized at 200 MPa; gray symbols: glasses decompressed at a rate of 78 kPa/s; white symbols: glasses decompressed at a rate of 39 kPa/s; rectangles: glasses decompressed to 150 MPa; triangles: glasses decompressed to 100 MPa; squares: glasses decompressed to 50 MPa; diamonds: glasses decompressed to 25 MPa. Error bars (standard deviations, Table 4) are indicated on the data points. The 25–200 MPa gas-melt saturation isobars (thin continuous lines labeled with pressure) and the equilibrium decompression trajectories (dashed curves) are computed with D-Compress (Burgisser et al., 2015), assuming closed-system behavior and an initial gas fraction of 0.05 wt.%.

Figure 4. Experimental fluid phase compositions calculated from mass balance as a function of final pressure P_f. (a) H_2O, (b) CO_2 and (c) SO_2 (all in mol%). In (c), the inset details the SO_2 concentrations near the Y axis to show the D-Compress results (dashed curve, Burgisser et al., 2015). Black continuous curve: experimental trend for the 39 kPa/s series pre- (200 MPa P_f) and post-decompression glasses (150–25 MPa P_f); gray continuous curve: experimental trend for the 78 kPa/s series pre- (200 MPa P_f) and post-decompression glasses (150–25 MPa P_f). See Table 3 for experimental compositions.

Figure 5. Sulfur partition coefficients between fluid and melt ($D_S^{fl/melt}$) as a function of final pressure P_f. (a) Data from this study (squares, Table 3). Black square: starting (or pre-decompression) glass synthesized at 200 MPa; gray squares: glasses decompressed at a rate of 78 kPa/s; white squares: glasses decompressed at a rate of 39 kPa/s. (b) Comparison between data from this study and those of Beermann (2010, black

circles), Fiege et al. (2015, gray circles) and Lesne et al. (2011c, white circles). The estimated error on $D_S^{fl/m}$ is ± 30% (error bar indicated on the black square).

Figure 6. H_2O, CO_2 and S concentrations in natural glasses from Stromboli (data from Métrich et al., 2010) and comparison with experimental glasses from the 78 (gray squares) and 39 kPa/s series (white squares, Tables 3; 4). (a) H_2O vs. CO_2 melt concentrations, (b) H_2O vs. S melt concentrations. Error bars (standard deviations, Table 4) are indicated on the data points. Stromboli glasses plotted include melt inclusions (MI) and embayments (Emb) from pumices emitted during large- and intermediate- scale paroxysms (LSP and ISP, respectively) and scoriae. Experimental glasses include a pre-decompression glass (black square); all the others are post-decompression glasses (squares). The degassing trends (dashed curves) were computed with D-Compress (Burgisser et al., 2015) assuming closed-system behavior and an initial gas fraction of 0.05 wt.%.

Figure 7. Evolution of the experimental H_2O/CO_2 and CO_2/SO_2 molar ratios during decompression and comparison with the natural data for gas composition during quiescent and explosive degassing. Natural H_2O/CO_2 values come from Aiuppa et al. (2010a), Burton et al. (2007) and Allard et al. (2008), and natural CO_2/SO_2 values from Allard et al. (1999; 2008), Burton et al. (2007), Aiuppa et al. (2009; 2010a), Allard (2010) and Aiuppa et al. (2011). See Table 3 for experimental compositions (mass balance calculations).

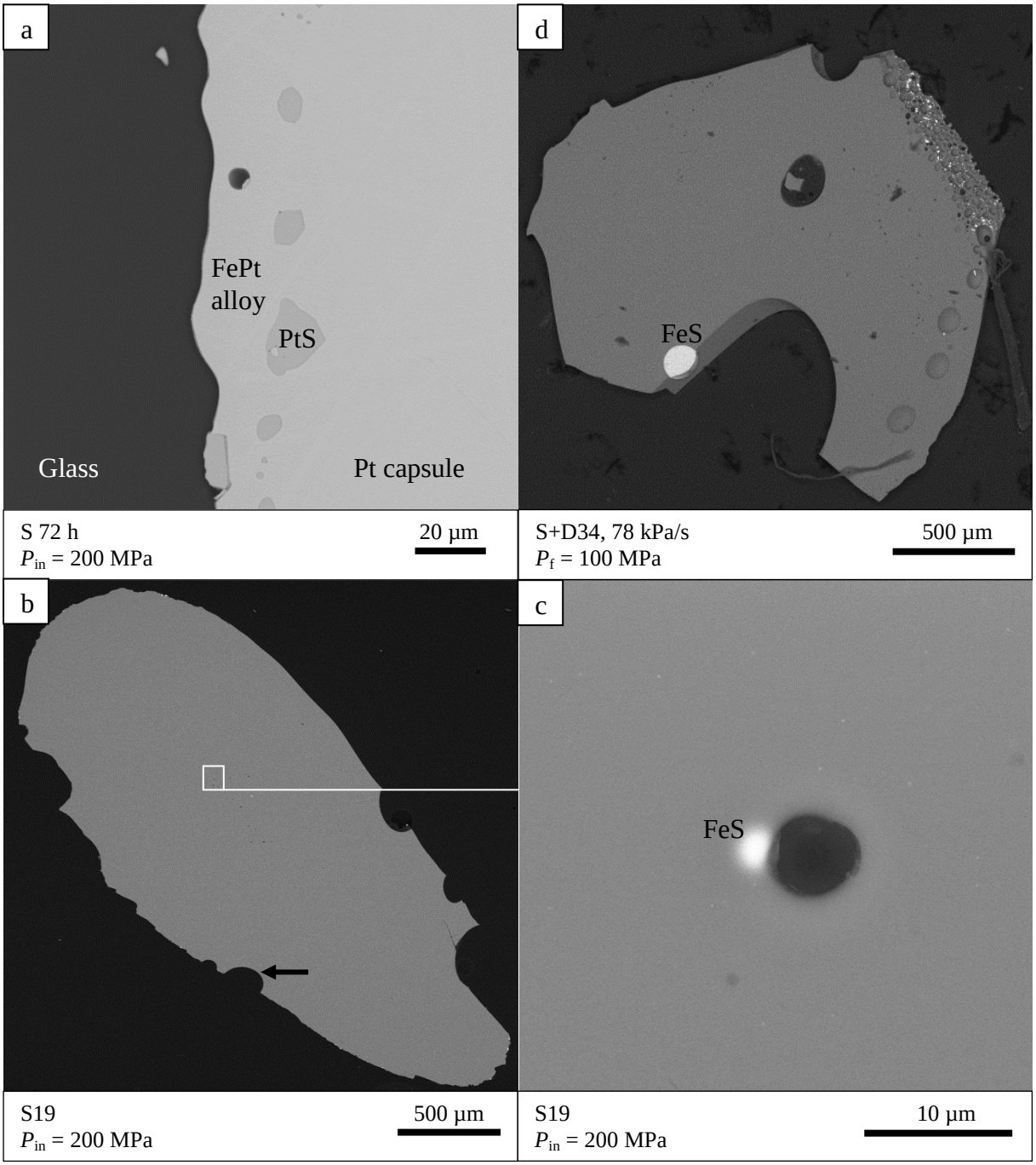

Le Gall et al. Fig. 1

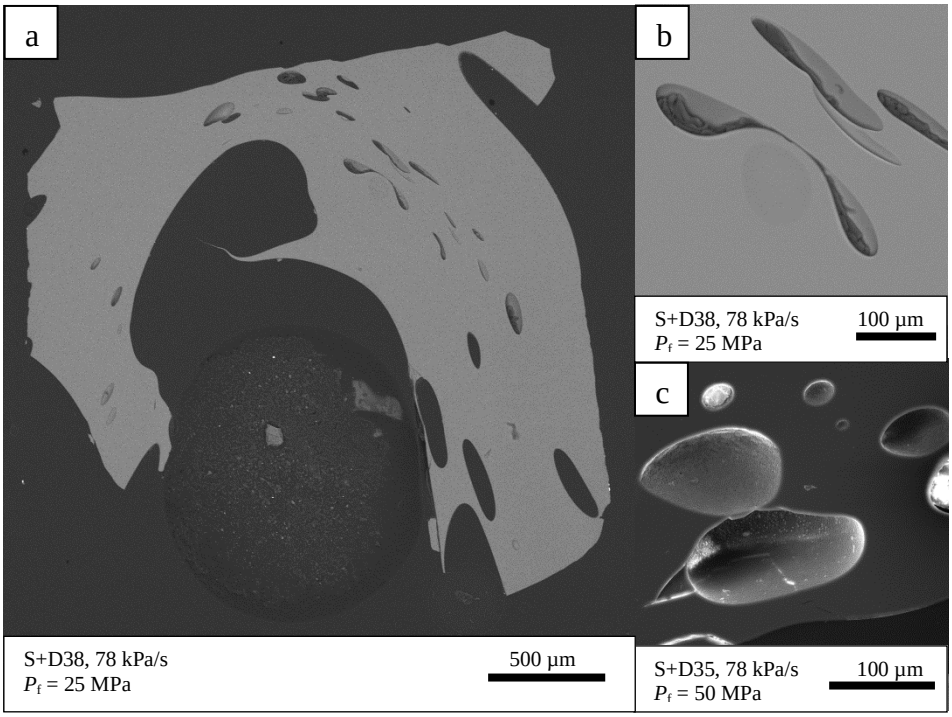

Le Gall et al. Fig. 2

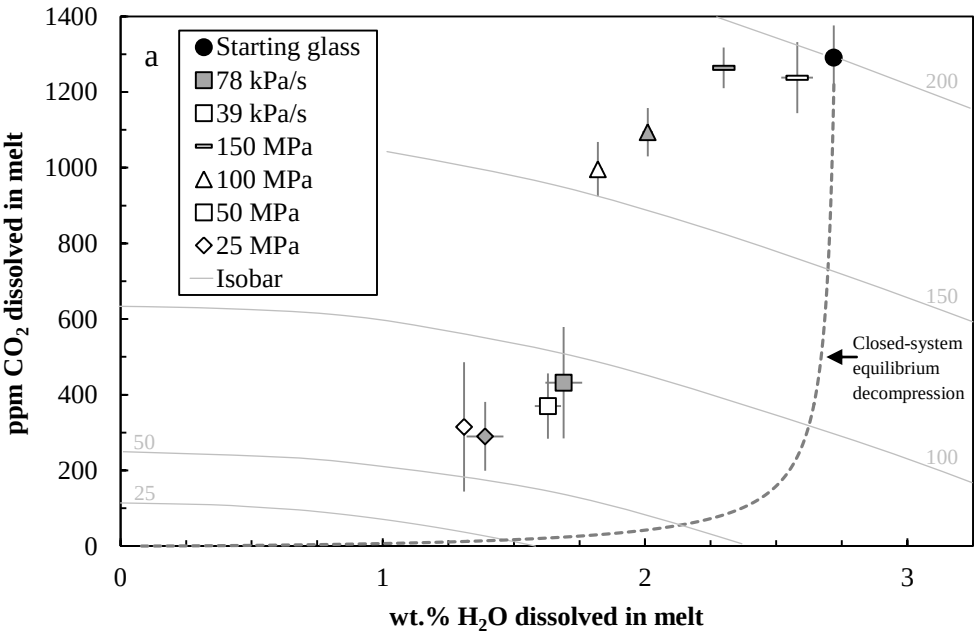

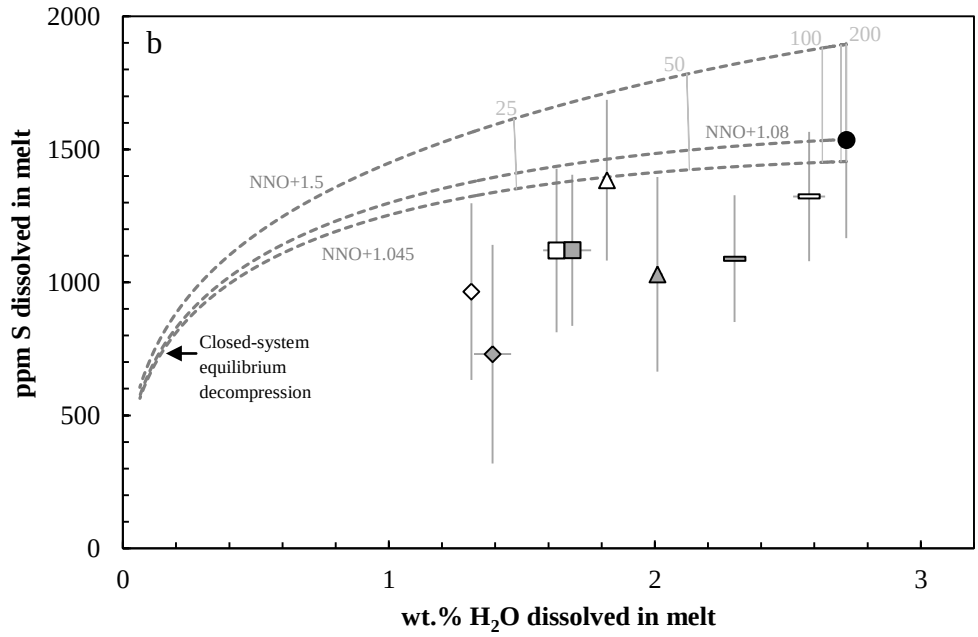

Le Gall et al. Fig. 3

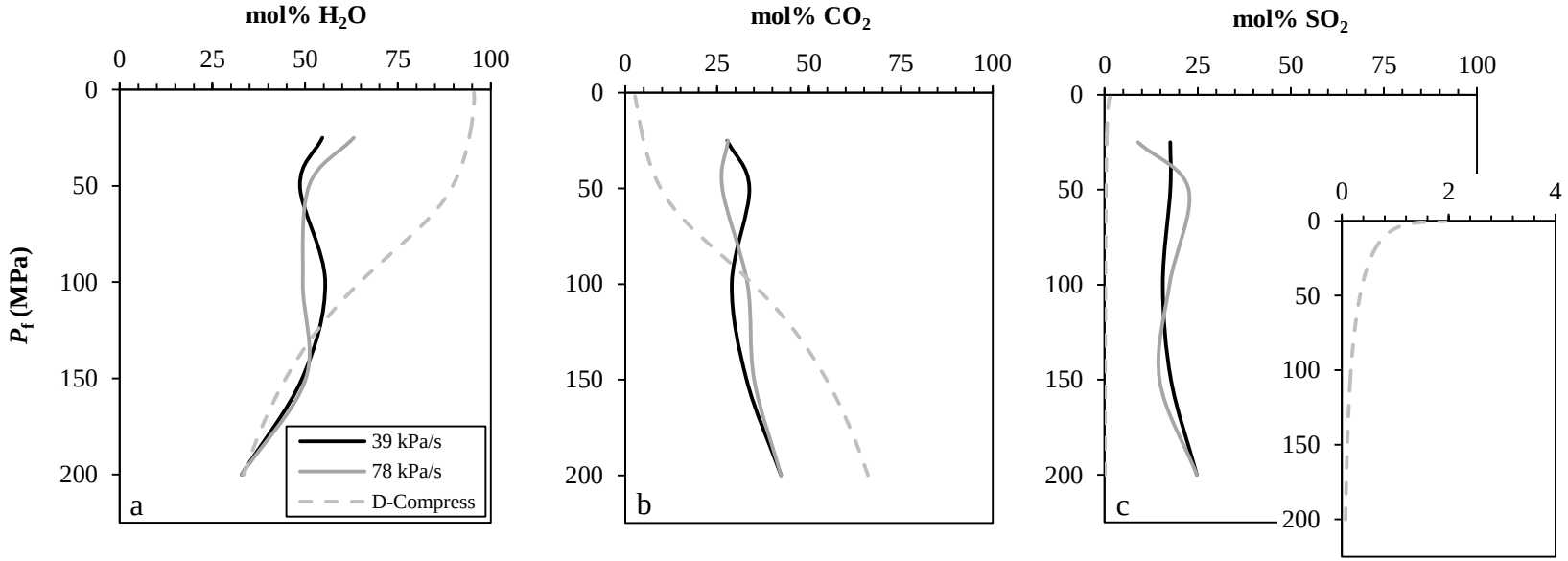

Le Gall et al. Fig. 4

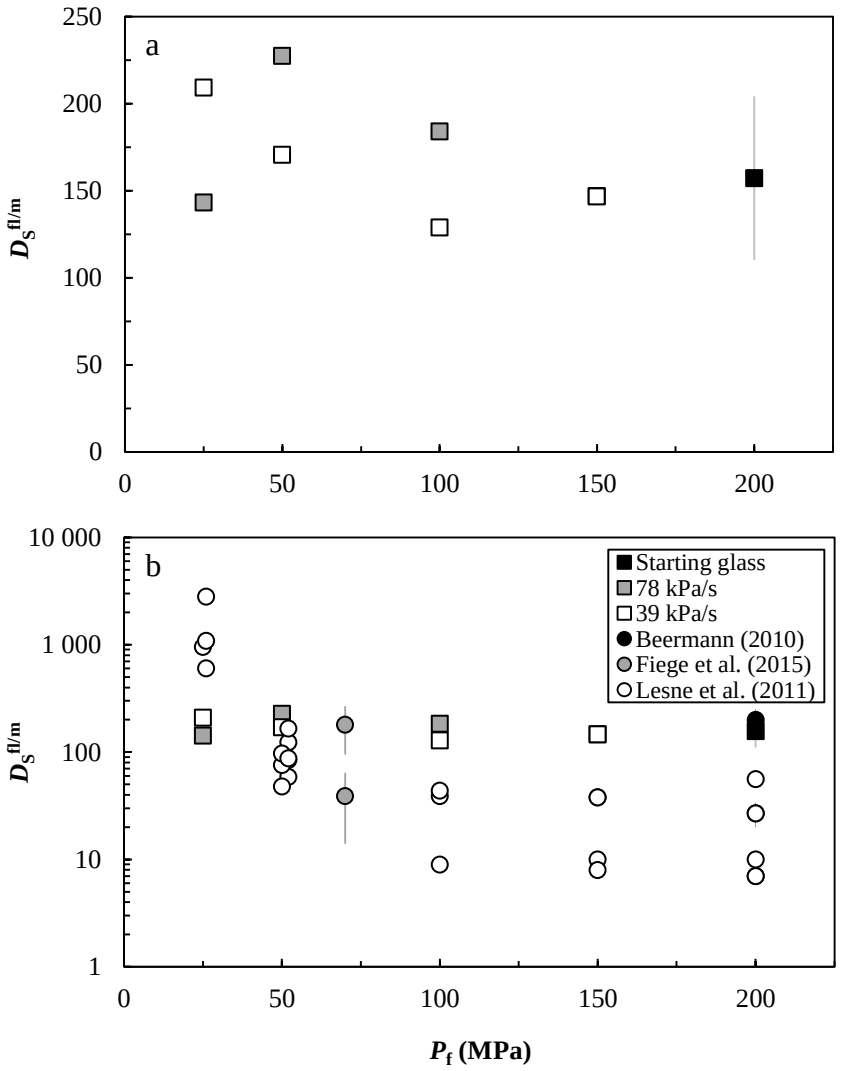

Le Gall et al. Fig. 5

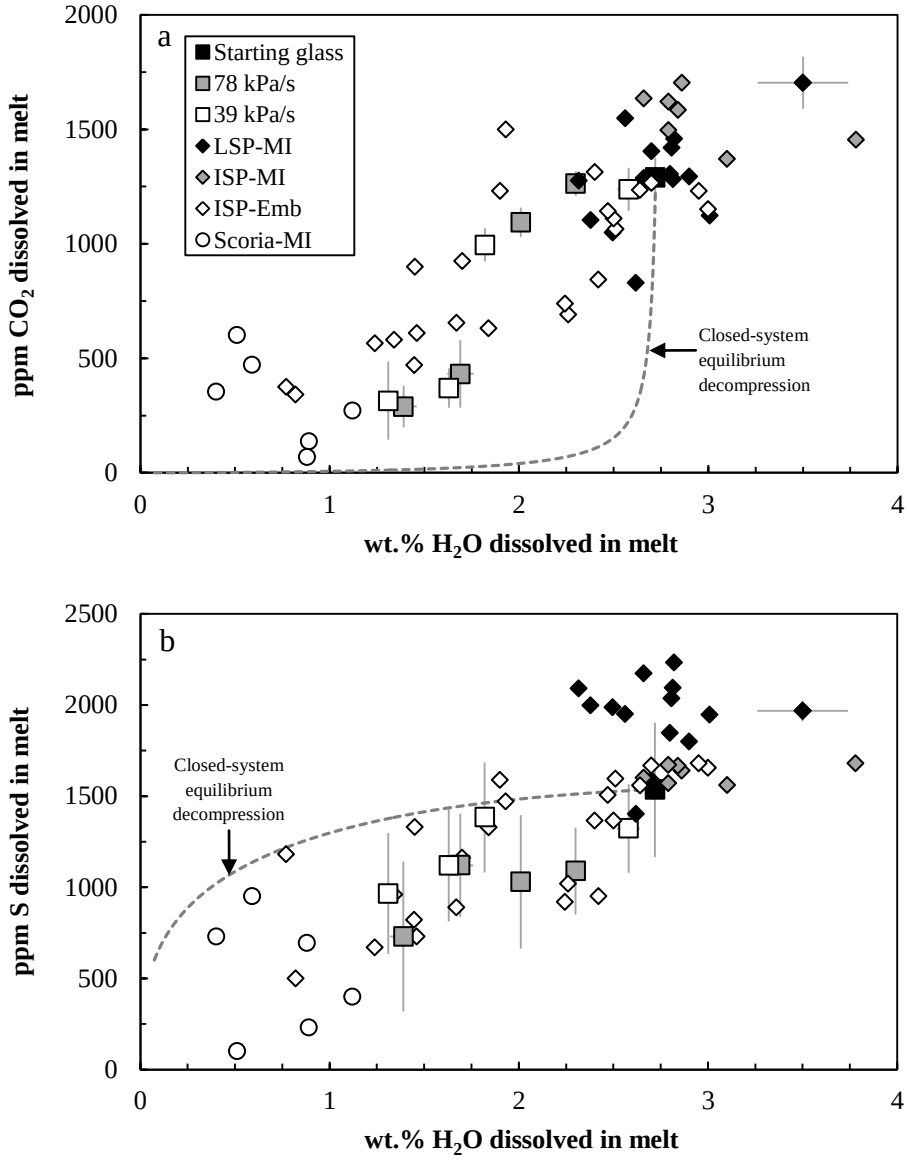

Le Gall et al. Fig. 6

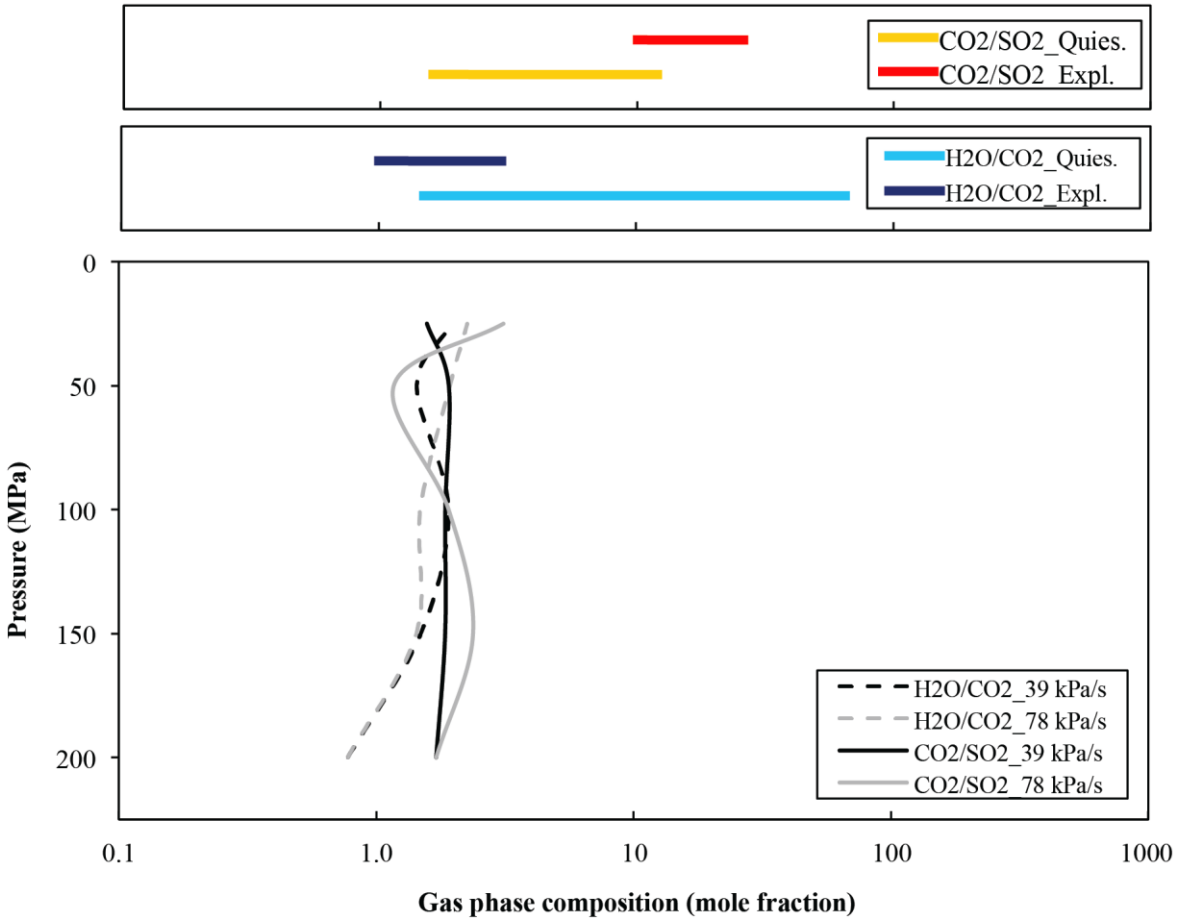

Le Gall et al. Fig. 7

Table 1. Composition of PST-9 golden pumice and starting glasses

Label	PST-9[a]	Glass[b] (*n* = 54)	Glass + 1% Fe[c] (*n* = 28)
SiO_2	49.4	50.9 (3)[d]	50.3 (3)
TiO_2	0.79	0.81 (8)	0.78 (9)
Al_2O_3	15.75	15.99 (28)	15.86 (21)
Fe_2O_3	1.3	nd	nd
FeO	6.5	7.7 (6)[e]	8.5 (3)[e]
MnO	0.15	0.16 (8)	0.11 (9)
MgO	7.96	7.21 (41)	7.53 (8)
CaO	12.73	12.34 (24)	12.11 (17)
Na_2O	2.27	2.39 (9)	2.29 (8)
K_2O	1.85	1.90 (12)	1.89 (8)
P_2O_5	0.43	0.55 (17)	0.52 (14)
Cr_2O_3	–	0.03 (4)	0.03 (3)
NiO	–	0.05 (6)	0.03 (5)
Total	99.1	97.4 (10)	98.8 (5)

Oxides are in wt.%.

[a] Whole-rock analysis performed at CRPG, Nancy, France (from Di Carlo et al., 2006).

[b] Electron microprobe analysis (normalized to 100%) of PST-9 glass (from Le Gall and Pichavant, 2015a).

[c] Electron microprobe analysis (normalized to 100%) of iron-enriched PST-9 glass used in this study.

[d] One standard deviation in terms of last unit cited.

[e] All Fe reported as FeO.

n: number of electron microprobe analyses.

nd: not determined.

Table 2. Experimental conditions

Run	XH_2O_{in}	XCS_{in}	T (°C)	$P_{synthesis}$ (MPa)	$t_{synthesis}$ (s)	P_{in} (MPa)	P_f (MPa)	t_{ramp} (s)	$\|dP/dt\|$ (kPa/s)	ΔFeO (%)	ΔS (%)	V (vol.%)
Synthesis experiment												
S19	0.46	0.63	1200	202.2	3900	200	–	–	–	–6	–23	0.00
Decompression experiments												
39 kPa/s series												
S+D32	0.54	0.64	1200	201.7	3600	200	150	1284	39	–5	–26	0.75
S+D33	0.54	0.63	1200	201.7	3660	200	100	2568	39	–5	–30	7.09
S+D37	0.43	0.59	1200	202.4	3600	200	50	3840	39	–16	–43	1.03
S+D40	0.48	0.59	1200	200.5	3960	200	25	4488	39	–12	–33	nd
78 kPa/s series												
S+D36	0.49	0.67	1200	202.0	3660	200	150	642	78	–8	–36	0.57
S+D34	0.48	0.63	1200	201.6	3840	200	100	1344	78	–8	–32	15.4
S+D35	0.52	0.53	1200	202.1	3720	200	50	1928	78	–13	–28	1.29
S+D38	0.56	0.67	1200	202.2	3600	200	25	2372	78	–9	–51	44.8

S19: synthesis experiment; S+D32 to S+D40: decompression experiments.

XH_2O_{in}: initial molar $H_2O/(H_2O+CO_2)$ in the charge; XCS_{in}: initial molar $CO_2/(CO_2+S)$; T: run temperature; $P_{synthesis}$: synthesis run pressure; $t_{synthesis}$: duration of the synthesis experiment; P_{in}: initial pressure before decompression; P_f: final pressure after decompression; t_{ramp}: duration of the ramp; $|dP/dt|$: decompression rate ($=10^6(P_{in}-P_f)/(gdt_{ramp})$), with g = 9.81 m/s^2 and d = 2.65 kg/m^3; ΔFeO: Amount (%) of FeO lost to the Pt capsule, the difference is made with the FeO content of PST-9 glass (see Table 1 for PST-9 glass composition, $\Delta FeO = 100\cdot(FeO_{glass}–FeO_{PST\text{-}9\ glass})/(FeO_{PST\text{-}9\ glass})$); ΔS: Amount (%) of S sequestered in PtS phases ($\Delta S = 100\cdot(mS_{initially\ introduced\ in\ the\ capsule}–mS_{introduced\ in\ the\ capsule\ corrected\ for\ the\ mS\ sequestred\ in\ PtS\ phases})/(mS_{initially\ introduced\ in\ the\ capsule})$), the mass (mg) of PtS (mPtS) formed was estimated by mass balance and the amount (%) of PtS (PtS) formed was determined by electron microprobe to calculate $mS_{introduced\ in\ the\ capsule\ corrected\ for\ the\ mS\ sequestred\ in\ PtS\ phases}$ ($=S*mS_{(initially\ introduced\ in\ the\ capsule)}–PtS*mPtS)/100$) with mS: mass of sulfur (mg), S: amount of sulfur (%); V: vesicularity (vol.% bubbles from 2D image analysis).

nd: not determined.

Table 3. Experimental compositions

Run	Volatiles dissolved in the melt			Volatiles dissolved in the fluid			
	H_2O (wt.%)[a]	CO_2 (ppm)[a]	S (ppm)[b]	H_2O (mol%)[c]	CO_2 (mol%)[c]	SO_2 (mol%)[c]	$D_S^{fl/m}$
Synthesis experiment							
S19	2.72 (2)	1291 (85)	1535 (369)	33	42	25	157
Decompression experiments							
39 kPa/s series							
S+D32	2.58 (6)	1238 (94)	1323 (243)	49	33	18	147
S+D33	1.82 (2)	996 (72)	1384 (302)	55	29	16	129
S+D37	1.63 (5)	370 (86)	1120 (307)	49	34	18	171
S+D40	1.31 (1)	315 (171)	965 (332)	55	28	18	209
78 kPa/s series							
S+D36	2.30 (1)	1264 (54)	1089 (238)	50	35	15	147
S+D34	2.01 (2)	1094 (64)	1030 (366)	49	33	17	184
S+D35	1.69 (7)	432 (147)	1121 (284)	51	26	23	228
S+D38	1.39 (7)	290 (91)	730 (411)	63	28	9	147

[a] Determined by IR spectroscopy.
[b] Determined by electron microprobe.
Standard deviations in parentheses.
[c] Determined by mass balance.
Volatiles dissolved in the fluid are expressed in mol%.
$D_S^{fl/m}$: fluid-melt partitioning coefficient of sulfur, $D_S^{fl/m} = S_{fluid}/S_{melt}$ (S_{fluid} and S_{melt} are the concentrations of sulfur in the fluid and in the melt, respectively, in wt.%). S_{fluid} was determined by mass balance calculations.

Table 4. FTIR data

Glass	*n*[a]	Thickness (µm)	Absorbance 3530 cm^{-1}	H_2O (wt.%)	Absorbance 1515 cm^{-1}	CO_2 (ppm)
Synthesis experiment						
S19	10	48 (1)[b]	1.260 (39)	2.72 (2)		
	10	108 (2)			0.315 (23)	1291 (85)
Decompression experiments						
39 kPa/s series						
S+D32	8	38 (3)	0.927 (83)	2.58 (6)		
	9	144 (4)			0.404 (30)	1238 (94)
S+D33	8	111 (2)	1.939 (51)	1.82 (2)	0.250 (14)	996 (72)
S+D37	6	44 (9)	0.694 (133)	1.63 (5)		
	5	48 (9)			0.041 (15)	370 (86)
S+D40	5	33 (6)	0.416 (75)	1.31 (1)		
	4	35 (4)			0.025 (14)	315 (171)
78 kPa/s series						
S+D36	8	67 (3)	1.477 (60)	2.30 (1)		
	10	75 (1)			0.214 (11)	1264 (54)
S+D34	10	80 (1)	1.546 (35)	2.01 (2)	0.199 (13)	1094 (64)
S+D35	5	46 (7)	0.754 (138)	1.69 (7)	0.047 (20)	432 (147)
S+D38	9	84 (8)	1.132 (137)	1.39 (7)		
	6	44 (3)			0.029 (10)	290 (91)

S19: glass synthesis experiment; S+D32 to S+D40: glass decompression experiments.
[a] Number of analytical spots.
[b] One standard deviation in terms of the last digit.

Synthèse générale et perspectives

1. Rappel des principaux résultats

Le principal enjeu de ce travail de thèse était d'apporter des contraintes sur le comportement des volatils majeurs (H_2O, CO_2, S) dissous dans les magmas basaltiques au cours des processus de dégazage (nucléation, croissance, coalescence, fragmentation) et, en particulier, de déterminer leur influence sur la nucléation des bulles. Les résultats importants de nos quatre ensembles d'expériences, faisant l'objet des chapitres iii, iv, v et vi, sont tout d'abord rappelés.

1.1. Basalte-H_2O

Les nucléations homogène et hétérogène des bulles d'H_2O interviennent toutes deux entre 150 et 200 MPa (Fig. 1) ; la présence de phases cristallines a soit peu (oxydes Fe–Ti), soit aucune (olivine, clinopyroxène) influence. Il s'ensuit un dégazage à l'équilibre chimique des liquides basaltiques hydratés jusqu'à 50–60 MPa, associé à de la croissance et de la coalescence de bulles, ainsi qu'à de l'"outgassing" (perte de bulles et de volatils par diffusion) favorisée par de faibles taux de décompression (< 3 m/s). Les liquides basaltiques hydratés se fragmentent autour de 25 MPa, suite à un second événement de nucléation homogène des bulles d'H_2O, intervenant entre 25 et 50 MPa. Cet événement tardif (i.e. superficiel) pourrait résulter d'une diminution de la diffusivité d'H_2O liée à une baisse de la teneur en H_2O du liquide silicaté à plus basse pression. Au cours de la décompression, l'équilibre textural n'est quasiment jamais atteint dans les liquides basaltiques hydratés. En effet, les verres après décompression ne montrent jamais de vésicularités s'approchant des valeurs d'équilibre. Néanmoins de fortes valeurs de vésicularités, proches de celles d'équilibre, sont trouvées dans les verres fragmentés à 25 MPa, suggérant que l'équilibre textural peut être rapidement atteint à basse pression (croissance expansive des bulles).

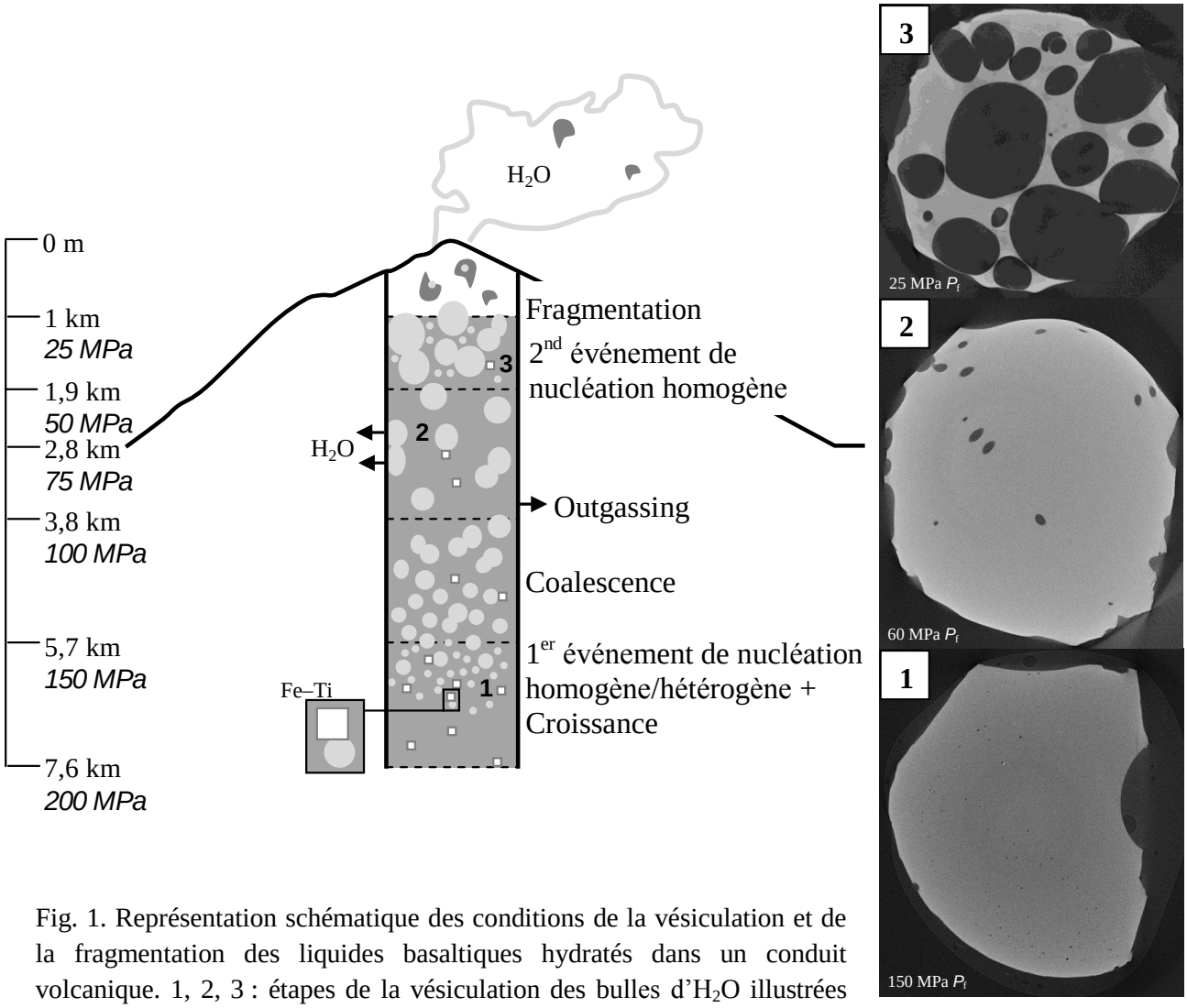

Fig. 1. Représentation schématique des conditions de la vésiculation et de la fragmentation des liquides basaltiques hydratés dans un conduit volcanique. 1, 2, 3 : étapes de la vésiculation des bulles d'H_2O illustrées par des images tomographiques des charges expérimentales.

1.2. Basalte-H_2O-CO_2

Dans les liquides basaltiques hydratés et carbonatés (contenant du CO_2), les bulles nucléent de façon homogène entre 150 et 200 MPa, ou entre 100 et 150 MPa selon la teneur en CO_2 (Fig. 2a, b). Les bulles nucléent plus tardivement de façon hétérogène, entre 100 et 200 MPa, voire entre 25 et 150 MPa, selon le rapport CO_2/H_2O de la bulle de gaz (Fig. 2a, b). De ces pressions de nucléation jusqu'à 25 MPa, le dégazage de ces liquides se fait systématiquement hors équilibre, chimique comme textural. Les bulles nucléent continuellement pendant la décompression, et l'arrivée de nouvelles bulles est associée à des processus de croissance et de coalescence (notamment entre 100 et 50 MPa), limités par la faible diffusivité du CO_2. Malgré de faibles vésicularités associées à la présence de CO_2, si la distance entre deux bulles est suffisamment courte, elles peuvent coalescer. La fragmentation de ces liquides n'a jamais été observée dans nos expériences de décompression, suggérant que

ce phénomène intervient à plus basse pression (P_f < 25 MPa). A noter que cette observation a des implications sur la génération des éruptions basaltiques explosives, dès lors que la fragmentation de ces liquides pourrait intervenir superficiellement (< 1 km), en lien avec l'arrivée de liquides basaltiques sursaturés en CO_2.

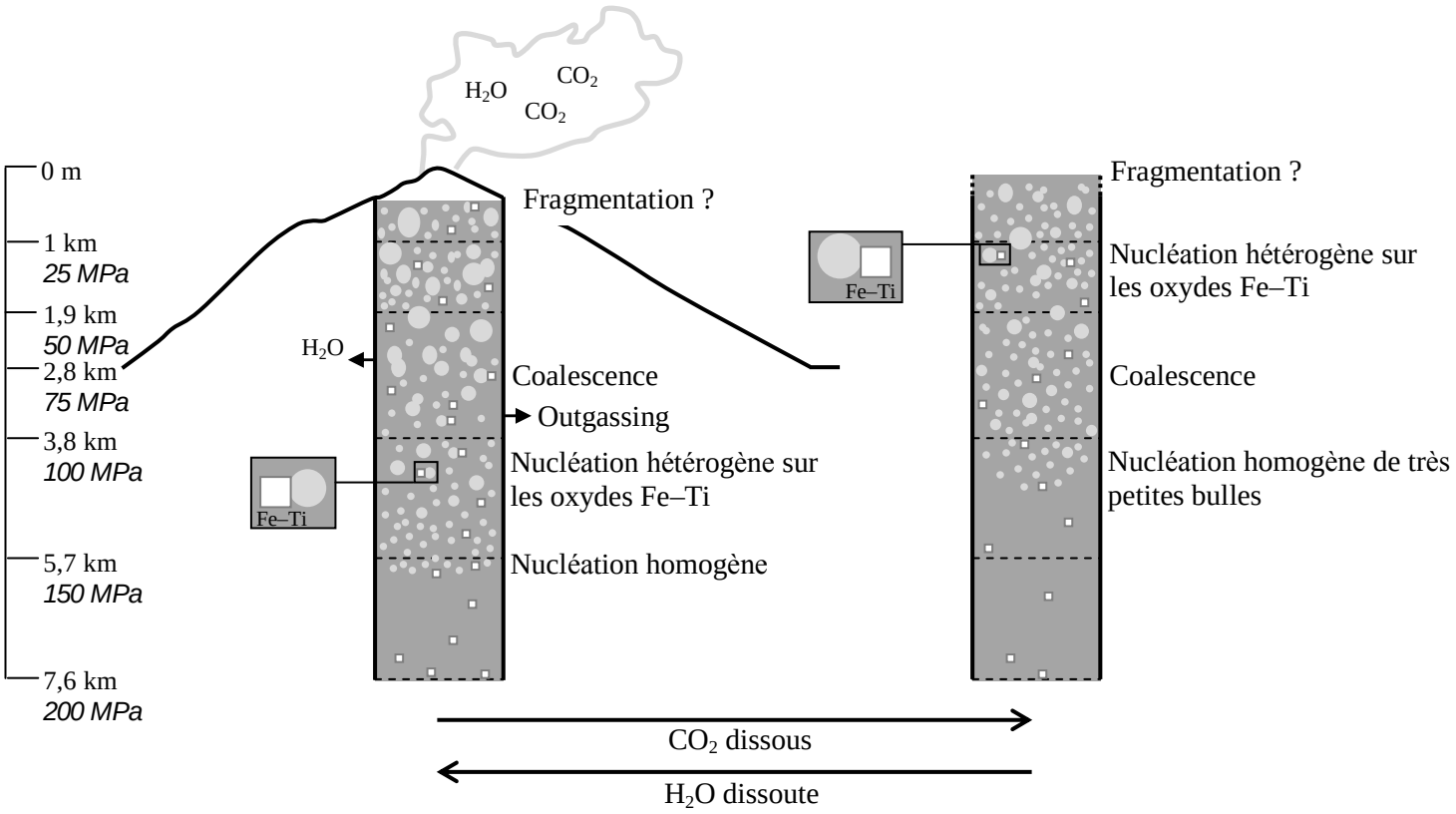

Fig. 2. Représentations schématiques des conditions de la vésiculation du système basalte-H_2O-CO_2 dans un conduit volcanique. (a) Cas d'un système basaltique riche en H_2O et pauvre en CO_2. (b) Cas d'un système basaltique pauvre en H_2O et riche en CO_2.

Il ressort de nos principaux résultats expérimentaux des rôles contrastés de H_2O et du CO_2 sur la vésiculation des bulles de gaz (notamment sur les mécanismes de croissance et de coalescence), en lien avec des différences de solubilité et de diffusivité. Ceci est illustré par des différences de texture de bulles entre les trois séries de volatils H_2O, CO_2 étudiées (Fig. 3).

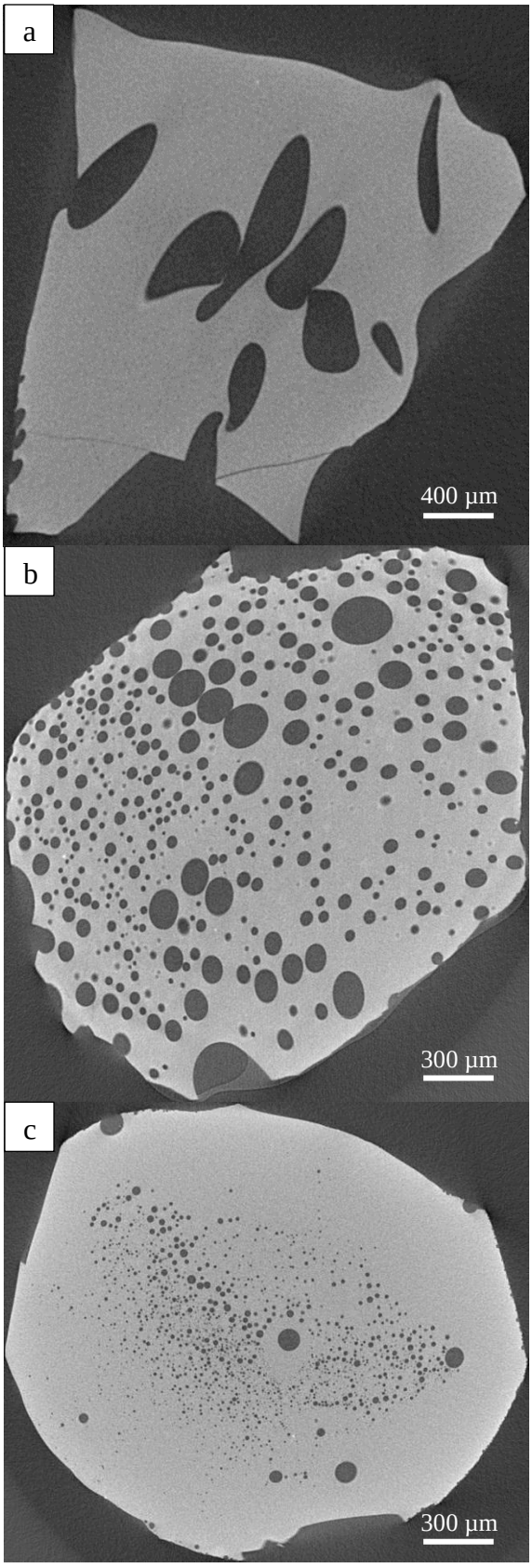

Fig. 3. Images tomographiques des textures de verres expérimentaux issus des séries #1 (a), #2 (b) et #3 (c) décomprimés à 25 MPa P_f à la vitesse de 3 m/s. Charges S+D38#1 (a), D28#2 (b), D25#3 (c), Chapitre iii.

Le CO_2 a une forte influence sur les processus de dégazage des magmas basaltiques. Comme préalablement démontré par Pichavant et al. (2013) pour les liquides basaltiques et communément admis pour les liquides plus riches en silice (ex. Gonnermann et Manga, 2005), le dégazage du CO_2 peut se faire hors équilibre. Pour cela, l'ascension du magma doit être suffisamment rapide. Le caractère continu de la nucléation est associé au maintien de fortes sursaturations en CO_2 dans le liquide, en accord avec le modèle numérique de Blower et al. (2002) et la théorie de Yamada et al. (2005 ; Fig. 4). Les bulles nucléent dans des "poches" de liquide sursaturé en CO_2, entre les bulles préexistantes ayant grossi par diffusion.

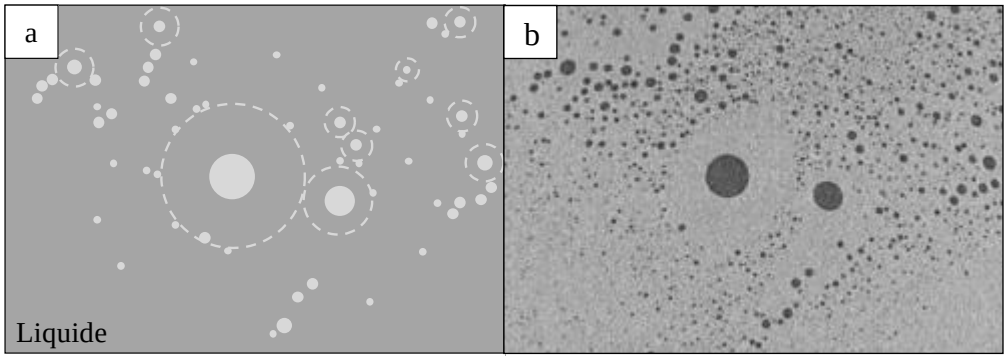

Fig. 4. (a) Illustration schématique de la nucléation continue des bulles d'H_2O-CO_2, d'après Blower et al. (2002) et Yamada et al. (2005). (b) Photo comparative d'un verre expérimental (détail de la charge D25#3, 25 MPa P_f, dP/dt = 3 m/s, Chapitre iii).

A noter que dans la lignée de travaux expérimentaux menés dans les liquides rhyolitiques (Cluzel, 2007), de fortes densités numériques de bulles sont produites en présence de CO_2.

1.3. Basalte-H_2O-CO_2-S

En présence de soufre, la nucléation homogène des bulles intervient entre 150 et 200 MPa (Fig. 5), c.-à-d. pour des pressions de sursaturation comparables à celles requises dans les systèmes basalte-H_2O et basalte-H_2O-CO_2. A noter que ces pressions de sursaturation sont supérieures à celles requises pour la nucléation hétérogène des bulles sur les sulfures de fer (≤ 1 MPa, Fig. 5). Le soufre n'a pas d'impact propre sur les comportements de H_2O et du CO_2 au cours du dégazage. Le dégazage du soufre se fait dans des conditions proches de l'équilibre, bien qu'il soit dégazé en plus grande quantité qu'attendu (comme H_2O en présence d'une phase volatile mixte). Avec un taux de décompression de 3 m/s, nous avons observé de la

coalescence de bulles (H_2O, CO_2, S) entre 50 et 25 MPa, à l'origine d'une micro poche de gaz ("gas slug") à 25 MPa (Fig. 5).

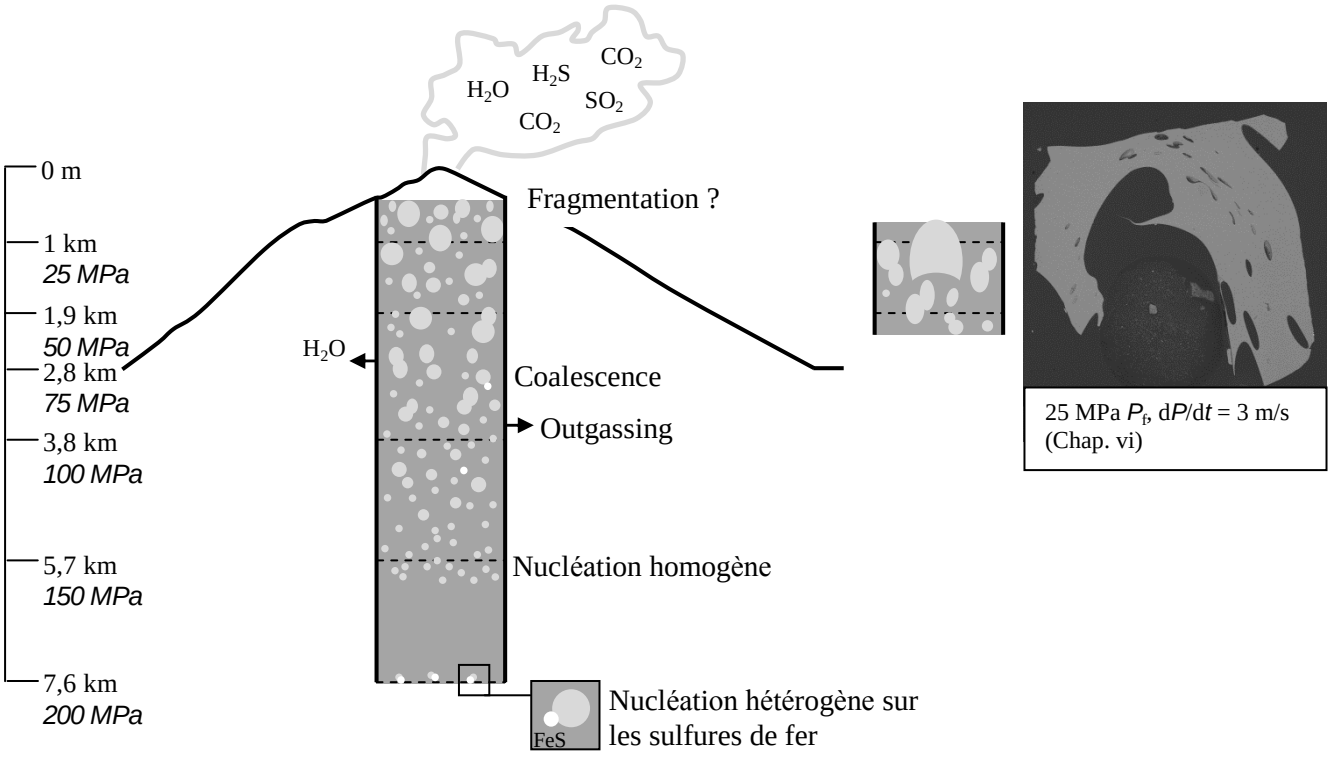

Fig. 5. Représentation schématique des conditions de la vésiculation du système basalte-H_2O-CO_2-S dans un conduit volcanique.

1.4. Influence de la vitesse d'ascension

Le taux de décompression n'a que peu d'influence sur la pression de nucléation des bulles (H_2O, CO_2, S), autrement dit sur la pression de sursaturation, dans les liquides basaltiques, tout comme dans les liquides rhyolitiques (ex. Mourtada-Bonnefoi et Laporte, 2004 ; Cluzel et al., 2008). En revanche, il influe sur la densité numérique de bulles ; celle-ci augmente généralement avec l'augmentation du taux de décompression, excepté dans les liquides basaltiques riches en CO_2 et pauvres en H_2O. Cette corrélation positive est en accord avec les observations de Mourtada-Bonnefoi et Laporte (2004) et Cluzel et al. (2008) dans les liquides rhyolitiques.

1.5. Implications pour le volcan Stromboli

Nos données, obtenues dans des conditions voisines des conditions naturelles, ont des implications volcanologiques directes, en particulier pour le Stromboli. Nos produits expérimentaux contenant du CO_2 reproduisent, ou approchent, les textures des produits basaltiques émis lors des éruptions paroxysmales (Stromboli) et Pliniennes (Etna, Masaya, Tarawera), notamment les densités numériques de bulles et les distributions de taille des bulles. Cela signifie que les processus de dégazage des magmas basaltiques sont assez bien reproduits par nos expériences de décompression. Les concentrations en H_2O, CO_2, S de nos verres expérimentaux, décomprimés entre 200 et 25 MPa, reproduisent la chimie des verres du Stromboli (teneur en volatils des inclusions vitreuses), ce qui signifie que le chemin de dégazage naturel est étroitement simulé par nos expériences de décompression. Nos données texturales associées à celles de Pichavant et al. (2013 ; taille et densité numérique de bulles, Fig. 6), nous ont finalement permis de contraindre l'ascension des ponces Stromboliennes depuis leur réservoir profond, en 43 à 128 min (correspondant à des vitesses d'ascension comprises entre 1 et 3 m/s). Ces conditions ont été obtenues sur la base d'hypothèses quant à l'évolution des paramètres texturaux en-dessous de 25 MPa. A savoir, la continuité puis l'arrêt de la nucléation des bulles avant le niveau de fragmentation, associés à la croissance et à la coalescence des bulles. A noter que pour les vitesses d'ascension inférieures à 1,5 m/s (1 et 0,64 m/s), la nucléation des bulles d'H_2O-CO_2 semble déjà terminée ou dominée par leur coalescence (processus limité dans les ponces Stromboliennes).

Les rapports molaires H_2O/CO_2 de la phase gazeuse expérimentale reproduisent de façon satisfaisante ceux mesurés au Stromboli lors des dégazages passif et explosif. Il en est de même pour les rapports molaires CO_2/SO_2 associés au dégazage passif, mais pas pour ceux associés aux éruptions normales et majeures. Cependant, d'après nos données ce pourrait être le cas à plus basse pression (P_f << 25 MPa).

Nos observations expérimentales (texturales et chimiques) supportent un modèle, pour l'origine des éruptions paroxysmales au Stromboli, de dégazage explosif de liquides sursaturés en CO_2 à basse pression (Pichavant et al., 2013).

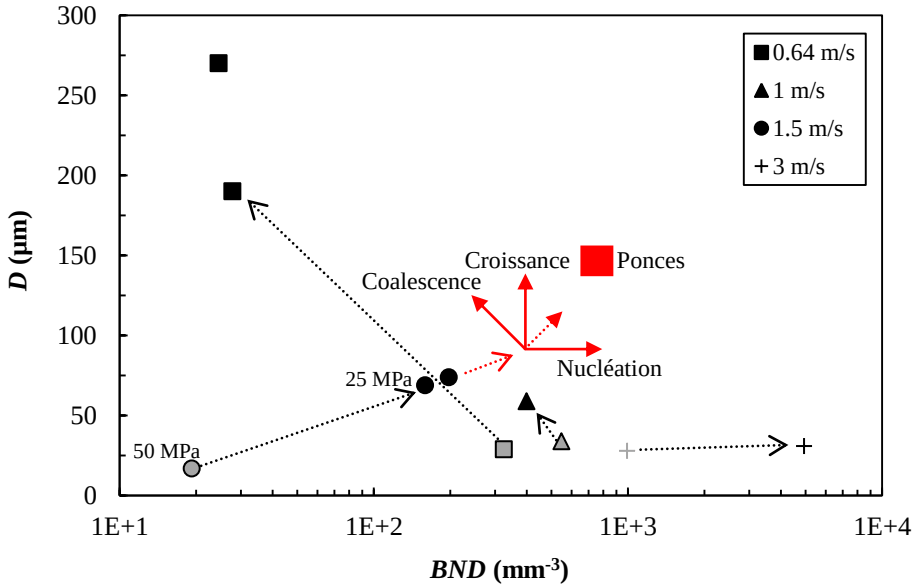

Fig. 6. Diagramme montrant l'évolution du diamètre moyen des bulles *D* en fonction de l'évolution de la densité numérique de bulles *BND*, entre 50 (symboles gris) et 25 MPa (symboles noirs). L'évolution des paramètres *D* et *BND* est retracée (flèches noires) pour les vitesses d'ascension de 0,64 (carrés), 1 (triangles), 1,5 (cercles) et 3 (croix) m/s ; 0,64 et 1 m/s : données de Pichavant et al. (2013) ; 1.5 et 3 m/s : données de cette étude (Chapitre iii, iv). Le domaine des ponces Stromboliennes (rectangle rouge, Polacci et al., 2006, 2009) est indiqué pour comparaison. Les flèches rouges indiquent l'évolution des paramètres texturaux (*D*, *BND*) attendue en fonction des processus de dégazage magmatique (coalescence, croissance, nucléation) intervenant au-dessous de 25 MPa.

2. Spécificités des liquides basaltiques

2.1. Nucléation homogène des bulles

Nos données concernant la nucléation homogène des bulles montrent que de bien plus faibles pressions de sursaturation ΔP_{HoN} sont requises dans les liquides basaltiques : < 50 MPa dans les systèmes basalte-H_2O et basalte-H_2O-CO_2-S et < 50–100 MPa dans le système basalte-H_2O-CO_2. Ces relativement faibles pressions de sursaturation impliquent de plus faibles tensions de surface dans les basaltes, comprises entre 0,054–0,059 et 0,091 N/m. Ces résultats sont en accord avec des conclusions portées sur les compositions dacitiques (Mangan et al., 2004), à savoir que le développement de fortes sursaturations en volatils est unique aux liquides rhyolitiques. A noter que l'influence du CO_2 sur la pression de sursaturation parait moindre dans les basaltes que dans les rhyolites (Mourtada-Bonnefoi et Laporte, 2002).

2.2. Nucléation hétérogène des bulles

La présence d'oxydes Fe–Ti dans le liquide basaltique n'abaisse pas les pressions de sursaturation requises à la nucléation des bulles, contrairement à ce qui est observé dans les rhyolites, celles-ci sont comparables dans le cas des nucléations hétérogène et homogène. Bien au contraire, en présence de fortes concentrations en CO_2 dans le liquide basaltique, la nucléation hétérogène des bulles est retardée ($\Delta P_{HeN} > \Delta P_{HoN}$), en lien avec le rapport CO_2/H_2O de la bulle. Les très faibles sursaturations trouvées dans les liquides rhyolitiques dans le cas de la nucléation hétérogène (≤ 1–5 MPa, Hurwitz et Navon, 1994) leur semblent spécifiques, comme énoncé par rapport aux dacites (Mangan et al., 2004).

La nucléation homogène des bulles est le mécanisme dominant dans les liquides basaltiques. Au cours de la décompression, contrairement à ce qui pourrait être attendu dans les liquides rhyolitiques, le premier événement de nucléation des bulles n'est pas hétérogène, bien qu'il prenne place à haute pression (i.e. en profondeur).

2.3. Caractéristiques texturales

Dans le système basaltique, en comparaison avec le système rhyolitique, la densité numérique de bulles ne devient pas stationnaire (marquant un arrêt ou un ralentissement de la nucléation, Toramaru, 1995 ; Mourtada-Bonnefoi et Laporte, 2004 ; Cluzel et al., 2008) mais évolue tout au long de la décompression. Ceci témoigne du caractère continu de la nucléation des bulles d'H_2O-CO_2 dans les basaltes, ainsi que de l'efficacité des processus de croissance et de coalescence dans le système basalte-H_2O, en lien avec la faible viscosité des liquides basaltiques. Ceci conduit à des distributions de taille de bulles plus complexes, exponentielles et en loi de puissance, comme observé dans les produits naturels. Alors que dans les systèmes rhyolitiques, les produits expérimentaux ont pour la plupart des distributions unimodales (ex. Mourtada-Bonnefoi et Laporte, 2002 ; Cluzel et al., 2008), traduisant un évènement unique de nucléation.

Contrairement à ce qui est prédit pour les liquides évolués, dans les liquides basaltiques l'efficacité du dégazage n'est pas principalement liée à la densité numérique de bulles ; un grand nombre de bulles ne certifie pas un état d'équilibre du dégazage. C'est ce qu'on observe dans les liquides contenant du CO_2, bien qu'ils génèrent de nombreuses bulles

(jusqu'à 10^4 mm^{-3}), le fait qu'elles soient petites (impliquant de trop grandes distances entre les bulles) limite l'exsolution du CO_2.

3. Améliorations et perspectives de recherche

L'objectif de ce travail de thèse était d'améliorer notre connaissance des conditions de la vésiculation des magmas basaltiques par une approche expérimentale. Si nous apportons des informations sur les mécanismes de nucléation, croissance et coalescence des bulles, ainsi que sur la fragmentation des magmas hydratés, nos observations ouvrent de nouvelles perspectives de recherche.

Tout d'abord, des modifications techniques peuvent être apportées, notamment dans les expériences menées avec du soufre. Les étapes de synthèse et de décompression pourraient être menées dans deux expériences distinctes pour mieux contrôler la composition des verres avant qu'ils ne soient décomprimés et éviter la présence d'une phase fluide initiale. Nous ne l'avons pas fait par manque de temps mais aussi, il faut le rappeler, face aux défaillances des capsules en Pt ; celles-ci se fragilisant dès 1 heure d'expérience. Il faut donc faire attention à ces problèmes, voir si mener deux expériences distinctes serait réalisable ou si la durée de vie des capsules est plus courte. Dans ce dernier cas, il pourrait être envisagé d'utiliser la technique de la double capsule, en utilisant des matériaux inertes au soufre, tels que le quartz, le graphite, l'olivine, … (cf. Webster et Botcharnikov, 2011). C'est d'ailleurs ce qui devrait être fait dans toutes les expériences menées en présence de soufre à haute température (> 1064°C, c.-à-d. > *T* de fusion de l'or), l'effet des réactions chimiques entre le soufre et le métal des capsules sur la solubilité ou le partage (liquide/gaz) de ce constituant volatil étant difficilement quantifiable (Webster et Botcharnikov, 2011).

Bien que la détermination de la composition de la phase gazeuse par bilan de masse se soit avérée satisfaisante, il a été envisagé au cours de cette thèse d'analyser la phase gazeuse contenue dans les capsules par chromatographie gazeuse. Cependant, par manque de temps et face aux problèmes techniques rencontrés (cristallisation du soufre, rééquilibration du soufre sous forme H_2S) cela n'a pas abouti. Dans le futur, il serait intéressant de mettre en place un

protocole expérimental et analytique dans ce sens, en collaboration avec l'INGV de Palerme comme initié.

Il serait intéressant de faire, dans nos verres expérimentaux pour commencer, des mesures FTIR plus précises, j'entends par là plus proches des bulles pour mieux contraindre les distributions (ou diffusions) de H_2O et du CO_2. Bien sûr les limites sont celles que nous avons rencontrées, à savoir la taille du spot (50 à 100 µm de diamètre) vis-à-vis de la répartition des bulles dans l'échantillon et de la qualité du spectre FTIR, ainsi que la possible inexistence de profils de diffusion dans nos échantillons (tout simplement).

Afin de contraindre avec précision les effets des volatils sur la nucléation des bulles, il serait aussi intéressant d'ajouter des paliers de décompression entre 200 et 150 MPa P_f. On distinguerait ainsi davantage les influences de l'H_2O, du CO_2 et du soufre sur les pressions de nucléation, tout en apportant plus de précisions sur les pressions de sursaturation requises au déclenchement des nucléations homogène et hétérogène des bulles.

Dans le cas de la nucléation hétérogène des bulles, notre étude systématique dans le système basalte-titanomagnétite-H_2O-CO_2 est l'une des rares (si ce n'est la seule) menée en présence de CO_2 dans les liquides silicatés. Pour améliorer notre connaissance de ce mécanisme en présence de CO_2 (confirmation de l'effet de composition de la bulle), davantage d'expériences seraient nécessaires, aussi bien dans les liquides basaltiques que dans les liquides plus évolués. Ainsi, il faudrait complexifier, par l'ajout de CO_2, les systèmes hydratés déjà étudiés (majoritairement rhyolitiques) ; l'influence du CO_2 pourrait minimiser l'importance de la nucléation hétérogène des bulles dans ces liquides, comme c'est le cas dans les liquides basaltiques.

Des expériences de décompression dans les systèmes basalte-H_2O-CO_2 et basalte-H_2O-CO_2-S pourraient être menées à plus basse pression (P_f < 25 MPa) pour valider, ou invalider, nos hypothèses quant aux évolutions des principaux paramètres texturaux (vésicularité, taille des bulles, densité numérique de bulles) et de la phase gazeuse

(augmentation du rapport CO_2/SO_2). Ces expériences pourraient aussi être menées dans une perspective de recherche sur le phénomène de la fragmentation des liquides basaltiques. En effet, mener des expériences de décompression à plus basse pression (P_f < 25 MPa) pourrait permettre d'observer la fragmentation des liquides basaltiques contenant du CO_2, et ainsi parvenir à une meilleure connaissance des mécanismes de la fragmentation (ex. influence de la composition et de la teneur en volatils). Des expériences de fragmentation systématiques pourraient également être menées dans le système basalte-H_2O, en conditions saturées et sous-saturées. Cela permettrait de documenter notre hypothèse quant à l'implication du second événement de nucléation des bulles d'H_2O, par l'étude des fragments émis.

Notre étude dans le système basalte-C-H-O-S souligne le manque de contraintes sur les solubilités du soufre dans nos conditions expérimentales (haute température, composition basaltique), notamment en présence d'une phase volatile mixte incluant le CO_2, ainsi qu'en conditions réductrices. Bien entendu ces expériences sont limitées par le comportement complexe du soufre (sa spéciation en fonction des conditions d'oxydoréduction et sa réaction avec le métal des capsules, Ag, Pt, Pd). De même, les diffusions de H_2O et du CO_2 dans les liquides basaltiques mériteraient d'être davantage contraintes. Cela permettrait de supporter, ou non, notre observation quant à la baisse de diffusivité de l'eau lorsque la teneur en eau du liquide diminue.

Nos données sur l'évolution du rapport molaire CO_2/SO_2 dans la phase fluide montrent peu de variation au cours de la décompression ; les comportements du CO_2 et du S étant peu découplés. Etant donné que les mesures de gaz montrent de fortes variations du rapport SO_2/HCl en lien avec l'activité volcanique (ex. Aiuppa et Federico, 2004), il serait intéressant de complexifier le système basaltique étudié en ajoutant le Cl, envisageant ainsi ce rapport comme le plus utile à la surveillance des volcans.

Enfin, l'une des questions importantes soulevée par notre étude concerne le partage des volatils majeurs (H_2O, CO_2, S) entre le liquide et la phase gazeuse. Au regard du comportement du CO_2 au cours du dégazage, ce partage paraît contrôlé par la diffusion des constituants volatils. Cependant, le comportement du soufre n'est pas en adéquation. Bien que

sa diffusivité soit inférieure à celle du CO_2, le soufre est perdu davantage qu'il devrait lors d'un dégazage à l'équilibre. Son comportement contraste donc fortement avec celui du CO_2. Le partage des constituants volatils dans le gaz dépend-il de leur capacité à diffuser du liquide vers la bulle, ou bien de leur volatilité ? Autrement dit, de l'affinité du volatil pour les constituants majeurs de la phase gazeuse (contrôle de la composition de la phase gazeuse, ex. Métrich et al., 2010).

Bibliographie

A …

Abràmoff, M.D., Magalhães, P.J., Ram, S.J., 2004. Image processing with ImageJ. Biophotonics International 11, 36–43.

Aiuppa, A., Federico, C., 2004. Anomalous magmatic degassing prior to the 5th April 2003 paroxysm on Stromboli. Geophysical Research Letters 31, L14607. doi:10.1029/2004GL020458

Aiuppa, A., Bertagnini, A., Métrich, N., Moretti, R., Di Muro, A., Liuzzo, M., Tamburello, G., 2010a. A model of degassing for Stromboli volcano. Earth and Planetary Science Letters 295, 195–204. doi:10.1016/j.epsl.2010.03.040

Aiuppa, A., Burton, M., Caltabiano, T., Giudice, G., Guerrieri, S., Liuzzo, M., Murè, F., Salerno, G., 2010b. Unusually large magmatic CO_2 gas emissions prior to a basaltic paroxysm: CO_2 gas emissions prior to a paroxysm. Geophysical Research Letters 37, L17303. doi:10.1029/2010GL043837

Aiuppa, A., Burton, M., Allard, P., Caltabiano, T., Giudice, G., Gurrieri, S., Liuzzo, M., Salerno, G., 2011. First observational evidence for the CO_2-driven origin of Stromboli's major explosions. Solid Earth 2, 135–142. doi:10.5194/se-2-135-2011

Aiuppa, A., Federico, C., Giudice, G., Giuffrida, G., Guida, R., Gurrieri, S., Liuzzo, M., Moretti, R., Papale, P., 2009. The 2007 eruption of Stromboli volcano: Insights from real-time measurement of the volcanic gas plume CO_2/SO_2 ratio. Journal of Volcanology and Geothermal Research 182, 221–230. doi:10.1016/j.jvolgeores.2008.09.013

Alidibirov, M.A., 1994. A model for viscous magma fragmentation during volcanic blasts. Bulletin of Volcanology 56, 459–465.

Allard, P., 2010. A CO_2-rich gas trigger of explosive paroxysms at Stromboli basaltic volcano, Italy. Journal of Volcanology and Geothermal Research 189, 363–374.

Allard, P., Aiuppa, A., Burton, M., Caltabiano, T., Federico, C., Salerno, G., La Spina, A., 2008. Crater gas emissions and the magma feeding system of Stromboli volcano. In: Calvari, S., Inguaggiato, S., Puglisi, G., Ripepe, M., Rosi, M. (Eds.), Learning from Stromboli: AGU Geophysics Monograph Series 182, 65–80.

B …

Bagdassarov, N.S., Dingwell, D.B., Webb, S.L., 1994. Viscoelasticity of crystal-and bubble-bearing rhyolite melts. Physics of the Earth and Planetary Interiors 83, 83–99.

Bagdassarov, N.S., Dorfman, A., Dingwell, D.B., 2000. Effect of alkalis, phosphorus, and water on the surface tension of haplogranite melt. American Mineralogist 85, 33–40.

Bai, L., Baker, D.R., Rivers, M., 2008. Experimental study of bubble growth in Stromboli basalt melts at 1 atm. Earth and Planetary Science Letters 267, 533–547. doi:10.1016/j.epsl.2007.11.063

Baker, D.R., Alletti, M., 2012. Fluid saturation and volatile partitioning between melts and hydrous fluids in crustal magmatic systems: The contribution of experimental measurements and solubility models. Earth-Science Reviews 114, 298–324.

Baker, D.R., Freda, C., Brooker, R.A., Scarlato, P., 2005. Volatile diffusion in silicate melts and its effects on melt inclusions. Annals of Geophysics 48, N. 4/5, 699–717.

Baker, D.R., Lang, P., Robert, G., Bergevin, J.-F., Allard, E., Bai, L., 2006. Bubble growth in slightly supersaturated albite melt at constant pressure. Geochimica et Cosmochimica Acta 70, 1821–1838.

Barberi, F., Rosi, M., Sodi, A., 1993. Volcanic hazard assessment at Stromboli based on review of historical data. Acta Vulcanol 3, 173–187.

Behrens, H., Stelling, J., 2011. Diffusion and Redox Reactions of Sulfur in Silicate Melts. Reviews in Mineralogy and Geochemistry 73, 79–111. doi:10.2138/rmg.2011.73.4

Bertagnini, A., Roberto, A., Pompilio, M., 2011. Paroxysmal activity at Stromboli: lessons from the past. Bulletin of Volcanology 73, 1229–1243. doi:10.1007/s00445-011-0470-3

Bertagnini, A., Métrich, N., Landi, P., Rosi, M., 2003. Stromboli volcano (Aeolian Archipelago, Italy): An open window on the deep-feeding system of a steady state basaltic volcano. Journal of Geophysical Research, 108 (B7), 2336. doi:10.1029/2002JB002146

Blank, J.G., Brooker, R.A., 1994. Experimental studies of carbon dioxide in silicate melts; solubility, speciation, and stable carbon isotope behavior. Reviews in Mineralogy and Geochemistry 30, 157–186.

Blower, J.D., Keating, J.P., Mader, H.M., Phillips, J.C., 2001. Inferring volcanic degassing processes from vesicle size distributions. Geophysical Research Letters 28, 347–350.

Blower, J.D., Keating, J.P., Mader, H.M., Phillips, J.C., 2002. The evolution of bubble size distributions in volcanic eruptions. Journal of Volcanology and Geothermal Research 120, 1–23.

Blundy, J., Cashman, K.V., Rust, A., Witham, F., 2010. A case for CO_2-rich arc magmas. Earth and Planetary Science Letters 290, 289–301.

Bonaccorso, A., Calvari, S., Linde, A., Sacks, S., Boschi, E., 2012. Dynamics of the shallow plumbing system investigated from borehole strainmeters and cameras during the 15 March, 2007 Vulcanian paroxysm at Stromboli volcano. Earth and Planetary Science Letters 357–358, 249–256. doi:10.1016/j.epsl.2012.09.009

Bolte, S., Cordelières, F.P., 2006. A guided tour into subcellular colocalization analysis in light microscopy. Journal of Microscopy 224, 213–232.

Bourgue, E., Richet, P., 2001. The effects of dissolved CO_2 on the density and viscosity of silicate melts: a preliminary study. Earth and Planetary Science Letters 193, 57–68.

Brugier, Y.A., Alletti, M., Pichavant, M., 2015. Fe pre-enrichment: A new method to counteract iron loss in experiments on basaltic melts. American Mineralogist 100, 2106–2111. doi: 10.2138/am-2015-5166

Buchanan, D.L., Nolan, J., 1979. Solubility of sulfur and sulfide immiscibility in synthetic tholeiitic melts and their relevance to Bushveld-complex rocks. The Canadian Mineralogist 17, 483–494.

Burgisser, A., Alletti, M., Scaillet, B., 2015. Simulating the behavior of volatiles belonging to the C–O–H–S system in silicate melts under magmatic conditions with the software D-Compress.

Computers & Geosciences 79, 1–14.

Burnham, C.W., 1979. The importance of volatile constituents. In: Yoder, H.S. (Eds.), The evolution of the igneous rocks (Fiftieth anniversary perspectives), Princeton University Press, Princeton, 439–482.

Burnham, C.W., Holloway, J.R., Davis, N.F., 1969. Thermodynamic properties of water to 1000°C and 10000 bars. Geological Society of America, Special Papers 132, 1–96.

Burton, M., Allard, P., Mure, F., La Spina, A., 2007. Magmatic Gas Composition Reveals the Source Depth of Slug-Driven Strombolian Explosive Activity. Science 317, 227–230. doi:10.1126/science.1141900

C …

Cluzel, N., 2007. Simulation expérimentale de l'ascension et de la vésiculation des magmas rhyolitiques : application à la cinétique de nucléation des bulles et implications volcanologiques. Thèse, Université de Clermont-Ferrand 2.

Cluzel, N., Laporte, D., Provost, A., Kannewischer, I., 2008. Kinetics of heterogeneous bubble nucleation in rhyolitic melts: implications for the number density of bubbles in volcanic conduits and for pumice textures. Contributions to Mineralogy and Petrology 156, 745–763. doi:10.1007/s00410-008-0313-1

Costantini, L., Houghton, B.F., Bonadonna, C., 2010. Constraints on eruption dynamics of basaltic explosive activity derived from chemical and microtextural study: the example of the Fontana Lapilli Plinian eruption, Nicaragua. Journal of Volcanology and Geothermal Research 189, 207–224.

D …

Di Carlo, I., 2004. Experimental simulation of pre-eruptive conditions of yellow pumice–Stromboli. Ph.D. thesis, University of Palermo.

Di Carlo, I., Pichavant, M., Rotolo, S.G., Scaillet, B., 2006. Experimental crystallization of a high-K arc basalt: the golden pumice, Stromboli volcano (Italy). Journal of Petrology 47, 1317–1343.

Di Roberto, A., Bertagnini, A., Pompilio, M., Gamberi, F., Marani, M.P., Rosi, A.M., 2008. Newly discovered submarine flank eruption at Stromboli volcano (Aeolian Islands, Italy). Geophysical Research Letters 35, L16310. doi:10.1029/2008GL034824

Dingwell, D.B., 1996. Volcanic dilemma: flow or blow? Science 273, 1054–1055.

Dixon, J.E., 1997. Degassing of alkalic basalts. American Mineralogist 82, 368–378.

Dixon, J.E., Pan, V., 1995. Determination of the molar absorptivity of dissolved carbonate in basanitic glass. American Mineralogist 80, 1339–1342.

Dixon, J.E., Stolper, E.M., Holloway, J.R., 1995. An experimental study of water and carbon dioxide solubilities in mid-ocean ridge basaltic liquids. Part I: calibration and solubility models. Journal of Petrology 36, 1607–1631.

E …

Edmonds, M., 2008. New geochemical insights into volcanic degassing. Philosophical Transactions of the Royal Society A: Mathematical, Physical and Engineering Sciences 366, 4559–4579. doi:10.1098/rsta.2008.0185

Epel'baum, M.B., 1980. Silicate melts with volatile components, Nauka, Moscow.

Epel'baum, M.B., Babashov, I.V., Salova, T.P., 1973. Surface tension of felsic magmatic melts at high temperatures and pressures. Geokhimiya 3, 461–464.

F …

Ferry, J.M., Baumgartner, L., 1987. Thermodynamic models of molecular fluids at the elevated pressures and temperatures of crustal metamorphism. Reviews in Mineralogy and Geochemistry 17, 323–365.

Fiege, A., Holtz, F., Cichy, S. B., 2014a. Bubble formation during decompression of andesitic melts. American Mineralogist 99, 1052–1062.

Fiege, A., Behrens, H., Holtz, F., Adams, F., 2014b. Kinetic vs. thermodynamic control of degassing of H_2O–S±Cl-bearing andesitic melts. Geochimica et Cosmochimica Acta 125, 241–264. doi:10.1016/j.gca.2013.10.012

Fiege, A., Holtz, F., Behrens, H., Mandeville, C.W., Shimizu, N., Crede, L.S., Göttlicher, J., 2015. Experimental investigation of the S and S-isotope distribution between H_2O–S ± Cl fluids and basaltic melts during decompression. Chemical Geology 393, 36–54.

Fortin, M.-A., Riddle, J., Desjardins-Langlais, Y., Baker, D.R., 2015. The effect of water on the sulfur concentration at sulfide saturation (SCSS) in natural melts. Geochimica et Cosmochimica Acta 160, 100–116.

Freda, C., Baker, D.R., Scarlato, P., 2005. Sulfur diffusion in basaltic melts. Geochimica et Cosmochimica Acta 69, 5061–5069.

G …

Gaonac'h, H., Stix, J., Lovejoy, S., 1996. Scaling effects on vesicle shape, size and heterogeneity of lavas from Mount Etna. Journal of Volcanology and Geothermal Research 74, 131–153.

Gardner, J.E., 2007. Heterogeneous bubble nucleation in highly viscous silicate melts during instantaneous decompression from high pressure. Chemical Geology 236, 1–12. doi:10.1016/j.chemgeo.2006.08.006

Gardner, J.E., Denis, M.-H., 2004. Heterogeneous bubble nucleation on Fe-Ti oxide crystals in high-silica rhyolitic melts. Geochimica et Cosmochimica Acta 68, 3587–3597. doi:10.1016/j.gca.2004.02.021

Gardner, J.E., Ketcham, R.A., 2011. Bubble nucleation in rhyolite and dacite melts: temperature dependence of surface tension. Contributions to Mineralogy and Petrology 162, 929–943. doi:10.1007/s00410-011-0632-5

Gardner, J.E., Hilton, M., Carroll, M.R., 1999. Experimental constraints on degassing of magma: isothermal bubble growth during continuous decompression from high pressure. Earth and Planetary Science Letters 168, 201–218.

Gondé, C., Martel, C., Pichavant, M., Bureau, H., 2011. In situ bubble vesiculation in silicic magmas. American Mineralogist 96, 111–124. doi:10.2138/am.2011.3546

Gonnermann, H.M., Manga, M., 2005. Nonequilibrium magma degassing: Results from modeling of the ca. 1340 A.D. eruption of Mono Craters, California. Earth and Planetary Science Letters 238, 1–16. doi:10.1016/j.epsl.2005.07.021

Gonnermann, H.M., Manga, M., 2007. The fluid mechanics inside a volcano. Annual Review of Fluids Mechanics 39, 321–356.

Gonnermann, H.M., Gardner, J.E., 2013. Homogeneous bubble nucleation in rhyolitic melt: Experiments and nonclassical theory. Geochemistry, Geophysics, Geosystems 14, 4758–4773.

Grove, T.L., Till, C.B., Krawczynski, M.J., 2012. The role of H_2O in subduction zone magmatism. Annual Review of Earth and Planetary Sciences 40, 413–439.

H …

Hirth, J.P., Pound, G.M., Pierre, G.S., 1970. Bubble nucleation. Metallurgical Transactions 1, 939–945.

Holloway, J.R., 1981. Volatile Interactions in Magmas, in: Newton, R.C., Navrotsky, A., Wood, B.J. (Eds.), Thermodynamics of Minerals and Melts, Advances in Physical Geochemistry. Springer New York, 273–293.

Holloway, J.R., 1987. Igneous fluids. Reviews in Mineralogy and Geochemistry 17, 211–233.

Houghton, B.F., Gonnermann, H.M., 2008. Basaltic explosive volcanism: constraints from deposits and models. Chemie der Erde-Geochemistry 68, 117–140.

Hurwitz, S., Navon, O., 1994. Bubble nucleation in rhyolitic melts: Experiments at high pressure, temperature, and water content. Earth and Planetary Science Letters 122, 267–280.

I …

Iacono-Marziano, G., Schmidt, B.C., Dolfi, D., 2007. Equilibrium and disequilibrium degassing of a phonolitic melt (Vesuvius AD 79 “white pumice”) simulated by decompression experiments. Journal of Volcanology and Geothermal Research 161, 151–164. doi:10.1016/j.jvolgeores.2006.12.001

Iacono-Marziano, G., Morizet, Y., Le Trong, E., Gaillard, F., 2012. New experimental data and semi-empirical parameterization of H_2O–CO_2 solubility in mafic melts. Geochimica et Cosmochimica Acta 97, 1–23.

J …

Jaupart, C., Tait, S., 1990. Dynamics of eruptive phenomena. Reviews in Mineralogy and Geochemistry 24, 213–238.

K …

Khitarov, N.I., Lebedev, E.B., Dorfman, A.M., Bagdasarov, N.S., 1979. Effect of temperature, pressure and volatiles on the surface tension of molten basalt. Geochemistry International 16, 78–86.

L …

La Spina, A., Burton, M.R., Harig, R., Mure, F., Rusch, P., Jordan, M., Caltabiano, T., 2013. New insights into volcanic processes at Stromboli from Cerberus, a remote-controlled open-path FTIR scanner system. Journal of Volcanology and Geothermal Research 249, 66–76.

Landi, P., Mtrich, N., Bertagnini, A., Rosi, M., 2004. Dynamics of magma mixing and degassing recorded in plagioclase at Stromboli (Aeolian Archipelago, Italy). Contributions to Mineralogy and Petrology 147, 213–227. doi:10.1007/s00410-004-0555-5

Lange, R.A., 1994. The effect of H_2O, CO_2, and F on the density and viscosity of silicate melts. Reviews in Mineralogy and Geochemistry 30, 331–369.

Lensky, N.G., Niebo, R.W., Holloway, J.R., Lyakhovsky, V., Navon, O., 2006. Bubble nucleation as a trigger for xenolith entrapment in mantle melts. Earth and Planetary Science Letters 245, 278–288.

Lesne, P., 2008. Etude expérimentale de la solubilité des volatils C-H-O-S dans les basaltes alcalins italiens. Simulations numériques du dégazage chimique : application à l'Etna. Thèse, Université d'Orléans.

Lesne, P., Scaillet, B., Pichavant, M., 2015. The solubility of sulfur in hydrous basaltic melts. Chemical Geology, in press.

Lesne, P., Scaillet, B., Pichavant, M., Beny, J.-M., 2011a. The carbon dioxide solubility in alkali basalts: an experimental study. Contributions to Mineralogy and Petrology 162, 153–168.

Lesne, P., Scaillet, B., Pichavant, M., Iacono-Marziano, G., Beny, J.-M., 2011b. The H_2O solubility of alkali basaltic melts: an experimental study. Contributions to Mineralogy and Petrology 162, 133–151.

Lesne, P., Kohn, S.C., Blundy, J.D., Witham, F., Botcharnikov, R., Behrens, H., 2011c. Experimental simulation of closed-system degassing in the system basalt–H_2O–CO_2–S–Cl. Journal of Petrology 52, 1737–1762.

M …

Mader, H.M., Brodsky, E.E., Howard, D., Sturtevant, B., 1997. Laboratory simulations of sustained volcanic eruptions. Nature 388, 462–464.

Mangan, M.T., Cashman, K.V., 1996. The structure of basaltic scoria and reticulite and inferences for vesiculation, foam formation, and fragmentation in lava fountains. Journal of Volcanology and Geothermal Research 73, 1–18.

Mangan, M.T., Sisson, T., 2000. Delayed, disequilibrium degassing in rhyolite magma: decompression

experiments and implications for explosive volcanism. Earth and Planetary Science Letters 183, 441–455.

Mangan, M.T., Sisson, T., 2005. Evolution of melt-vapor surface tension in silicic volcanic systems: Experiments with hydrous melts. Journal of Geophysical Research 110, B01202. doi:10.1029/2004JB003215

Mangan, M.T., Sisson, T.W., Hankins, W.B., 2004. Decompression experiments identify kinetic controls on explosive silicic eruptions. Geophysical Research Letters 31, L08605. doi:10.1029/2004GL019509

Marsh, B.D., 1988. Crystal size distribution (CSD) in rocks and the kinetics and dynamics of crystallization. Contributions to Mineralogy and Petrology 99, 277–291.

Martel, C., 1996. Conditions pré-éruptive et dégazage des magmas andésitique de la Montagne Pelée (Martinique) : étude pétrologique et expérimentale. Thèse, Université d'Orléans.

Masotta, M., Ni, H., Keppler, H., 2014. In situ observations of bubble growth in basaltic, andesitic and rhyodacitic melts. Contributions to Mineralogy and Petrology 167, 976. doi:10.1007/s00410-014-0976-8

McMillan, P.F., 1994. Water solubility and speciation models. Reviews in Mineralogy and Geochemistry 30, 132–156.

Mercalli, G., 1907. Vulcani attivi della Terra. Ulrico Hoepli.

Métrich, N., Wallace, P.J., 2008. Volatile abundances in basaltic magmas and their degassing paths tracked by melt inclusions. Reviews in Mineralogy and Geochemistry 69, 363–402.

Métrich, N., Bertagnini, A., Di Muro, A., 2010. Conditions of magma storage, degassing and ascent at Stromboli: new insights into the volcano plumbing system with inferences on the eruptive dynamics. Journal of Petrology 51, 603–626.

Métrich, N., Bertagnini, A., Landi, P., Rosi, M., 2001. Crystallization driven by decompression and water loss at Stromboli volcano (Aeolian Islands, Italy). Journal of Petrology 42, 1471–1490.

Métrich, N., Bertagnini, A., Landi, P., Rosi, M., Belhadj, O., 2005. Triggering mechanism at the origin of paroxysms at Stromboli (Aeolian Archipelago, Italy): the 5 April 2003 eruption. Geophysical Research Letters 32, L103056. doi:10.1029

Moore, J.C., Vrolijk, P., 1992. Fluids in accretionary prisms. Reviews of Geophysics 30, 113–135.

Mourtada-Bonnefoi, C.C., 1998. Volcanologie physique : Dynamique thermochimique des chambres magmatiques et vésiculation des magmas rhyolitiques. Thèse, Université de Clermont-Ferrand 2.

Mourtada-Bonnefoi, C.C., Laporte, D., 1999. Experimental study of homogeneous bubble nucleation in rhyolitic magmas. Geophysical Research Letters 26, 3505–3508.

Mourtada-Bonnefoi, C.C., Laporte, D., 2002. Homogeneous bubble nucleation in rhyolitic magmas: an experimental study of the effect of H_2O and CO_2. Journal of Geophysical Research 107 (B4). doi:10.1029/2001JB00290

Mourtada-Bonnefoi, C.C., Laporte, D., 2004. Kinetics of bubble nucleation in a rhyolitic melt: an experimental study of the effect of ascent rate. Earth and Planetary Science Letters 218, 521–

537.

N …

Navon, O., Lyakhovsky, V., 1998. Vesiculation processes in silicic magmas. In: Gilbert, J.S. & Sparks, R.S.J. (Eds.) The Physics of Explosive Volcanic Eruptions. Geological Society, London, Special Publications 145, 27–50.

Navon, O., Chekhmir, A., Lyakhovsky, V., 1998. Bubble growth in highly viscous melts: theory, experiments, and autoexplosivity of dome lavas. Earth and Planetary Science Letters 160, 763–776.

Newman, S., Lowenstern, J.B., 2002. VolatileCalc: a silicate melt–H_2O–CO_2 solution model written in Visual Basic for Excel. Computers & Geosciences 28, 597–604.

O …

Okumura, S., Nakashima, S., 2006. Water diffusion in basaltic to dacitic glasses. Chemical Geology 227, 70–82.

P …

Papale, P., 1999. Strain-induced magma fragmentation in explosive eruptions. Nature 397, 425–428.

Papale, P., Moretti, R., Barbato, D., 2006. The compositional dependence of the saturation surface of H_2O+ CO_2 fluids in silicate melts. Chemical Geology 229, 78–95.

Persikov, E.S., Bukhtiyarov, P.G., Nekrasov, A.N., 2010. Water diffusion in basalt and andesite melts under high pressures. Geochemistry International 48, 213–225.

Pichavant, M., Pompilio, M., D'Oriano, C., Di Carlo, I., 2011. Petrography, mineralogy and geochemistry of a primitive pumice from Stromboli: implications for the deep feeding system. European Journal of Mineralogy 23, 499–517.

Pichavant, M., Di Carlo, I., Le Gac, Y., Rotolo, S.G., Scaillet, B., 2009. Experimental constraints on the deep magma feeding system at Stromboli volcano, Italy. Journal of Petrology 50, 601–624.

Pichavant, M., Di Carlo, I., Rotolo, S.G., Scaillet, B., Burgisser, A., Le Gall, N., Martel, C., 2013. Generation of CO_2-rich melts during basalt magma ascent and degassing. Contributions to Mineralogy and Petrology 166, 545–561.

Pioli, L., Erlund, E., Johnson, E., Cashman, K., Wallace, P., Rosi, M., Granados, H.D., 2008. Explosive dynamics of violent Strombolian eruptions: the eruption of Parícutin Volcano 1943–1952 (Mexico). Earth and Planetary Science Letters 271, 359–368.

Polacci, M., Baker, D.R., Bai, L., Mancini, L., 2008. Large vesicles record pathways of degassing at basalt volcanoes. Bulletin of Volcanology 70, 1023–1029. doi 10.1007/s00445-007-0184-8

Polacci, M., Baker, D.R., Mancini, L., Tromba, G., Zanini, F., 2006. Three-dimensional investigation of volcanic textures by X-ray microtomography and implications for conduit processes.

Geophysical Research Letters 33, L13312. doi:10.1029/2006GL026241

Polacci, M., Baker, D.R., Mancini, L., Favretto, S., Hill, R.J., 2009. Vesiculation in magmas from Stromboli and implications for normal Strombolian activity and paroxysmal explosions in basaltic systems. Journal of Geophysical Research 114, B01206. doi:10.1029/2008JB005672

Pownceby, M.I., O'Neill, H.S.C., 1994. Thermodynamic data from redox reactions at high temperatures. III. Activity-composition relations in Ni-Pd alloys from EMF measurements at 850–1250 K, and calibration of the NiO+ Ni-Pd assemblage as a redox sensor. Contributions to Mineralogy and Petrology 116, 327–339.

Proussevitch, A.A., Sahagian, D.L., Tsentalovich, E.P., 2007. Statistical analysis of bubble and crystal size distributions: Formulations and procedures. Journal of Volcanology and Geothermal Research 164, 95–111.

R …

Richet, P., Whittington, A., Holtz, F., Behrens, H., Ohlhorst, S., Wilke, M., 2000. Water and the density of silicate glasses. Contributions to Mineralogy and Petrology 138, 337–347.

Robie, R. A., Hemingway, B. S., Fisher, J. R., 1979. Thermodynamic properties of minerals and related substances at 298.15 K and 1 bar (10^5 pascals) pressure and at higher temperatures. US Geological Survey, Bulletin 1452.

Rosi, M., Bertagnini, A., Landi, P., 2000. Onset of the persistent activity at Stromboli volcano (Italy). Bulletin of Volcanology 62, 294–300.

Rosi, M., Pistolesi, M., Bertagnini, A., Landi, P., Pompilio, M., Di Roberto, A., 2013. Stromboli volcano, Aeolian Islands (Italy): present eruptive activity and hazards. Geological Society, London, Memoirs 37, 473–490.

S …

Sable, J.E., Houghton, B.F., Del Carlo, P., Coltelli, M., 2006. Changing conditions of magma ascent and fragmentation during the Etna 122 BC basaltic Plinian eruption: evidence from clast microtextures. Journal of Volcanology and Geothermal Research 158, 333–354.

Sable, J.E., Houghton, B.F., Wilson, C.J.N., Carey, R.J., 2009. Eruption mechanisms during the climax of the Tarawera 1886 basaltic Plinian eruption inferred from microtextural characteristics of the deposits. Studies in volcanology. The legacy of George Walker. Geological Society, London, 129–154.

Shea, T., Houghton, B.F., Gurioli, L., Cashman, K.V., Hammer, J.E., Hobden, B.J., 2010. Textural studies of vesicles in volcanic rocks: an integrated methodology. Journal of Volcanology and Geothermal Research 190, 271–289.

Shishkina, T.A., Botcharnikov, R.E., Holtz, F., Almeev, R.R., Portnyagin, M.V., 2010. Solubility of H_2O-and CO_2-bearing fluids in tholeiitic basalts at pressures up to 500MPa. Chemical Geology 277, 115–125.

Sigurdsson, H., Houghton, B., McNutt, S., Rymer, H., Stix, J., 2015. The encyclopedia of volcanoes. Elsevier.

Simakin, A.G., Armienti, P., Epel'baum, M.B., 1999. Coupled degassing and crystallization: experimental study at continuous pressure drop, with application to volcanic bombs. Bulletin of Volcanology 61, 275–287.

Sparks, R.S.J., 1978. The dynamics of bubble formation and growth in magmas: a review and analysis. Journal of Volcanology and Geothermal Research 3, 1–37.

Sparks, R.S.J., Barclay, J., Jaupart, C.P.M.A., Mader, H.M., Phillips, J.C., 1994. Physical aspects of magma degassing I. Experimental and theoretical constraints on vesiculation. American Society of Mineralogy Reviews 30, 413–445.

Sparks, R.S.J., Bursik, M.I., Carey, S.N., Gilbert, J., Glaze, L.S., Sigurdsson, H., Woods, A.W., 1997. Volcanic plumes. Wiley.

Spieler, O., Kennedy, B., Kueppers, U., Dingwell, D.B., Scheu, B., Taddeucci, J., 2004. The fragmentation threshold of pyroclastic rocks. Earth and Planetary Science Letters 226, 139–148.

Spilliaert, N., 2006. Dynamiques de remontée, dégazage et éruption des magmas basaltiques riches en volatils: traçage par les inclusions vitreuses et modélisation des processus dans le cas de l'Etna, 2000-2002. Thèse, Institut de physique du globe de Paris-IPGP.

Stolper, E., 1982. The speciation of water in silicate melts. Geochimica et Cosmochimica Acta 46, 2609–2620.

Symonds, R.B., Rose, W.I., Bluth, G.J., Gerlach, T.M., 1994. Volcanic-gas studies; methods, results, and applications. Reviews in Mineralogy and Geochemistry 30, 1–66.

T …

Taylor, J.R., Wall, V.J., Pownceby, M.I., 1992. The calibration and application of accurate redox sensors. American Mineralogist 77, 284–295.

Toramaru, A., 1989. Vesiculation process and bubble size distributions in ascending magmas with constant velocities. Journal of Geophysical Research 94, 17523–17542.

Toramaru, A., 1990. Measurement of bubble size distributions in vesiculated rocks with implications for quantitative estimation of eruption processes. Journal of Volcanology and Geothermal Research 43, 71–90.

Toramaru, A., 1995. Numerical study of nucleation and growth of bubbles in viscous magmas. Journal of Geophysical Research 100, 1913–1931.

Toramaru, A., 2006. BND (bubble number density) decompression rate meter for explosive volcanic eruptions. Journal of Volcanology and Geothermal Research 154, 303–316.

Toramaru, A., 2014. On the second nucleation of bubbles in magmas under sudden decompression. Earth and Planetary Science Letters 404, 190–199.

V …

Vetere, F., Behrens, H., Misiti, V., Ventura, G., Holtz, F., De Rosa, R., Deubener, J., 2007. The viscosity of shoshonitic melts (Vulcanello Peninsula, Aeolian Islands, Italy): insight on the

magma ascent in dikes. Chemical Geology 245, 89–102.

W …

Wallace, P.J., 2005. Volatiles in subduction zone magmas: concentrations and fluxes based on melt inclusion and volcanic gas data. Journal of Volcanology and Geothermal Research 140, 217–240.

Wallace, P.J., Plank, T., Edmonds, M., Hauri, E.K., 2015. The encyclopedia of volcanoes. Elsevier.

Watson, E.B., Wark, D.A., Delano, J.W., 1993. Initial report on sulfur diffusion in magmas. EOS Transactions American Geophysical Union 74, 620.

Webster, J.D., Botcharnikov, R.E., 2011. Distribution of Sulfur Between Melt and Fluid in S-O-H-C-Cl-Bearing Magmatic Systems at Shallow Crustal Pressures and Temperatures. Reviews in Mineralogy and Geochemistry 73, 247–283. doi:10.2138/rmg.2011.73.9

Wilson, T.M., Jenkins, S., Stewart, C., 2014. Impacts from Volcanic Ash Fall. Volcanic Hazards, Risks and Disasters 47.

Witham, F., Blundy, J., Kohn, S.C., Lesne, P., Dixon, J., Churakov, S.V., Botcharnikov, R., 2012. SolEx: a model for mixed COHSCl-volatile solubilities and exsolved gas compositions in basalt. Computers & Geosciences 45, 87–97.

Y …

Yamada, K., Tanaka, H., Nakazawa, K., Emori, H., 2005. A new theory of bubble formation in magma. Journal of Geophysical Research 110, B02203. doi:10.1029/2004JB003113

Z …

Zellmer, G.F., Edmonds, M., Straub, S.M., 2015. Volatiles in subduction zone magmatism. Geological Society, London, Special Publications 410, 1–17.

Zhang, Y., 1999. A criterion for the fragmentation of bubbly magma based on brittle failure theory. Nature 402, 648–650.

Zhang, Y., Stolper, E.M., 1991. Water diffusion in a basaltic melt. Nature 351, 306–309.

Zhang, Y., Ni, H., 2010. Diffusion of H, C, and O components in silicate melts. Reviews in Mineralogy and Geochemistry 72, 171–225.

Zhang, Y., Xu, Z., Zhu, M., Wang, H., 2007. Silicate melt properties and volcanic eruptions. Reviews of Geophysics 45, RG4004. doi:10.1029/2006RG000216

Chapitre i

Figure i.1. Représentation schématique des processus de dégazage des magmas intervenant dans le conduit volcanique.

Figure i.2. Régimes de séparation magma/gaz en fonction de la vitesse d'ascension dans les systèmes basaltiques, d'après Edmonds (2008).

Fig. i.3. Illustration de la sursaturation en H_2O d'un magma lors de son ascension dans le conduit volcanique. Initialement, l'eau est dissoute dans le liquide silicaté.

Figure i.4. Schémas illustrant la nucléation homogène des bulles de gaz à l'échelle du liquide silicaté (b) et à l'échelle du conduit volcanique (c). (a) Etat initial du liquide silicaté : avant l'événement de nucléation homogène des bulles, les volatils sont sous forme dissoute.

Figure i.5. Schémas illustrant la nucléation hétérogène des bulles de gaz au sein du liquide silicaté (a) et dans le conduit volcanique (c). (b) Relation de mouillage entre cristal, liquide et bulle.

Figure i.6. Distributions unimodale, en loi de puissance et exponentielle de la taille des bulles, d'après Blower et al. (2002).

Figure i.7. Modèle numérique de Blower et al. (2002).

Figure i.8. Teneurs en H_2O et en CO_2 dans les inclusions vitreuses (Iv) et les embayments (Emb.) des ponces et des scories Stromboliennes, d'après Métrich et al. (2010).

Figure i.9. Photos d'une éruption effusive (a), d'une éruption Strombolienne (b) et de l'éruption paroxysmale du 5 avril 2003 au Stromboli (c).

Figure i.10. Détermination de la pression de nucléation des bulles (P_N), ou pression de sursaturation en volatils (ΔP_N), lors de l'étape de décompression.

Figure i.11. Géolocalisation du volcan Stromboli (vue satellite *Google Earth*).

Figure i.12. Représentation schématique du système d'alimentation du Stromboli, d'après Bonaccorso et al. (2012).

Figure i.13. Photo de la ponce PST-9.

Figure i.14. Illustration de la corrélation entre la composition des gaz (rapports molaires CO_2/SO_2 et H_2O/CO_2) et l'activité volcanique du Stromboli ((a) Aiuppa et al., 2009 ; (b) Aiuppa et al., 2010a).

Chapitre ii

Figure ii.1. Image MEB de sulfures de platine formés par interaction entre la charge et la capsule en Pt.

Figure ii.2. Schéma du remplissage des capsules.

Figure ii.3. Quantité d'H_2O (% pds) produite au cours des expériences de synthèse.

Figure ii.4. Photo d'un des deux autoclaves à chauffage interne utilisés.

Figure ii.5. Schéma du remplissage des capsules sensors.

Figure ii.6. Images tomographiques de verres synthétisés dépourvus de cristaux et de bulles.

Figure ii.7. Déroulement d'une expérience de décompression.

Figure ii.8. Découpe des cylindres de verre.

Figure ii.9. Schémas représentatifs du volume total (a) et d'un sous-volume de l'échantillon (b).

Figure ii.10. Exemples de segmentation manuelle de l'image tomographique d'un verre décomprimé à 25 MPa (a). (b) Extraction des bulles et (c) des oxydes.

Figure ii.11. Exemples d'images MEB où de très petites bulles sont présentes (a, b) et où la relation bulle-sulfure de fer est détaillée (c).

Figure ii.12. Cartographies de la répartition des éléments S (a), Fe (b) et Pt (c) dans une capsule en Pt.

Figure ii.13. Exemple de spectre IR typique pour l'analyse de l'eau et du CO_2 (CO_3^{2-}).

Synthèse générale et perspectives

Figure 1. Représentation schématique des conditions de la vésiculation et de la fragmentation des liquides basaltiques hydratés dans un conduit volcanique.

Figure 2. Représentations schématiques des conditions de la vésiculation du système basalte-H_2O-CO_2 dans un conduit volcanique. (a) Cas d'un système basaltique riche en H_2O et pauvre en CO_2. (b) Cas d'un système basaltique pauvre en H_2O et riche en CO_2.

Figure 3. Images tomographiques des textures de verres expérimentaux issus des séries #1 (a), #2 (b) et #3 (c) décomprimés à 25 MPa P_f à la vitesse de 3 m/s.

Figure 4. (a) Illustration schématique de la nucléation continue des bulles d'H_2O-CO_2, d'après Blower et al. (2002) et Yamada et al. (2005). (b) Photo comparative d'un verre expérimental.

Figure 5. Représentation schématique des conditions de la vésiculation du système basalte-H_2O-CO_2-S dans un conduit volcanique.

Figure 6. Diagramme montrant l'évolution du diamètre moyen des bulles *D* en fonction de l'évolution de la densité numérique de bulles *BND*, entre 50 et 25 MPa.

Chapitre i

Tableau i.1. Composition chimique de la ponce PST-9

Chapitre ii

Tableau ii.1. Compositions chimiques des deux verres de départ enrichi et non en fer

Nolwenn LE GALL

Ascension et dégazage des magmas basaltiques – Approche expérimentale

Résumé :

Afin de parvenir à une meilleure compréhension de la dynamique d'ascension et d'éruption des magmas basaltiques, nous avons réalisé des expériences de décompression à haute pression (200–25 MPa) et haute température (1200°C) spécifiquement orientées pour documenter la nucléation des bulles de gaz ; ce processus, qui constitue la première étape du dégazage magmatique, conditionne l'évolution de la phase gazeuse (force motrice des éruptions explosives) dans le conduit volcanique. Quatre principaux ensembles d'expériences ont été menés afin de mieux comprendre le rôle des volatils majeurs (H_2O, CO_2, S), ainsi que les effets de la vitesse d'ascension et de la présence de cristaux sur la cinétique de vésiculation (nucléation, croissance, coalescence) des bulles dans les magmas basaltiques. L'objectif est de comprendre les mécanismes qui contrôlent les caractéristiques texturales (nombre, taille, forme des bulles) et chimiques (teneur en volatils dissous, composition des gaz) des produits naturels et de les approcher expérimentalement. Dans ce sens, les verres expérimentaux ont été analysés avant et après décompression sur le plan textural (microtomographie par rayons X, MEB) et chimique (FTIR, microsonde électronique). Nos résultats démontrent une forte influence du CO_2 sur les processus ainsi que sur le mode (équilibre vs. déséquilibre) de dégazage des magmas basaltiques, en lien avec des différences de solubilité et de diffusivité entre les espèces volatiles. Nos données, obtenues dans des conditions voisines des conditions naturelles, ont des implications volcanologiques pour l'interprétation des textures de bulles et des mesures de gaz en sortie de conduit, ainsi que, plus spécifiquement, pour la dynamique des éruptions paroxysmales au Stromboli.

Mots clés : dégazage, basalte, volatil, nucléation, bulle, Stromboli

Basaltic magma ascent and degassing – Experimental approach

Abstract:

For a better understanding of the dynamics of ascent and eruption of basaltic magmas, we have performed high pressure (200–25 MPa) and high temperature (1200°C) decompression experiments specifically oriented to document gas bubble nucleation processes. Bubble nucleation occurs first during magma degassing and, so, it is critical to understand bubble nucleation processes to constrain the evolution of the gas phase (which is the driving force of explosive eruptions) in the volcanic conduit. Four main sets of experiments were conducted to better assess the role of the major volatiles (H_2O, CO_2, S), as well as the effects of ascent rate and crystals, on bubble vesiculation (nucleation, growth, coalescence) kinetics in basaltic magmas. The aim of the study is to understand the mechanisms which control the textural (number, size, shape of bubbles) and the chemical (dissolved volatile concentrations, gas composition) characteristics of natural products, and also to approach them experimentally. In this way, experimental melts, before and after decompression, were analysed texturally (by X-ray microtomography and MEB) and chemically (by FTIR and electron microprobe). Our results demonstrate a strong influence of CO_2 on degassing mode (equilibrium vs. disequilibrium) and mechanisms, which are shown to be controlled by differences in solubility and diffusivity between the main volatile species. Finally, our data, obtained under conditions closely approaching natural eruptions, have volcanological implications for the interpretation of bubble textures and gas measurements, as well as, more specifically, for the dynamics of Strombolian paroxysms.

Keywords : degassing, basalt, volatile, nucleation, bubble, Stromboli

Institut des Sciences de la Terre d'Orléans
ISTO - UMR7327 CNRS / Université d'Orléans
1A, rue de la Férollerie
45071 Orléans Cedex 2
France